FOUR-DIMENSIONAL PASSIVE VELOCITY TOMOGRAPHY OF A LONGWALL PANEL

Kramer Davis Luxbacher

Thesis submitted to the faculty of the Virginia Polytechnic Institute and State University in partial fulfillment of the requirements for the degree of

Master of Science
In
Mining & Minerals Engineering

Dr. Erik Westman, Chairman
Dr. Thomas Novak
Dr. Mario Karfakis

December 12, 2005
Blacksburg, VA

Keywords: Velocity Tomography, Stress Redistribution, Longwall Mining

FOUR-DIMENSIONAL PASSIVE VELOCITY TOMOGRAPHY OF A LONGWALL PANEL

Kramer Davis Luxbacher

ABSTRACT

Velocity tomography is a noninvasive technology that can be used to determine rock mass response to ore removal. Velocity tomography is accomplished by propagating seismic waves through a rock mass to measure velocity distribution of the rock mass. Tomograms are created by mapping this velocity distribution. From the velocity distribution relative stress in the rock mass can be inferred, and this velocity distribution can be mapped at specific time intervals.

Velocity tomography is an appropriate technology for the study of rockbursts. Rockbursts are events that occur in underground mines as a result of excessive strain energy being stored in a rock mass and sometimes culminating in violent failure of the rock. Rockbursts often involve inundation of broken rock into open areas of the mine. They pose a considerable risk to miners and can hinder production substantially.

The rock mass under investigation in this research is the strata surrounding an underground coal mine in the western United States, utilizing longwall mining. The mine has experienced rockbursts. Seismic data were collected over a nineteen day period, from July 20th, 1997 to August 7th, 1997, although only eighteen days were recorded. Instrumentation consisted of sixteen receivers, mounted on the surface, approximately 1,200 feet above the longwall panel of interest. The system recorded and located microseismic events, and utilized them as seismic sources.

The data were analyzed and input into a commercial program that uses an algorithm known as simultaneous iterative reconstruction technique to generate tomograms. Eighteen tomograms were generated, one for each day of the study. The tomograms consistently display a high velocity area along the longwall tailgate that

redistributes with face advance. Numerical modeling and mine experience confirm that the longwall tailgate is subject to high stress. Additionally, microseismic events are correlated with the velocity tomograms.

Velocity tomography proves to be an effective method for the study of stress redistribution and rockburst phenomena at underground longwall coal mines, because it generates images that are consistent with prior information about the stress state at the mine and with numerical models of the stress in the mine.

ACKNOWLEDGEMENTS

First, I would like to thank my advisor, Dr. Erik Westman, for his invaluable advice and guidance. I also appreciate the encouragement and support of my committee members, Dr. Thomas Novak and Dr. Mario Karfakis. I would also like to express my appreciation for the opportunities afforded me by the National Science Foundation and the Department of Mining and Minerals Engineering at Virginia Tech.

Also, I would like to thank Dr. Peter Swanson at the National Institute for Occupational Safety and Health for providing the raw data for this research, and for his assistance in completing the research.

Next, I could not have completed this research with the support of my family, especially my husband, Mark.

Finally, I am indebted to the coal miners I have worked with who taught me a great deal about underground mining and the importance of improving safety through research.

TABLE OF CONTENTS

LIST OF FIGURES

LIST OF TABLES

CHAPTER 1: INTRODUCTION

Underground coal mining has seen drastic improvements in productivity with the advent of longwall mining. However, unique hazards and risks are associated with underground coal mining, and one of the foremost challenges related to these hazards is roof characterization and control. Quantifying stress redistribution in a rock mass is complicated as it relies on both the properties of the rocks that compose the mass and the structure of the rock mass. Tomographic imaging of stress redistribution underground has been achieved with some success, but direct application to production and safety has been limited.

Imaging of stress redistribution in underground coal mines is of paramount importance in understanding failure mechanisms of mine roof. Roof failure occurs on all scales from localized falls to large rockbursts. Rockbursts are sudden and violent failures of overstressed rock ("30 C.F.R. §57.3461" 2005) that result in the release of large amounts of energy, often causing expulsion of material or airblasts. Rockbursts pose a considerable danger to miners and can result in extensive production delays. If the stress redistribution associated with these failures can be imaged and characterized, this could eventually lead to prediction of rockbursts.

5,054 recordable accidents were reported in underground coal mines in the United States in 2004. Of these, 1,627, or 32%, were due to fall of roof or rib. Lost time accidents due to fall of roof or rib in the United States underground coal industry averaged 57 days lost per miner injured (MSHA 2005a). At 4.04 tons per man hour (NMA 2005) this equates to a significant loss in production. Additionally, fall of roof or rib in underground mines accounted for 19% of coal mining fatalities, both underground and surface, between January 1st, 2001 and November 1st, 2005 (MSHA 2005c). This accident data is summarized in Figure 1.1:

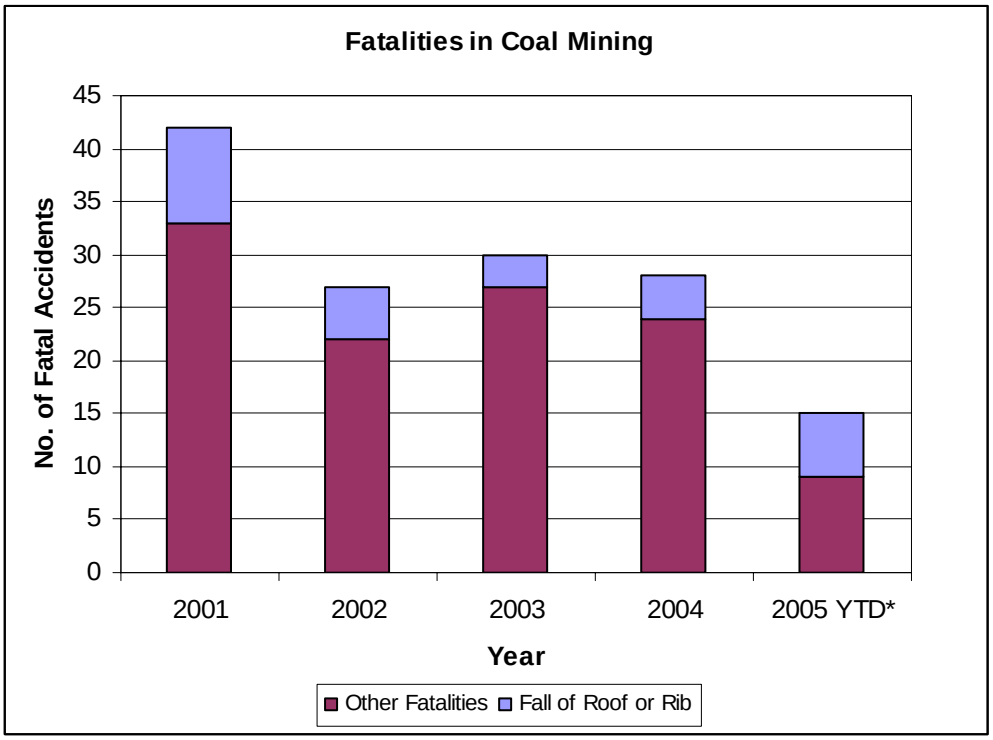

Figure 1.1. Fatal Accidents in Coal Mining in the United States.[*]

Velocity tomography has been utilized as a method for inferring stress distribution in rocks, both in the laboratory and in mines, but has yet to yield comprehensive understanding of the phenomenon. Monitoring of coal mine roof in the past has relied on localized measurement of the roof, with inferences being made about the state of stress over a large area. Tomography has the unique ability to probe and image a large area of a mine, noninvasively.

Rock mass tomography involves propagating energy through the rock mass, and measuring quantitative parameters of the energy. In this case, seismic waves are propagated through the rock mass and their travel times are measured. The velocities resulting from these travel times are used to infer information about the state of stress in the rock mass.

The research presented involves generating tomograms for 18 days of production at an underground longwall coal mine in the western United States. The data utilized for generating the tomograms were collected from a microseismic event location

[*] YTD refers to November 1, 2005.

network. The tomograms are compared with microseismic events and rate of longwall face advance, to determine the effects these parameters have on stress redistribution. Since no traditional stress measurements in the area during the survey are available, the results are also compared to a numerical model of the stress state.

CHAPTER 2: LITERATURE REVIEW

Utilization of seismic velocity tomography in underground mines requires an understanding of rock mechanics and tomography. Stress redistribution in underground mines results from the removal of ore. Rock and fracture mechanics provide an understanding of how stress is transferred and how rock fails. However, application of rock mechanics theory is limited by *a priori* knowledge of the rock mass.

Velocity tomography allows for the entire rock mass to be explored in a noninvasive way by relating p-wave velocity to the elastic properties of rock and inferring the stress state of the rock mass. However, tomography only provides a model of the solid being imaged. An understanding of rock mechanics and expected stress redistribution in an underground mine is essential in evaluating tomograms.

2.1 Failure of Rock

2.1.1 ROCK MECHANICS

A brief review of rock mechanics is instrumental in understanding stress redistribution in an underground mine. Stress in a mine is caused by various phenomena. Gravitational stress, tectonic stress, and thermal stress may all be present in an underground mine (Herget, G. 1988).

Stress is defined as a force over an area. Newton's first law defines force as equal to mass multiplied by acceleration. In order to determine gravitational stress in a mine, the overburden may be divided into columns of material. The mass of the column multiplied by gravitational acceleration, 9.8 m/s^2 (32.2 ft/s^2), is the force acting on the area. The force multiplied by the cross-sectional area of the column gives the vertical stress component due to gravity, σ_v, in the area. In integral form σ_v may be defined as follows:

$$\sigma_v = \int_0^z \rho g \, dz$$

$$\rho = \text{density} = \frac{\text{mass}}{\text{volume}} \qquad \left(\frac{\text{lbs}}{\text{ft}^3}\right) \qquad [2.1]$$

g = acceleration due to gravity $\left(\text{ft/s}^2\right)$

z = depth $\left(\text{ft}\right)$

(Herget, G. 1988).

Defining the horizontal stress component due to gravity is more complex, and is dependent on geologic structure, such as faulting and jointing, and on the other characteristics of the rock mass. In a strictly elastic rock mass the horizontal component, σ_H, is defined as:

$$\sigma_H = \frac{\upsilon}{1-\upsilon}\sigma_V \qquad \left(\text{psi}\right)$$

where, υ is Poisson's ratio

$$\upsilon = \frac{\Delta D/D}{\Delta L/L} = \frac{\text{axial strain}}{\text{lateral strain}} \qquad \left(\text{unitless}\right) \qquad [2.2]$$

where, D = diameter $\left(\text{ft}\right)$

L = Length $\left(\text{ft}\right)$

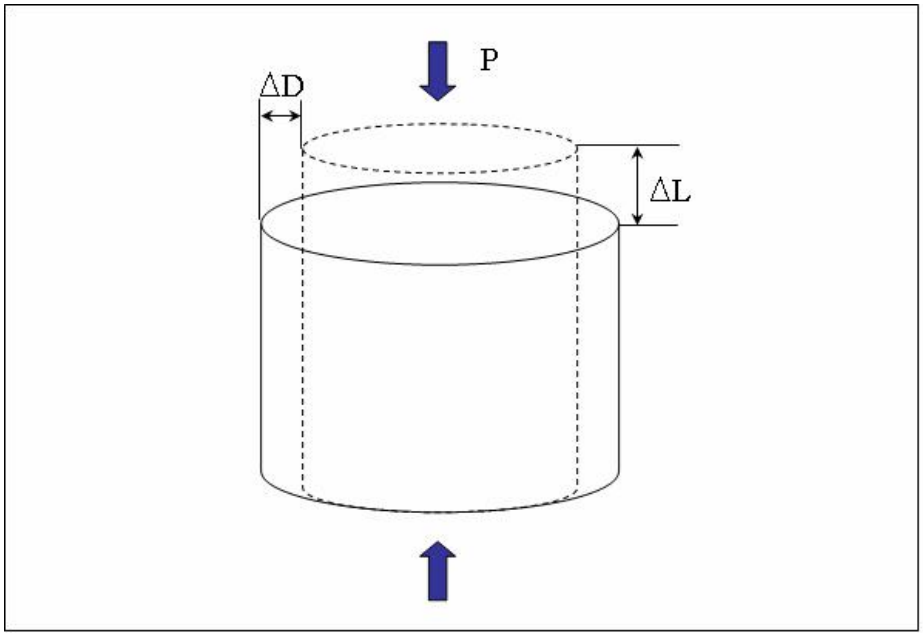

Figure 2.1. Poisson's Ratio (Peng, S. S. 1986).

Of course, the perfectly elastic requirement is never met *insitu*, and the horizontal component is often estimated from site measurements.

A schematic illustrating determination of Poisson's ratio in a laboratory specimen is shown in Figure 2.1 for a load P applied parallel to the long axis of a cylindrical sample. Typical values for Poisson's ratio are in the range of 0.15 to 0.35 (Herget, G. 1988).

Tectonic stresses result from the movement of plates in the earth, and can vary regionally. They may create a horizontal stress component, which, when added to the gravitational horizontal stress component, can exceed the vertical stress component (Herget, G. 1988). Kelly and Gale found that in many Australian coal mines the principal horizontal stress component was as much as 2.5 times the vertical stress component (Kelly, M. and W. Gale 2000).

Stress may also be caused by temperature change in rock. Very deep mines may experience thermal expansion of rock. According to Herget, the linear coefficient of thermal expansion in sandstone is 10.8 x 10^{-8}m per 1°C (1988). However, in the United States, most coal mines are not deep enough to experience substantial thermal stress.

2.1.2 FRACTURE MECHANICS

Rocks generally exhibit two distinct failure behaviors, elastic-plastic and elastic-brittle behavior (Blès, J. L. and B. Feuga 1986). In order to define elastic-plastic and elastic-brittle behavior, strain must first be defined. Strain, ε, refers the compression or the extension of rock resulting from the application of force to the body, divided by the original dimension of the rock. For example, strain in a cylindrical rock sample refers to the change in length of the sample when pressure is applied parallel to the long axis, so:

$$\varepsilon = \frac{\Delta L}{L} \qquad (\text{unitless}) \qquad [2.3]$$

(Peng, S. S. 1986).

A stress-strain curve is particularly instructive in examining rock failure. Typical curves are shown in Figure 2.2 for elastic-plastic and elastic-brittle behavior:

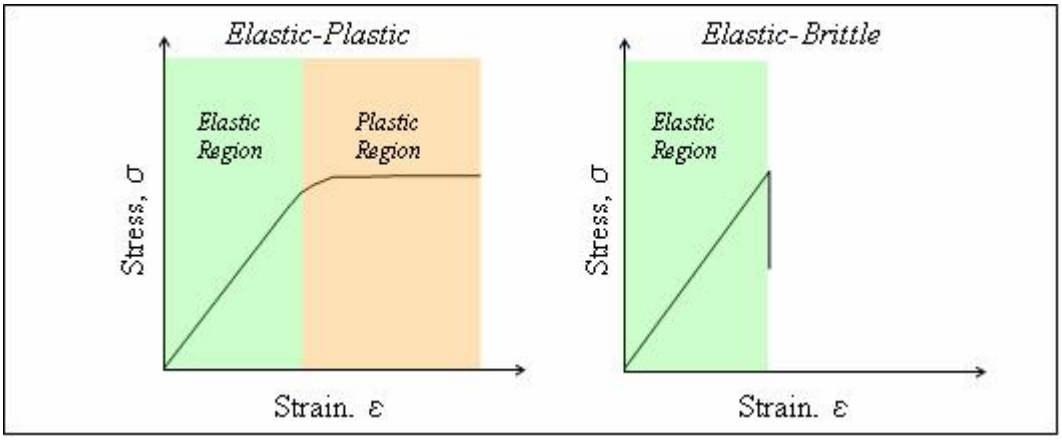

Figure 2.2. Generalized Stress-Strain curves for Elastic-Plastic and Elastic-Brittle Failure. (Blès, J. L. and B. Feuga 1986).

Young's modulus, *E*, the slope of the stress-strain curve, is a useful descriptor for elasticity of rocks and is equal to:

$$E = \frac{\sigma}{\varepsilon} \qquad (\text{psi}) \qquad [2.4]$$

Other measures of elasticity include the bulk modulus, *K*, and the shear modulus, μ, also known as the modulus of rigidity. Equations for both moduli are displayed below:

$$K = \frac{E}{3(1-\upsilon)} \qquad (\text{psi}) \qquad [2.5]$$

$$\mu = \frac{E}{2(1+\upsilon)} \qquad (\text{psi}) \qquad [2.6]$$

(Herget, G. 1988)

Failure of rock occurs when stress exceeds rock strength, at the maximum point on the stress-strain curve. Mechanics of the failure are dependent on the characteristics of the rock, including existing fractures. A number of failure criteria have been developed to describe the relationship between stress and failure in rock. Some of the

most prominent of these are the Coulomb Criterion, Mohr-Coulomb Criterion, and Hoek-Brown Criterion (Blès, J. L. and B. Feuga 1986).

In 1773 Coulomb proposed the following equation describing shear failure in materials (Blès, J. L. and B. Feuga 1986, Herget, G. 1988):

$$\tau = S_0 + \mu\sigma$$

where,

S_0 = inherent shear strength or cohesion [2.7]

$\mu = \tan\phi$

ϕ = internal angle of friction

Mohr developed a circle relating stresses at failure as illustrated in Figure 2.3:

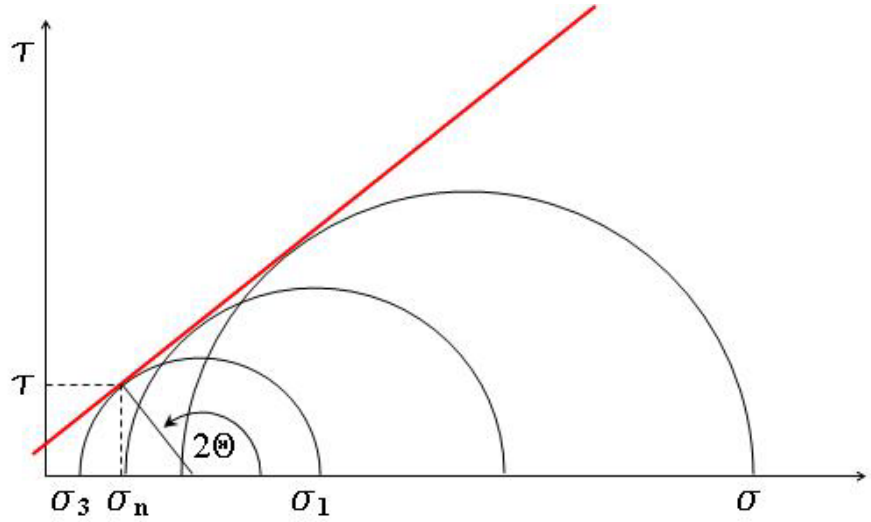

Figure 2.3. Typical Mohr Circle Diagram. (Herget, G. 1988)

When Mohr's circle touches or exceeds the envelope failure occurs. The envelope does not necessarily have to be linear, simply tangential to the circles (Herget, G. 1988). The Mohr-Coulomb Criterion is defined as follows (Edelbro, C. 2004):

$$\sigma_1 = \frac{2\cos\phi}{1-\sin\phi} + \frac{1+\sin\phi}{1-\sin\phi}\sigma_3 \qquad (\text{psi}) \qquad [2.8]$$

The stresses, σ_1 and σ_3, represent major and minor principal stresses at failure, respectively. Herget describes the Mohr-Coulomb criteria in detail (1988).

In 1980, Hoek and Brown presented the following criteria for peak triaxial strength:

$$\sigma_1 = \sigma_3 + \sqrt{m\sigma_3\sigma_c + s\sigma_c^2} \qquad (\text{psi})$$

Where, [2.9]

σ_c = uniaxial compressive strenth of rock material

The factor, *m*, is dependent on mineralogy, composition and grain size while *s* is dependent on tensile strength and degree of fracturization (Hoek, E. and E. T. Brown 1980, Herget, G. 1988, Edelbro, C. 2004). By including *s* and *m* Hoek and Brown were attempting to present a criterion that could be used to characterize a relatively large rock mass (Hoek, E. and E. T. Brown 1980). However, for a nonhomogenous rock mass, calculation is still cumbersome.

These criteria were presented to give some concept of the relationships between stress and failure. The criteria can be applied with success in the laboratory, but in the field it is more difficult to quantify stress behavior and failure over a large rock mass, so often various rock mass quality designations are used. However, rock mass quality designations do not quantify stress behavior or failure characteristics, they only characterize the state of the rock mass. These designations include the Rock Quality Designation, RQD (Deere, D. U. 1964), the Rock Mass Quality Index, Q (Barton, N. 1987), the Rock Mass Rating system, RMR (Bieniaski, Z. T. 1989), the Coal Mine Roof Rating, CMRR (Molinda, G. M. and C. Mark 1994), and various other empirical relationships.

In 1921 Griffith proposed a failure envelope for glass. The failure envelope has little practical application to rock mechanics as it applies strictly to brittle materials (Edelbro, C. 2004), but his theory did explain fracture propagation in rocks. Griffith hypothesized that fracture occurs when the maximum tangential stress near the end of a microfracture exceeds material strength (Griffith, A. A. 1921). The resulting merger of these microfractures form damage zones and cause stress redistribution, which can lead to micro- and macro-failure (Young, R. P. and D. S. Collins 2001). Microfracture opening and closing is instrumental in failure mechanisms of rock. As a rock is stressed existing microfractures are closed under pressure, and as the rock approaches failure the microfractures tend to merge, eventually leading to

macrocracking and ultimate failure. The stage when the microfractures first close is denoted by the initial nonlinearity in the stress-strain curve (Thill, R. E. 1973).

2.1.3 ROCK CHARACTERISTICS AND WAVE PROPAGATION

Rocks can be examined noninvasively by propagating ultrasonic or seismic waves through them, which can provide information about the structure and elastic properties of a rock (Jackson, M. J. and D. R. Tweeton 1994). This technique can be applied on a small scale in the laboratory or on a much larger scale in a mine. Wave propagation through a rock mass is dependent on many characteristics of the rock mass including rock type, fracture, anisotropy, porosity, stress, and boundary conditions.

First, a brief review of wave diffraction including Fermat's principle and Snell's Law is essential in understanding the path a wave takes through a rock mass. Fermat's principle was originally applied to a beam of light by the French mathematician Pierre de Fermat in 1657, and states, "The actual path taken between two points by a beam of light is the one which is traversed in the least time" (Mahoney, M. S. 1973). Fermat's principle also applies to sound waves. This principle is relevant to wave propagation in rock masses, because a rock mass is rarely homogenous, so the fastest path for a wave is seldom a straight line. The schematic in Figure 2.4 illustrates the principle, by showing that the fastest path from A to B is not necessarily the shortest.

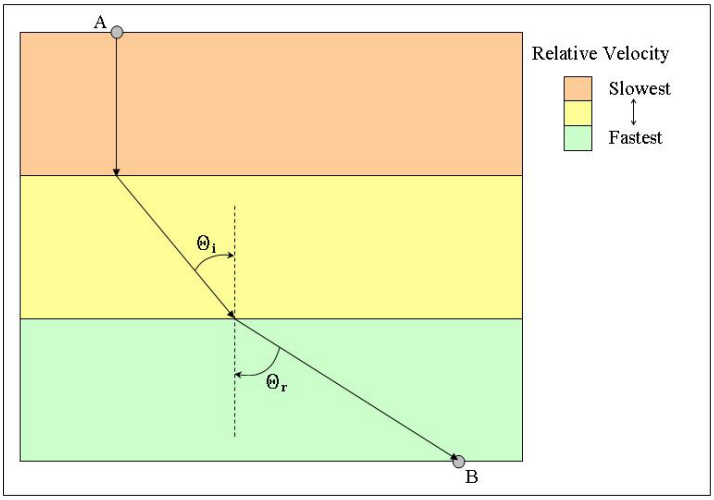

Figure 2.4. Fermat's Principle.

Snell's law, named for Willebrord Snell, who discovered it in 1621, is derived from Fermat's Principle and describes the relationship between the angle of incidence and angle of refraction. Snell's law is displayed in Equation 2.10:

$$n_i \sin\theta_i = n_r \sin\theta_r$$

where,

$$\text{n} = \text{the index of refraction} \Rightarrow \frac{\text{c}}{\text{v}}$$

c = the speed of sound $\left(\text{ft/s}\right)$ [2.10]

v = phase velocity $\left(\text{ft/s}\right)$

θ_{i} = the angle of the incident wave from the normal $\left(\text{degrees}\right)$

θ_{r} = the angle of the refracted wave from the normal $\left(\text{degrees}\right)$

When examining seismic waves in a solid, four types of waves are considered: p-waves, s-waves, Rayleigh waves, and Love waves. P-waves and s-waves are both body waves; they travel across the medium. Rayleigh waves and Love waves are surface waves; they only travel along the free surface of an elastic body (Sharma, P. V. 1986).

P-waves are also known as longitudinal waves or primary waves. As p-waves propagate a medium the particles of the medium expand and contract. The velocity of p-waves, $V_{p,}$ is:

$$V_p = \sqrt{\frac{(1-\upsilon)Eg}{(1+\upsilon)(1-2\upsilon)\gamma}}$$

where,

υ = Poisson's Ratio	(unitless)	
γ = density	(lb/ft^3)	[2.11]
g = gravitational acceleration	(ft/s^2)	
μ = shear modulus	(psf)	
K = bulk modulus	(psf)	
E = Young's Modulus	(psf)	

Particle motion in s-waves, or shear waves, is perpendicular to the direction of travel, and the velocity of shear waves is given by:

$$V_s = \sqrt{\frac{Eg}{2(1+\upsilon)\gamma}} \qquad [2.12]$$

(Obert, L. and W. I. Duvall 1967).

Figure 2.5 illustrates the difference in particle motion between p-waves and s-waves:

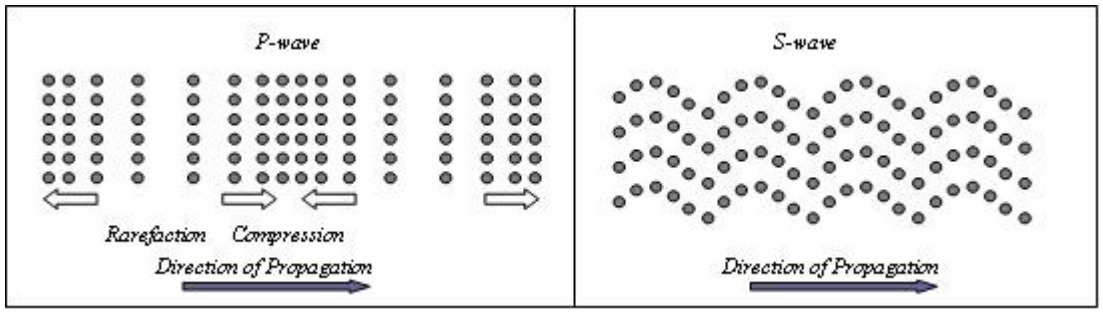

Figure 2.5. Body Wave Motion (Sharma, P. V. 1986)

Rayleigh waves and Love waves travel only along the free surface of an elastic solid, and Love waves can only travel along the free surface of an inhomogenous elastic solid. Rayleigh waves are a combination of longitudinal and transverse motion while Love waves consist of horizontal transverse motion (Sharma, P. V.

1986). P-waves and s-waves are most often used in geophysical velocity investigations.

In 1923 Adams and Williamson studied the compressibility of a number of rocks and found that, in general, the compressibility of rocks falls off as pressure is increased. Compressibility is defined as the reciprocal of the bulk modulus, *K* (Goodman, R. E. 1989), displayed in Equation 2.5, so it follows that Young's Modulus increases steadily with low pressures and then flattens out with higher pressures. Recalling Equation 2.11 and assuming that density increase is negligible, an increase in Young's Modulus will result in increasing p-wave velocity for lower pressures, and a plateau at higher pressures.

An increase in p-wave velocity in rocks with application of pressure is attributed to the closure of cracks and pore space (Wyllie, M. R. J., et al. 1958, Thill, R. E. 1973, Toksöz, M. N., et al. 1976, Seya, K., et al. 1979, Young, R. P. and S. C. Maxwell 1992). Open pores and microfractures will either diffract seismic waves or cause a decrease in velocity as the wave travels through the open space. Most rocks show some decrease in porosity with pressure and an increase in p-wave velocity, with the exception of some rocks such as dolomite with a high matrix density (Yale, D. P. 1985). Generally, the p-wave velocity gradient is highest at low pressures and then begins to level out at higher pressures (Prasad, M. and M. H. Manghnani 1997). Velocity can be used to infer stress distribution, but it is important to note that the relationship is not linear.

Toksöz indicates that saturation and pore fluid also affect velocity, mainly because the waves will travel through the medium that fills the pore space. He notes higher velocities for brine saturation than for gas saturation (1976). Clay content has also been shown to influence p-wave velocity, but to much less of a degree than porosity (Tosaya, C. and A. Nur 1982).

2.2 Stress Behavior in Underground Mines

2.2.1 Factors Contributing to Stress Redistribution

Herget likens stress around an opening to laminar flow distribution as illustrated in Figure 2.6. He indicates that there will be a crowding of stream lines at the sides of an obstacle and a slowing in front of and behind the obstacle.

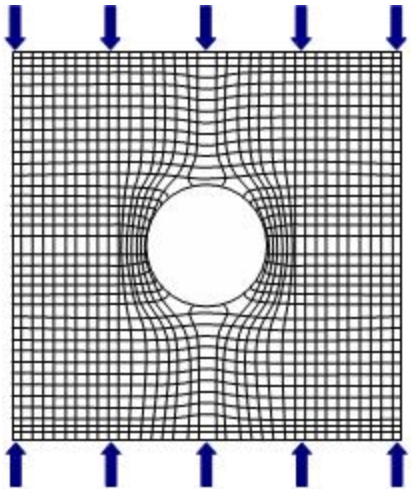

Figure 2.6. Principal Stress Trajectories around an Opening (Herget, G. 1988).

Stress redistribution around excavated areas results in regions of tensile and compressive stress. The following parameters will influence the excavation damage zone (Martino, J. B. and N. A. Chandler 2004):

1. In situ stress magnitudes, orientations, and ratios
2. Shape of the tunnel
3. The excavation method (blast or cut)
4. Geology
5. Environmental factors
6. Nearby excavations

2.2.2 Abutment Stress

Abutment stress is a result of stress redistribution due to the extraction of ore, and occurs along or near the boundary where material has been removed (Peng, S. S. and H. S. Chiang 1983). An undisturbed coal seam with competent roof and floor strata will have a fairly uniform stress distribution. As coal is removed this distribution is disrupted and the load is either transferred to another intact area or failure occurs. In

longwall mining this stress is transferred immediately in front of the face, and to the sides of the panel (headgate and tailgate). Failure of the roof strata behind the longwall shields allows for pressure relief.

Very competent strata above a longwall system, such as massive sandstone, may not cave immediately, contributing to extremely high abutment stress in front of the face which can result in rockbursts on the face, or damage to shields due to rapid dynamic loading (Haramy, K. Y., et al. 1988). Kneisley and Haramy indicated that a fast retreat rate may promote caving so that excess time-dependent loading ahead of the face may be avoided (Kneisley, R. O. and K. Y. Haramy 1992). Kelly and Gale also refer to time dependent loading indicating that production delays can lead to convergence of shields and roof failure at the face (Kelly, M. and W. Gale 2000).

The exact distribution of the abutment load is dependent upon the properties of the roof strata and the mining geometry, but general stress abutment schematics are displayed below in Figure 2.7. In Figure 2.7, the red line indicates approximate relative stress.

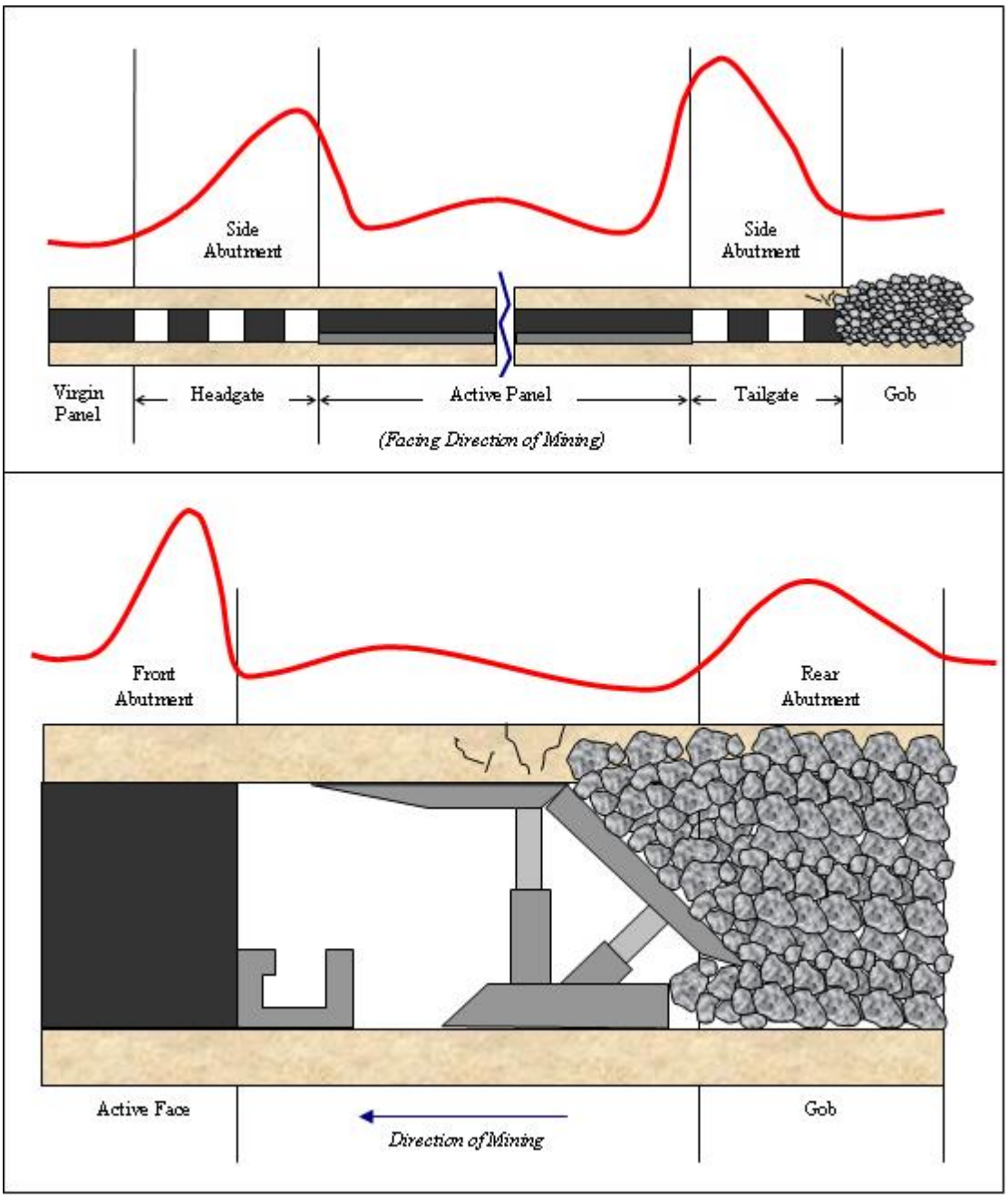

Figure 2.7. Typical Longwall Abutment Stress.

As illustrated in Figure 2.7, abutment stress is usually larger on the tailgate, if it is adjacent to a mined out panel. Front abutment pressure is detectable at a lateral distance of about one times the overburden, but is more evident about 100 feet outby the face at which point stress starts to increase to its peak at 3 to 20 feet outby the face. In weak roof, maximum abutment stress along the faceline occurs at the headgate and tailgate corners, but in more competent roof a peak may occur mid-face depending upon the face length (Peng, S. S. and H. S. Chiang 1983).

In addition to vertical stress redistribution, joints, faults and horizontal stress orientation may contribute to larger abutment stresses and more erratic failure. Even in optimum conditions gob failure is rarely uniform (Maleki, H. 2002).

2.2.3 ROCKBURSTS

Rockbursts, also referred to as bumps, mountain bumps, air blasts, bounces, and bursts, are violent and sudden ground failures that cause expulsion of material into excavated areas. They are accompanied by a seismic tremor and the expelled material can range from less than a ton to hundreds of tons. They may also be accompanied by floor heave and roof falls (Bräuner, G. 1994).

In coal mines, rockbursts almost always occur where the roof or the roof and floor are massive and competent. Additionally, they generally occur at depths greater than 1,000 feet, although isolated bursts have been recorded in more shallow mines (Bräuner, G. 1994, Ellenberger, J.L. and K. A. Heasley 2000).

Rockbursts are the result of stored strain energy being released at the time of rock failure. The stored strain energy, W_0, is calculated as follows (Herget, G. 1988):

$$W_0 = \frac{1}{2}\frac{Q_0^2}{E}$$

where,

W_0 is per unit volume $\left(\frac{\text{inch - pound force}}{\text{inch}^3}\right)$ [2.13]

Q_0 = failure strength (psi)

E = Young's Modulus (psi)

Equation 2.13 explains why violent rockbursts often occur in coal seams overlain by massive sandstone roof. The high failure strength of the sandstone allows for large values of stored strain energy, so that when failure occurs it may be catastrophic.

Aside from the danger to miners of flying material, rockbursts pose other serious hazards. They may be accompanied by an airblast which can disrupt mine ventilation. Also, in coal mines, the violent failure of the coal seam may propagate float dust through air, along with a release of methane, which promotes an explosive atmosphere (Bräuner, G. 1994).

2.3 Stress Analysis in Mines

2.3.1 NUMERICAL METHODS

Numerical stress analysis methods have found widespread application in rock mechanics and mine stress modeling. There are many types of numerical modeling, but most routines fit into one of the following classifications: finite element methods; boundary element methods; discrete element methods; or some combination of the three.

Finite element methods are continuum methods and can be used for any process that is governed by a differential equation. The structure, a rock mass, for instance, is divided into elements that are connected at nodes. The displacement at the nodes can be calculated and related to strain and stress (Pande, G. N., et al. 1990).

Boundary element methods are also continuum methods, and only the surface of the body is divided into elements. In a rock mass this would be the outside of the rock mass, and any interface where material properties change. This method is very efficient for homogenous and linear elastic behavior in rocks, but is not as flexible as the finite element method (Pande, G. N., et al. 1990).

The discrete element method involves discretizing the body into elements of practically any shape and assigning the elements material and contact properties. The

contact relationships between elements are monitored with time, and the equations of dynamic equilibrium for each element are solved to meet the requirements for contact and boundary conditions. Unlike boundary element and finite element methods, discrete element is a discontinuum method. This method can be computationally expensive and requires careful selection of material behavior (Pande, G. N., et al. 1990).

LAMODEL (Laminate Model) is a boundary element, displacement-discontinuity, routine that calculates stresses and displacements in thin, tabular seams. It simulates the overburden as a stack of homogenous isotropic layers with the same Poisson's ratio and Young's Modulus, and with frictionless interfaces. *LAMODEL* is available through the National Institute for Occupational Safety and Health (NIOSH) and has been used extensively for stress modeling (Bauer, E. R., et al. 1997, Ellenberger, J. L., et al. 2003, Zingano, A. C., et al. 2005).

UDEC, FLAC^{2D}, and *FLAC*^{3D} (Fast Lagrangian Continua Analysis), commercial programs available through Itasca, have also been implemented in a number of studies (Badr, S., et al. 2003, Gale, W. J., et al. 2004, Vandergrift, T. L. and J. Garcia 2005, Zingano, A. C., et al. 2005). FLAC is a continuum code utilizing finite difference formulation. Other codes used to model mine behavior include *BESOL* (Karabin, G. J. and M. A. Evanto 1999), *MUDEC* (Haramy, K. Y., et al. 1988), and Free Hexagonal Element Method (Procházka, P. P. 2002).

2.3.2 MICROSEISMIC MONITORING

A microseismic event is a subaudible seismic event produced by a rock under stress, and characterized by short duration and small amplitude (Obert, L. and W. I. Duvall 1967). Microseismic event locations tend to advance with face advance in longwall mining, and rate of advance has been found to be related to microseismic event frequency (Ellenberger, J. L., et al. 2001). Additionally, microseismic event location tends to coincide with peak abutment stress location, suggesting that the events are the result of stress redistribution in the mine (Heasley, K. A., et al. 2001).

Microseismic event monitoring has been implemented as a predictor of roof failure. For example, a study Moonee Colliery in Australia revealed an increase in event frequency prior to roof failure, which allowed for miners to be warned of possible failure (Iannacchione, A., et al. 2005).

2.4 Tomography

2.4.1 INTRODUCTION

The word tomography is derived from the Greek word *tomos*, which means to slice or section (*Webster's Third New International Dictionary, Unabridged* 2002). Tomography involves the noninvasive imaging of a solid body; the body can be a manmade structure, a human body, or a geologic structure. Tomographic imaging can be conducted on practically any scale. Tomography involves dividing the body in question into grid cells in a two-dimensional situation or cubes called voxels in a three-dimensional situation, with the goal of estimating some characteristic value of the solid for each cell, so that a complete image can be generated (Cox, M. 1999).

2.4.2 APPLICATIONS

Applications of tomography are extensive; tomography is utilized in medicine, geology, mining, structural investigations, and fluid flow processes.

Tomography has been widely employed in medicine for diagnostic purposes. Computer axial tomography (CAT scans), nuclear magnetic resonance imaging (MRI), and positron emission tomography (PET), are all diagnostic technologies that utilize tomography. Medical tomography allows physicians to noninvasively examine the inside of the human body and detect anomalies.

Tomography has additional implications for structural imaging and materials science. For example, x-ray computed tomography has been utilized to determine air void distribution in asphalt samples, which can be used to characterize roadway wear (Masad, E., et al. 2002). X-ray tomography has also been used to image flaws in

turbine blades (Bronnikov, A. V. and D. Killian 1999), while guided ultrasonic wave tomography has been used for determination of flaws in composite materials used for aerospace structures (Leonard, K. R., et al. 2002).

In fluid flow processes, MRI can be used to determine liquid to solid ratios, fluid flow mechanics, and to image chemical reactions (Hall, L. D. 2005). Additionally, cross-flow in pipes has been imaged using ultrasonic waves (Rychagov, M. N. and H. Ermert 1996).

Finally, tomography has been employed extensively in mining and geology. Hoversten and others used electromagnetic tomography for reservoir visualization (Hoversten, G. M., et al. 2001), while seismic tomography has been used to image contaminant flow in sand models (McKenna, J., et al. 2001). Tomography has applications in exploration as it is useful for imaging geologic structures and ore bodies (Bellefleur, G. and M. Chouteau 2001). It can be used to detect voids near active mines in order to avoid unexpected inundation of gas or water (Maillol, J. M., et al. 1999). Also, velocity transmission tomography has been used as an indicator of stress in underground mines (Kormendi, A., et al. 1986, Maxwell, S. C. and R. P. Young 1996, Friedel, M. J., D. F. Scott. and T. J. Williams 1997, Maxwell, S. C. and R. P. Young 1998, Westman, E. C. 2004).

2.4.3 VARIATIONS OF TOMOGRAPHY

A number of methods have been employed to collect the data that is used to generate a tomogram. All methods take advantage of some characteristic of the solid being imaged, including electrical resistivity and conductivity, flow characteristics, molecular response to magnetism, and p- and s-wave velocity.

Electrical resistance tomography uses electrodes to measure electrical resistivity. Resistivity is dependent upon chemical, hydraulic, and thermal components of a solid (Daily, W., et al. 2004). Electromagnetic tomography has been accomplished through use of natural electromagnetic waves to characterize fluid flow and content in faults (Bedrosian, P. A., et al. 2004).

Positron emission tomography is a tracer method. It involves using a tracer that emits positrons as it decays, the positron emission is then measured and imaged. It is useful for fluid flow in rocks (Degueldre, C., et al. 1996) and has extensive applications in the medical field, including imaging of the brain (Degueldre, C., et al. 1996, Ishiwata, K., et al. 2005).

Nuclear magnetic resonance imaging, more commonly known as magnetic resonance imaging, relies on the measurement of relaxation of hydrogen nuclei contained in water. It requires placing the solid being imaged in a uniform magnetic field, then applying pulses of electromagnetic energy, which excite hydrogen nuclei. As the hydrogen nuclei relax back to their normal state they emit energy, which is the parameter measured to create the tomogram (Baraka-Lokmane, S., et al. 2001).

Travel time tomography can be accomplished using ultrasonic or seismic waves. A schematic showing approximate frequency intervals of various waves is displayed in Figure 2.8:

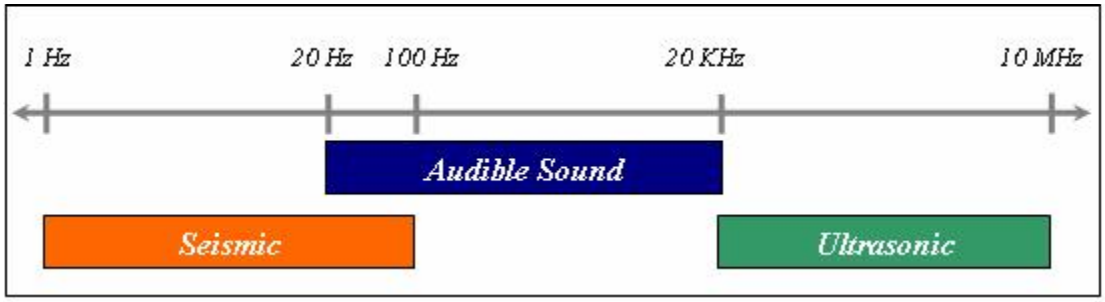

Figure 2.8. Frequency of Waves.

The wavelength used must be small enough to resolve the structure being imaged, but there must also be adequate energy to propagate the length of the medium being imaged with sufficient strength. It is generally agreed that resolution of a tomogram is dependent upon wavelength (Watanabe, T. and K. Sassa 1996, Scott, D. F., et al. 1997, Watanabe, T., et al. 1999). If ray density is sufficient, however, Friedel indicates that it is possible to resolve to one-half wavelength (Friedel, M. J., et al. 1996), and it has also been found that the 1st Fresnel zone radius is a good order of magnitude estimator (Williamson, P. R. 1991). A Fresnel zone is the zone of

influence around the path of a surface wave, and is dependent upon velocity and path length (Yoshizawa, K., et al. 2005).

Seismic tomography is generally limited to diffraction, attenuation, p-wave velocity, s-wave velocity, or some combination of the four. Diffraction of a wave occurs when a wave meets a discontinuity in a solid and scatters (Schlumberger 2005). Diffraction tomography requires examination of the scattered wave field, and is often much more computationally expensive and difficult to calculate than travel time transmission tomography (Williamson, P. R. 1991, Jackson, M. J. and D. R. Tweeton 1994). Diffraction tomography is based on the wave equation while transmission tomography is dependent on the ray equation (Lo, T-W., et al. 1988). Also, diffraction tomography is most useful in relatively homogenous materials (Goulty, N. R. 1993). A feature of diffraction tomography is that it provides a qualitative image of velocity contrasts while ray tomography provides a quantitative image of velocity contrasts (Pratt, R. G. and N. R. Goulty 1991).

To produce a tomogram using attenuation tomography the amplitude at the source and at the receiver, and the travel time must be measured. The signal decline between the source and receiver is the attenuation. Weathered and cracked rocks have a higher attenuation than intact rock. Attenuation imaging is more sensitive to cracking than velocity imaging (Lockner, D. A., et al. 1977, Watanabe, T. and K. Sassa 1996). Figure 2.9 illustrates wave attenuation.

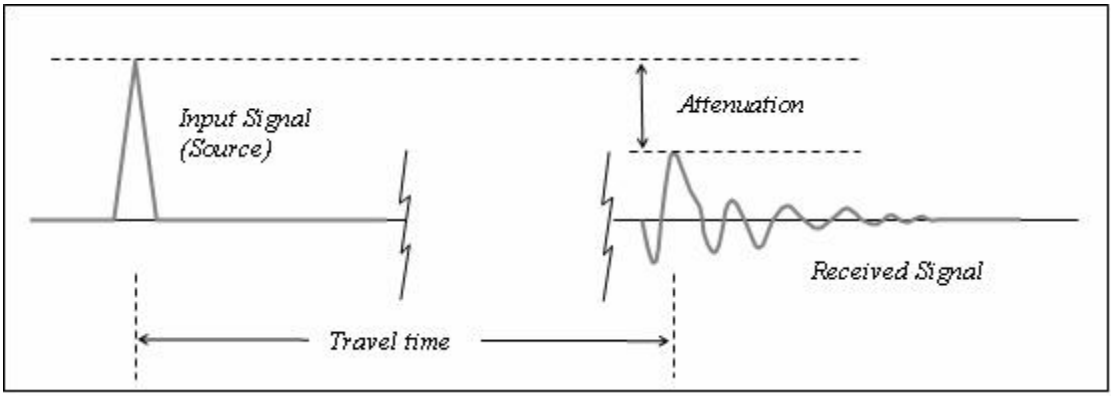

Figure 2.9. Attenuation of a Wave (Westman, E. C. 2004)

P-wave travel time tomography is often desirable due to the relative simplicity and accuracy of determining the arrival time. Manthei indicates that determining the s-wave arrival time is much more uncertain than for p-waves (1997). Yet, the ability of p-wave travel time tomography to image low velocity anomalies is limited. Wielandt found that diffracted waves interfere with transmitted waves for low velocity anomalies, and that the observed travel time is not indicative of the relative velocity in this instance. He also indicated that p-waves travel around the low-velocity anomalies (Wielandt, E. 1987). Nolet refers to this as the Wielandt effect (Nolet, Guust 1987, Jackson, M. J. and D. R. Tweeton 1994). Ivansson describes the use of damping and synthetic tomography analysis to avoid this problem (Ivansson, S. 1985). P-wave velocity tomograms may image high velocity regions fairly well, while underestimating the low velocity regions (Jackson, M. J. and D. R. Tweeton 1994, Vasco, D. W., et al. 1995).

2.4.4 INVERSE THEORY

The framework for tomography was established by Radon who proved that an infinite number of rays passing through a two-dimensional object at an infinite number of angles could be used to perfectly reconstruct the object (Radon, J. 1917). The theory also applies to three-dimensional objects. If a finite number of rays are passed though the object then this is referred to as a sample of the Radon transform. Deans gives an instructive description of the Radon Transform when he describes using a probe to characterize some internal aspect of a solid (Deans, S. R. 1983). In the case of velocity tomography presented in the thesis, the probe is a seismic wave while the solid is the rock mass under examination. The velocity distribution of the rock mass is an unknown function, f. After probing the rock mass with seismic waves, a velocity profile function, $\check{f}$ is determined.

Inverse theory entails making inferences about something from measured data (Menke, W. 1989). Most inverse theory problems are ill-posed. Hadamard defined the well-posed problem as follows (Hadamard, J. 1902, Hadamard, J. 1952, Yagola, A. G., et al. 2001, Mosegaard, K. and A. Tarantola 2002):

- A solution exists.
- The solution is unique.
- The solution depends on continuous data.

A tomography problem rarely meets these requirements. In fact, inverse problems often have an infinite number of solutions, with a few solutions that are appropriate in light of *a priori* information (Hole, J. 2005). The inverse problem is usually overdetermined or underdetermined. The overdetermined problem has more data than unknowns, which does not allow for a unique solution. For example, in the three-dimensional velocity tomography problem an overdetermined system has more rays than voxels. Conversely, an underdetermined system would have less rays than voxels (Tarantola, A. 1987, Menke, W. 1989, Manthei, G. 1997).

Velocity tomography is based on the relationship between time, distance, and velocity of a ray traveling through a medium:

$$v = \frac{d}{t} \rightarrow vt = d$$

$$t = \int_S^R \frac{1}{v} \bullet dl = \int_S^R p \bullet dl$$

$$t_i = \sum_{j=1}^{M} p_j d_{ij} \quad (i = 1 \ldots N)$$

Where, [2.14]

v = velocity (ft/s)

d = distance (ft)

t = time (sec)

p = slowness (inverse velocity) (s/ft)

N = number of rays

M = number of voxels

The velocity, distance, and time for the length of the entire ray is known, but the velocity, distance and time for the length of the ray in an individual voxel or grid cell is not known. The distance in each grid cell can be solved for easily, but the time and velocity are still unknown. Using inverse theory, the time and velocity can be solved for as follows

$$\mathbf{T} = \mathbf{DP} \rightarrow \mathbf{P} = \mathbf{D}^{-1}\mathbf{T}$$

where,

$\mathbf{T}$ = Travel time per ray matrix, 1 x N

$\left(t_i = \text{travel time of the } i^{th} \text{ ray}\right)$

$\mathbf{D}$ = Distance per ray per grid cell matrix, N x M [2.15]

$\left(d_{ij} = \text{distance of } i^{th} \text{ ray in } j^{th} \text{ pixel}\right)$

$\mathbf{P}$ = Slowness per grid cell matrix, 1 x M

$\left(p_j = \text{slowness of } j^{th} \text{ pixel}\right)$

Overdetermined and underdetermined problems result in a singular distance matrix, **D,** which cannot be inverted (Jackson, M. J. and D. R. Tweeton 1994). A singular matrix is a matrix with no inverse and a determinant of zero. Take the following trivial two-dimensional inverse tomography problem as an example:

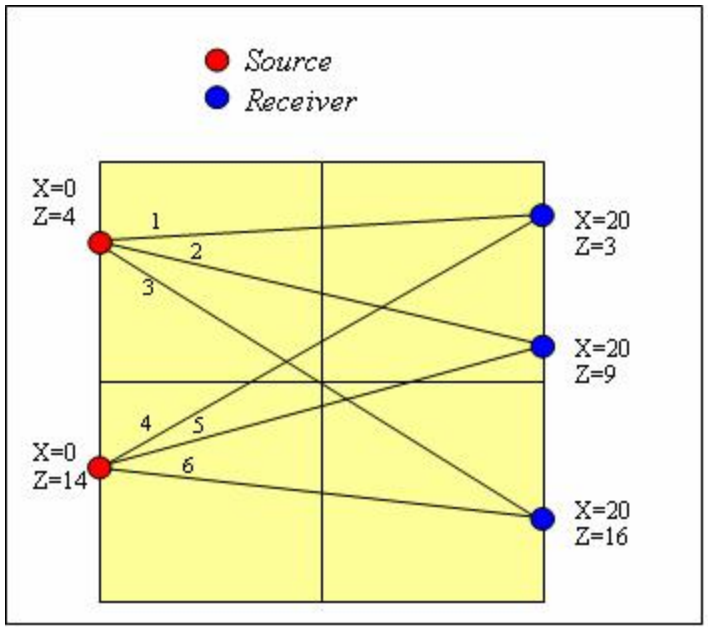

Table 2.1. *Trivial Traveltime Data.*

Ray	*Distance (ft)*	*Arrival Time (ms)*
1	20.0	0.073
2	20.6	0.076
3	23.3	0.089
4	22.8	0.084
5	20.6	0.075
6	20.1	0.074

$$\mathbf{T} = \mathbf{DP}$$

$$\begin{bmatrix} 0.073 \\ 0.076 \\ 0.089 \\ 0.084 \\ 0.075 \\ 0.074 \end{bmatrix} = \begin{bmatrix} 10.0 & 10.0 & 0 & 0 \\ 10.3 & 10.3 & 0 & 0 \\ 11.7 & 0 & 0 & 11.7 \\ 3.1 & 11.4 & 8.3 & 0 \\ 0 & 4.1 & 10.3 & 6.2 \\ 0 & 0 & 10.0 & 10.0 \end{bmatrix} \begin{bmatrix} p_1 \\ p_2 \\ p_3 \\ p_4 \end{bmatrix}$$

Figure 2.10. Inverse Tomography Schematic.

The matrix **D** cannot be inverted for this trivial problem, because it is overdetermined. In order to manage the dilemma of inverting a singular matrix other methods have been developed to solve the inverse travel time problem displayed in Equation 2.15.

The algorithms developed to solve the inverse equation include Least Squares, Damped Least Squares, Singular Value Decomposition (SVD), Algebraic Reconstruction Technique (ART), Simultaneous Iterative Reconstruction Technique (SIRT), and Multiplicative Algebraic Reconstruction Technique (MART).

The Least Squares method requires solving the following equation:

$$\mathbf{P} = (\mathbf{D}^{\mathbf{T}}\mathbf{D})^{-1}\mathbf{D}^{\mathbf{T}}\mathbf{T} \qquad [2.16]$$

(Jackson, M. J. and D. R. Tweeton 1994)

When the matrix $\mathbf{D}^{\mathbf{T}}\mathbf{D}$ is singular, then another method of least squares, damped least squares is employed, and is of the form:

$$\mathbf{P} = (\mathbf{D}^{\mathbf{T}}\mathbf{D} + \lambda\mathbf{I})^{-1}\mathbf{D}^{\mathbf{T}}\mathbf{T} \qquad [2.17]$$

Where λ is a tradeoff parameter that controls the minimization of the data misfit and the model norm (Aki, K. and W. H. K. Lee 1976, Spakman, W. 1993, Hole, J. 2005) and $\mathbf{I}$ is the identity matrix. The data misfit is the difference between the measured and predicted data, while the norm is a way of sizing and ranking data. One of the more common norms is L_2 norm which is given by:

$$L_2 = \|\mathbf{d}\|_2 = \left[\sum_i |e_i|^2\right]^{1/2} \qquad [2.18]$$

where, e is a vector, travel time, in the case of velocity tomography

(Menke, W. 1989).

However, norms can be calculated for L_1 to L_∞. Norms allow for data-weighting so that a better model fit may be obtained.

Singular value decomposition (Golub, G. H. and C. Reinsch 1971) is an appropriate algorithm for small problems that requires decomposing the data into eigenvectors, but for large problems SVD produces large dense matrices which can become cumbersome (Bording, R. P., et al. 1987).

The iterative techniques, including ART, SIRT, and MART, are useful for nonlinear problems (Nowack, R. L. and L. W. Braile 1993). These techniques

involve perturbing the equations from some starting model until a solution converges, but there is always the possibility of a lack of convergence. The typical iterative algorithm perturbs the matrix equation as follows:

$$\mathbf{T'} = \mathbf{DP'}$$

Prime notation indicates the initial model

$$\mathbf{dT} = \mathbf{T} - \mathbf{T'} \qquad [2.19]$$

$$\mathbf{dp'} = \mathbf{D}^{\mathrm{T}}\mathbf{dT}$$

$$\mathbf{P''} = \mathbf{p'} + \mathbf{dP'}$$

(Jackson, M. J. and D. R. Tweeton 1994)

While ART requires changing one equation or ray at a time, then updating the model and continuing to the next equation, SIRT allows for all the equations to be solved, and then averaged before the model is updated. (Morgan, C. L. and M. D. Miller 1983, Stewart, R. R. 1991, Chang, J., et al. 1996). SIRT solutions tend to converge more slowly than ART solutions, but the advantage is that the SIRT solution also tends to diverge more slowly than the ART solution, and give more reliable results (Gilbert, P. 1972, Dines, K. A. and R. J. Lytle 1979). Figure 2.11 displays the experimental convergence differences determined by Dines and Lytle for SIRT and ART.

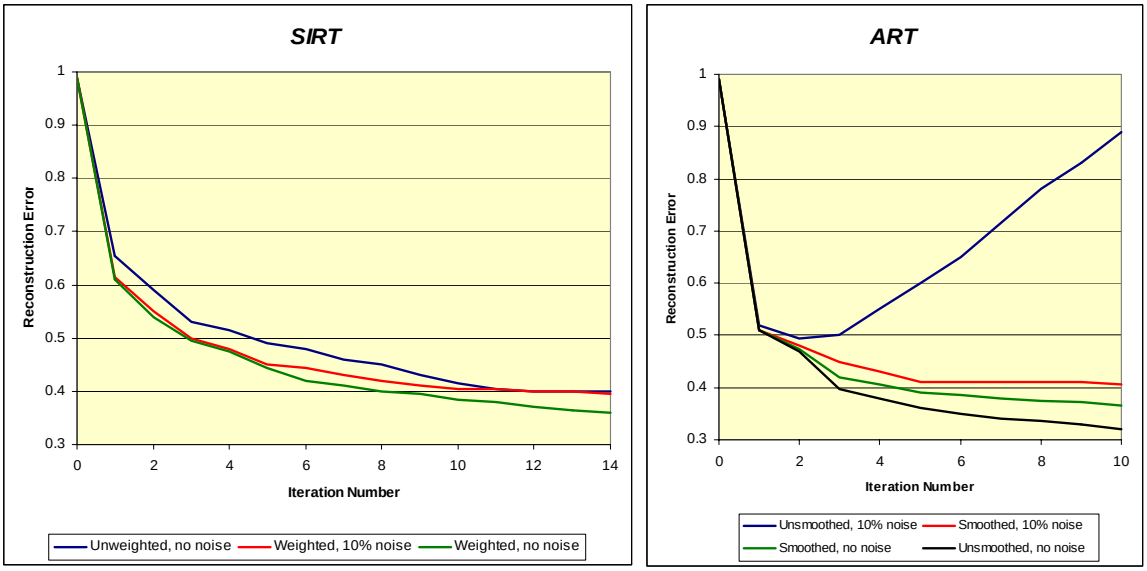

Figure 2.11. Experimental Convergence for SIRT and ART
(Dines, K. A. and R. J. Lytle 1979).

MART is similar to ART, except that instead of perturbing the model by adding or subtracting from it, a multiplicative correction is made (Stewart, R. R. 1991).

2.4.5 SOURCES OF ERROR

Sources of error in tomographic imaging include measurement error in the equipment used to collect the data, geometry of the experiment, the inherent geometry of the velocity contrasts, inaccurate data analysis, and errors in the inversion process.

Experiment geometry plays an important role in constructing an accurate tomographic image. A well-planned geometry allows for each pixel or voxel to be well-constrained. Hobro and others suggest generating synthetic tomograms to analyze proposed geometry prior to experiments (Hobro, J.W.D., et al. 2003). In reality, it is difficult to achieve optimum geometry in the geophysical context where very large areas are being measured, especially when passive sources are being used (Dyer, B. and M. H. Worthington 1988, Meglis, I. L., et al. 2004). A passive source is a source that is not directly controlled by the researcher. Passive sources may be microseismic events that may be clustered due to geologic structure, or as a function of mining geometry. Passive sources do not allow for equal source-receiver spacing. Scott and others indicated that including the maximum number of intersecting ray paths at different angles through the body being imaged is of paramount importance (Scott, D. F., et al. 1997). Achieving this maximum number of intersecting raypaths and angles can be difficult with passive sources, because they may result in more biased ray geometry. Watanabe and Sassa have attributed some inconsistencies in transmission travel time tomography to low density and insufficient angle variation (1996). Additionally, if the geometry of the velocity anomaly is complex, it is more difficult to image. Examples of passive source geometry and active source geometry for a longwall mining section are displayed in Figure 2.12.

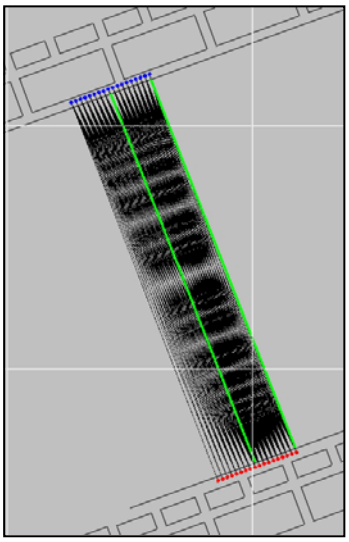

Simple Active Source Geometry
Sources (Red) and Receivers (Blue) are on 10 ft. spacing. Sensors are "leapfrogged" ahead of face.

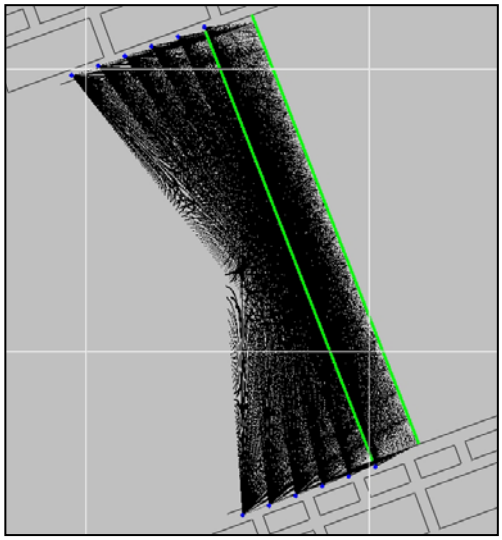

Shearer Active Source Geometry
Receivers (Blue) are "leapfrogged" ahead of face on 50 ft. spacing. The Shearer functions as a source with measurements taken approximately every 50 ft.

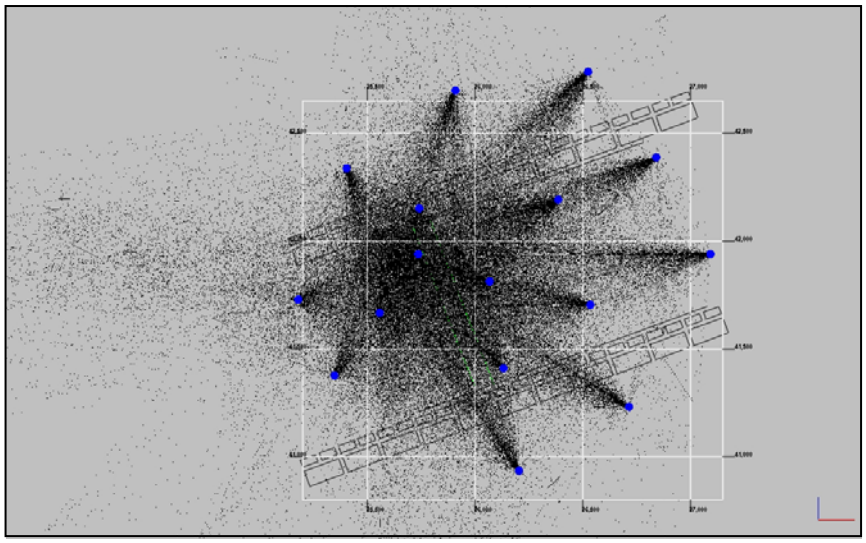

Passive Source Geometry
Receivers (Blue) are on surface. Microseismic event locations are determined and utilized as sources.

Figure 2.12. Active and Passive Source Geometries on a Longwall.

Source and receiver geometry can also influence resolution of a tomogram. Traditionally, resolution of a picture refers to the size of the pixel. The seismic wavelength generally determines the resolution of the image, but only if spatial sampling, or ray density, is sufficient (Watanabe, T., et al. 1999). Resolution of a tomogram, **R**, is represented in matrix form. The closer the matrix is to the identity matrix, **I**, the better the resolution. For a tomogram with M pixels the resolution

matrix will be M x M. Each diagonal term of the matrix represents a pixel. The off diagonal terms represent the relationship between the pixel under study and the other pixels (Tarantola, A. 1987). Tarantola gives a detailed account of calculation and analysis of the resolution matrix.

When determining pixel size the goal is to optimize resolution and variance. Variance is a measure of uncertainty in the pixel, while resolution refers to image "sharpness." The schematic in Figure 2.13 represents the tradeoff between resolution and variance:

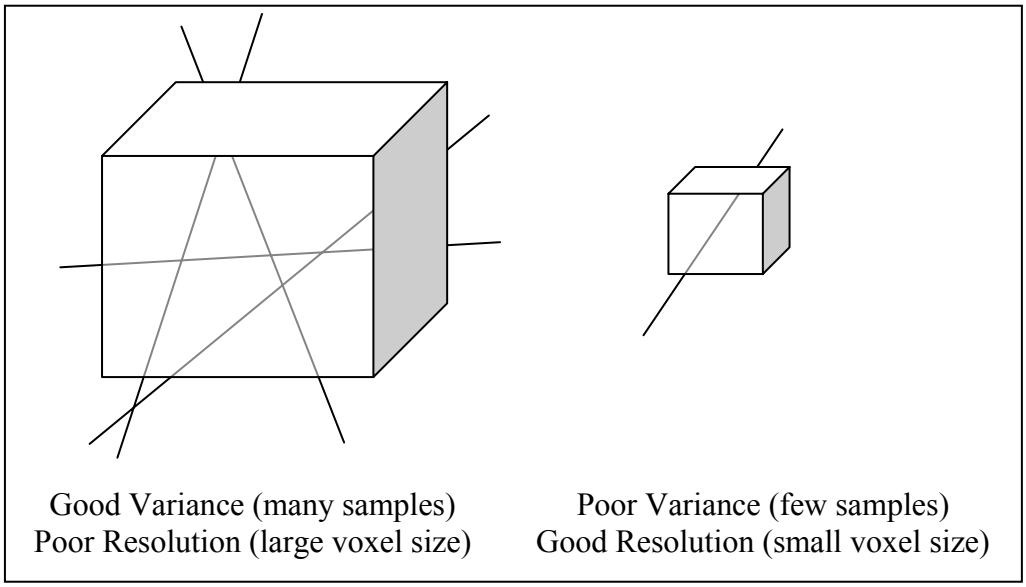

Figure 2.13. Resolution and Variance of a Tomogram (Menke, W. 1989).

Poor data can result in artifacts in the tomogram. An inaccurate travel time measurement that is an outlier in the data set can result in unusually large or small velocity contrasts in the tomogram that are not representative of the true velocity profile of the solid (Martínez, J. L. F., et al. 2003). Smoothing is one method of minimizing an artifact. When smoothing a tomogram, a smoothing constraint is applied to each node in the tomogram. Each node is then weighted according to the surrounding nodes (Tweeton, D. 2001). The drawback is that a tomogram can be oversmoothed and legitimate anomalies can be smoothed out of the image.

2.5 Previous Tomography Studies

2.5.1 The Velocity-Stress Relationship

Early research involved a series of laboratory tests in which the compressibility of a number of rock samples under increasing load were examined, and it was determined that at low pressures the compressibility fell rapidly and then leveled out (Adams, L. H. and E. D. Williamson 1923).

Nur and Simmons subjected cylindrical samples of Barre granite to uniaxial loading, and varied the angle of the load. They then measured p- and s- wave velocity in the sample, and found a clear velocity increase with increased stress. They also found that the magnitude of the velocity increase was dependent on the stress direction and direction of compressional wave propagation. The most profound velocity change occurred when the wave was propagated perpendicular to the load (Nur, A. and G. Simmons 1969).

Toksöz and others used observed laboratory data, much of it from Nur and Simmons 1969 study, to model velocity for *in situ* rock given the parameters of porosity, saturation, overburden, and pore fluid pressure (Toksöz, M. N., et al. 1976).

Eberhart-Phillips and others measured the effects of pressure, clay content, and porosity on velocity of 64 sandstone samples, and they also found an exponential increase in velocity at low pressures that tapered off to a linear increase for higher pressures (Eberhart-Phillips, D., et al. 1989).

2.5.2 Laboratory Experiments

Scott and others generated tomograms of dry Berea sandstone cores using ultrasonic waves as the cores underwent indentation testing. They also generated numerical models of the stress in the cores as they were loaded and found favorable correlation between the two techniques (1994). Chow and others generated tomograms with cores of Lac du Bonnet grey granite under uniaxial cyclic loading, and found that as damage occurred in the sample, low velocity regions corresponded

with the damaged zone (1995). Jansen and others imaged thermal stress induced cracking in a cubic sample of granite (1991).

2.5.3 FIELD EXPERIMENTS

Tomography has been implemented to determine stress in underground mines with varying degrees of success. Stress distribution in numerous underground structures has been imaged, including pillars, tunnels, longwall panels, and minewide tomography.

A sill pillar has been imaged with active sources, and it was concluded that low velocity areas corresponded with locations of previous rockbursts (Maxwell, S. C. and R. P. Young 1993). Maxwell and Young also conducted tomographic imaging of another mine pillar using active source geometry (1996), while Friedel and others conducted active source imaging of the footprint left by two pillars on the mine floor (1996). Active source imaging has been implemented for pillar tomography at Homestake Mine (Scott, D. F., et al. 1999, Scott, D. F., et al. 2004), and Watanabe and Sassa imaged both a pillar and a triangular area between two drifts (1996). Manthei used active source geometry to image pillars in a potash mine (1997).

Tunnels have also been studied extensively to determine stress redistribution around openings. Many of these studies have been conducted at the Underground Research Lab (URL) in Canada where experiments can be well controlled. Passive source (Maxwell, S. C. and R. P. Young 1995, Maxwell, S. C. and R. P. Young 1996) and active source studies (Meglis, I. L., et al. 2004) of tunnels at the URL can be found in the literature.

The advantage of tunnel and pillar studies is a relatively simple and small scale geometry, which allows for optimum source and receiver placement. Larger scale studies are more difficult to design, but have been conducted successfully. Kormendi and others implemented in seam receivers with active source geometry for a longwall panel in an underground coal mine. They found that high velocity areas advanced with the face and were typical of stress redistribution encountered on a longwall (Kormendi, A., et al. 1986). In 1993, Maxwell and Young used active source

monitoring in a mine, and generated tomograms with known sources. Then they generated tomograms by using the active sources as "simulated passive sources" and compared the two sets of tomograms. Maxwell and Young used passive source technology from a minewide seismic monitoring system, and correlated high velocity areas with increased seismic activity (1996). Friedel and others used active sources to span drifts at Lucky Friday and Homestake mines, and discovered high velocity areas in the working faces (1997). Westman and others used roofbolt mounted receivers with the longwall shearer as an active source to image a longwall panel in an underground coal mine and found high stress areas from midface towards the tailgate (1996).

CHAPTER 3: SITE DESCRIPTION AND EXPERIMENTAL PROCEDURE

3.1 Site Description

3.1.1 GENERAL DESCRIPTION AND GEOLOGY

Raw data for this study were collected between July 7th, 1997 and August 8th, 1997 at an underground coal mine in the western United States. The mine employs longwall mining, and has produced an average of 7.5 million tons per year between 1995 and 2004 (MSHA 2005b). Average overburden at the site is approximately 1,200 ft. The longwall is mining in the Wadge Seam, which is approximately 10 feet thick, and the coal produced is classified as low sulphur, high BTU, group C bituminous coal (Sollars, P. K. and M. A. Alspaugh 1998).

A simplified geologic column is displayed in Figure 3.1:

Figure 3.1. Simplified Geologic Column (Kneisley, R. O. and K. Y. Haramy 1992).

The panel under examination is located on a syncline, and the elevation profile of the panel is displayed in Figure 3.2.

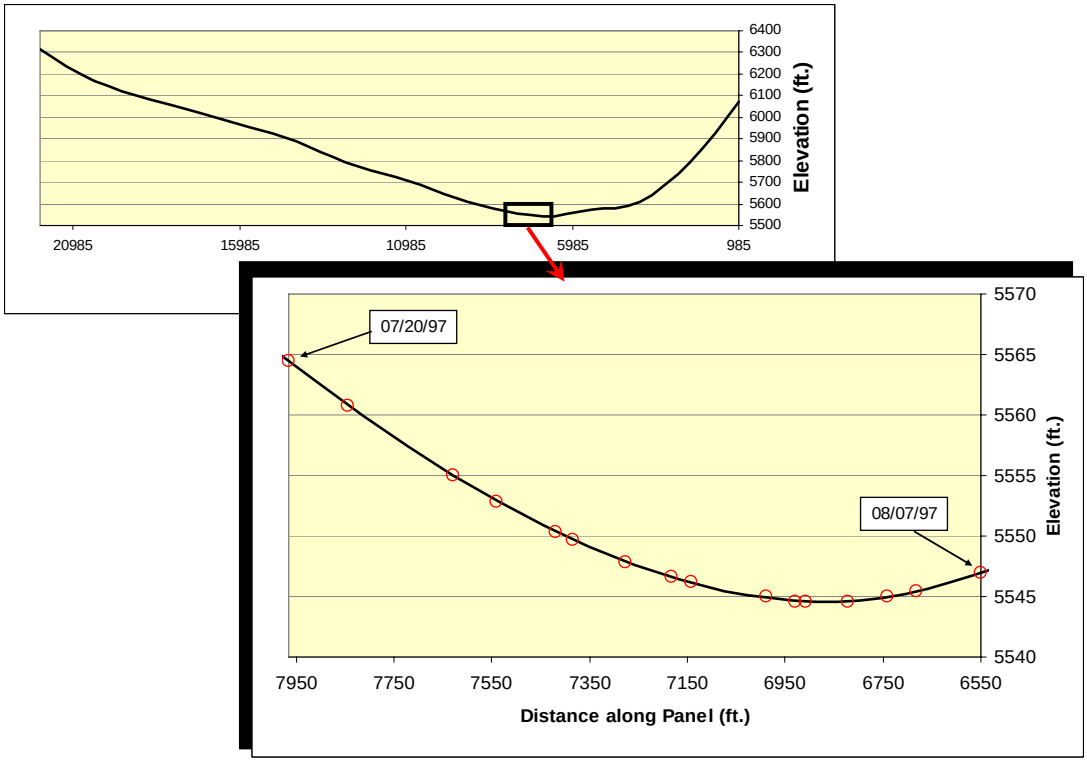

Figure 3.2. Seam Profile of Longwall Panel.

3.1.2 LONGWALL PANEL GEOMETRY

The mine operates longwall panels that are approximately 18,000 feet long and 815 feet wide. Figure 3.3, shows pillar geometry for the panel of interest. It is interesting to note that the adjacent panels to both sides of the active panel are unmined. Typically, the panel on the tailgate side would have been previously mined. All crosscuts and entries are 20 feet wide. On the tailgate side large pillars are positioned against the coal block, and these pillars are 200 feet by 95 feet, on centers. Yield pillars on the tailgate side are located against the adjacent panel, and they are 105 feet by 55 feet, on centers. On the headgate side the yield pillars are located against the active panel, and they are 95 feet by 55 feet, on centers. The large pillars on the headgate side, located against the adjacent panel, are 95 feet by 190 feet, on centers. Mining is advancing in the southwest direction, and face locations are shown for each day studied. Over the course of the study the face advanced 1,415 feet, averaging about 79 feet per day. Tomograms were not generated for July 29th, as data was not supplied for that day.

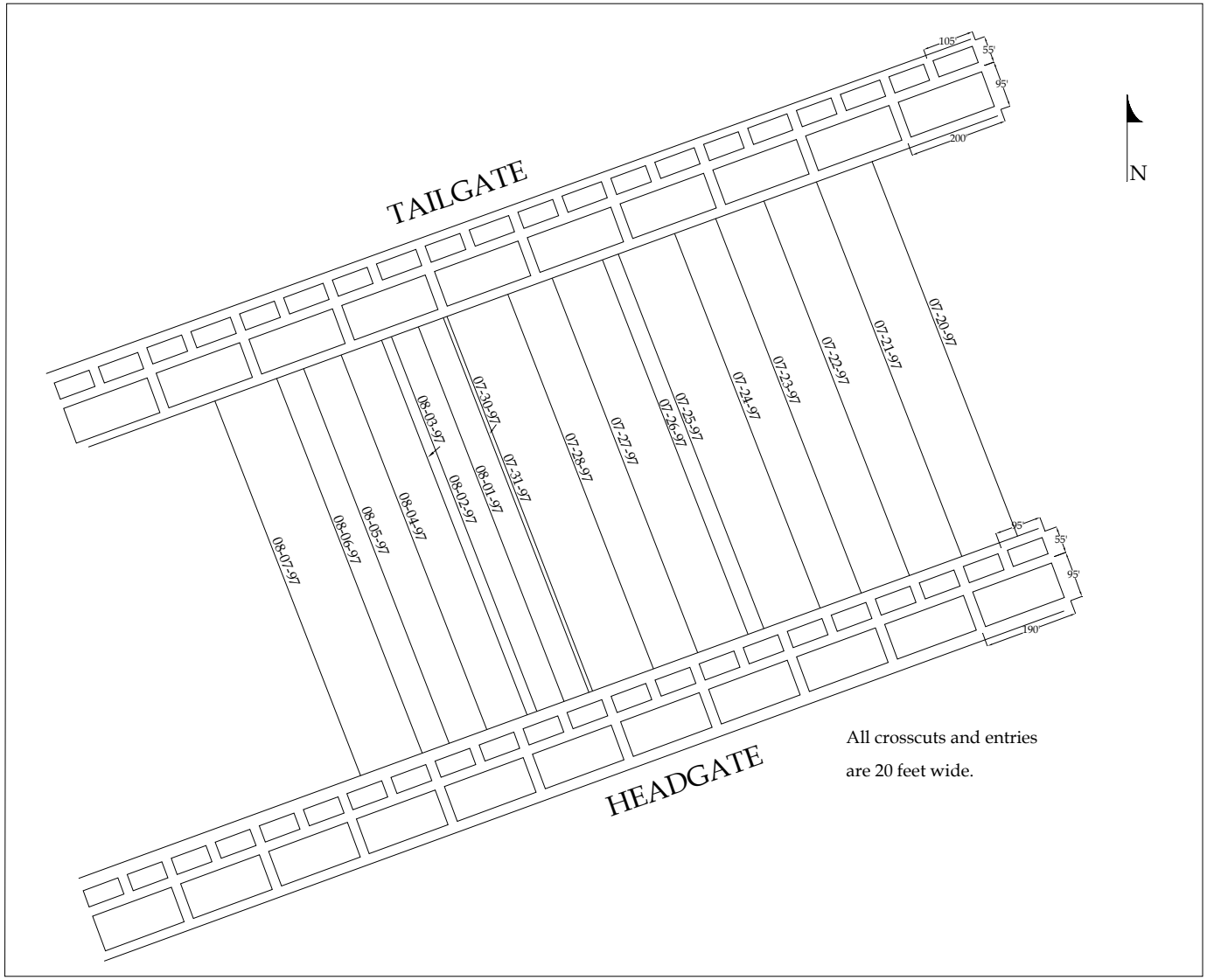

Figure 3.3. Longwall Panel Geometry.

3.1.3 SOURCE AND RECEIVER GEOMETRY

Sixteen geophones were assembled on the surface to monitor and locate microseismic events. Figure 3.4 displays a plan view of the geophone locations and the area of the longwall panel that is of interest.

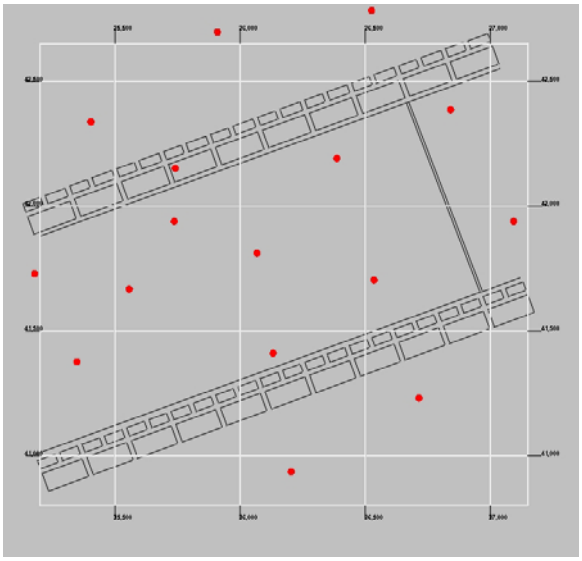

Figure 3.4. Geophone Locations.

The geophones are referred to as receivers while the microseismic events are referred to as sources, denoting the source of the seismic waves used to explore the rock mass.

The utilization of microseismic events as sources is an example of passive source geometry. The advantage of passive source geometry is that a large number of measurements can be collected at once, and they can be monitored remotely. However, the drawback is that the experimenter has less control over raypath geometry. When active source geometry is utilized, the experimenter can position the sources so that the optimum number of raypaths traverse the area of interest.

3.2 Data Analysis

The tomograms presented in this research are velocity tomograms generated from travel time and distance data. The arrival times of the p-waves generated by microseismic events are measured at the geophones located on the surface. Event

locations were previously determined (Swanson, P. 2005), so distances between sources and receivers are known. The data utilized in this research were collected by NIOSH in 1997.

3.2.1 DATA DESCRIPTION

The raw data received from NIOSH includes 172,632 p-wave arrival times, and 11,696 microseismic events over 18 days, from July 20th, 1997 to August 7th, 1997. Data were not provided for July 29th, 1997. The data files give the source coordinates, the microseismic event coordinates, relative magnitude of the events, traveltime residuals for event location, and the number of stations used to locate the event. Events that were located by less than 10 stations were not included in the data file.

3.2.2 DATA RECONCILIATION

First, the data were organized by day. Next, p-wave arrival times were plotted against raypath distance, excluding arrival times of zero, as shown in Figure 3.5:

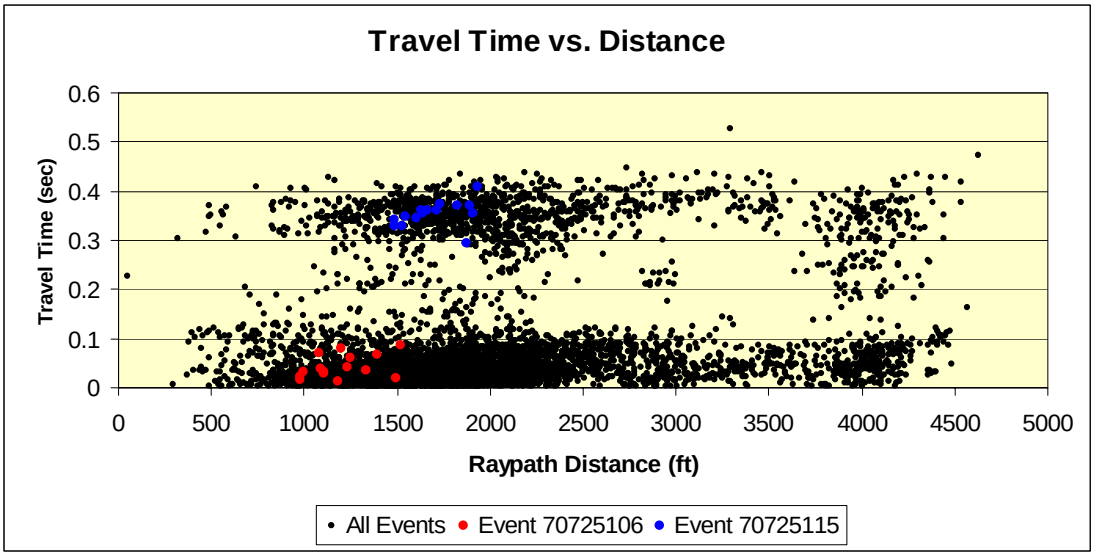

Figure 3.5. Travel Time vs. Distance Plot for 07-25-97.

Figure 3.5 displays all raypaths plotted in black, and two microseismic events plotted in blue and red. In examining the two events, it is obvious that there is a

linear correlation between the raypaths for individual events. Most events displayed a similar relationship. It was determined that an arrival time error was introduced into either the measurement or the event location that must be corrected for by normalizing the events. The equation of the line for the set of raypaths that comprise each event was determined, and the points were then corrected so that each intercept was equal to zero, assuming that at a distance of zero feet, velocity must equal zero. Additionally, any velocities higher than 30,000 ft/s were removed. A maximum of 30,000 ft/s was determined from published research, both field and laboratory. Research in underground mines and on laboratory specimens, including underground coal mines and sandstone specimens have published maximum p-wave velocity values ranging from about 7,381 ft/s to 24,934 ft/s (Tosaya, C. and A. Nur 1982, Kormendi, A., et al. 1986, Maxwell, S. C. and R. P. Young 1993, Jones, S. M. 1995, Ma, Q., et al. 1995, Maxwell, S. C. and R. P. Young 1996, Manthei, G. 1997, Scott, D. F., et al. 1997). From this data range, 30,000 ft/s was determined to be an appropriate maximum velocity. The resulting points are displayed in Figure 3.6.

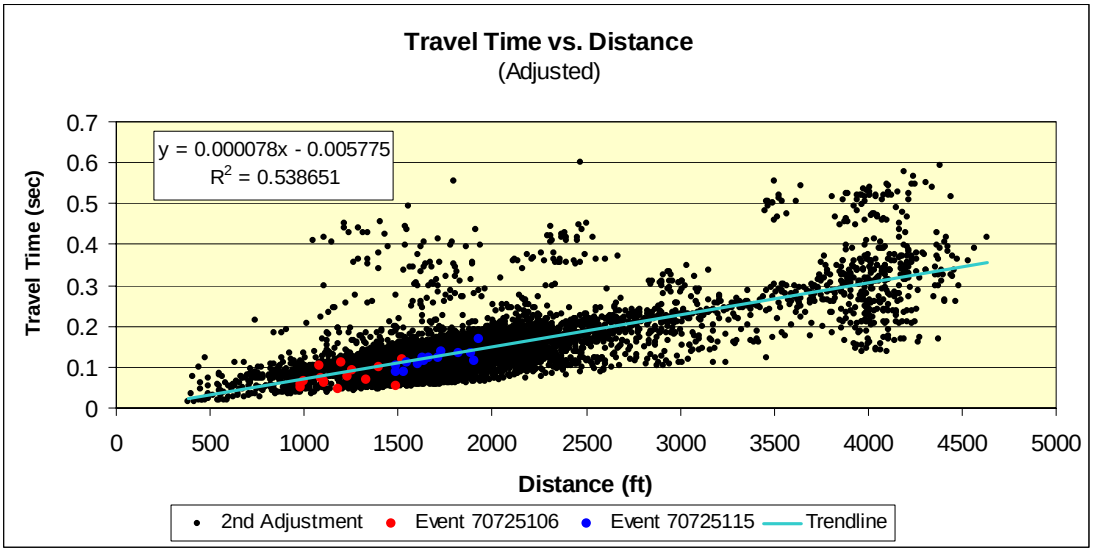

Figure 3.6. Adjusted Travel Time vs. Distance Data for 07-25-97.

3.3 Inversion

The data were given as a set of travel times and ray distances. The objective is to discretize the rock mass surrounding the longwall into voxels, and determine the

velocity in each voxel. From this velocity determination relative stress can be inferred. Because the solution to the problem is not unique, there are more voxels than measured rays, an iterative inversion technique was employed.

3.3.1 INVERSION TECHNIQUE

After adjusting the arrival times, a text file, including distance and travel time for each ray, is created for input into *GeoTOM*. *GeoTOM* is a commercial package that inverts for slowness, and then plots velocity in the form of tomograms. *GeoTOM* utilizes an iterative technique called SIRT, simultaneous iterative reconstruction technique, in the inversion process and relies on the following relationship to perform the inversion:

$$t = \int_R^S \frac{1}{v} \bullet dl = \int_R^S p \bullet dl$$

$$t_i = \sum_{j=1}^{M} p_j d_{ij}$$

$$\mathbf{T} = \mathbf{DP}$$

$$\mathbf{P} = \mathbf{D^{-1}P}$$

$$\mathbf{T'} = \mathbf{DP'}$$

$$\mathbf{dT} = \mathbf{T} - \mathbf{T'}$$

$$\mathbf{dP'} = \mathbf{D^T dT}$$

$$\mathbf{P''} = \mathbf{P'} + \mathbf{dP'}$$

where,

t = travel time (sec)

T = travel time matrix, 1xN, where N is the number of rays measured.

v = velocity (ft/s)

p = slowness, inverse velocity (s/ft)

P = slowness matrix, 1xM, where M is the number of voxels in the tomgram.

d = raypath distance (ft)

D = distance matrix, NxM, the distance of the ith ray in the jth voxel. [3.1]

Prime notation refers to the initial model.

As illustrated in Equation 3.1, the process is based on the assumption that the line integral from the source to the receiver of the slowness is equal to the traveltime. In applying this relationship to each voxel the matrix relationships are formed.

3.3.2 INPUT PARAMETERS

A voxel size of 50 feet by 50 feet by 50 feet was input into *GeoTOM*. This size was determined to be sufficiently small to ascertain the general stress trend, but sufficiently large that low and high velocity artifacts would not disrupt interpretation of the tomogram.

GeoTOM allows a number of other input parameters including an initial velocity model, anisotropy, smoothing, and the number of curved and straight ray iterations to perform.

The initial velocity model allows for *GeoTOM* to perform the inversion more efficiently and accurately. SIRT is an iterative technique, so the algorithm must have an initial velocity value to perturb for the first iteration. The initial velocity model was provided with the raw data from NIOSH, and is displayed in Figure 3.7. The approximate location of the Wadge coal seam is displayed in black. The velocity layers are also tabulated in Table 3.1.

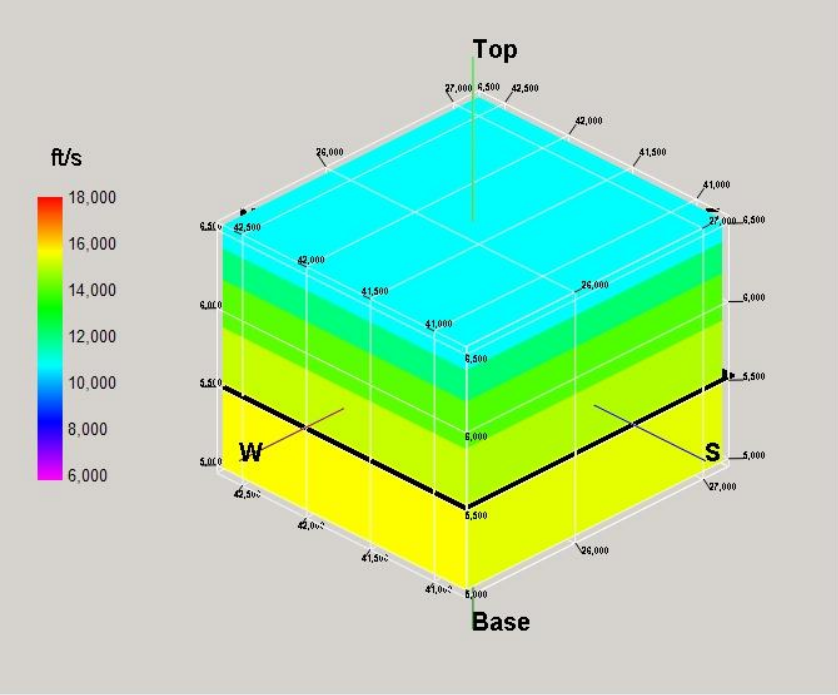

Figure 3.7. Initial Velocity Model.

Table 3.1. Initial Velocity Model.

Velocity (ft/s)	Top Elevation (ft)	Bottom Elevation (ft)
10,020	7,000	6,407
12,880	6,407	6,158
13,560	6,158	5,897
13,900	5,897	5,548
14,080	5,548	Infinite

In addition to the layered initial velocity model an anisotropy vector was also provided. This vector is normal to the layers of the initial velocity model. The anisotropy vector is [-0.068096, 0.057140, 0.996041], and was also input into *GeoTOM*.

Anisotropy refers to the variation of a characteristic of a material with the direction of measurement (Schlumberger 2005). In this situation, anistotropy refers to the variation in p-wave velocity as measured parallel or perpendicular to the bedding layers. Cox indicates that the ratio between p-wave velocity parallel to the bedding plane and perpendicular to the bedding plane is generally between 1.0 and 1.45

(1999). The magnitude of anisotropy was determined experimentally. The data from August 6th, 1997 were inverted five times, at 30 iterations each, with anisotropy magnitudes of 0.8, 0.9, 1.0, 1.1, and 1.2, and with all other parameters being held constant. *GeoTOM* outputs a file of travel time residuals when an inversion is performed. These residuals were examined to determine the optimum anisotropy. The graph in Figure 3.8 summarizes the anisotropy test.

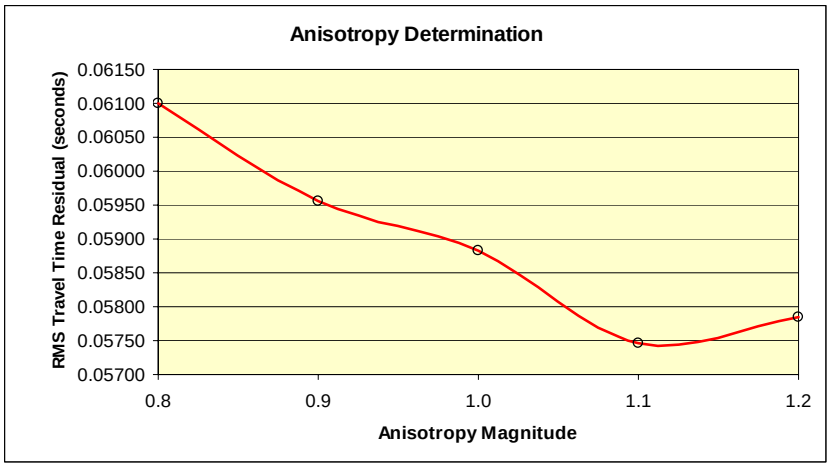

Figure 3.8. Experimental Determination of Anisotropy Magnitude.

As evidenced in Figure 3.10, the anisotropy vector of 1.1 produced minimum root-mean-square residuals. Root-mean-square residuals are calculated as follows:

$$RMS = \sqrt{\frac{1}{N}\sum_{i=1}^{n} x_i^2} \qquad [3.2]$$

where x_i is the residual for the i^{th} ray in seconds.

Next, the appropriate ray assumption must be determined. *GeoTOM* will calculate raypaths based on a straight ray assumption or a curved ray assumption. The straight ray calculation is simply the straight line distance between the source and the receiver, while the curved ray calculation allows for ray bending according to Snell's Law. Figure 3.9 displays RMS residuals for the straight ray assumption and curved ray assumption, illustrating that the residuals are smaller for the straight ray assumption.

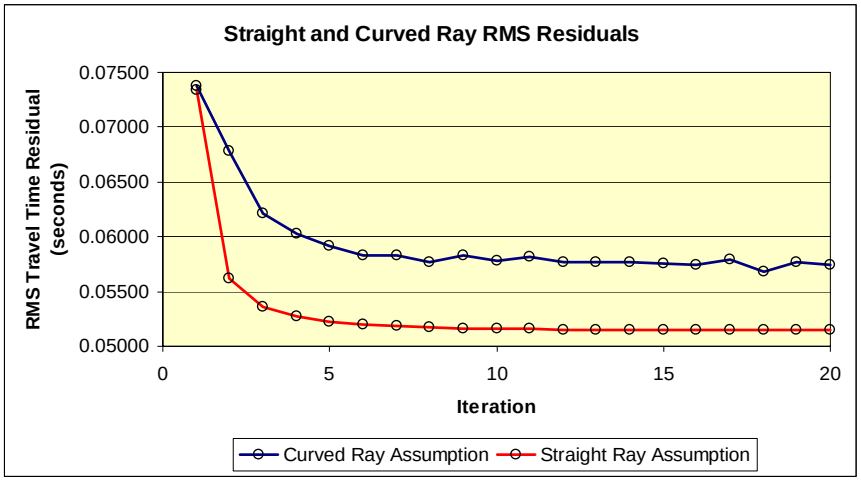

Figure 3.9. RMS Residuals for Straight and Curved rays for August 6th, 1997.

However, Snell's Law implies that for the layered initial velocity model the straight ray assumption is not valid. Additionally, sum residuals are significantly smaller for the curved ray assumption, as illustrated in Figure 3.10. Sum residuals are simply the sum of the travel time residuals for each ray in the iteration. Sum residuals are not a measure of the magnitude of the residuals, but rather of their distribution about zero. The higher sum residuals for the straight ray assumption indicate that the straight ray algorithm consistently underestimates the raypath length.

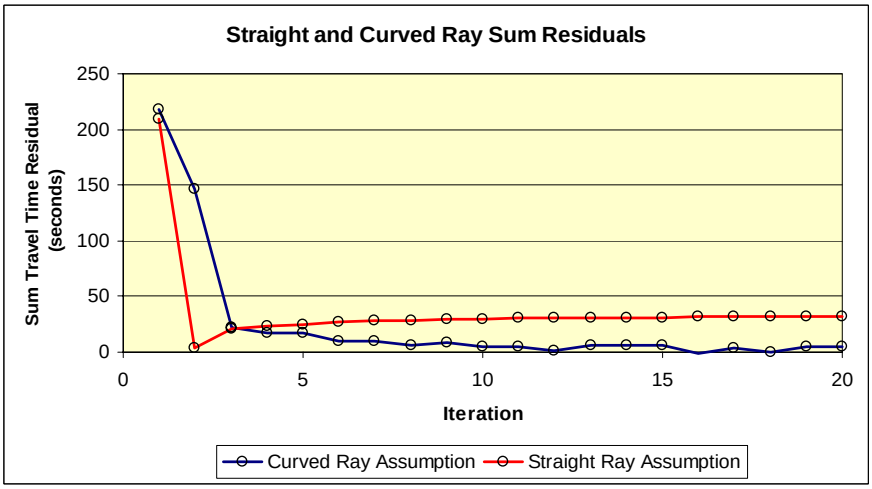

Figure 3.10. Sum Residuals for Straight and Curved Rays for August 6th, 1997.

Clement and Knoll ran synthetic tomograms for cross borehole data with straight and curved ray algorithms and found similar results in their tests; the RMS error was smaller for the straight ray algorithm than for the curved ray algorithm. They still

concluded that the curved ray algorithm was favorable because it more accurately portrayed their model. Yet, they stated that the curved ray algorithm can better model diffraction and will allow for more sharply defined boundaries (Clement, W. P. and M. D. Knoll 2000). By this reasoning it was determined that the curved ray assumption was appropriate for this data.

Finally, the optimum number of iterations must be determined. The graph displayed in Figure 3.11 indicates that after approximately 10 iterations there is not a significant reduction in RMS residuals:

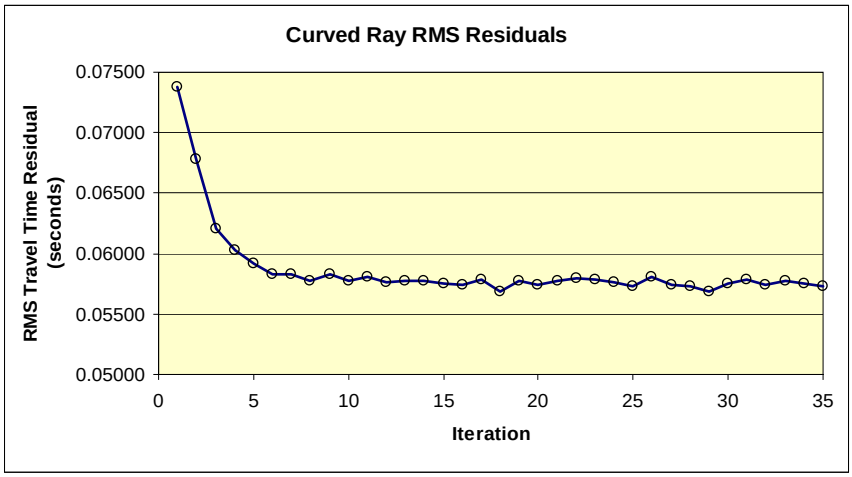

Figure 3.11. RMS Residuals for 35 Curved Ray Iterations for August 6th, 1997.

Only the residual data for August 6th, 1997 is presented here, but similar results were found for the other seventeen days. A comparison of RMS residuals for all eighteen days at 10 curved ray iterations each is presented in Figure 3.12:

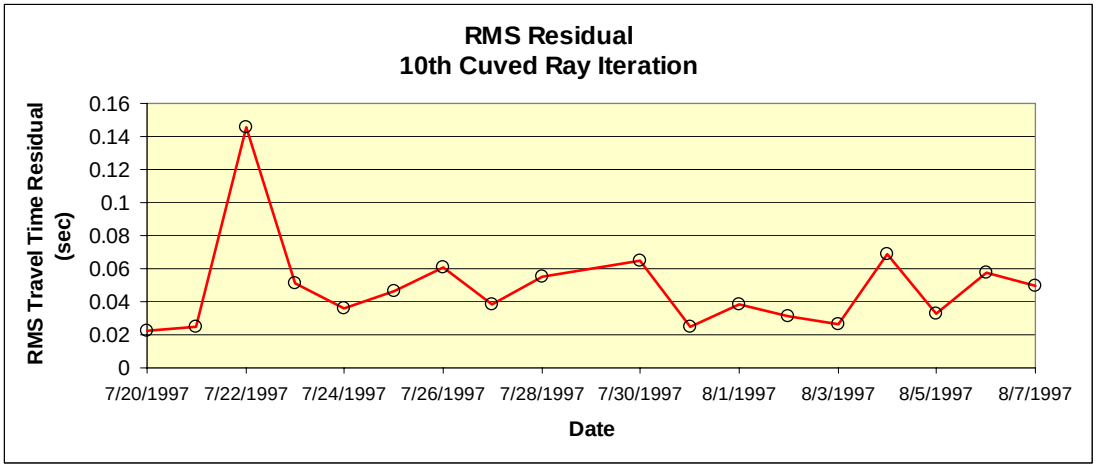

Figure 3.12. RMS Residuals.

The relative RMS residual may be used as an indicator of how well the model fits the data for any given day.

The minimum and maximum scale velocity values of 6,000 ft/s and 18,000 ft/s were determined by trial-and-error. These values provided sufficient contrast in the tomograms.

A smoothing constant was applied in all directions. Smoothing replaces the velocity value at a node by a weighted average of the velocity at that node and the surrounding nodes. Smoothing can help to remove inconsistencies in the model, but if a model is oversmoothed important anomalies can be removed. A fairly small smoothing constant of 0.02 was chosen to avoid oversmoothing.

In summary, the following parameters were input into *GeoTOM*:

Table 3.2. Input Parameters for GeoTOM.

Parameter	Value	Units
Minimum x coordinate	25,200	feet
Maximum x coordinate	27,150	feet
Node Spacing (x)	50	feet
Number of Nodes (x)	39	
Minimum y coordinate	40,800	feet
Maximum y coordinate	42,650	feet
Node Spacing (y)	50	feet
Number of Nodes (y)	37	
Minimum z coordinate	5,000	feet
Maximum z coordinate	6,500	feet
Node Spacing (z)	50	feet
Number of Nodes (z)	39	
Anisotropy Vector	[-0.068, 0.057, 0.996]	
Anisotropy Magnitude	1.1	
Minimum Velocity	6,000	ft/s
Maximum Velocity	18,000	ft/s
Number of Straight Ray Iterations	0	
Number of Curved Ray Iterations	10	
Smoothing	0.02	

Finally, *GeoTOM* outputs tomograms similar to the one displayed in Figure 3.13.

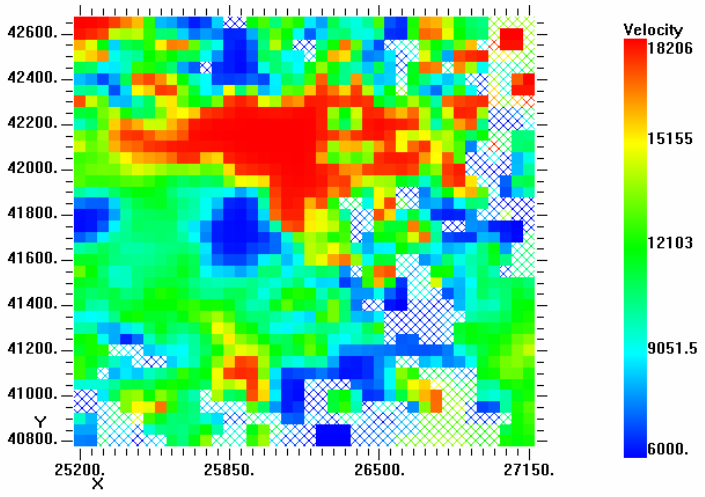

Figure 3.13. Tomogram at Z = 5,550 ft., Seam Level, for August 6th, 1997.

3.4 Three-Dimensional Modeling

GeoTOM creates three-dimensional models, but only allows for one slice to be viewed at a time. *RockWorks*, a commercial geotechnical package, allows for the *GeoTOM* tomograms to be viewed as a solid model. The model can be sliced, rotated, and filtered. *GeoTOM* outputs a .dat file, which includes a node location, the number of rays passing through the node, and the velocity at the node. This file is imported into *RockWorks*. The file is filtered so that only nodes with at least 5 rays are included in the model. Filtering nodes with less then 5 rays helps avoid artifacts in the model. For example, if a node has only one ray passing through it and that ray velocity is unreasonable, then the node will show an unusually large or small value, which appears as an artifact on the tomogram. Nodes with at least 5 rays passing through them are well-constrained and less likely to produce artifacts.

RockWorks then creates a solid model using user specified geometry. Geometry and voxel dimensions are the same as specified above in *GeoTOM* input parameters. An isotropic inverse distance algorithm is used to extrapolate between the nodes and generate a solid model. The isotropic inverse distance algorithm assigns node values based on the distance a node is from known node values (Rockworks Manual 2002). Known node values refer to the nodes that were specified in the *GeoTOM* file.

Displayed in Figure 3.14 are a sliced solid model, a solid model, and a filtered solid model generated by *RockWorks*.

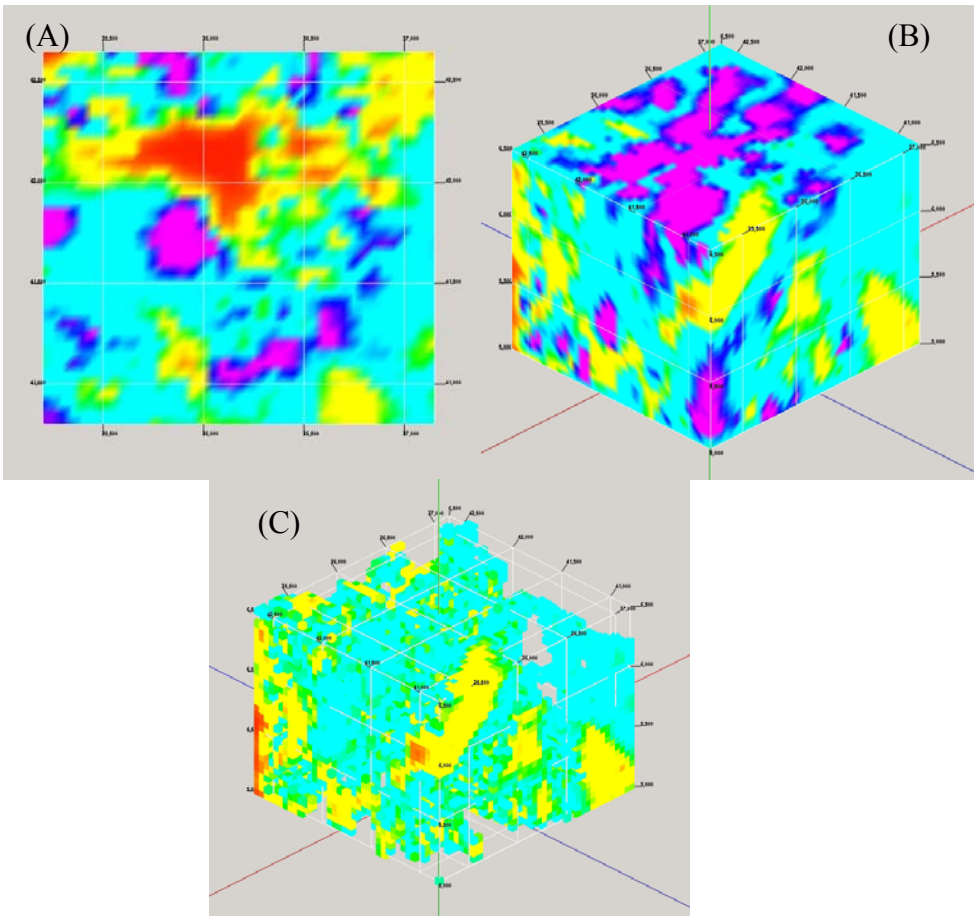

Figure 3.14. a.) Solid Model Sliced at Z = 5,550 feet. b.) Solid Model for August 6th, 1997. c.) Solid Model with Velocity Values Less than 10,000 ft/s Filtered.

The flow chart in Figure 3.15, summarizes the procedure used to generate tomograms.

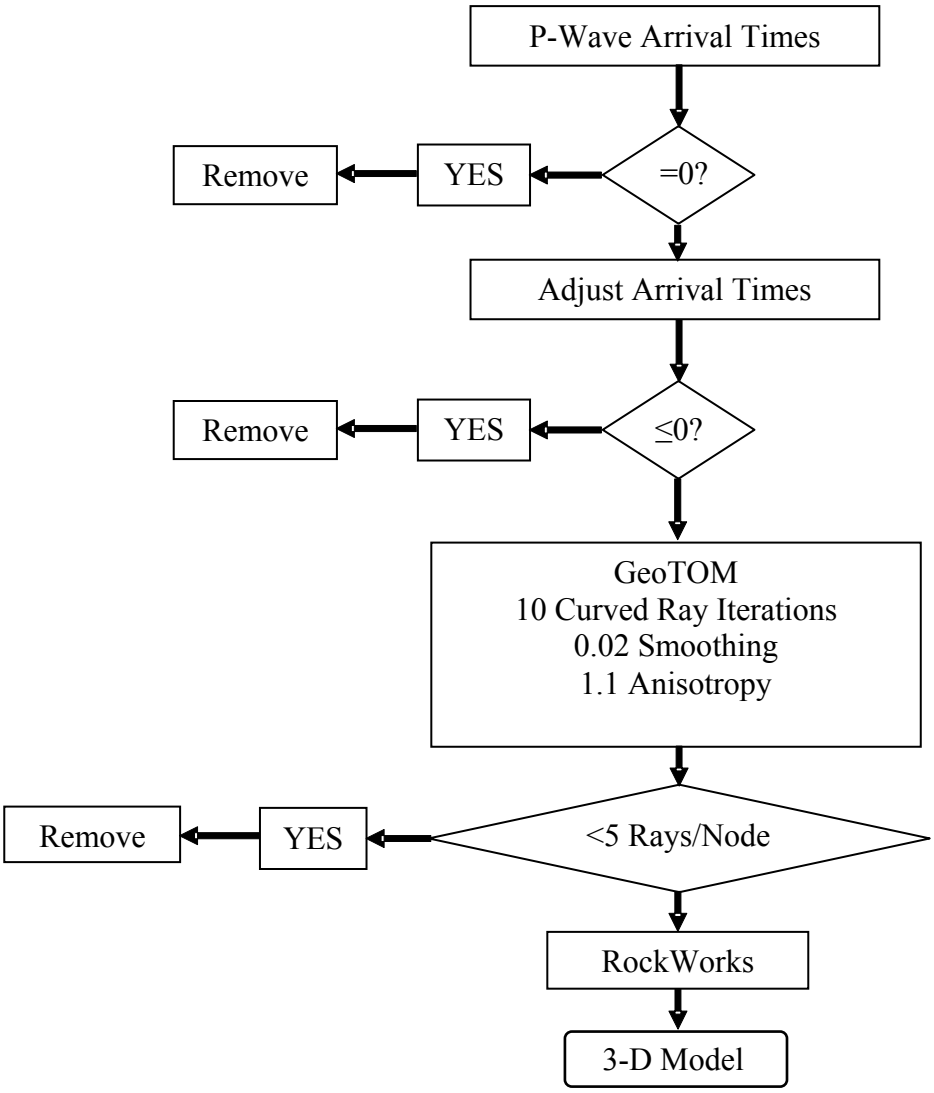

Figure 3.15. Procedure for Tomogram Generation.

Due to the tabular nature of coal deposits plan views of the three-dimensional model are effective. The roof, floor, and seam can all be separated and viewed individually.

3.5 NUMERICAL MODELING

In order to validate the stress distribution displayed by the tomograms, some simple numerical modeling was performed. *LAMODEL*, a displacement discontinuity program, available through NIOSH was used to model the stress at the seam level.

LAMODEL was written specifically for tabular deposits, and treats the rock mass as a series of frictionless plates.

LAMODEL requires a number of input parameters in order to model the behavior of the coal seam and the overburden material. Since no testing of material was incorporated into this research these parameters were determined using published values of similar material.

First, the overburden parameters including Poisson's ratio, elastic modulus, lamination layer thickness, and vertical stress gradient are input. Since the coal seam is overlain and underlain by massive competent sandstone, sandstone is used as the overburden material. Approximately 15 feet above the seam is a 25 foot thick sandstone formation and the underlying seam is Troutcreek Sandstone. Also, approximately 700 to 750 feet above the seam is the 200 foot thick Twentymile sandstone unit. Previous research in the mine gives Poisson's ratio and the elastic modulus for the sandstone. A lamination layer thickness of 25 ft was determined to represent the sandstone immediately over the seam. The vertical stress gradient was also taken from previously published research. The parameters for the overburden are tabulated below:

Table 3.3. Overburden Input Parameters.

Parameter	Units	Value
Poisson's Ratio	-	0.31
Elastic Modulus (E)	psi	3210000
Lamination Layer	ft	25
Vertical Stress Gradient	psi/ft	0.95376

Next, *LAMODEL* prompts for coal properties, including the coal modulus, plastic modulus, coal strength, and Poisson's ratio. The default values listed in Table 3.4 were accepted. Coal properties can be difficult to determine and may vary substantially among samples.

Table 3.4. Coal Input Parameters.

Parameter	Units	Value
Coal Modulus	psi	3000000
Plastic Modulus	psi	0
Coal Strength	psi	900
Poisson's Ratio	-	0.33

Finally, gob properties are established including, an initial gob modulus, upper limit stress, gob height factor, gob load ratio, and a final modulus, calculated by the program. The upper limit stress is recommended to be 2 to 4 times the virgin stress to keep the model stable, and 4,000 psi is consistent with experimental data for gob consisting of strong sandstone. The program recommends a gob height factor of one to six. The gob load ratio is the average gob load over the maximum gob load – values of 0.5 to 0.9 are recommended. Gob parameters are tabulated in Table 3.5:

Table 3.5. Gob Input Parameters.

Parameter	Units	Value
Initial Gob Modulus	psi	500
Upper Limit Stress	psi	4000
Gob Height Factor	-	2
Gob Load Ratio	-	0.7
Final Modulus	-	13005.3

LAMODEL allows for the geometry of the longwall panel, as shown in Figure 3.3, to be input into the program. Additionally, *LAMODEL* will run the routine in steps. The steps allow for each of the 18 face locations to be read into the program. Each step is one of the 18 days, and *LAMODEL* takes into account the material removed when calculating stress redistribution.

CHAPTER 4: EXPERIMENTAL RESULTS

4.1 Tomograms

4.1.1 DISPLAY OF TOMOGRAMS

Because the tomograms are generated with passive source geometry, each image is produced with different ray geometries, and levels of confidence vary. There are three parameters which can be examined to determine the relative validity of each tomogram. First, an examination of the time-distance plots will provide an indication of how well the data is reduced. In Appendix A, the initial and adjusted time-distance plots for each day are displayed. Additionally, the total number of points in the initial data set, in the adjusted data set, and the percentage of points removed between the two sets are displayed. Figure 4.1 shows the adjusted data sets and statistics for 07-22-97 and for 08-01-97.

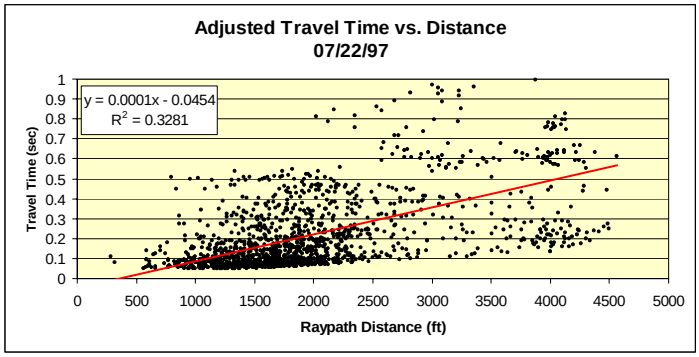

Date	7/22/1997	
Number of Microseismic Events	329	
Face Advance	113	ft
Number of Original Points	4897	
Number of Adjusted Points	1435	
Data Points Removed	70.70%	%
RMS Residual for Final Iteration	0.1459	sec
Average Velocity	13468.69	ft/s

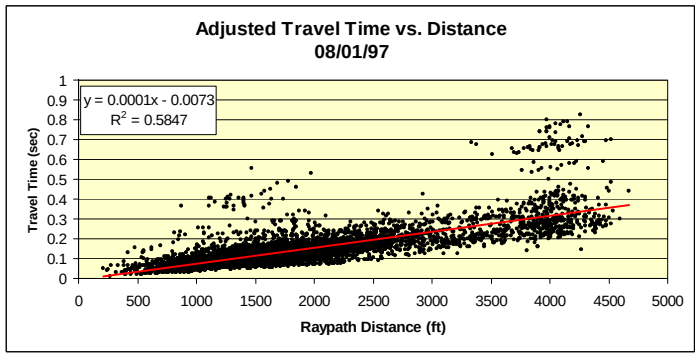

Date	8/1/1997	
Number of Microseismic Events	819	
Face Advance	153	ft
Number of Original Points	12096	
Number of Adjusted Points	11722	
Data Points Removed	3.09%	%
RMS Residual for Final Iteration	0.03818	sec
Average Velocity	14695.64	ft/s

Figure 4.1. Travel Time vs. Distance Plots and Statistics for 07-22-97 and 08-01-97.

In comparing the two plots it is obvious that 07-22-97 exhibits more scatter than 08-01-97 with R^2 values of 0.3281 and 0.5847, respectively. Next, in adjusting the events 70.70% of the points recorded on 07-22-97 were removed while only 3.09% of the points recorded on 08-01-97 were removed. This would indicate that each individual event on 07-22-97 showed an unusual amount of scatter. From examining the scatter plots, the data for 08-01-97 will produce a more accurate tomogram than the data for 07-22-97.

The next parameter to examine is the RMS residual. The RMS residual gives an idea of how well the model, the tomogram, fits the data, the adjusted distance and travel time points. The RMS residuals for the tenth iteration for 07-22-97 and 08-01-97 are 0.1459 and 0.03818, respectively. This would indicate that the model for 08-01-97 better fits the data.

The third, and most important parameter, is the ray density. The more rays that traverse an area, the better constrained the area. The best way to image ray density is to plot ray density on the same scale as the tomogram under examination. Ray density plots for 07-22-97 and 08-01-97 at seam level, Z = 5,500 feet, are displayed below in Figure 4.2.

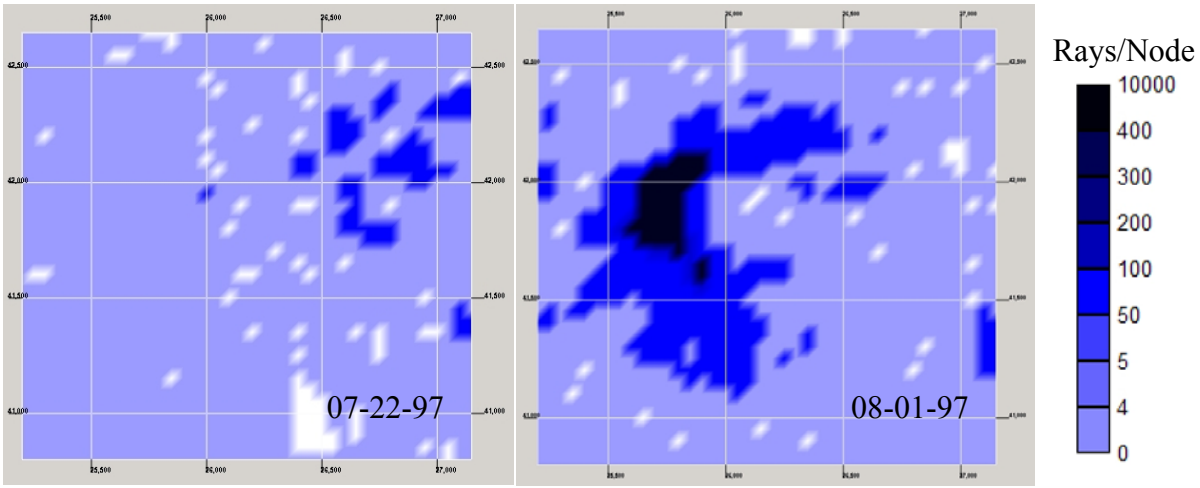

Figure 4.2. Ray Density Plots for 07-22-97 and 08-01-97.

In examining the ray density plots it is evident that there is more coverage on 08-01-97, as compared to 07-22-97.

By considering the three parameters discussed above, more confidence should be placed in the tomogram for 08-01-97 than for 07-22-97. Appendices B, C, D, and E contain floor, seam, roof, and vertical section velocity tomograms, respectively. Each tomogram is displayed with a ray density plot to allow the reader to ascertain relative validity. The ray density plots are always displayed in blue scale to distinguish them from velocity tomograms.

In examining the entire dataset, two days in particular stand out as having very poor ray density, excessive scatter, and high RMS residuals. They are 07-22-97 and 08-01-97. Little or no confidence should be placed in these tomograms, and they will not be considered when discussing consistency in the tomograms. Also, the velocity tomogram produced for 07-20-97, shows poor ray density, but reasonable correlation, with an R^2 value of 0.74. The sparse ray density is due to the fact that microseismic recording did not begin until about 7:00 pm on 07-20-97, the first day of the study.

4.1.2 FLOOR LEVEL TOMOGRAMS

As indicated in the previous chapter the seam elevation for this dataset ranges between 5,545 and 5,565 feet. Since the voxels in the tomographic model are 50 feet by 50 feet by 50 feet, a seam elevation of 5,550 feet is appropriate. In order to view the stress distribution in the floor of the mine the model is sliced at 5,400 feet to produce a two-dimensional velocity tomogram. Historically, this mine has stored strain energy in the floor, so it is important to analyze the stress redistribution in the floor. The floor level tomograms for each of the days under study are displayed in Figure 4.3. The tomograms for 07-22-97 and 07-30-97 are excluded as there was little linear correlation in the data, and poor ray density. The tomograms are displayed in succession, from left to right, top to bottom. Each tomogram also displays the longwall panel geometry and face location. Appendix B presents all eighteen tomograms, and ray density plots with each tomogram.

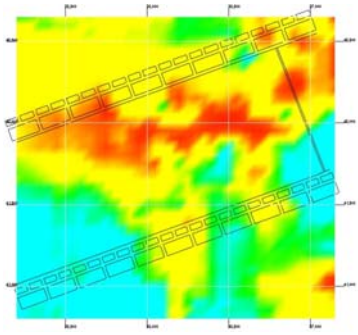

07-20-97

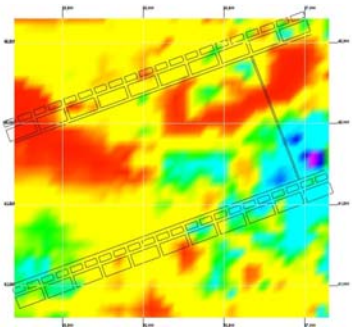

07-21-97

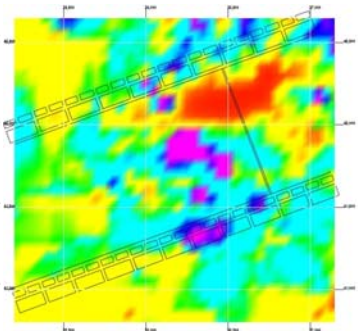

07-23-97

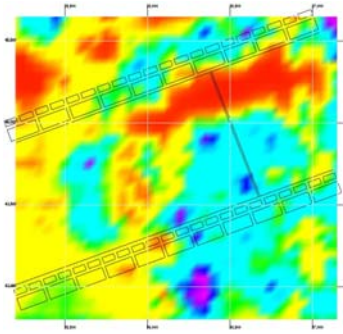

07-24-97

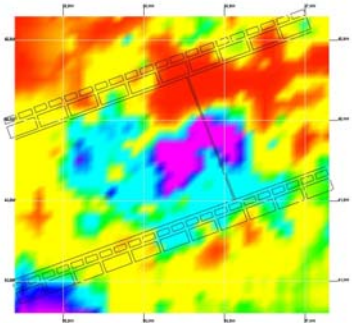

07-25-97

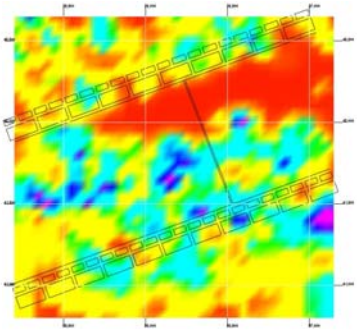

07-26-97

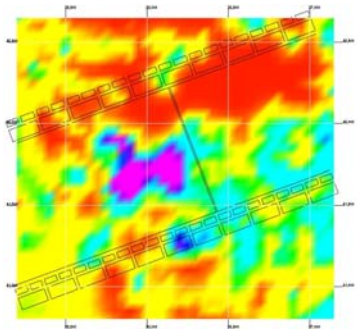

07-27-97

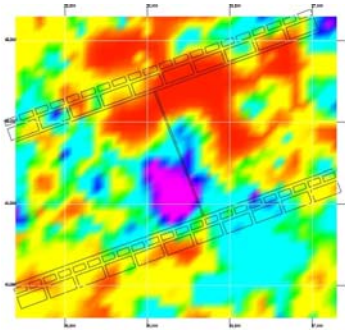

07-28-97

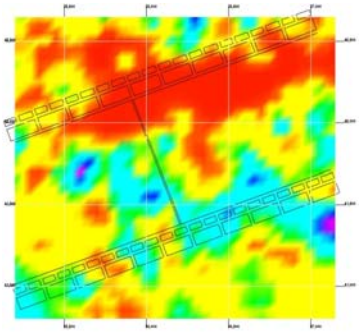

07-31-97

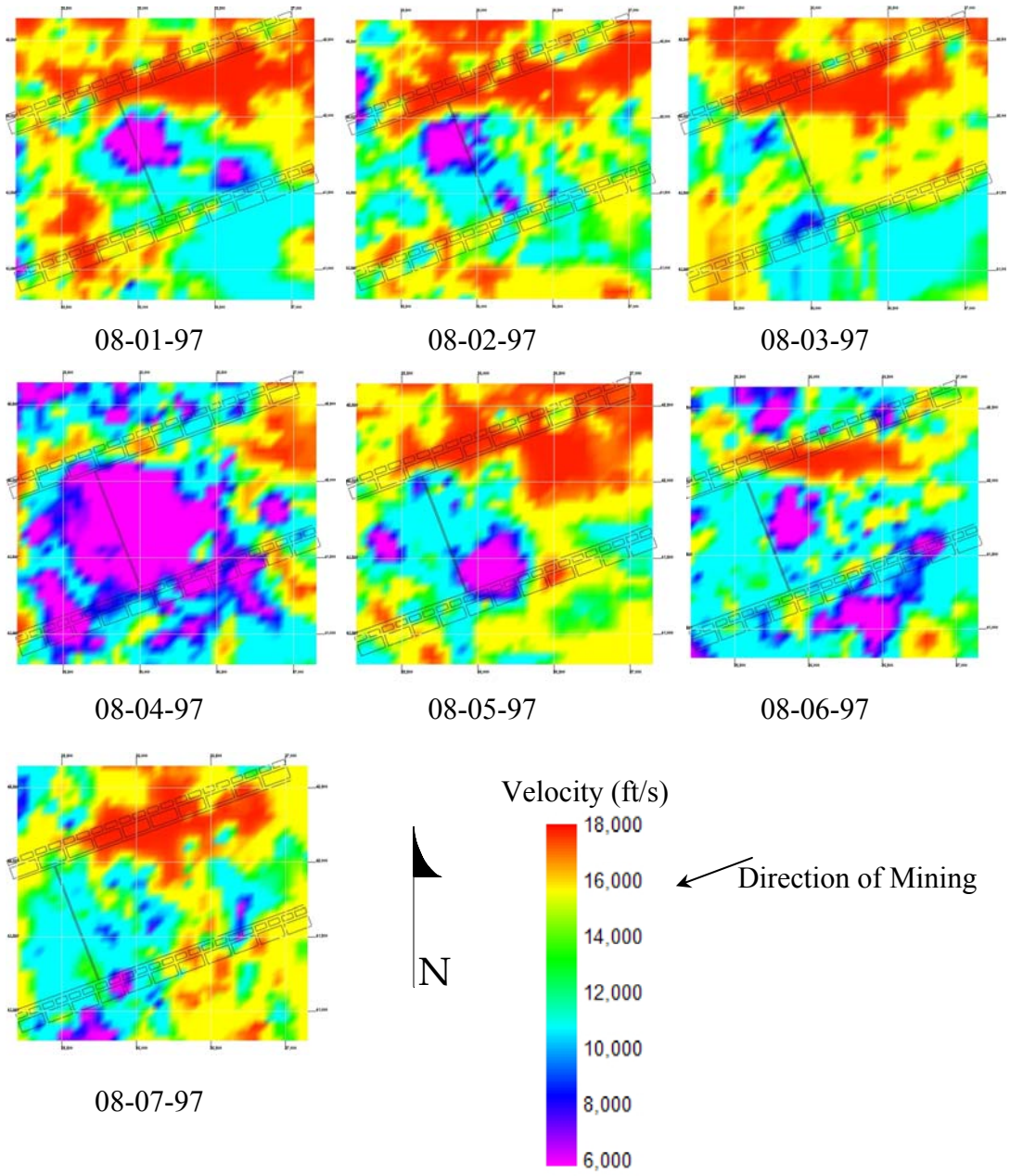

Figure 4.3. Floor Level Velocity Tomograms, Z = 5,400 feet.

In examining the floor level tomograms, there is a consistently high velocity zone present along the tailgate of the longwall panel, indicating a zone of high stress. The exception to this observation is 08-04-97 which exhibits a large low velocity area. Another consistent anomaly is the low velocity area that occurs at, or just inby the longwall face that is especially evident on 07-23-97, 07-25-97, 07-27-97, 07-28-97, 08-01-97, 08-02-97, 08-04-97, and 08-05-97.

4.1.3 SEAM LEVEL TOMOGRAMS

In order to view stress redistribution at seam level the three-dimensional tomogram is sliced at Z = 5,550 feet. Again, the tomograms are displayed in succession in Figure 4.4, excluding 07-22-97 and 07-30-97. Appendix C displays all eighteen tomograms in addition to ray density plots.

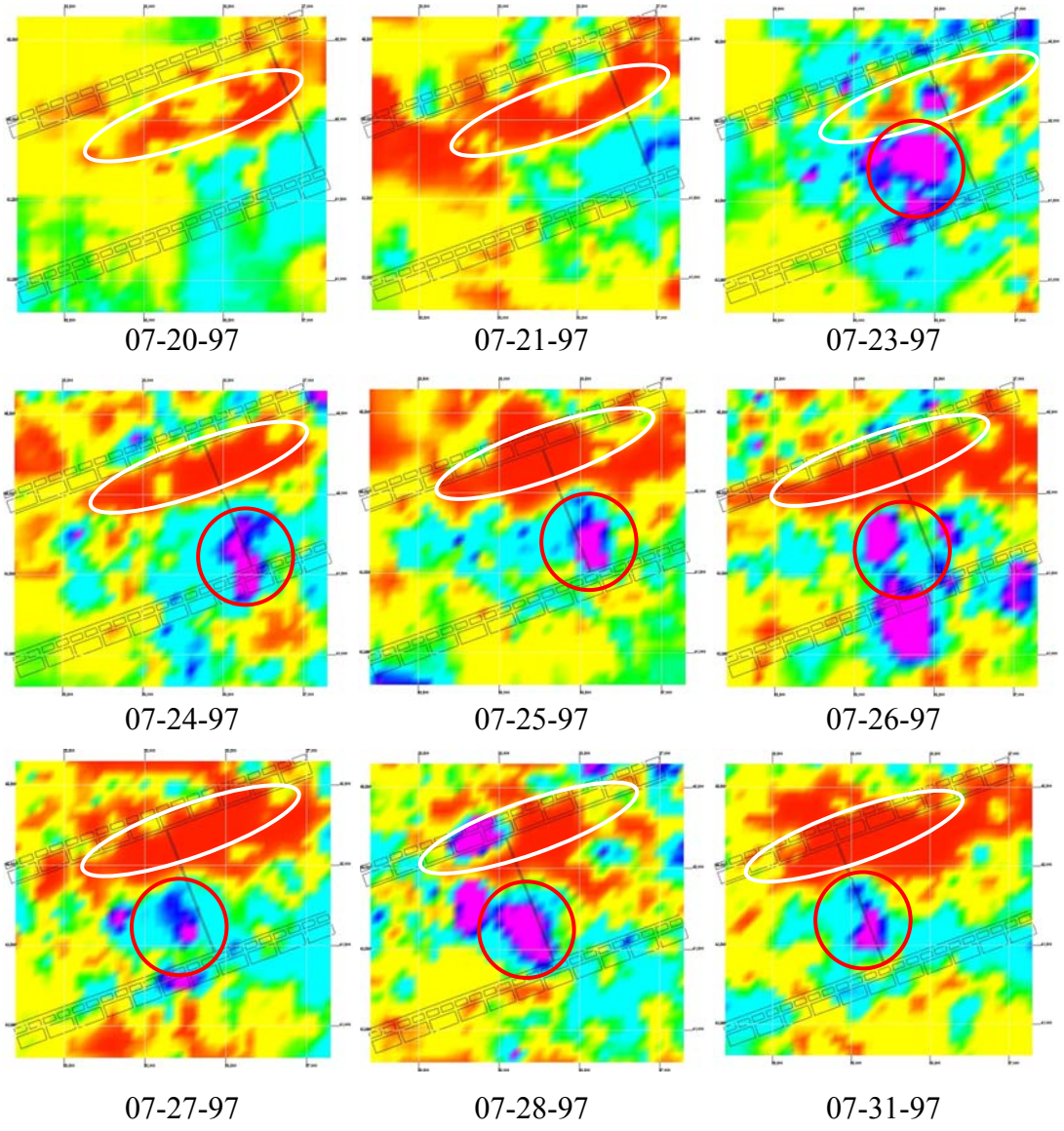

07-20-97 07-21-97 07-23-97

07-24-97 07-25-97 07-26-97

07-27-97 07-28-97 07-31-97

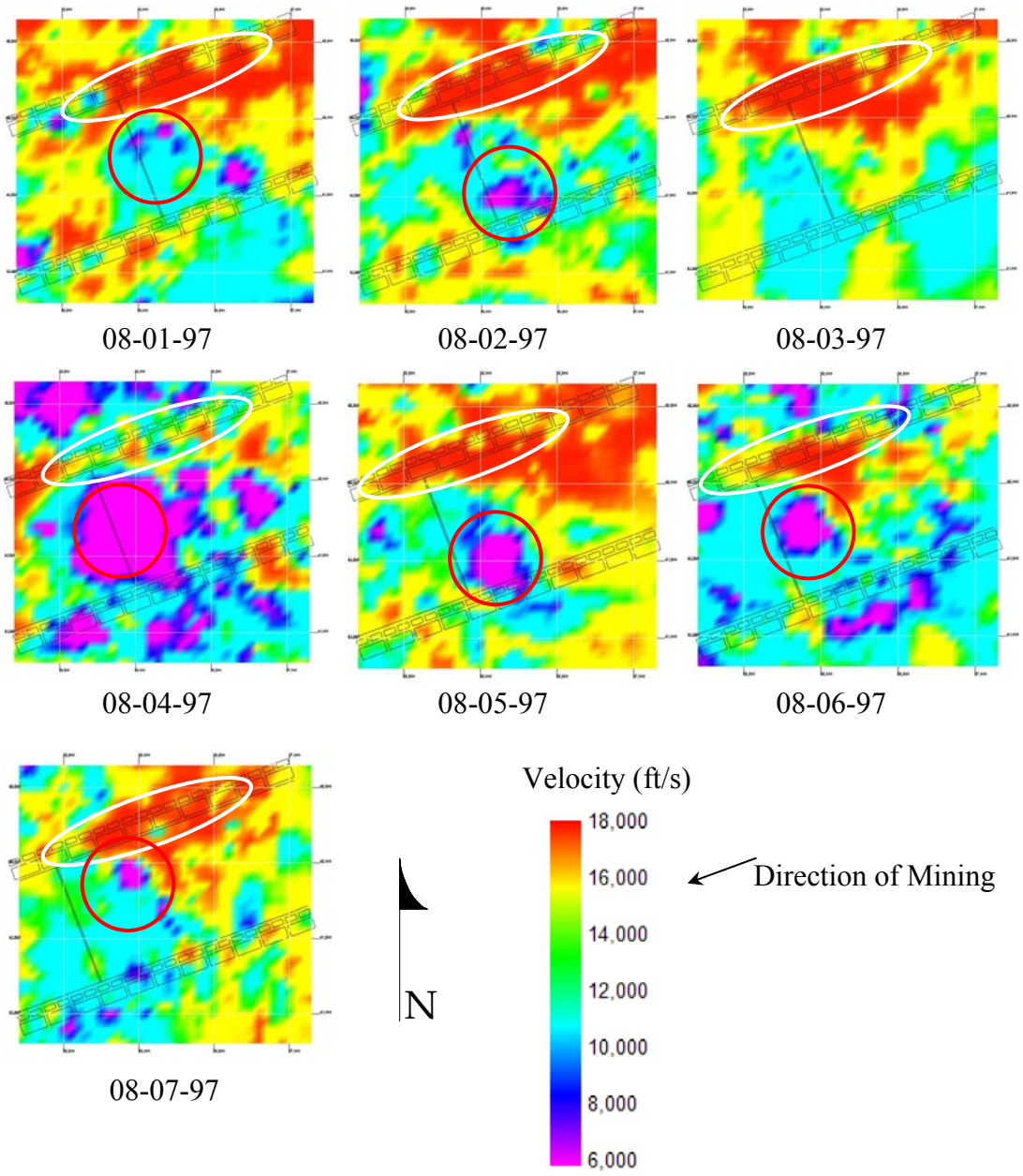

Figure 4.4. Seam Level Velocity Tomograms, Z =5,550 feet.

In examining the seam level tomograms, many of the same features are observed as were observed in the floor level tomograms. Again, a high velocity zone is evident along the tailgate for every day studied, with the exception of 08-04-97, which again shows a low stress zone. The high velocity zone is surrounded by a white oval in Figure 4.4. The high velocity zone appears to redistribute with face advance, but remains relatively stationary. Also, the low velocity zone at, or just outby the face is

again evident on many of the tomograms. The low velocity zone, where evident, is surrounded by a red circle. This low velocity zone advances with the face.

Appendix H is an animation of the seam level tomograms, excluding 07-20-97 and 07-30-97. The tomograms in the animation are filtered so that only velocity values above 14,000 ft/s are displayed. The animation allow face advance to be observed with stress redistribution.

4.1.4 ROOF LEVEL TOMOGRAMS

Next, the three-dimensional model is sliced at 5,700 feet to view the stress redistribution in the roof. Velocity tomograms for each day, excluding 07-22-97 and 07-30-97 are displayed in succession in Figure 4.5. Appendix D displays the velocity tomograms for each of the eighteen days of the study, along with ray density plots.

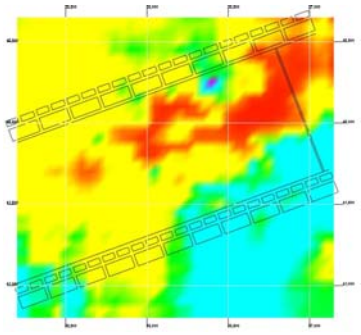

07-20-97

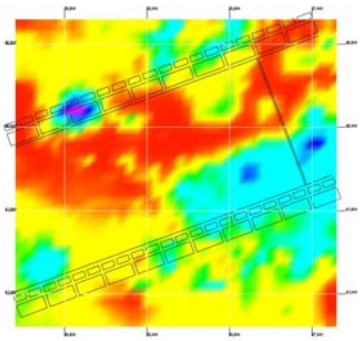

07-21-97

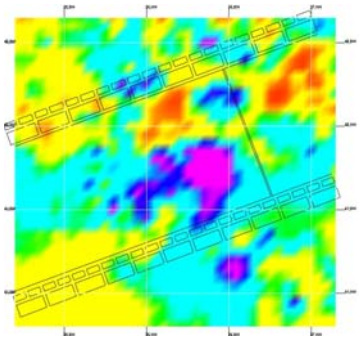

07-23-97

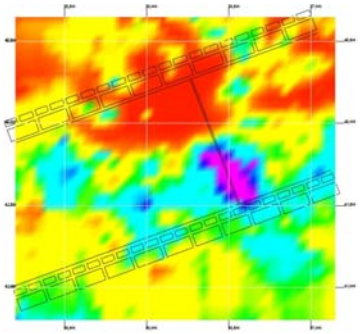

07-24-97

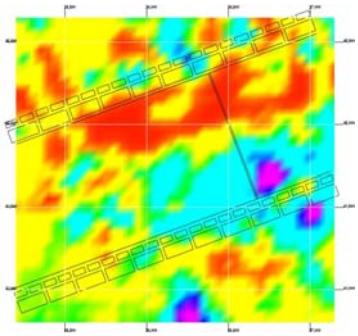

07-25-97

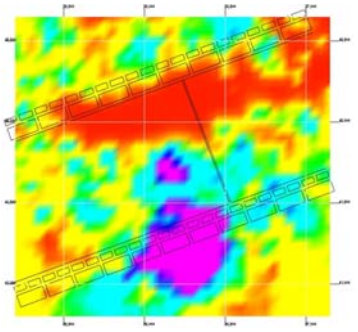

07-26-97

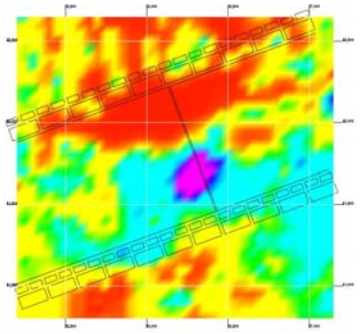

07-27-97

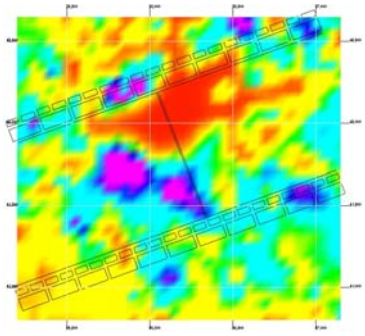

07-28-97

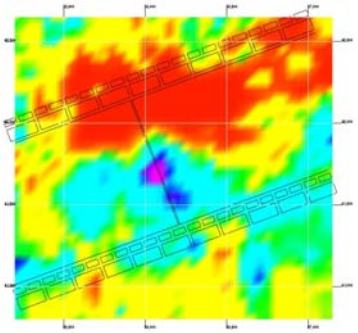

07-31-97

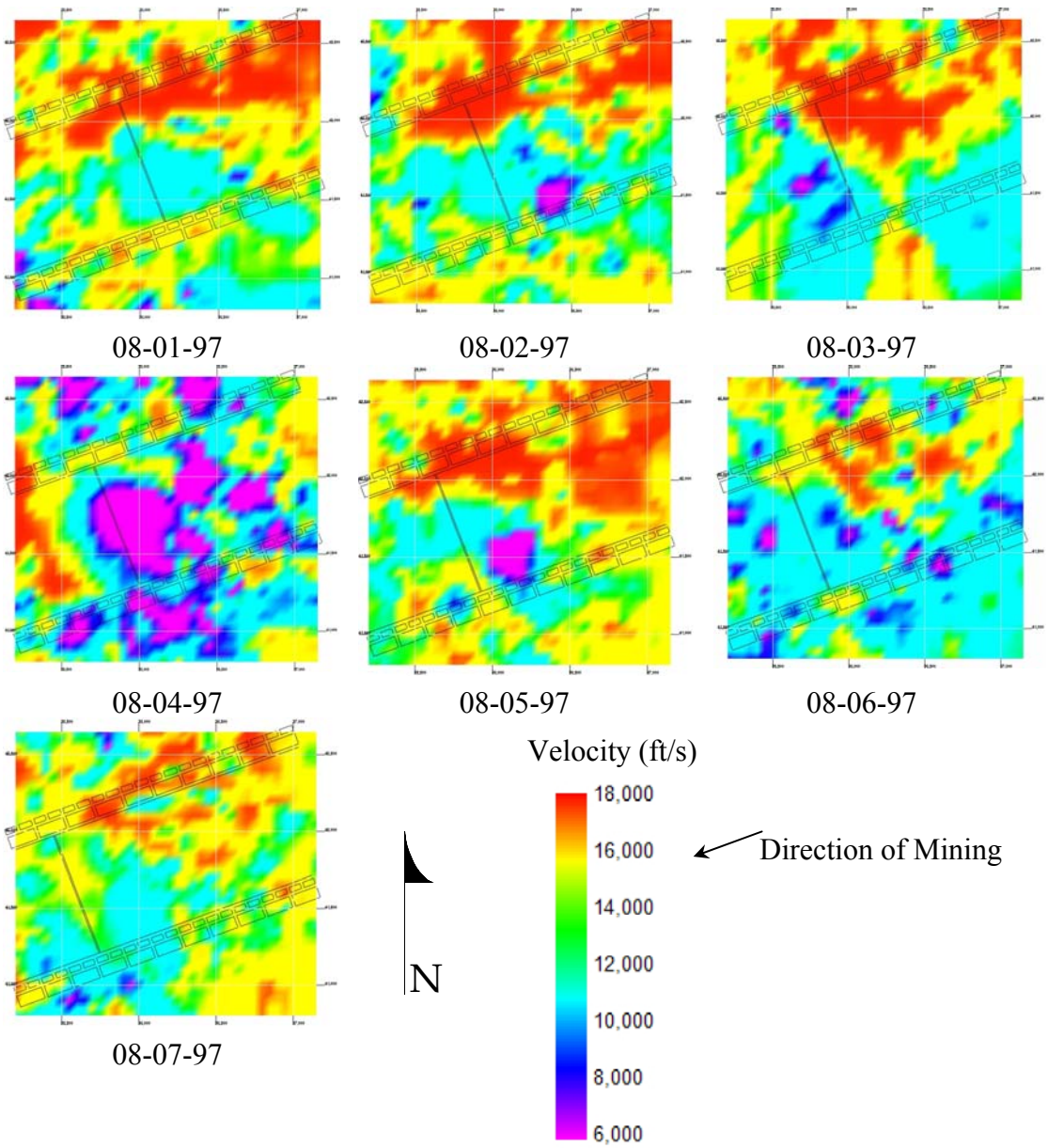

Figure 4.5. Roof Level Velocity Tomograms, Z = 5,700 feet.

Examination of the roof level tomograms also indicate similar features. Once again, a high velocity zone along the tailgate is evident, indicating high stress in this region. Also, the tomogram for 08-04-97 at roof level shows widespread low stress regions in contrast to the surrounding tomograms. The low stress zone at the face is again obvious on many of the tomograms. There is no obvious image of gob inby the face location, however. According to Ellenberger, seismic events ahead of the advancing face are often due to compressional failure, while events in the gob are due

to tensile failure and produce far less energy (Ellenberger, J. L., et al. 2001). With fewer events detected in the gob, fewer raypaths traverse this area. Additionally, the gob, which will consist largely of highly fractured rock, would be a low velocity area, and are subject to the Wielandt effect, where low velocity anomalies are more difficult to image than high velocity anomalies (Jackson, M. J. and D. R. Tweeton 1994). The low velocity anomaly is probably a indicator of gob, although it covers less area than expected.

4.1.5 MIDFACE TOMOGRAMS

Next the solid model is sliced at Y = 41,800 feet. This provides a vertical profile at approximately midface as shown below in Figure 4.6.

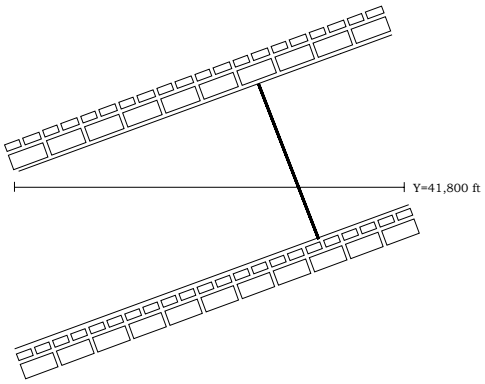

Figure 4.6. Plan View of Vertical Slice Location for 07-24-97.

The slice at Y = 41,800 feet gives an image of the rock mass response in the roof and the floor as the coal is removed. Figure 4.7 displays the velocity tomograms for each day of the study, excluding 07-22-97 and 07-30-97. Appendix E displays all eighteen tomograms in addition to ray density plots and longwall panel maps showing the slice location.

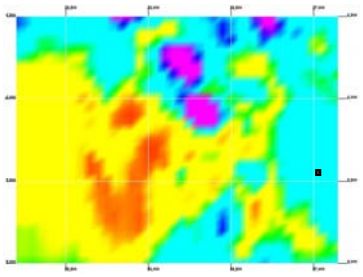

07-20-97

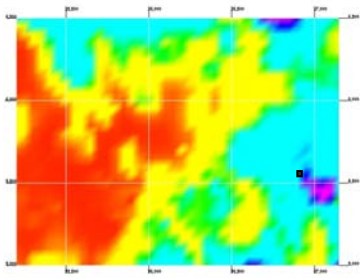

07-21-97

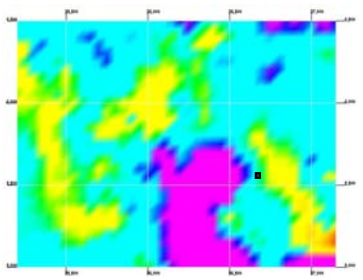

07-23-97

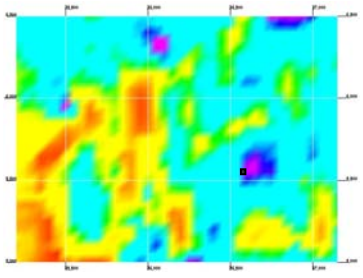

07-24-97

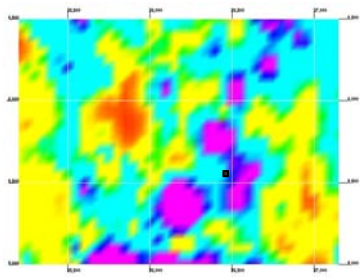

07-25-97

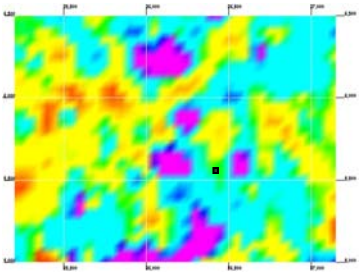

07-26-97

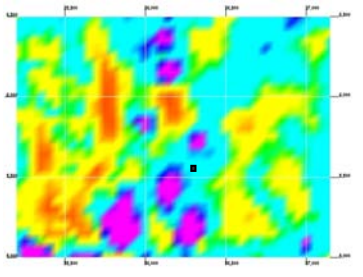

07-27-97

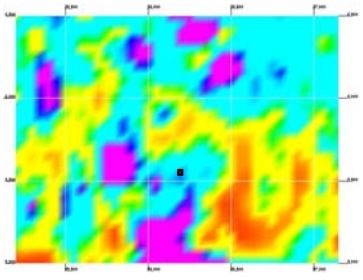

07-28-97

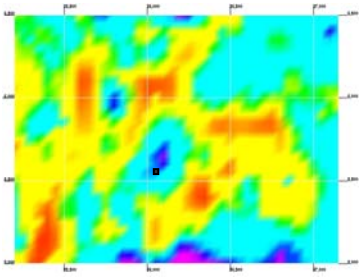

07-31-97

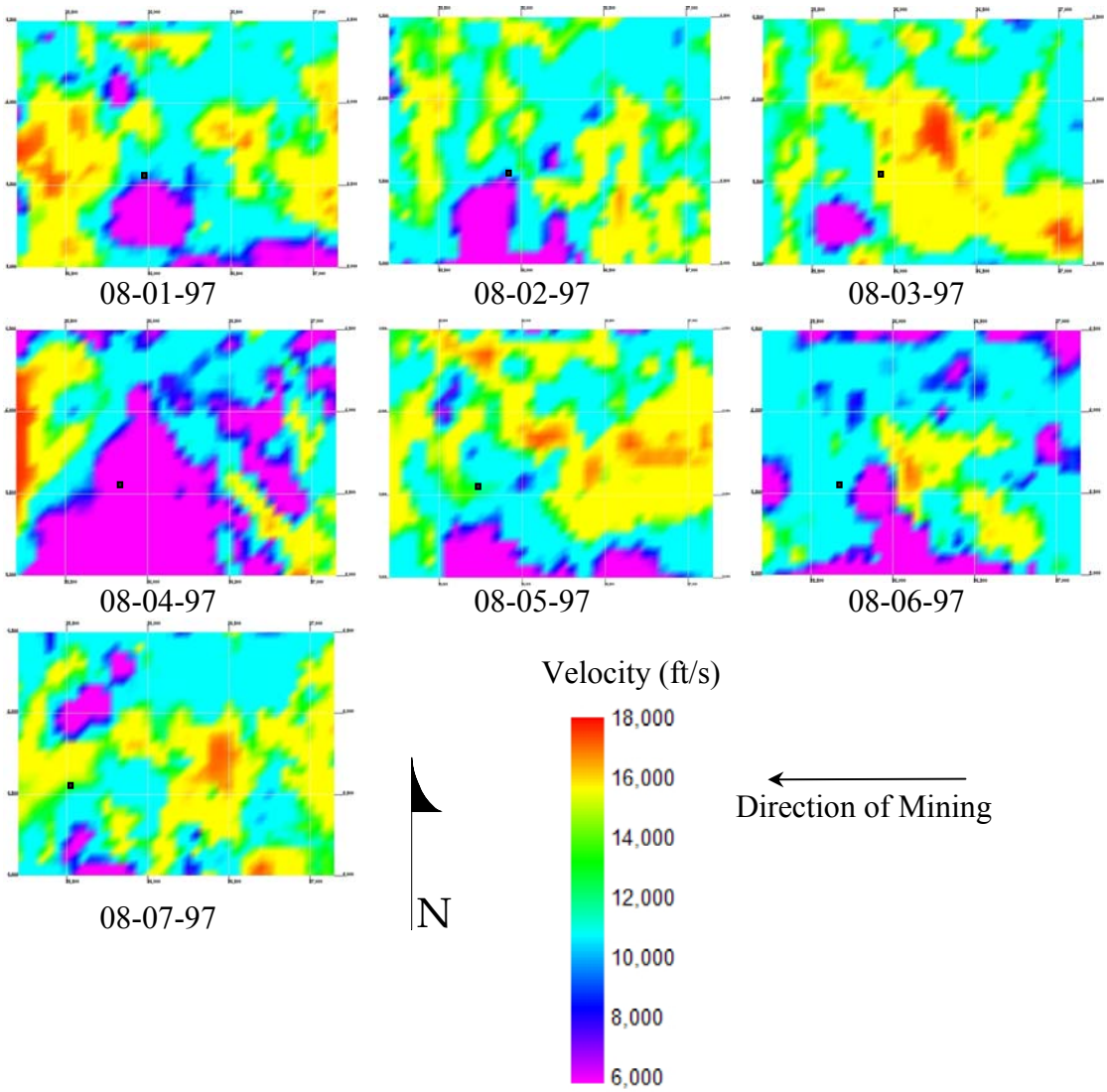

Figure 4.7. Velocity Tomograms, Midface Profile, Y = 41,800 feet.

In the vertical profiles shown above, the black square represents approximate face location. This profile was sliced from east to west, as shown in Figure 4.6. However, the longwall panel runs from the northeast to the southwest, so the profile shows a view that is closer to the headgate for 07-20-97 to 07-26-97. The profile on 07-27-97 is located at approximately midface, while the proceeding profiles move towards the tailgate. However, most of the tomograms consistently show a low stress anomaly immediately behind the face location. This anomaly is especially evident for 07-21-97, 07-24-97, 07-25-97, 07-26-97, 07-28-97, 07-31-97, 08-01-97, 08-02-97, 08-04-97, 08-05-97, 08-06-97.

4.2 Microseismic Event Correlation

4.2.1 Microseismic Event Locations and Frequency

Microseismic events are often a function of rate of advance, although other factors also influence frequency. Figure 4.8 displays a graph of face advance and microseismic activity. Although the relationship is not directly proportional, there is a general increase in microseismic activity with increased production.

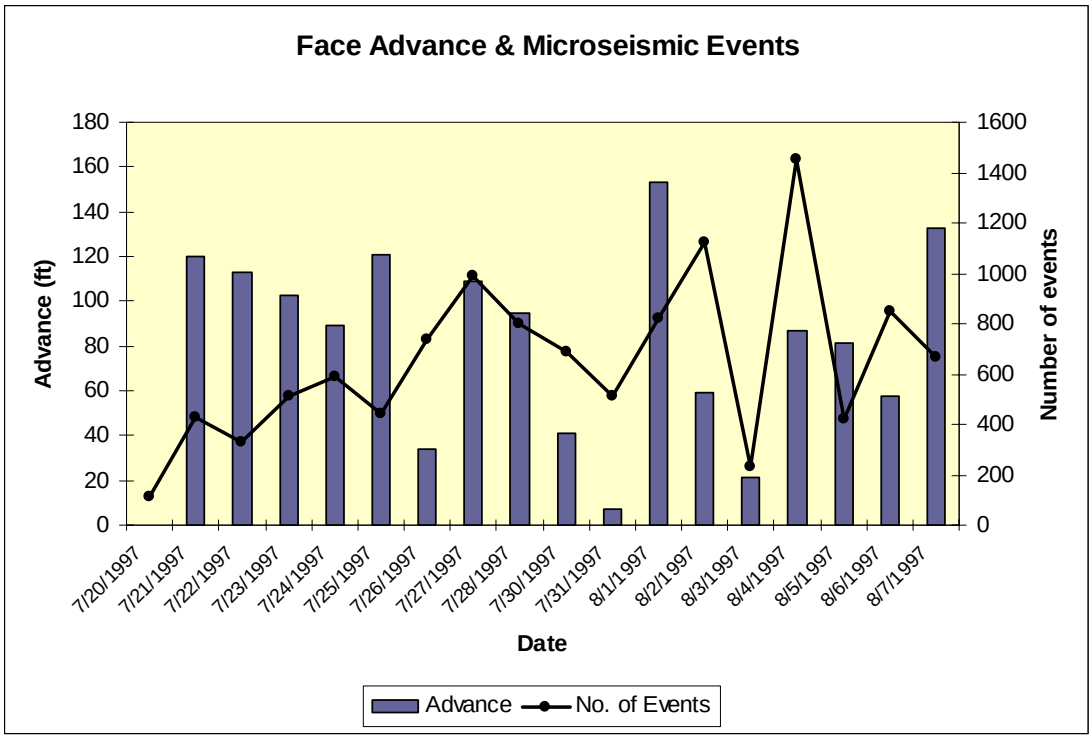

Figure 4.8. Microseismic Event Frequency and Face Advance.

Heasley found, when studying seismicity around longwall panels, that most events occurred immediately in front of the face, clustered near the headgate (2001). Similarly, most events were clustered immediately in front of the longwall face for this dataset, but events were also dispersed along the tailgate side behind the face. Figure 4.9 displays seismicity in relation to the longwall panel for 07-26-97, 07-27-97. and 07-28-97, days that are generally representative of the dataset. The events are plotted as spheres, and they are sized according to relative magnitude.

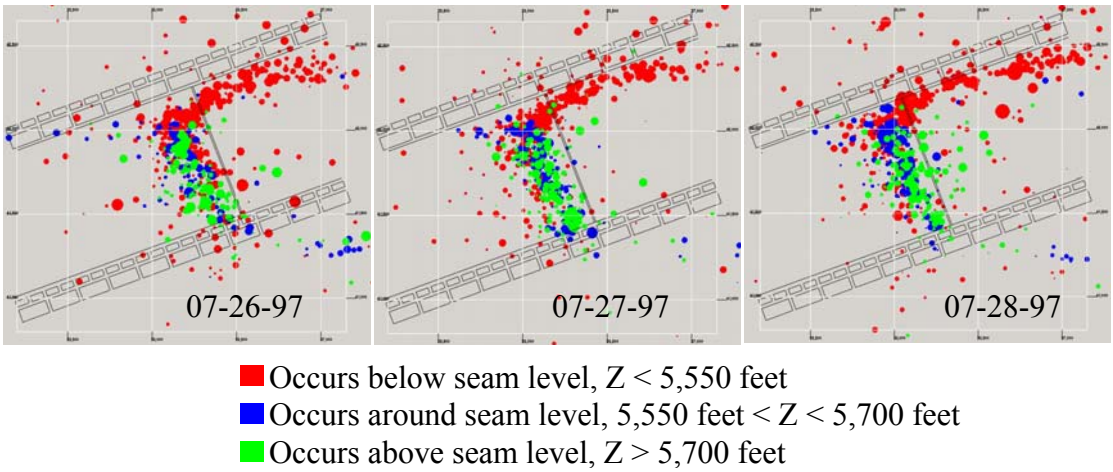

Figure 4.9. Distribution of Microseismic Events on 07-26-97, 07-27-97, and 07-28-97.

The events that occur in front of the longwall face appear to occur at various elevations, while the microseismic events that occur along the tailgate occur almost exclusively below the seam. Appendix F displays microseismic events for each day with a tomogram at seam level. The tomograms are plotted at 55% transparency so that all events can be seen, and the events occurring below the seam appear darker. The tomograms consistently show microseismic events along the tailgate occurring below seam level. This microseismic event distribution would indicate that much of the strain energy stored along the tailgate is stored and released in the floor.

4.2.2 Microseismic Events and Velocity Distribution

Microseismic event location correlates with velocity change in the tomograms. In examining Appendix F, microseismic events along the tailgate occur inside the high velocity zone for practically every tomogram.

Additionally, it is interesting to examine the microseismic activity between 08-03-97 and 08-04-97. In viewing the tomograms, 08-04-97 seems to be an anomalous day. Rather than seeing the high stress area along the tailgate that is typical of the other days, the tomograms for 08-04-97 display widespread low velocity zones. 1,450 microseismic events were recorded on 08-04-97, more than were recorded on any other day under study. The previous day, 08-03-97, saw relatively little face advance,

21 feet, and few events, only 229 were recorded. Tomograms with seismic events for the two days are displayed in Figure 4.10.

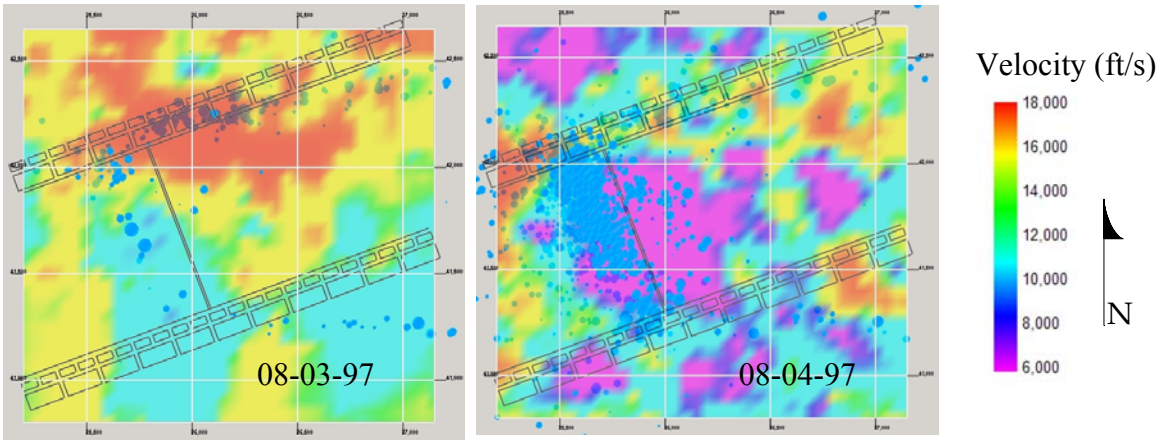

Figure 4.10. Velocity Tomograms with Seismic Events.

It is possible that the extreme low velocity distribution observed on the tomogram for 08-04-97 is the result of massive stress release due to the number of microseismic events. It is also important to note that the data points for 08-04-97, shown in Appendix A, displayed a large degree of scatter. This amount of scatter may have been due to the number of events. The RMS residual 08-04-97 was reasonable, 0.06 seconds, and ray density was also reasonable, as illustrated in Appendices B, C, and D. It is likely that the unusual velocity distribution for the tomogram generated for 08-04-97 can be explained by microseismic activity, which resulted massive stress release, and is not due simply to error.

4.3 LAMODEL Comparison

4.3.1 LAMODEL Results

The velocity tomograms for the dataset indicated clearly that a high velocity region occurs along the tailgate of the longwall. Typically this would be due to abutment loading due to gob on the tailgate side. However, the panels on both the tailgate and headgate sides of the active panel are unmined, so tailgate abutment stress is not a factor. The high tailgate velocity, and presumably high stress on the tailgate, can be explained by pillar geometry. The pillar geometry on the tailgate and headgate sides

is not symmetrical. Immediately adjacent to the tailgate side of the longwall block are large pillars, while immediately adjacent to the headgate side of the longwall block are smaller yield pillars. The yield pillars are designed to yield after the face has advanced beyond them to relieve stress. However, the large pillars do not yield, but continue to load, resulting in higher stress along the tailgate.

The *LAMODEL* plots display consistent stress redistribution. *LAMODEL* takes into account only pillar geometry and ore removal. Geologic anomalies, such as faults, are not included in the stress calculation. Therefore, the stress redistribution is consistent as the face advances. *LAMODEL* plots for all eighteen days are displayed in Appendix G at Z = 5,550 feet, seam level. Displayed below are three *LAMODEL* plots, 07-20-97, 07-31-97, and 08-07-04, which are representative of the stress change with face advance. The plots are at Z = 5,550 feet, seam level.

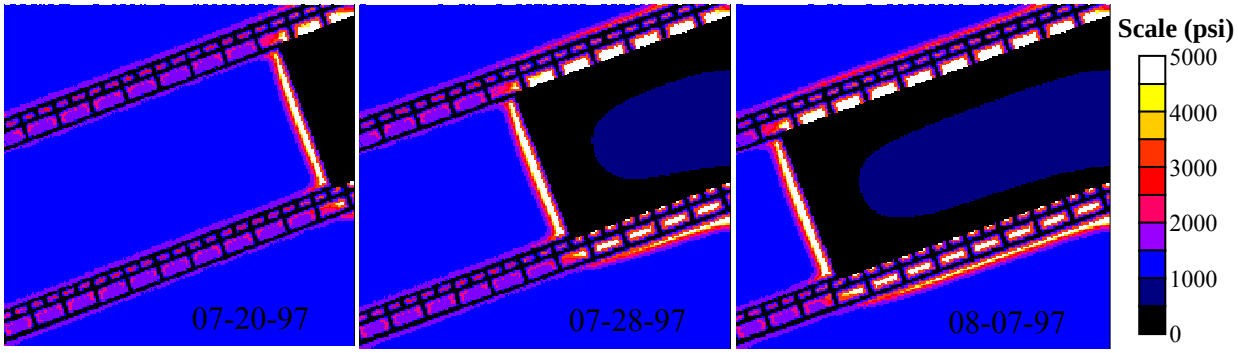

Figure 4.11. LAMODEL Plots for 07-20-97, 07-31-97, and 08-01-97 at Z = 5,550 feet.

The *LAMODEL* plots verify a high stress zone along the face, headgate and tailgate, with a relatively higher stress zone along the tailgate, advancing with the face.

4.3.2 LAMODEL AND VELOCITY TOMOGRAM COMPARISON

The LAMODEL plots verified high stress along the tailgate as inferred in the velocity tomograms. However, the velocity tomograms and *LAMODEL* plots are not similar for a number of reasons. First, *LAMODEL* models only vertical stress,

horizontal stress at the site is not taken into account. Also, *LAMODEL* does not model any geological anomalies such as faulting. Horizontal stress and geological anomalies contribute to the image generated in velocity tomograms.

Next, pixel size plays an important role. The velocity tomograms have a voxel size of 50 feet by 50 feet by 50 feet. Entry width on the panel is 20 feet, so on the tomograms the highly stressed pillars along the tailgate should appear to be smeared on the velocity tomogram. A high stress region exists immediately in front of the face in the *LAMODEL* plots that is not obvious on the velocity tomograms. This region is relatively narrow and may not be not be obvious because the length of the seismic waves was too long. Also, the nature of the velocity-stress relationship indicates that a velocity tomogram will not produce the same image as a stress model. Figure 4.12 displays a velocity-pressure curve determined in the laboratory for sandstone:

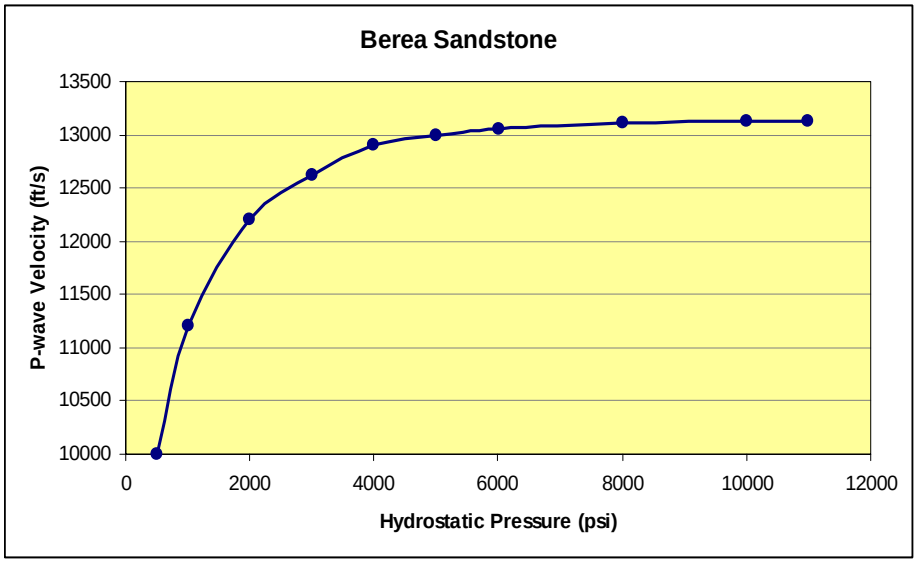

Figure 4.12. P-wave Velocity vs. Pressure for Berea Sandstone (King, M. S. 1966).

The velocity stress relationship is almost linear at low pressures, leveling out at higher pressures. This relationship explains the relatively larger high velocity area seen in the velocity tomograms, as compared to the stress plot. Above a certain stress level, velocity will change very little, and a velocity tomogram will not be able to differentiate stress changes above this level.

Overall, considering the factors described that contribute to the differences between the stress model and the velocity tomograms, the tomograms provide a reasonable image of stress expected around the longwall panel.

CHAPTER 5: CONCLUSIONS

Velocity tomograms of an underground coal mine implementing longwall mining produced reasonable images of velocity distribution. Inferred stress distribution correlates well with numerical modeling of the longwall panel.

The mine under study has reported three rockbursts, referred to as bounces at this mine, to MSHA in the past three years. None of the bounces caused injury, but all three occurred on the longwall tailgate and resulted in tailgate blockage, impeding travel. The velocity tomograms generated in this research consistently indicate a high stress area along the tailgate, advancing with the face. This high stress area is confirmed by the bounces reported by the mine, by numerical modeling through LAMODEL, and by microseismic activity in the area.

With the exception of tomograms produced for 07-22-97 and 07-30-97, velocity tomography produced consistent images of the floor, seam, and roof of the longwall panel. The anomalous tomograms appear to be due to errors in data measurement and filtering.

The consistency of the tomograms and the high velocity area along the tailgate, which has historically stored excessive strain energy, in addition to the correlation found with *LAMODEL* indicate that velocity tomography is an excellent technology for studying rockbursts.

The passive source geometry implemented in this research is not ideal for producing tomograms, however. Implementation of an active source with receivers closer to the seam level would improve the tomograms drastically, and allow for more detailed study near the panel. Use of the active source geometry in tandem with passive source geometry would be especially useful, as the passive source geometry provided important microseismic information. For example, the consistent microseimic events in the floor strata inby the longwall face confirm that strain energy is being stored in the floor strata on the tailgate side.

Additionally, *insitu* stress measurements of the panel and laboratory testing of the roof and floor strata to determine p-wave velocity under pressure would allow for the velocity-stress relationship to be further explored. If the velocity-stress relationship for a mine is well defined, more information about the stress state can be inferred from velocity tomography.

In addition to the study of the strata, personal observation could provide important information about rockbursts and respective change in velocity tomography. Rockbursts are only reported to MSHA if they cause harm to persons, impede ventilation, or impede travel. Many small bumps, although unreported, are noticed by people working underground, and recording their time and location would allow for changes in velocity tomograms to be explored.

Velocity tomography proves to be a useful tool for examining stress redistribution in an underground longwall mine in response to coal removal. This technology provided consistent images that correlate well with numerical modeling, microseismic events, and mine experience, which indicate that the tailgate is a high stress zone, prone to rockbursts. Velocity tomography imaged high velocities in rockburst prone areas, and can be used to further study rockburst phenomena.

REFERENCES

"30 C.F.R. §57.3461." Code of Federal Regulations: Mineral Resources, Department of Labor

Adams, L. H., and E. D. Williamson. "On the Compressibility of Minerals and Rocks at High Pressures." *Journal of the Franklin Institute* 195 (1923): 475-531.

Aki, K., and W. H. K. Lee. "Determination of Three-Dimensional Velocity Anomalies under a Seismic Array Using First P Arrival Times from Local Earthquakes." *Journal of Geophysical Research* 81, no. 23 (1976): 4381-4399.

Badr, S., R. Mendoza, S. Kieffer, M. Salamon, and U. Ozbay. "Numerical Modeling of Longwalls in Deep Coal Mines." Paper presented at the 22nd International Conference on Ground Control in Mining, Morgantown, WV 2003.

Baraka-Lokmane, S., G. Teutsch, and I. G. Main. "Influence of Open and Sealed Fractures on Fluid Flow and Water Saturation in Sandstone Cores Using Magnetic Resonance Imaging." *Geophysical Journal International* 147, no. 2 (2001): 263.

Barton, N. "Rock Mass Classification and Tunnel Reinforcement Using the Q System." *ASTM Speical Technical Publication* 984 (1987): 59-84.

Bauer, E. R., G. J. Chekan, and L. J. Steiner. "Stability Evaluation of Extended Cut Mining in Underground Coal Mines." *International Journal of Rock Mechanics and Mining Sciences and Geomechanics Abstracts* 34, no. 3 (1997): 664.

Bedrosian, P. A., M. J. Unsworth, G. D. Egbert, and C. H. Thurber. "Geophysical Images of the Creeping Segment of the San Andreas Fault; Implications for the Role of Crustal Fluids in the Earthquake Process." *Tectonophysics* 385, no. 1-4 (2004): 137-158.

Bellefleur, G., and M. Chouteau. "Massive Sulphide Delineation Using Borehole Radar; Tests at Mcconnell Nickel Deposit, Sudbury, Ontario." *Journal of Applied Geophysics* 47, no. 1 (2001): 45-51.

Bieniaski, Z. T. *Engineering Rock Mass Classifications*. New York: Wiley, 1989.

Blès, J. L., and B. Feuga. *The Fracture of Rocks*. Translated by J. Wanklyn, *Studies in Geology*. New York: North Oxford Academic Publisher Ltd., 1986.

Bording, R. P., A. Gersztenkorn, L. R. Lines, J. A. Scales, and S. Treitel. "Applications of Seismic Travel-Time Tomography." *Geophysical Journal of the Royal Astronomical Society* 90, no. 2 (1987): 285-303.

Bräuner, G. *Rockbursts in Coal Mines and Their Prevention*. Rotterdam: AA Balkema, 1994.

Bronnikov, A. V., and D. Killian. "3d Tomography of Turbine Blades." Paper presented at the International Symposium on Computerized Tomography for Industrial Applications and Image Processing in Radiology, Berlin, March 15-17 1999.

Chang, J., H. L. Graber, R. L. Barbour, and R. Aronson. "Recovery of Optical Cross-Section Perturbations in Dense-Scattering Media by Transport-Theory-Based Imaging Operators and Steady-State Simulated Data." *Applied Optics* 35, no. 20 (1996): 3963-3978.

Chow, T. M., I. L. Meglis, and R. P. Young. "Progressive Microcrack Development in Tests on Lac Du Bonnet Granit - Ii. Ultrasonic Tomographic Imaging." *International Journal of Rock Mechanics, Mining Sciences, and Geomechanics Abstracts* 32, no. 8 (1995): 751-761.

Clement, W. P., and M. D. Knoll. "Tomographic Inversion of Crosshole Radar Data: Confidence in Results." Paper presented at the Symposium on the Application of Geophysics to Environmental and Engineering Problems, Arlington, VA, February 20-24 2000.

Cox, M. *Static Corrections for Seismic Reflection Surveys*. Tulsa, OK: Society of Exploration Geophysicts, 1999.

Daily, W., A. Ramirez, A. Binley, and D. LaBrecque. "Electrical Resistance Tomography." *The Leading Edge* 23, no. 5 (2004): 438-442.

Deans, S. R. *The Radon Transform & Some of Its Applications*. New York: John Wiley & Sons, 1983.

Deere, D. U. "Technical Description of Rock Cores for Engineering Purposes." *Rock Mechanics and Engineering Geology* 1 (1964): 17-22.

Degueldre, C., H. Pleinert, P. Maguire, E. Lehman, J. Missimer, J. Hammer, K. Leenders, H. Böck, and D. Townsend. "Porosity and Pathway Determination in Crystalline Rock by Positron Emission Tomography and Neutron Radiography." *Earth and Planetary Science Letters* 140, no. 1-4 (1996): 213-225.

Dines, K. A., and R. J. Lytle. "Computerized Geophysical Tomography." *Proceedings of the IEEE* 67, no. 7 (1979): 1065-1074.

Dyer, B. , and M. H. Worthington. "Some Sources of Distortion in Tomographic Velocity Images." *Geophysical Prospecting* 36, no. 3 (1988): 209-222.

Eberhart-Phillips, D., D-H. Han, and M. D. Zoback. "Empirical Relationships among Seismic Velocity, Porosity, and Clay Content in Sandstone." *Geophysics* 54, no. 1 (1989): 82-89.

Edelbro, C. "Evaluation of Rock Mass Strength Criteria." Luleå University of Technology, 2004.

Ellenberger, J. L., F. E. Chase, C. Mark, K. A. Heasley, and J. K. Marshall. "Using Site Case Histories of Multiple Seam Coal Mining to Advance Mine Design." 22nd International Conference on Ground Control in Mining, Morgantown, WV, August 2003.

Ellenberger, J. L., K. A. Heasley, P. L. Swanson, and J. Mercier. "Three Dimensional Microseismic Monitoring of a Utah Longwall." Rock Mechanics in the National Interest, Lisse, Netherlands, July 2001.

Ellenberger, J.L., and K. A. Heasley. "Coal Mine Seismicity and Bumps: Historical Case Studies and Current Field Activity." Paper presented at the The 19th International Conference on Ground Control in Mining, Morgantown, WV, August 2000.

Friedel, M. J., D. F. Scott. and T. J. Williams. "Temporal Imaging of Mine-Induced Stress Change Using Seismic Tomography." *Engineering Geology* 46, no. 2 (1997): 131-141.

Friedel, M. J., M. J. Jackson, E. M. Willams, M. S. Olson, and E. Westman. "Tomographic Imaging of Coal Pillar Conditions: Observations and Implications." *International Journal of Rock Mechanics, Mining Science. & Geomechanics Abstracts* 33, no. 3 (1996): 279-290.

Gale, W. J., C. Mark, D. C. Oyler, and J. Chen. "Computer Simulation of Ground Behaviour and Rock Bolt Interaction at Emerald Mine." Paper presented at the The 23rd International Conference on Ground Control in Mining, Morgantown, WV, August 2004.

Gilbert, P. "Iterative Methods for the Three-Dimensional Reconstruction of an Object from Projects." *Journal of Theoretical Biology* 36 (1972): 105-117.

Golub, G. H., and C. Reinsch. *Contribution I-10: Singular Value Decomposition and Least Squares Solution*. Edited by F. L. Bauer. Vol. 2, *Linear Algebra: Handbook for Automatic Computation*. New York: Springer-Verlag, 1971.

Goodman, R. E. *Introduction to Rock Mechanics*. 2nd ed. New York: John Wiley and Sons, 1989.

Goulty, N. R. *Controlled-Source Tomography for Mining and Engineering Applications*. Edited by H. M. Iyer and K. Hirahara, *Seismic Tomography: Theory and Practice*. London: Chapman and Hall, 1993.

Griffith, A. A. "The Phenomena of Rupture and Flow in Solids." *Philosophical Transactions of the Royal Society of London. Series A, Mathematical and Physical Sciences* 221 (1921): 163-198.

Hadamard, J. *Lectures on Cauchy's Problem in Linear Partial Differential Equations*. New York: Dover Publications, 1952.

———. "Sur Les Problèmes Aux Dérivées Partielles Et Leur Signification Physique." *Princeton University Bulletin*, no. 49-52 (1902).

Hall, L. D. "Roles for Magnetic Resonance Imaging in Process Tomography." *IEEE Sensors Journal* 5, no. 2 (2005): 125-133.

Haramy, K. Y., J. A. Magers, and J. P. McDonnel. "Mining under Strong Roof." Paper presented at the 7th International Conference on Ground Control in Mining, Morgantown, WV, August 3-5 1988.

Heasley, K. A., J. L. Ellenberger, and P. W. Jeran. "An Analysis of Rock Failure around a Deep Longwall Using Microseismics." Paper presented at the 20th International Conference on Ground Control in Mining, Morgantown, WV, August 2001.

Herget, G. *Stresses in Rock*. Rotterdam: AA Balkema, 1988.

Hobro, J.W.D., S. C. Singh, and T. A. Minshull. "Three-Dimensional Tomographic Inversion of Combined Reflection and Refraction Seismic Traveltime Data." *Geophysical Journal International* 152, no. 1 (2003): 79-93.

Hoek, E., and E. T. Brown. "Empirical Strength Criterion for Rock Masses." *Journal of the Geotechnical Engineering Division* 106, no. GT9 (1980): 1013-1036.

Hole, J. "Inverse Theory and Geoscience Applications Lecture Notes." Blacksburg, VA: Virginia Polytechnic Institute & State University. Department of Geosciences, 2005.

Hoversten, G. M., G. A. Newman, H. F. Morrison, E. Gasperikova, and J.-I. Berg. "Reservoir Characterization Using Crosswell Electromagnetic Inversion: A Feasibility Study for the Snorre Field, North Sea." *Geophysics* 66, no. 4 (2001): 1177-1189.

Iannacchione, A., T. S. Bajpayee, and J. Edwards. "Forecasting Roof Falls with Monitoring Technologies - a Look at the Moonee Colliery Experience." 24th International Conference on Ground Control in Mining, Morgantown, WV, August 2-4 2005.

Ishiwata, K., M. Mishina, Y. Kimura, K. Oda, T. Sasaki, and K. Ishii. "First Visualization of Adenosine a~1~a Receptors in the Human Brain by Positron Emission Tomography with [^1^1c]Tmsx " *Synapse* 55, no. 2 (2005): 133-136.

Ivansson, S. "A Study of Methods for Tomographic Velocity Estimation in the Presence of Low Velocity Zones." *Geophysics* 50, no. 6 (1985): 969-988.

Jackson, M. J. , and D. R. Tweeton. "Migratom - Geophysical Tomography Using Wavefront Migration and Fuzzy Constraints; Report of Investigations 9497." United States Department of the Interior: Bureau of Mines, 1994.

Jansen, D. P., D. A. Hutchins, and R. P. Young. "Acoustic Imaging of Thermally Fractured Rock." Paper presented at the Proceedings of the Ultrasonics Symposium 1991.

Jones, S. M. "Velocities and Quality Factors of Sedimentary Rocks at Low and High Effective Pressures." *Geophysical Journal International* 123, no. 3 (1995): 774-780.

Karabin, G. J. , and M. A. Evanto. "Experience with the Boundary-Element Method of Numerical Modeling to Resolve Complex Ground Control Problems." Paper presented at the Proceedings of the 2nd International Workshop on coal pillar mechanics and design, June 1999 1999.

Kelly, M., and W. Gale. "Ground Behavior About Longwall Faces and Its Effect on Mining." ACARP (Australian Coal Association Research Program), 2000.

King, M. S. "Wave Velocities as a Function of Changes in Overburden Pressure and Pore Fluid Saturants." *Geophysics* 31, no. 1 (1966): 50-73.

Kneisley, R. O., and K. Y. Haramy. "Large-Scale Strata Response to Longwall Mining: A Case Study: Report of Investigations." United States Bureau of Mines, 1992.

Kormendi, A., T. Bodoky, L. Hermann, L. Dianiska, and T. Kalman. "Seismic Measurements for Safety in Mines." *Geophysical Prospecting* 34, no. 7 (1986): 1022-1037.

Leonard, K. R., E. V. Malyarenko, and M. K. Hinders. "Ultrasonic Lamb Wave Tomography." *Inverse Problems* 18 (2002): 1795-1808.

Lo, T-W., M. N. Toksöz, S-H. Xu, and R-S. Wu. "Ultrasonic Laboratory Tests of Geophysical Tomographic Resolution." *Geophysics* 53, no. 7 (1988): 947-956.

Lockner, D. A., J. B. Walsh, and J. D. Byerlee. "Changes in Seismic Velocity and Attenuation During Deformation of Granite." *Journal of Geophysical Research* 82, no. 33 (1977): 5374-5378.

Ma, Q., T. E. Scott, and J. C. Roegiers. "Modeling Induced Acoustic Velocity Anisotropy During Triaxial Tests of Rocks." Paper presented at the Proceeding of the 35th U. S. Rock Mechanics Symposium, Reno, NV, June 5-7 1995.

Mahoney, M. S. *The Mathematical Career of Pierre De Fermat*. Princeton, NJ: Princeton University Press, 1973.

Maillol, J. M., M.-K. Seguin, O. P. Gupta, H. M. Akhuari, and N. Sen. "Electrical Resistivity Tomography Survey for Delineating Uncharted Mine Galleries in West Bengal, India." *Geophysical Prospecting* 47, no. 1 (1999): 103.

Maleki, H. "The Application of Geotechnical Monitoring to Stability Evaluation and Mine Design." Paper presented at the SME Annual Meeting, Phoenix, Arizona, Feb. 25-27, 2002 2002.

Manthei, G. "Seismic Tomography on a Pillar in a Potash Mine." Paper presented at the Proceedings of the 4th International Symposium on Rockbursts and Seismicity in Mines, Krakow, Poland, August 11-14 1997.

Martínez, J. L. F., C. O. M. Pérez, L. M. P. Gonzáles, J. P. F. Alvarez, and P. C. Suárez. "Geostatistical Analysis of Inverse Problem Variables." *Mathematical Geology* 35, no. 8 (2003): 953-969.

Martino, J. B., and N. A. Chandler. "Excavation-Induced Damage Studies at the Underground Research Laboratory." *International Journal of Rock Mechanics and Mining Sciences* 41, no. 8 (2004): 1413-1426.

Masad, E., V. K. Jandhyala, N. Dasgupta, S. M. Somadevan, and N. Shashidhar. "Characterization of Air Void Distribution in Asphalt Mixes Using X-Ray Computed Tomography." *Journal of Materials in Civil Engineering* 14, no. 2 (2002): 122-129.

Maxwell, S. C., and R. P. Young. "A Comparision between Controlled Source and Passive Source Velocity Images." *Bulletin of the Seismological Society of AMerica* 83, no. 6 (1993): 1813-1834.

———. "A Controlled in-Situ Investigation of the Relationship between Stress, Velocity and Induced Seismicity." *Geophysical Research Letters* 22, no. 9 (1995): 1049-1052.

———. "Propagation Effects of an Underground Excavation." *Tectonophysics* 289, no. 1-3 (1998): 17-30.

———. "Seismic Imaging of Rock Mass Responses to Excavation." *International Journal of Rock Mechanics, Mining Science, and Geomechanics Abstracts* 33, no. 7 (1996): 713-724.

McKenna, J., D. Sherlock, and B. Evans. "Time-Lapse 3-D Seismic Imaging of Shallow Subsurface Contaminant Flow." *Journal of Contaminant Hydrology* 53, no. 1-2 (2001): 133-150.

Meglis, I. L., T. Chow, C. D. Martin, and R. P. Young. "Assessing in Situ Microcrack Damage Using Ultrasonic Velocity Tomography." *International Journal of Rock Mechanics, Mining Science, and Geomechanics* 42 (2004): 25-34.

Menke, W. *Geophysical Data Analysis: Discrete Inverse Theory (Revised Edition)*. 2nd ed, *International Geophysics Series*. San Diego: Harcourt Brace Jovanovich, 1989.

Molinda, G. M., and C. Mark. "A Practical Rock Mass Rating for Coal Mines." U. S. Department of Interior, 1994.

Morgan, C. L., and M. D. Miller. *Basic Principles of Computed Tomography*. Baltimore: University Park Press, 1983.

Mosegaard, K., and A. Tarantola. *Probalistic Approach to Inverse Problems*, *International Handobook Fo Earthquake and Engineering Seismology*: Academic Press for the International Association of Seismology and Physics of the Earth Interior, 2002.

Accident, Injury, and Illness Data Files Mine Safety and Health Administration, November 2, 2005 Available from http://www.cdc.gov/niosh/mining/data/.

Data Retrieval System Mine Safety and Health Administration, November 2, 2005 Available from www.msha.gov.

Fatalities Year-to-Date: Coal Mine Safety and Health Administration, November 2, 2005 Available from www.msha.gov.

Facts About Coal National Mining Association, November 2, 2005 Available from www.nma.org.

Nolet, Guust. *Seismic Wave Propagation and Seismic Tomography*. Edited by Guust Nolet, *Seismic Tomography with Applications in Global Seismology and Exploration Geophysics*. Dordrecht, Holland: D. Reidel Publishing Company, 1987.

Nowack, R. L., and L. W. Braile. *Refracton and Wide-Angle Reflection Tomography: Theory and Results*. Edited by H. M. Iyer and K. Hirahara, *Seismic Tomography: Theory & Practice*. London: Chapman and Hall, 1993.

Nur, A., and G. Simmons. "Stress-Induced Velocity Anisotropy in Rock: An Experimental Study." *Journal of Geophysical Research* 74, no. 27 (1969): 6667-6674.

Obert, L., and W. I. Duvall. *Rock Mechanics and the Design of Structures in Rock*. New York: John Wiley and Sons, Inc., 1967.

Pande, G. N., G. Beer, and J. R. Williams. *Numerical Methods in Rock Mechanics*. Chinchester: John Wiley and sons, 1990.

Peng, S. S. *Coal Mine Ground Control*. New York: Wiley, 1986.

Peng, S. S., and H. S. Chiang. *Longwall Mining*. New York: Wiley, 1983.

Prasad, M. , and M. H. Manghnani. "Effects of Pore and Differential Pressure on Compressional Wave Velocity and Quality Factor in Berea and Michigan Sandstones." *Geophysics* 62, no. 4 (1997): 1163-1176.

Pratt, R. G., and N. R. Goulty. "Combining Wave-Equation Imaging with Traveltime Tomography to Form High Resolution Images from Crosshole Data." *Geophysics* 56, no. 2 (1991): 208-224.

Procházka, P. P. "Application of Discrete Element Methods to Fracture Mechanics of Rock Burst." *Engineering Fracture Mechanics* 71, no. 4 (2002): 601-618.

Radon, J. "Über Die Bestimmung Von Funktionen Durch Ihre Integralwerte Längs Gewisser Mannigfaltigkeiten." *Berichte Sachsische Akademie der Wissenschaften. Leipzig, Math. - Phys. Kl.* 69 (1917): 262-267.

Rockworks Manual. RockWare, Golden, CO. 2002

Rychagov, M. N., and H. Ermert. "Cross-Flow Visualization by Acoustic Ct Measurements." *Ultrasonics* 34, no. 2-5 (1996): 517-522.

Oilfield Glossary 2005 [cited October 19 2005]. Available from http://www.glossary.oilfield.slb.com.

Scott, D. F., J. M. Girard, T. J. Williams, and D. K. Denton. "Comparison of Seismic Tomography, Strain Relief, and Ultrasonic Velocity Measurements to Evaluate Stress in an Underground Pillar." Society for Mining, Metallurgy, and Exploration, Inc. Annual Meeting, Denver, Colorado, March 1-3 1999.

Scott, D. F., T. J. Willams, and M. J. Friedel. "Investigation of a Rockburst Site, Sunshine Mine, Kellogg, Idaho." Paper presented at the Proceedings of the 4th International Symposium on Rockbursts and Seismicity in Mines, Krakow, Poland, August 11-14 1997.

Scott, D. F., T. J. Williams, D. Tesarik, D. K. Denton, S. J. Knoll, and J. Jordan. "Geophysical Methods to Detect Stress in Underground Mines: Report of Investigations." National Institute for Occupational Safety & Health - Spokane Research Laboratory, 2004.

Scott, T. E. , Q. Ma, and J.-C. Roegiers. "Dynamic Stress Mapping Utilizing Ultrasonic Tomography." Paper presented at the The Proceedings of the 1st North American Rock Mechanics Symposium 1994.

Seya, K., I. Suzuki, and H. Fujiwara. "The Change in Ultrasonic Wave Velocities in Triaxially Stress Brittle Rock." *Journal of Physics of the Earth* 27, no. 5 (1979): 409-421.

Sharma, P. V. *Geophysical Methods in Geology*. New York: Elsevier, 1986.

Sollars, P. K., and M. A. Alspaugh. "Twentymile Coal's East Mine District Panel Conveyor Systems." Paper presented at the SME Annual Meeting, Orlando, Florida, February 1998 1998.

Spakman, W. *Iterative Strategies for Non-Liear Travel Time Tomography Using Global Earthquake Data*. Edited by H. M. Iyer and K. Hirahara, *Seismic Tomography: Theory & Practice*. London: Chapman and Hall, 1993.

Stewart, R. R. *Exploration Seismic Tomography: Fundamentals*. Edited by S. N. Domenico. Vol. 3, *Course Notes Series*. Tulsa: Society of Exploration Geophysicists, 1991.

Swanson, P., February 3 2005.

Tarantola, A. *Inverse Problem Theory: Methods for Data Fitting and Model Parameter Estimation*. New York: Elsevier, 1987.

Thill, R. E. "Acoustic Methods for Monitoring Failure in Rock." Paper presented at the 14th Symposium on Rock Mechanics, Universtiy Park, PA 1973.

Toksöz, M. N., C. H. Cheng, and A. Timur. "Velocities of Seismic Waves in Porous Rocks." *Geophysics* 41, no. 4 (1976): 621-645.

Tosaya, C. , and A. Nur. "Effects of Diagenesis and Clays on Compressional Velocities in Rocks." *Geophysical Research Letters* 9, no. 1 (1982): 5-8.

Tweeton, D. "Installing and Running the Three-Dimensional Tomography Program Geotomcg." Apple Valley, MN: GeoTom, LLC, 2001.

Vandergrift, T. L., and J. Garcia. "Highwall Mining in a Multiple-Seam, Western United States Setting Design and Performance." 24th Internatioanl Conference on Ground Control in Mining, Morgantown, WV, August 2-4 2005.

Vasco, D. W., J. E. Jr. Peterson, and E. L. Majer. "Beyond Ray Tomography: Wavepaths and Fresnel Volumes." *Geophysics* 60, no. 6 (1995): 1790-1804.

Watanabe, T., T. Matsuoka, and Y. Ashida. "Seismic Traveltime Tomography Using Fresnel Volume Approach." Paper presented at the 69th SEG Meeting, Houston 1999.

Watanabe, T., and K. Sassa. "Seismic Attenuation Tomography and Its Application to Rock Mass Evaluation." *International Journal of Rock Mechanics and Mining Sciences* 33, no. 5 (1996): 467-477.

Webster's Third New International Dictionary, Unabridged Merriam-Webster, 2002 [cited October 14 2005]. Available from http://unabridged.merriam-webster.com/.

Westman, E. C. "Use of Tomography for Inference of Stress Redistribution in Rock." *IEEE Transactions on Industry Applications* 40, no. 5 (2004): 1413-1417.

Westman, E. C., K. Y. Harmay, and A. D. Rock. "Seismic Tomography for Longwall Stress Analysis." Paper presented at the Proceedings of the 15th International Conference on Ground Control in Mining, Golden, CO. 1996.

Wielandt, E. *On the Validity of the Ray Approximation for Interpreting Delay Times*. Edited by Guust Nolet, *Seismic Tomography with Applications in Global Seismology and Exploration Geophysics*. Dordrecht, Holland: D. Reidel Publishing Company, 1987.

Williamson, P. R. "A Guide to the Limits of Resolution Imposed by Scattering in Ray Tomography." *Geophysics* 56, no. 2 (1991): 202-207.

Wyllie, M. R. J., A. R. Gregory, and G. H. F. Gardner. "An Experimental Investigation of Factors Affecting Elastic Wave Velocities in Porous Media." *Geophysics* 23, no. 3 (1958): 459-493.

Yagola, A. G., A. S. Leonov, and V. N. Titarenko. "Data Errors and an Error Estimation for Ill-Posed Problems." *Inverse Problems in Engineering* 10, no. 2 (2001): 117-129.

Yale, D. P. "Recent Advances in Rock Physics." *Geophysics* 50, no. 12 (1985): 2480-2491.

The Australian National University Research School of Earth Sciences - Extending Surface Wave Tomography 2005 [cited October 29 2005]. Available from http://wwwrses.anu.edu.au/seismology/ar00/eswm.html.

Young, R. P. , and D. S. Collins. "Seismic Studies of Rock Fracture at the Underground Research Laboratory, Canada." *International Journal of Rock Mechanics and Mining Sciences* 38, no. 6 (2001): 787-799.

Young, R. P., and S. C. Maxwell. "Seismic Characterization of a Highly Stressed Rock Mass Using Tomographic Imaging and Induced Seismicity." *Journal of Geophysical Research* 97, no. B9 (1992): 12,361-312,373.

Zingano, A. C., J. C. Koppe, and J. F. Costa. "Modeling the Arc-Effect of a Coal Mine Roof." 24th International Conference on Ground Control in Mining, Morgantown, Wv, August 2-4 2005.

APPENDIX A

Data Statistics

TIME VS. DISTANCE PLOTS
DAILY STATISTICS

07-20-97
Time vs. Distance Plots and Data Statistics

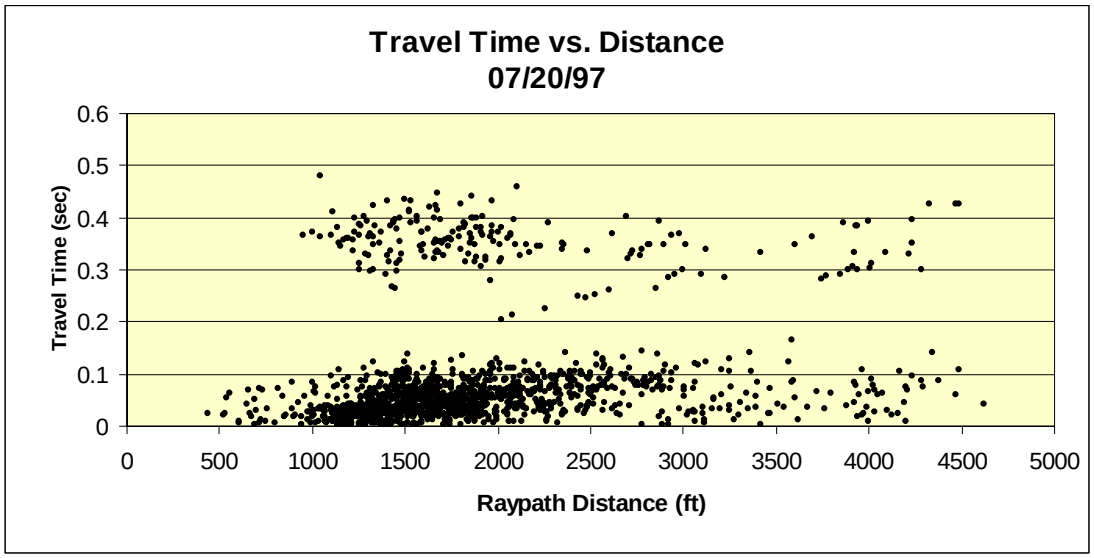

Figure A.1. Initial Time vs. Distance Plot.

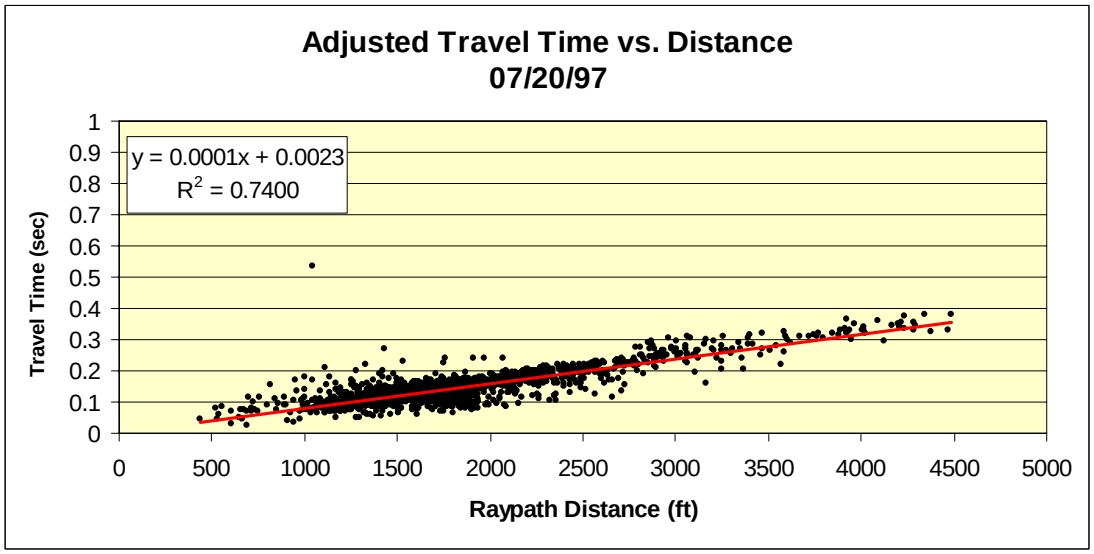

Figure A.2. Adjusted Time vs. Distance Plot.

Table A.1. Microseismic Data Statistics.

Date	7/20/1997	
Number of Microseismic Events	111	
Number of Original Points	1461	
Number of Adjusted Points	1410	
Data Points Removed	3.49%	%
RMS Residual for Final Iteration	0.0225	sec
Average Velocity	13072.88	ft/s

07-21-97

Time vs. Distance Plots and Data Statistics

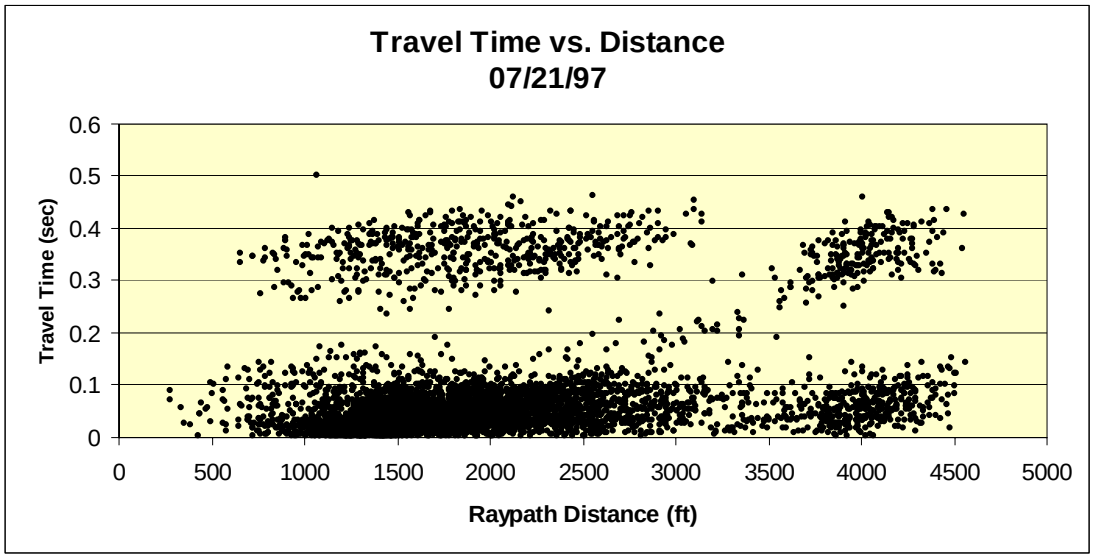

Figure A.3. Initial Time vs. Distance Plot.

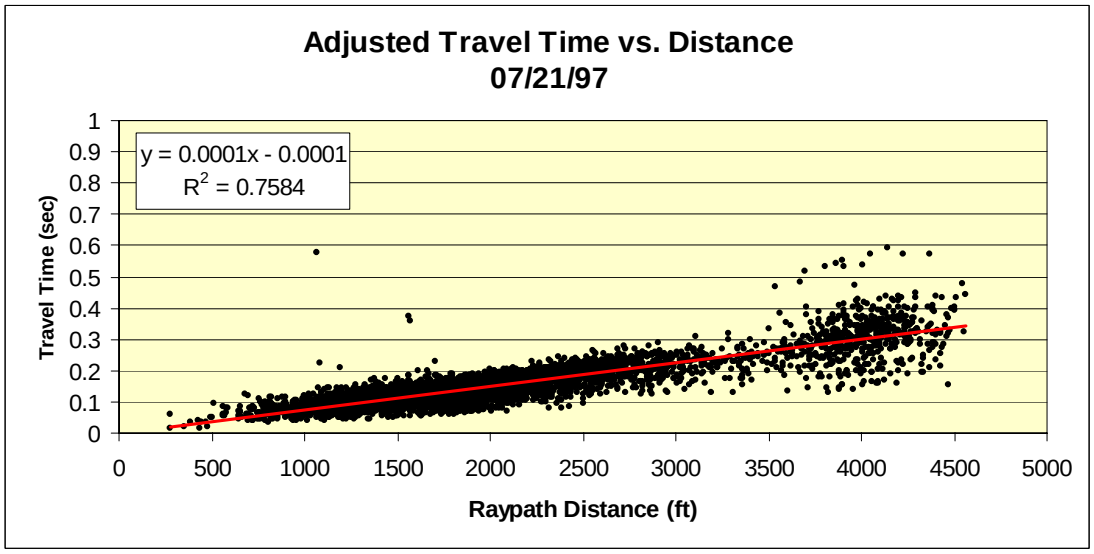

Figure A.4. Adjusted Time vs. Distance Plot.

Table A.2. Microseismic Data Statistics.

Date	7/21/1997	
Number of Microseismic Events	430	
Face Advance	120	ft
Number of Original Points	5978	
Number of Adjusted Points	5795	
Data Points Removed	3.06%	%
RMS Residual for Final Iteration	0.02513	sec
Average Velocity	13961.12	ft/s

07-22-97

Time vs. Distance Plots and Data Statistics

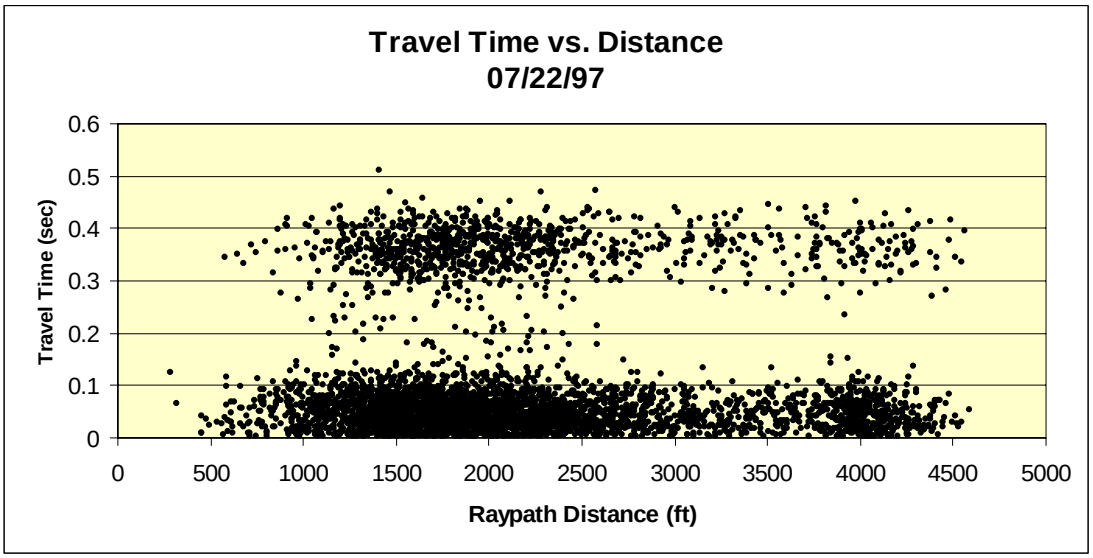

Figure A.5. Initial Time vs. Distance Plot.

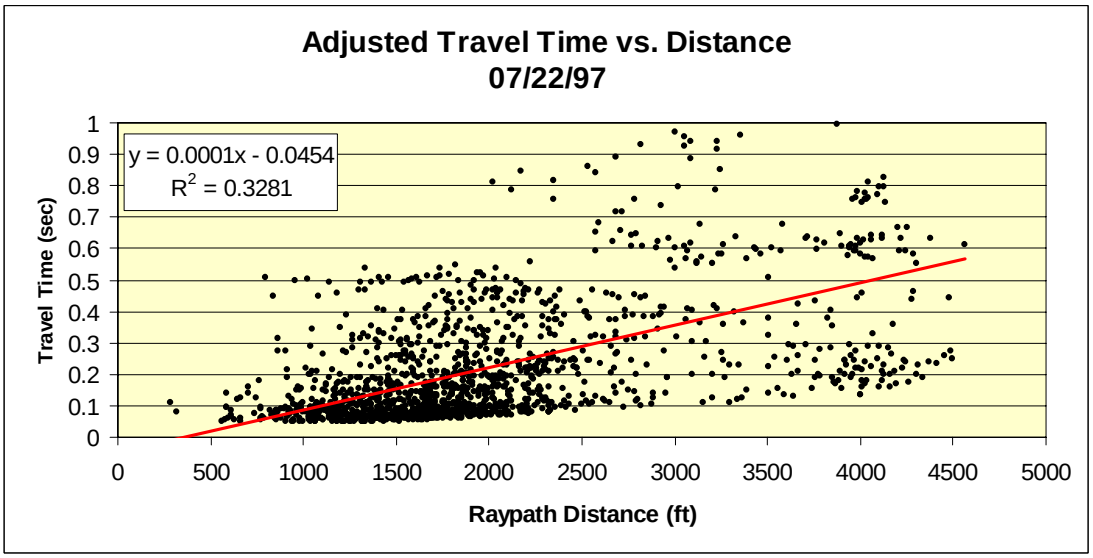

Figure A.6. Adjusted Time vs. Distance Plot.

Table A.3. Microseismic Data Statistics.

Date	7/22/1997	
Number of Microseismic Events	329	
Face Advance	113	ft
Number of Original Points	4897	
Number of Adjusted Points	1435	
Data Points Removed	70.70%	%
RMS Residual for Final Iteration	0.1459	sec
Average Velocity	13468.69	ft/s

07-23-97
Time vs. Distance Plots and Data Statistics

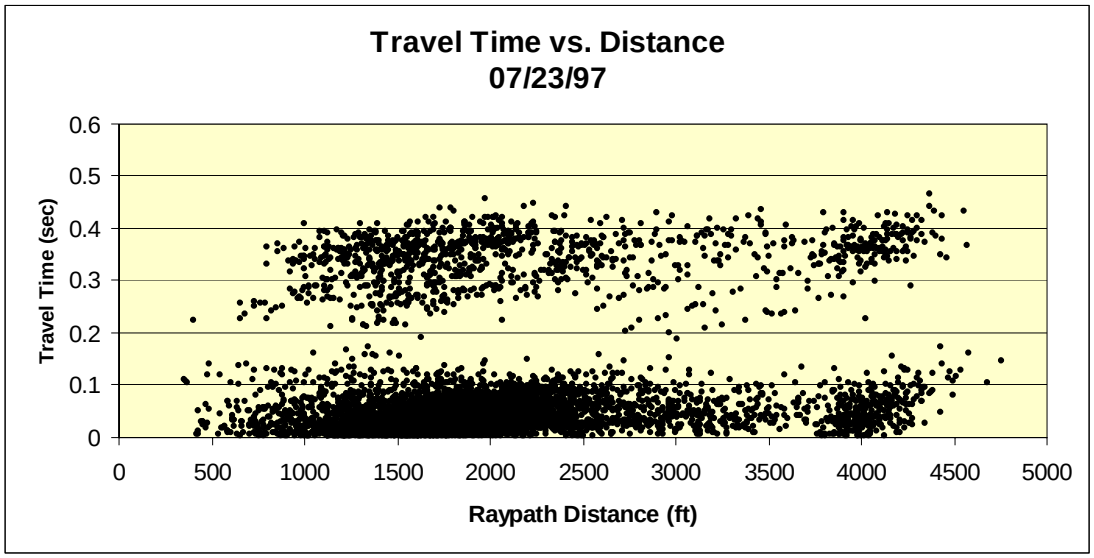

Figure A.7. Initial Time vs. Distance Plot.

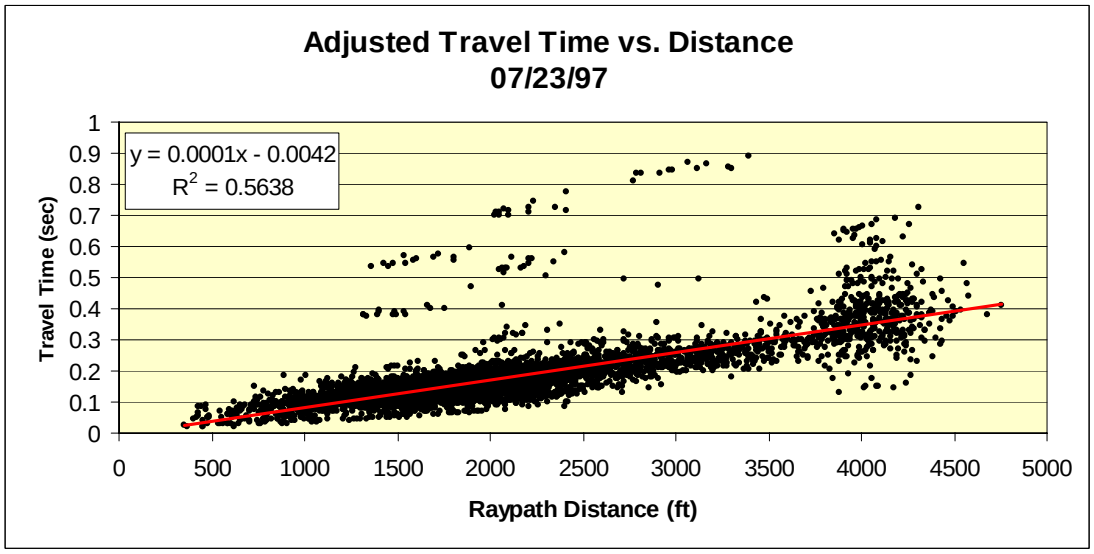

Figure A.8. Adjusted Time vs. Distance Plot.

Table A.4. Microseismic Data Statistics.

Date	7/23/1997	
Number of Microseismic Events	511	
Face Advance	103	ft
Number of Original Points	7498	
Number of Adjusted Points	7250	
Data Points Removed	3.31%	%
RMS Residual for Final Iteration	0.05119	sec
Average Velocity	12309.88	ft/s

07-24-97
Time vs. Distance Plots and Data Statistics

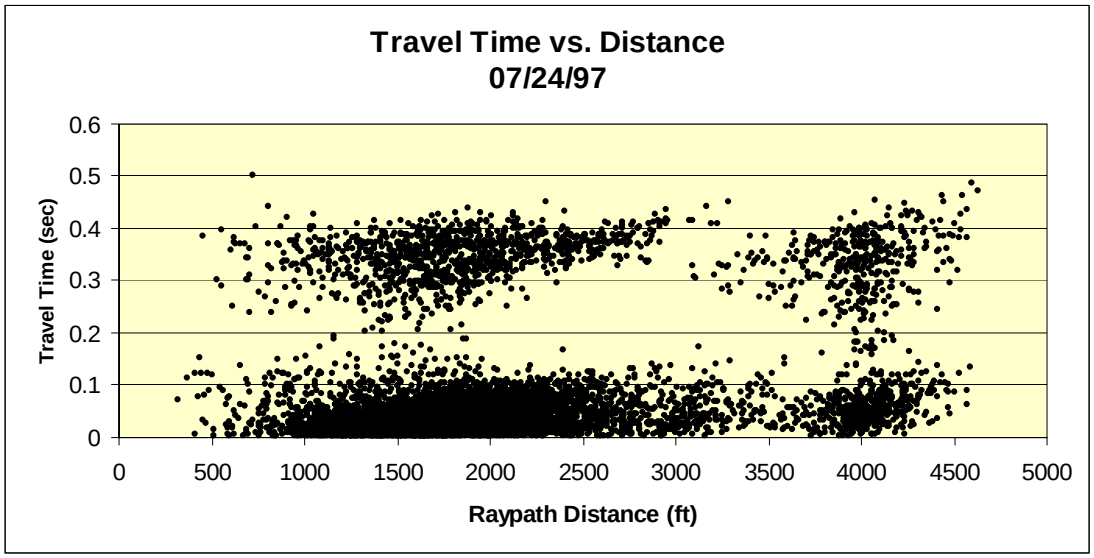

Figure A.9. Initial Time vs. Distance Plot.

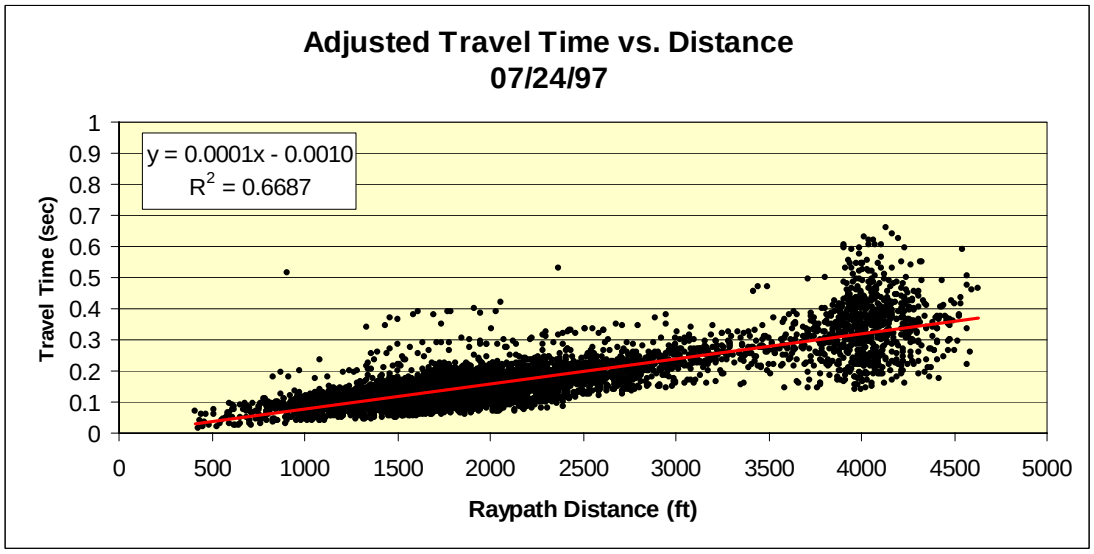

Figure A.10. Adjusted Time vs. Distance Plot.

Table A.5. Microseismic Data Statistics.

Date	7/24/1997	
Number of Microseismic Events	591	
Face Advance	89	ft
Number of Original Points	8716	
Number of Adjusted Points	8326	
Data Points Removed	4.47%	%
RMS Residual for Final Iteration	0.03637	sec
Average Velocity	13328.61	ft/s

07-25-97
Time vs. Distance Plots and Data Statistics

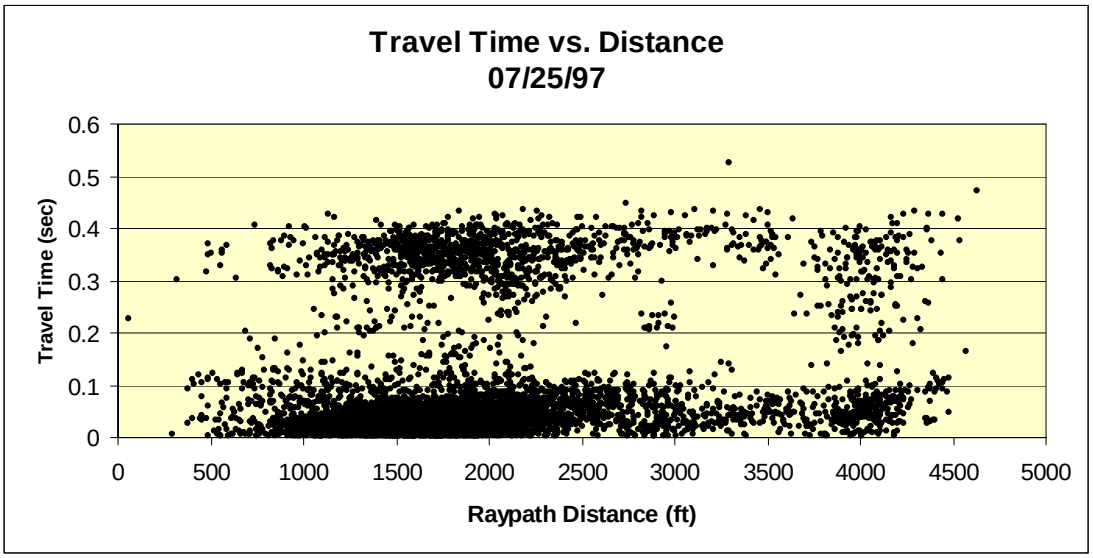

Figure A.11. Initial Time vs. Distance Plot.

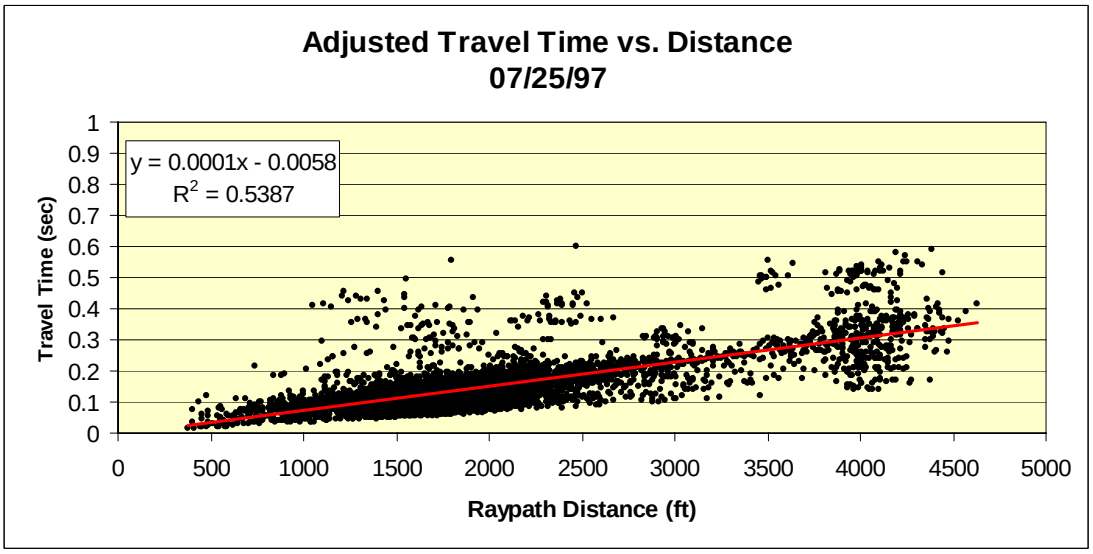

Figure A.12. Adjusted Time vs. Distance Plot.

Table A.6. Microseismic Data Statistics.

Date	7/25/1997	
Number of Microseismic Events	445	
Face Advance	121	ft
Number of Original Points	6511	
Number of Adjusted Points	5859	
Data Points Removed	10.01%	%
RMS Residual for Final Iteration	0.04666	sec
Average Velocity	14736.08	ft/s

07-26-97
Time vs. Distance Plots and Data Statistics

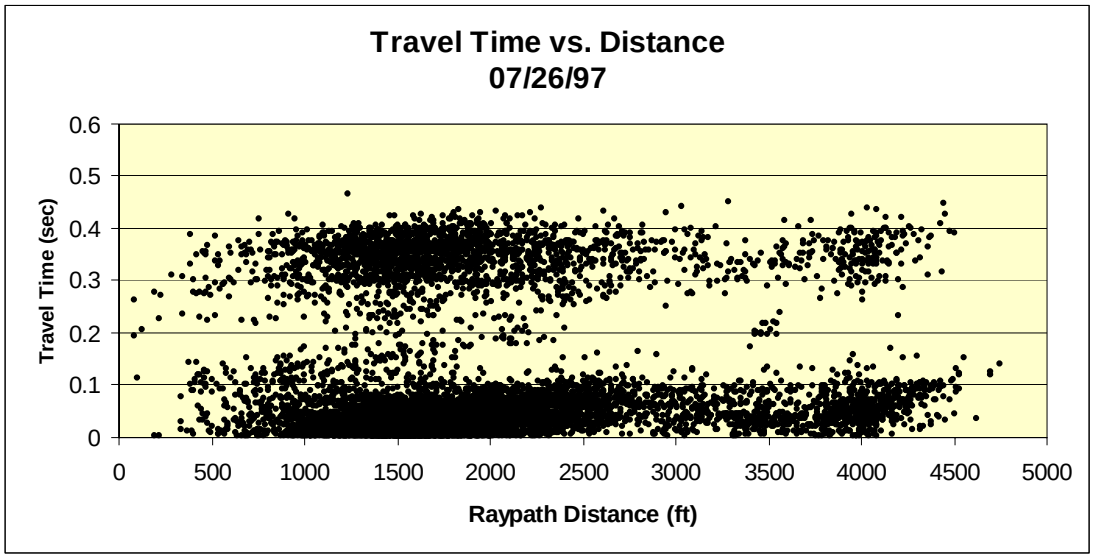

Figure A.13. Initial Time vs. Distance Plot.

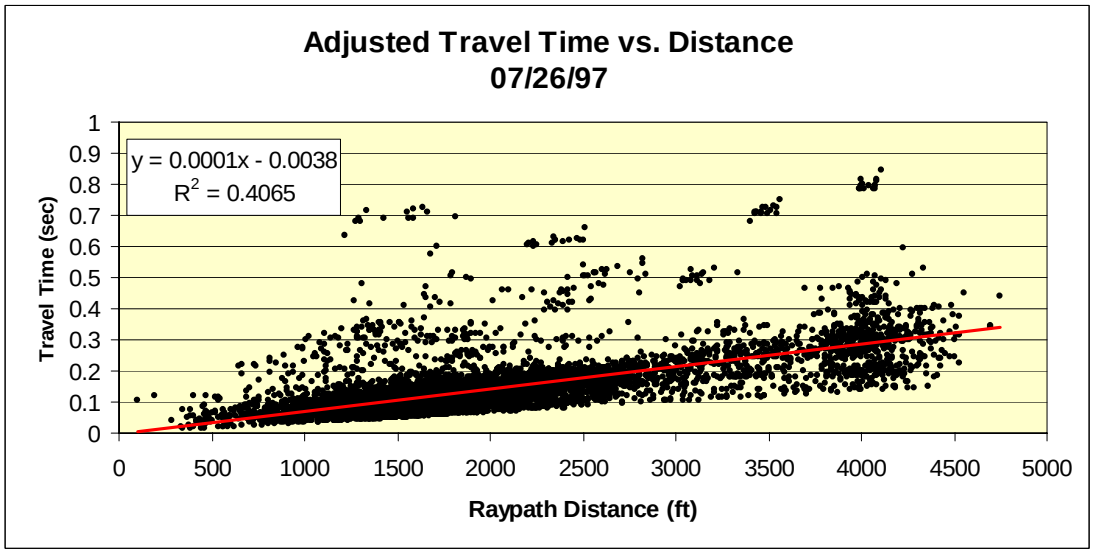

Figure A.14. Adjusted Time vs. Distance Plot.

Table A.7. Microseismic Data Statistics.

Date	7/26/1997	
Number of Microseismic Events	739	
Face Advance	34	ft
Number of Original Points	10810	
Number of Adjusted Points	9163	
Data Points Removed	15.24%	%
RMS Residual for Final Iteration	0.06053	sec
Average Velocity	16148.84	ft/s

07-27-97
Time vs. Distance Plots and Data Statistics

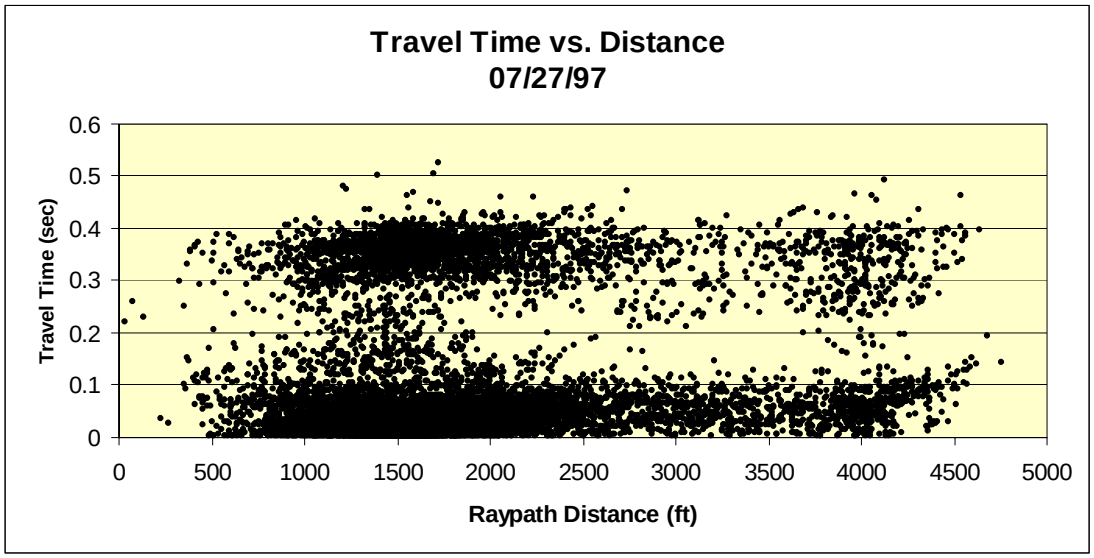

Figure A.15. Initial Time vs. Distance Plot.

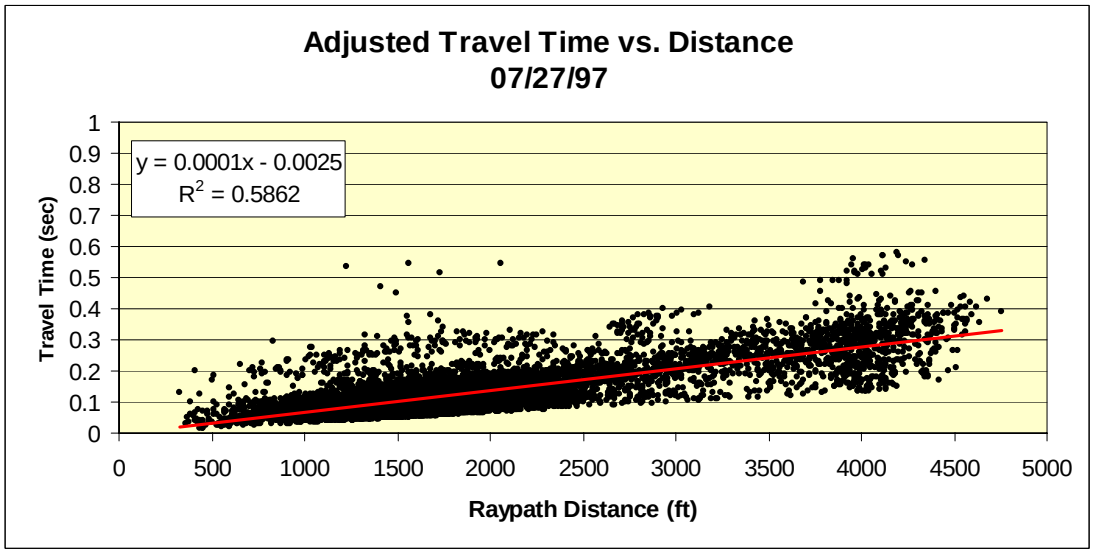

Figure A.16. Adjusted Time vs. Distance Plot.

Table A.8. Microseismic Data Statistics.

Date	7/27/1997	
Number of Microseismic Events	109	
Face Advance	986	ft
Number of Original Points	14189	
Number of Adjusted Points	12235	
Data Points Removed	13.77%	%
RMS Residual for Final Iteration	0.03813	sec
Average Velocity	17481.08	ft/s

07-28-97
Time vs. Distance Plots and Data Statistics

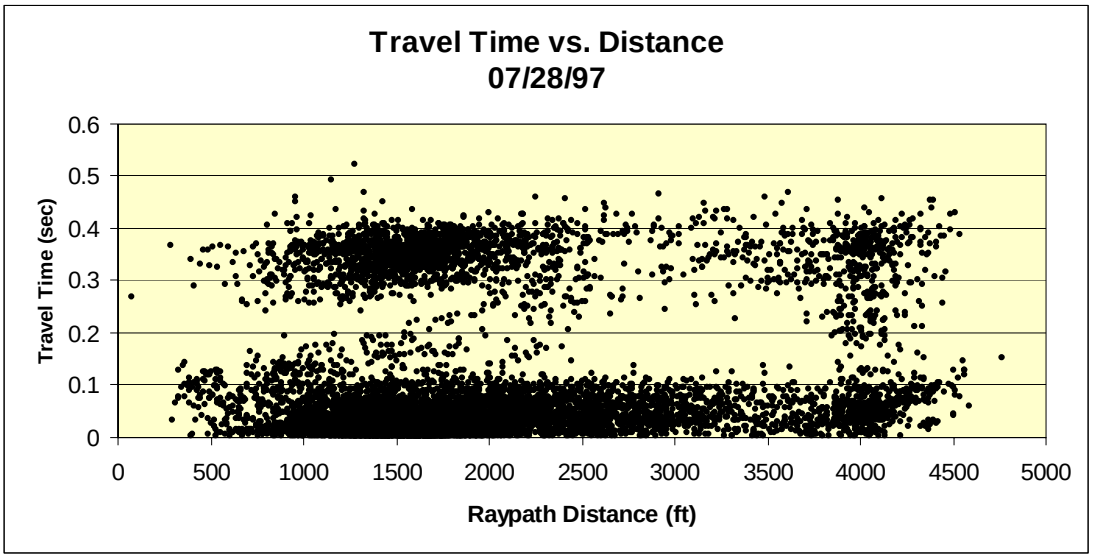

Figure A.17. Initial Time vs. Distance Plot.

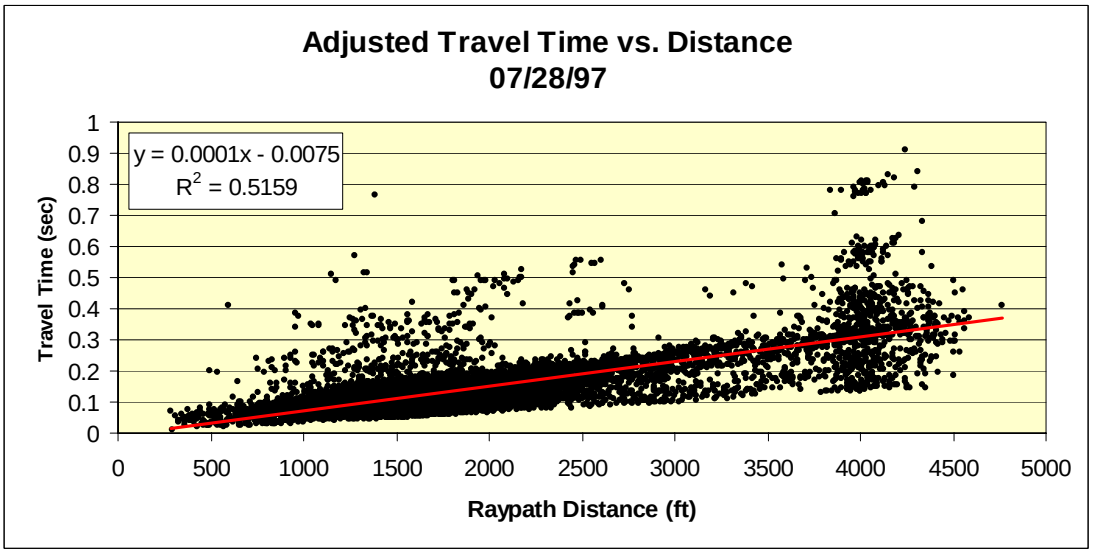

Figure A.18. Adjusted Time vs. Distance Plot.

Table A.9. Microseismic Data Statistics.

Date	7/28/1997	
Number of Microseismic Events	799	
Face Advance	95	ft
Number of Original Points	11809	
Number of Adjusted Points	11090	
Data Points Removed	6.09%	%
RMS Residual for Final Iteration	0.05538	sec
Average Velocity	15728.16	ft/s

07-30-97
Time vs. Distance Plots and Data Statistics

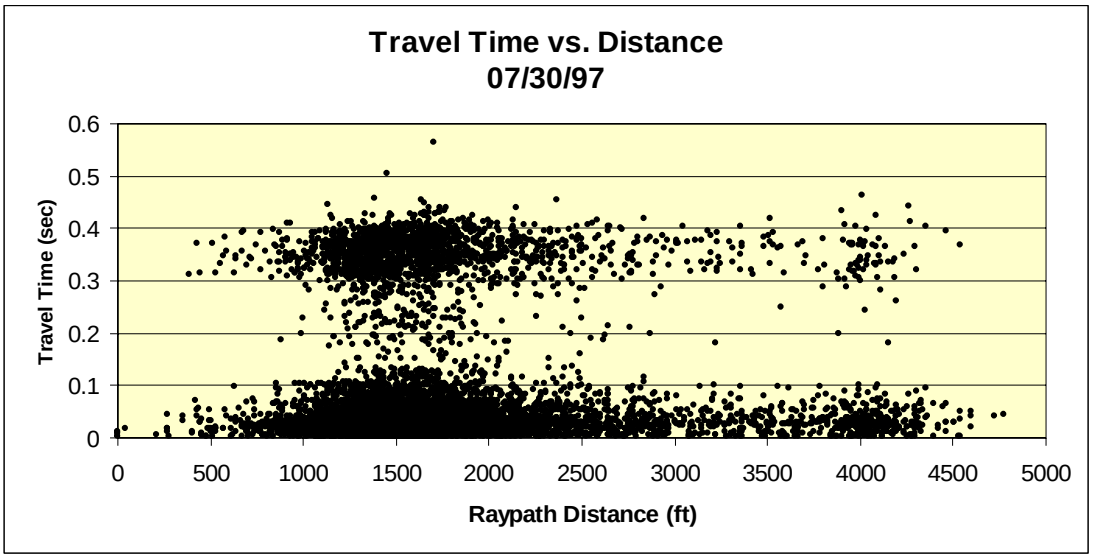

Figure A.19. Initial Time vs. Distance Plot.

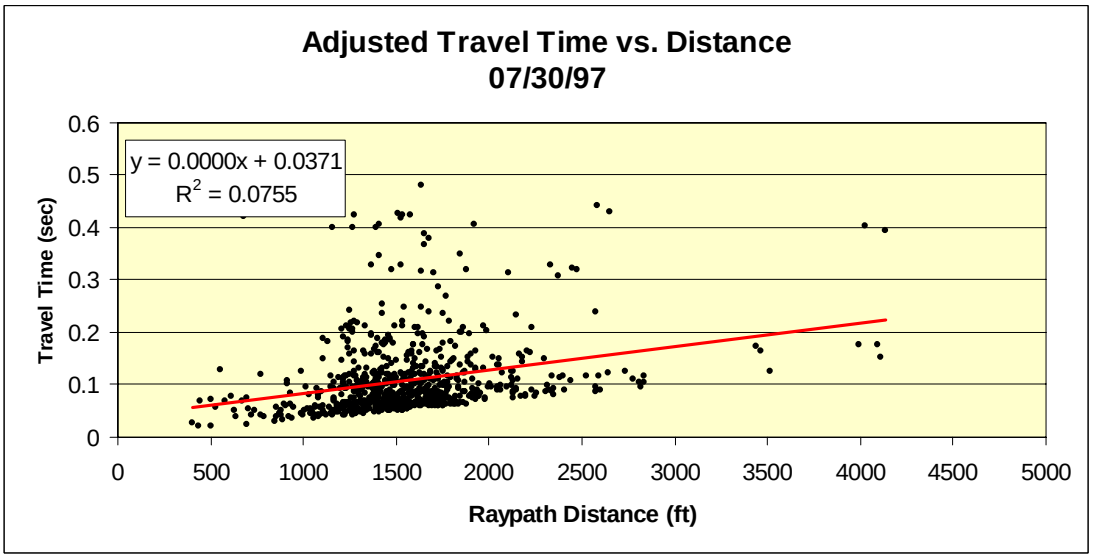

Figure A.20. Adjusted Time vs. Distance Plot.

Table A.10. Microseismic Data Statistics.

Date	7/30/1997	
Number of Microseismic Events	687	
Face Advance	41	ft
Number of Original Points	10004	
Number of Adjusted Points	762	
Data Points Removed	92.38%	%
RMS Residual for Final Iteration	0.06478	sec
Average Velocity	17904.20	ft/s

07-31-97

Time vs. Distance Plots and Data Statistics

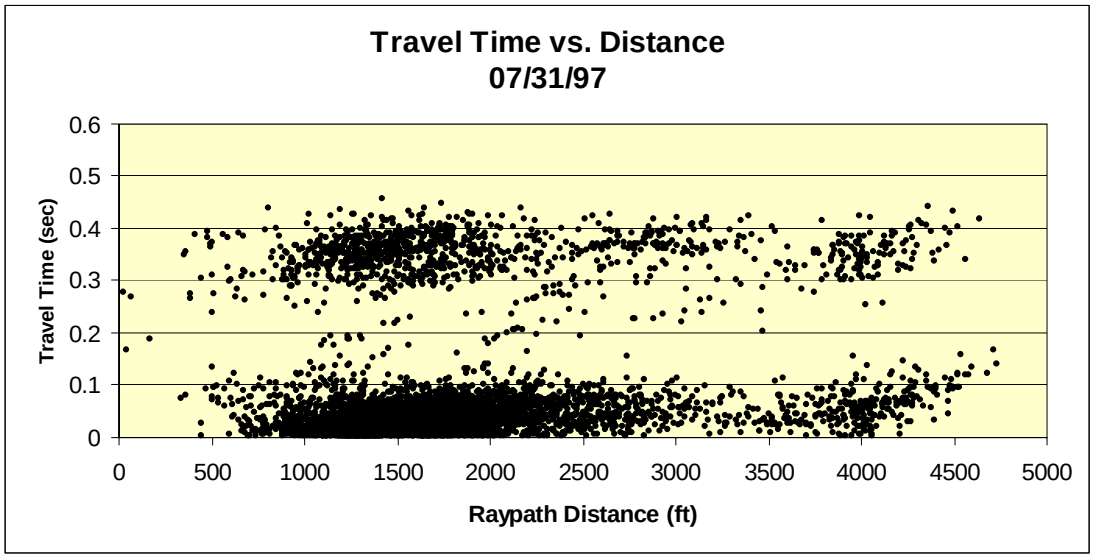

Figure A.21. Initial Time vs. Distance Plot.

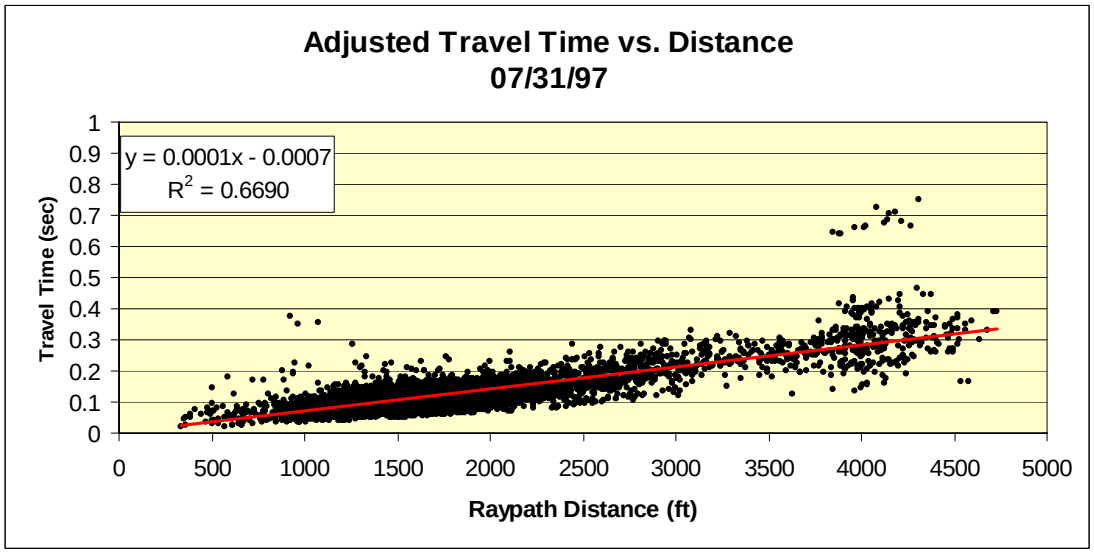

Figure A.22. Adjusted Time vs. Distance Plot.

Table A.11. Microseismic Data Statistics.

Date	7/31/1997	
Number of Microseismic Events	515	
Face Advance	7	ft
Number of Original Points	7631	
Number of Adjusted Points	7441	
Data Points Removed	2.49%	%
RMS Residual for Final Iteration	0.02491	sec
Average Velocity	14928.99	ft/s

08-01-97

Time vs. Distance Plots and Data Statistics

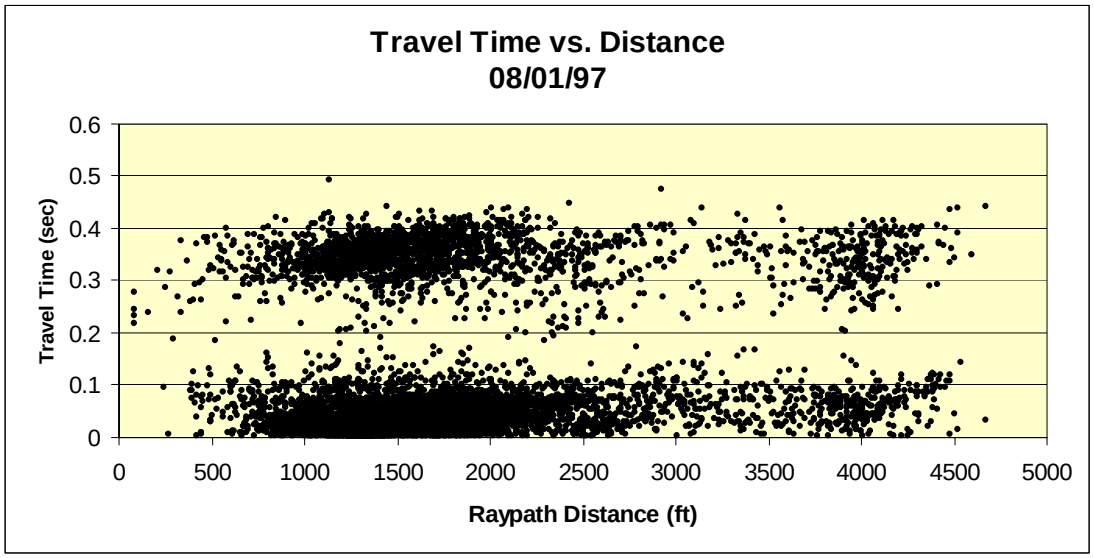

Figure A.23. Initial Time vs. Distance Plot.

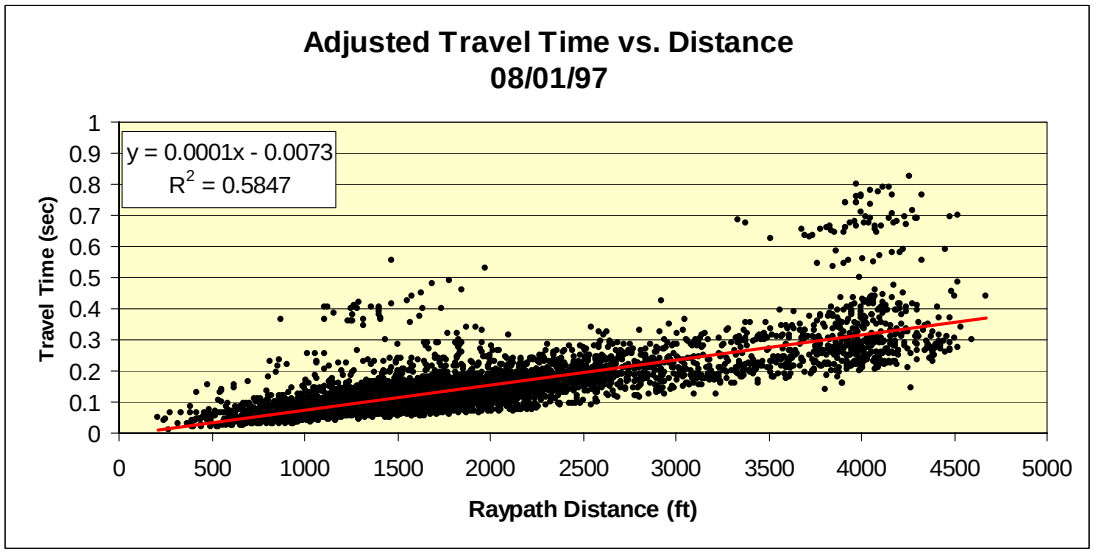

Figure A.24. Adjusted Time vs. Distance Plot.

Table A.12. Microseismic Data Statistics.

Date	8/1/1997	
Number of Microseismic Events	819	
Face Advance	153	ft
Number of Original Points	12096	
Number of Adjusted Points	11722	
Data Points Removed	3.09%	%
RMS Residual for Final Iteration	0.03818	sec
Average Velocity	14695.64	ft/s

08-02-97
Time vs. Distance Plots and Data Statistics

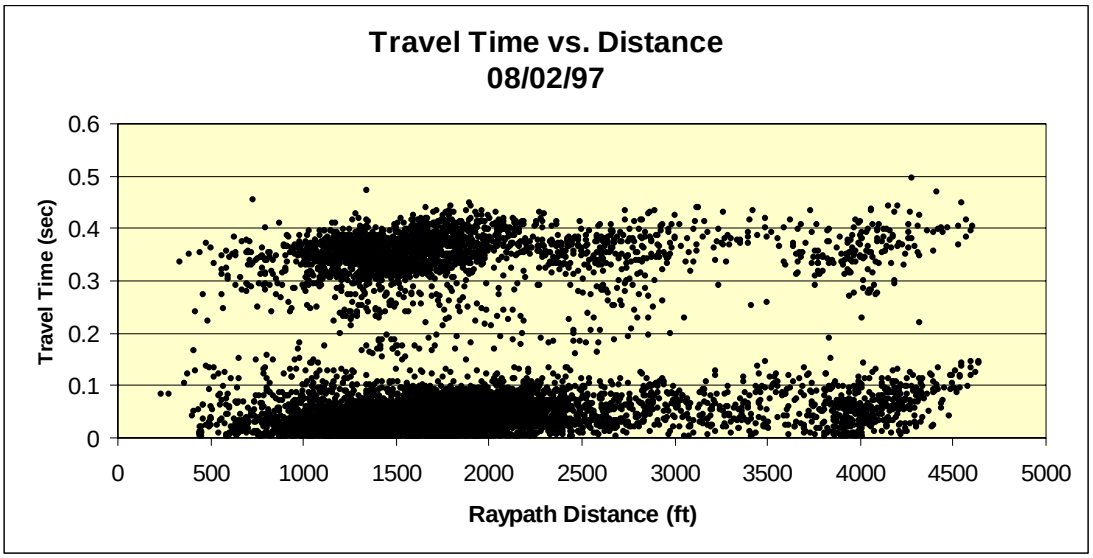

Figure A.25. Initial Time vs. Distance Plot.

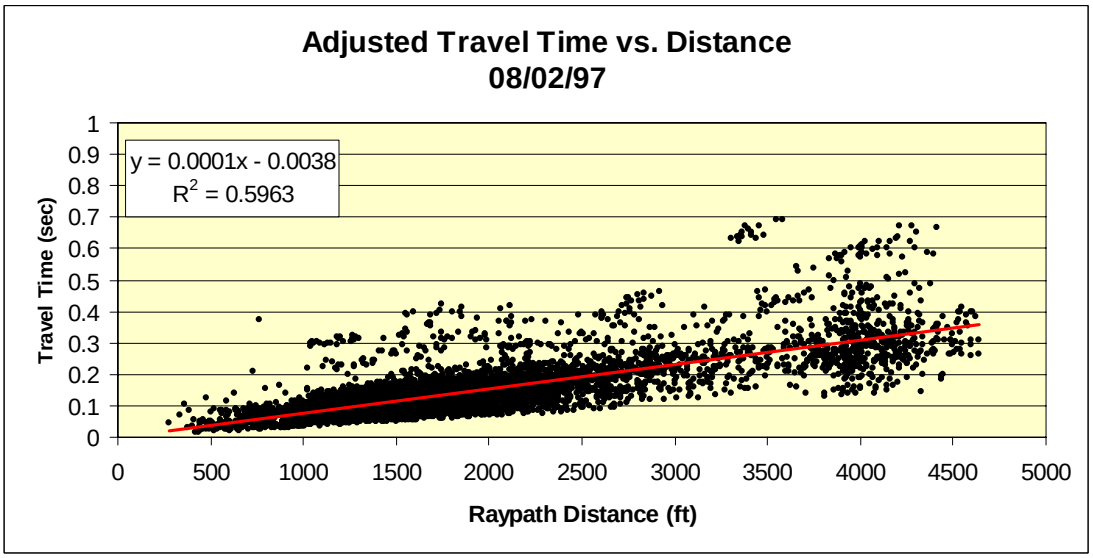

Figure A.26. Adjusted Time vs. Distance Plot.

Table A.13. Microseismic Data Statistics.

Date	8/2/1997	
Number of Microseismic Events	1123	
Face Advance	59	ft
Number of Original Points	16579	
Number of Adjusted Points	16240	
Data Points Removed	2.04%	%
RMS Residual for Final Iteration	0.03115	sec
Average Velocity	15806.70	ft/s

08-03-97
Time vs. Distance Plots and Data Statistics

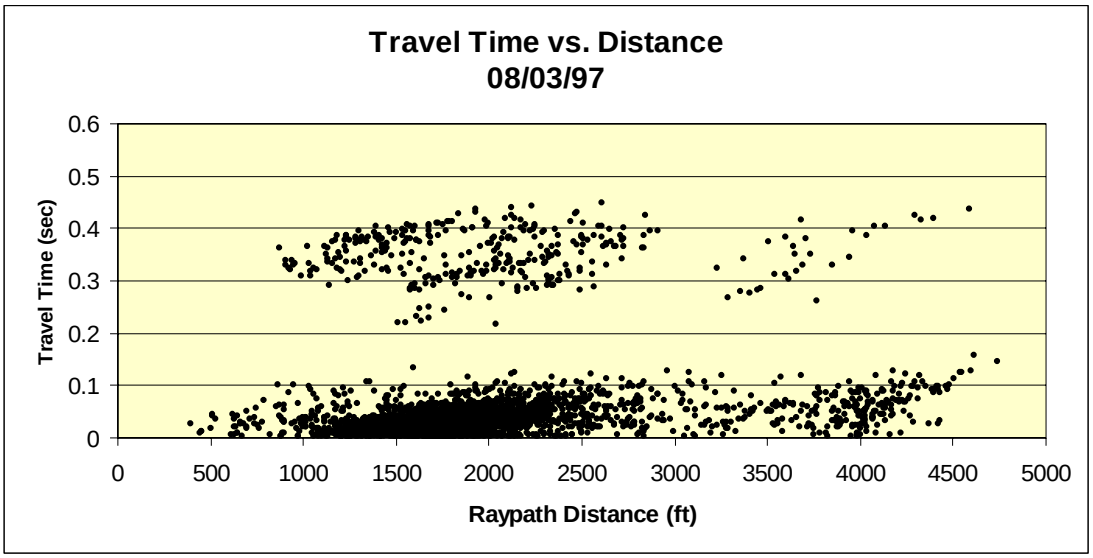

Figure A.27. Initial Time vs. Distance Plot.

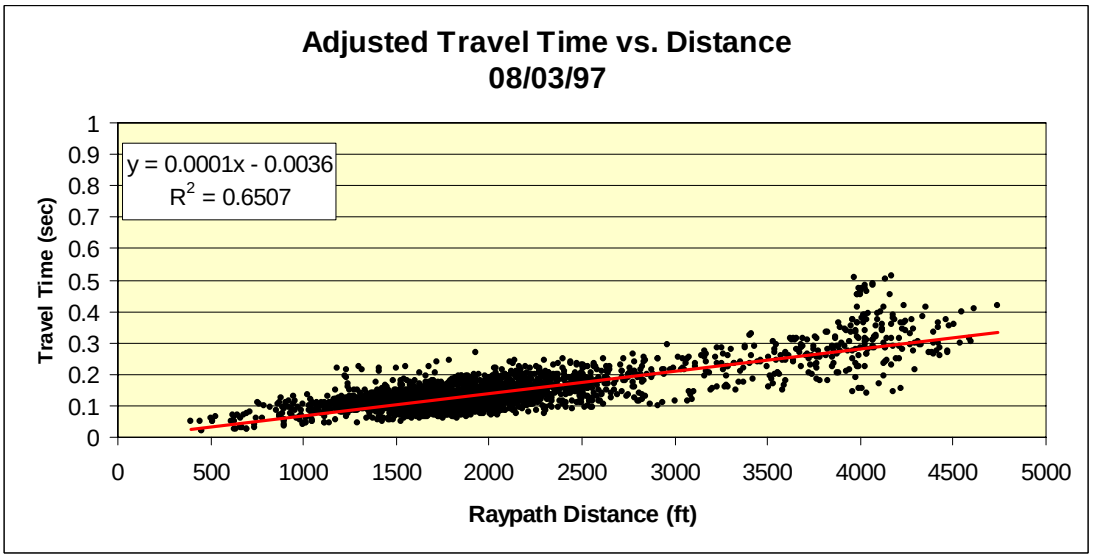

Figure A.28. Adjusted Time vs. Distance Plot.

Table A.14. Microseismic Data Statistics.

Date	8/3/1997	
Number of Microseismic Events	229	
Face Advance	21	ft
Number of Original Points	3362	
Number of Adjusted Points	3258	
Data Points Removed	3.09%	%
RMS Residual for Final Iteration	0.02677	sec
Average Velocity	15223.29	ft/s

08-04-97
Time vs. Distance Plots and Data Statistics

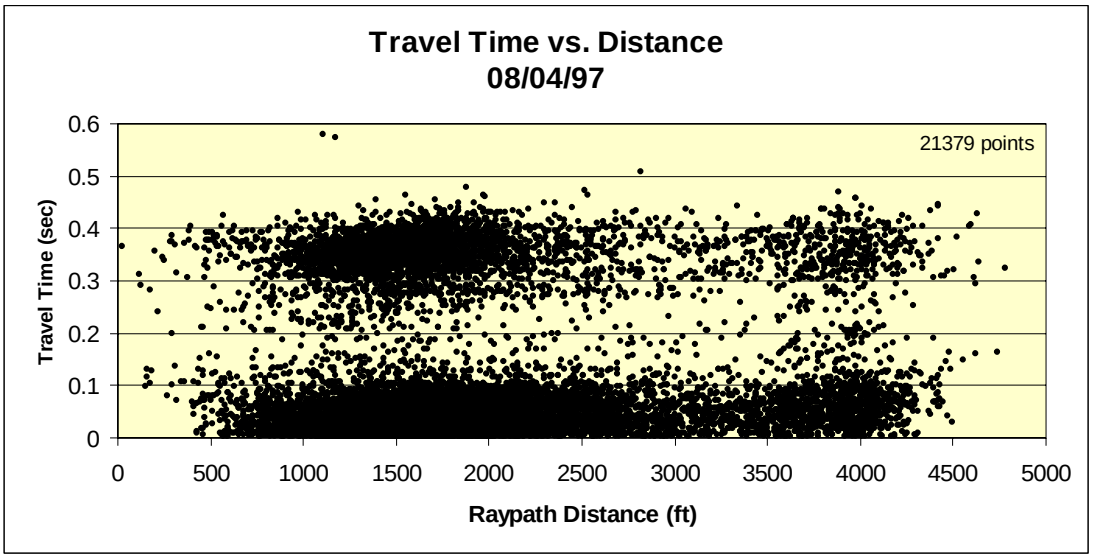

Figure A.29. Initial Time vs. Distance Plot.

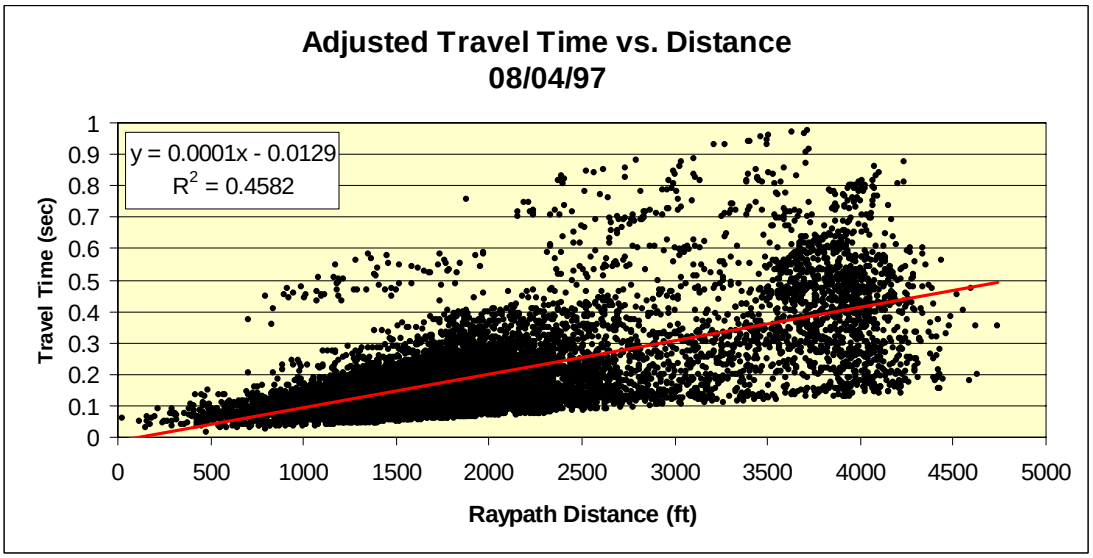

Figure A.30. Adjusted Time vs. Distance Plot.

Table A.15. Microseismic Data Statistics.

Date	8/4/1997	
Number of Microseismic Events	1450	
Face Advance	87	ft
Number of Original Points	21379	
Number of Adjusted Points	19186	
Data Points Removed	10.26%	%
RMS Residual for Final Iteration	0.06867	sec
Average Velocity	14431.93	ft/s

08-05-97
Time vs. Distance Plots and Data Statistics

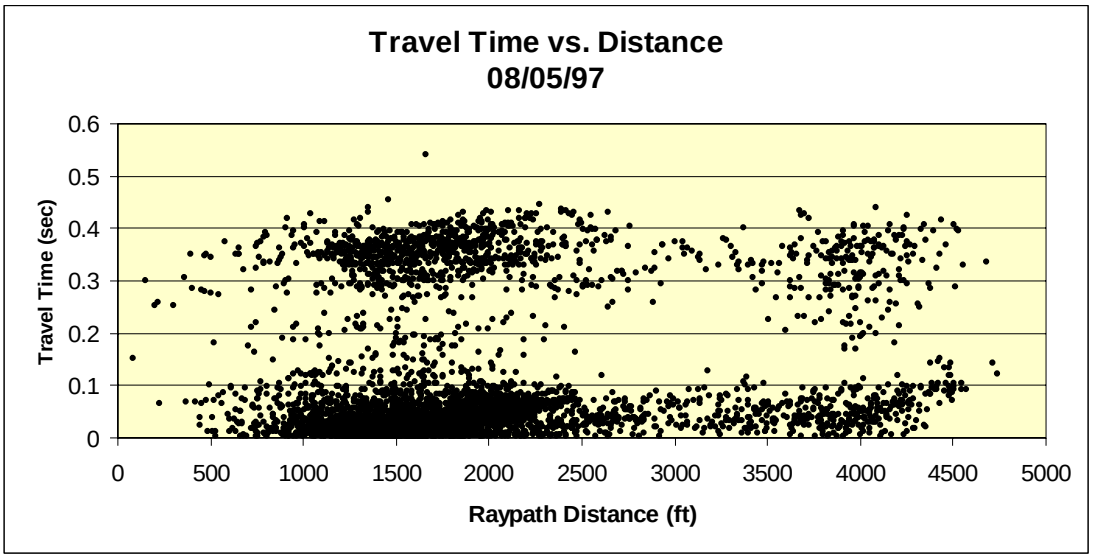

Figure A.31. Initial Time vs. Distance Plot.

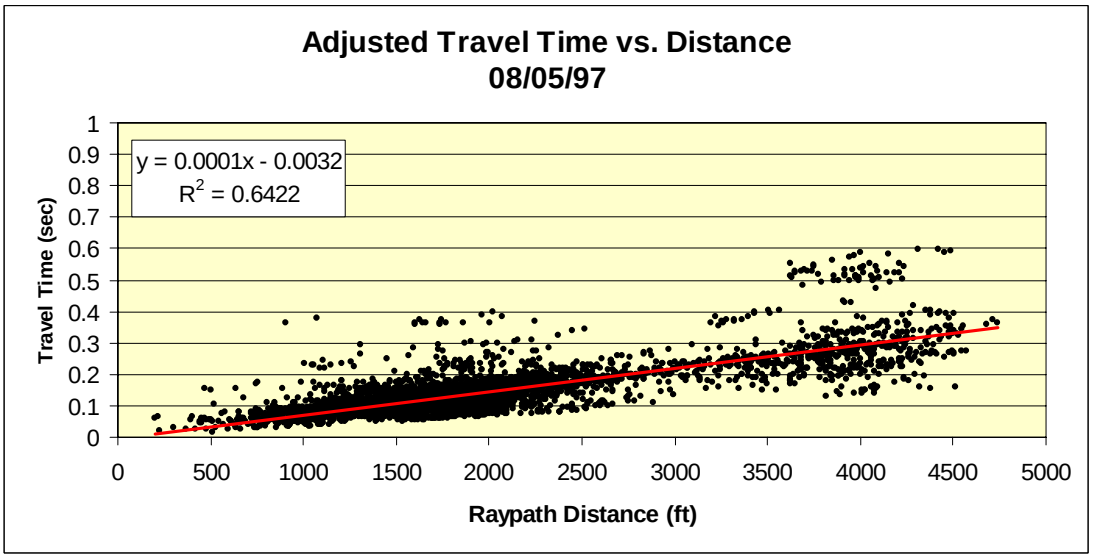

Figure A.32. Adjusted Time vs. Distance Plot.

Table A.16. Microseismic Data Statistics.

Date	8/5/1997	
Number of Microseismic Events	419	
Face Advance	81	ft
Number of Original Points	6147	
Number of Adjusted Points	5908	
Data Points Removed	3.89%	%
RMS Residual for Final Iteration	0.03244	sec
Average Velocity	14624.55	ft/s

08-06-97
Time vs. Distance Plots and Data Statistics

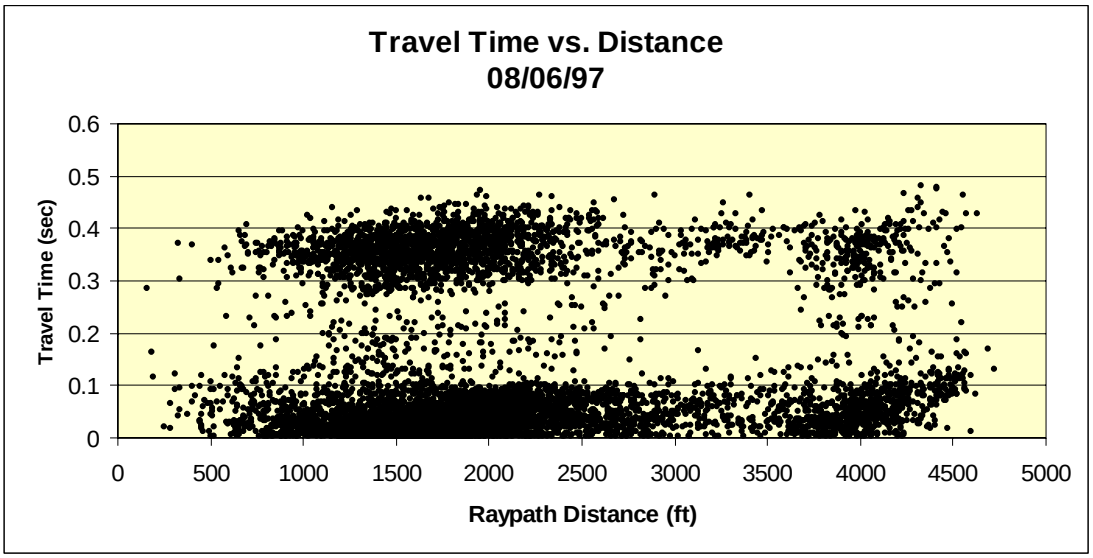

Figure A.33. Initial Time vs. Distance Plot.

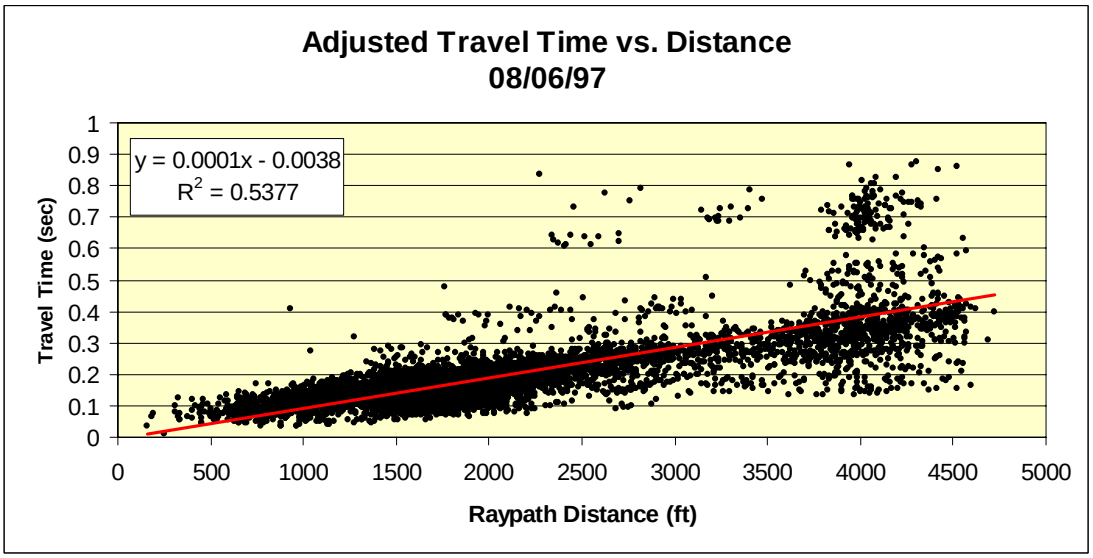

Figure A.34. Adjusted Time vs. Distance Plot.

Table A.17. Microseismic Data Statistics.

Date	8/6/1997	
Number of Microseismic Events	847	
Face Advance	58	ft
Number of Original Points	12390	
Number of Adjusted Points	12229	
Data Points Removed	1.30%	%
RMS Residual for Final Iteration	0.05774	sec
Average Velocity	11852.76	ft/s

08-07-97
Time vs. Distance Plots and Data Statistics

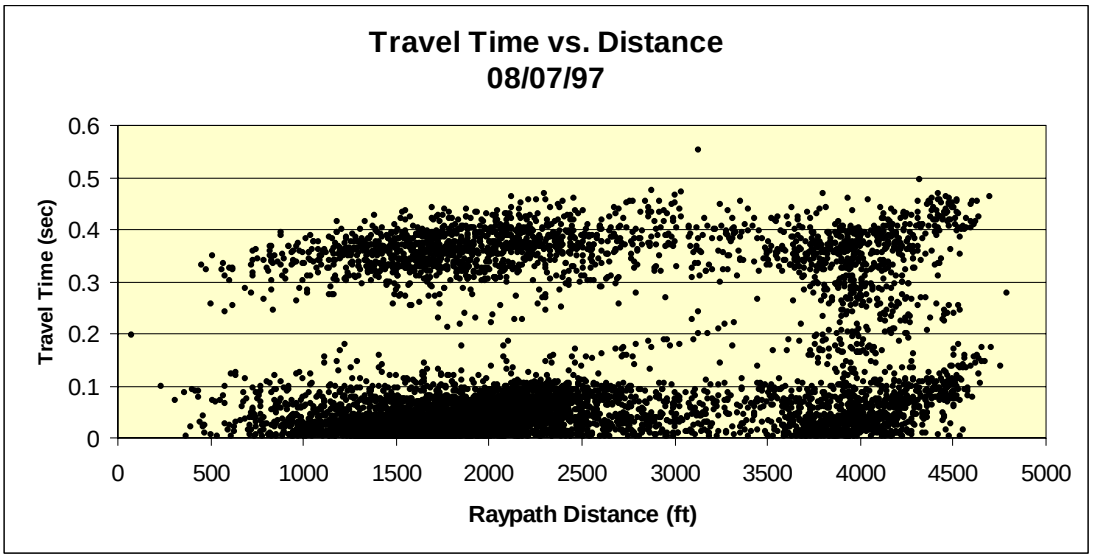

Figure A.35. Initial Time vs. Distance Plot.

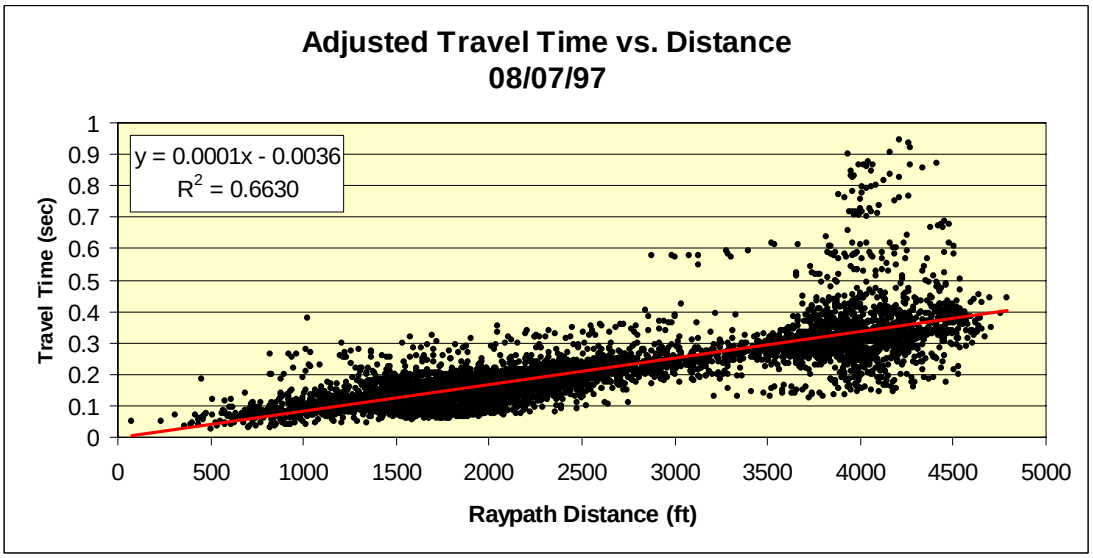

Figure A.36. Adjusted Time vs. Distance Plot.

Table A.18. Microseismic Data Statistics.

Date	8/7/1997	
Number of Microseismic Events	666	
Face Advance	133	ft
Number of Original Points	9666	
Number of Adjusted Points	9391	
Data Points Removed	2.85%	%
RMS Residual for Final Iteration	0.04971	sec
Average Velocity	12588.16	ft/s

APPENDIX B

Velocity Tomograms & Ray Density Plots

FLOOR LEVEL
Z = 5, 400 FEET

07-20-97
Plan View at Z = 5,400 feet (Floor Level)

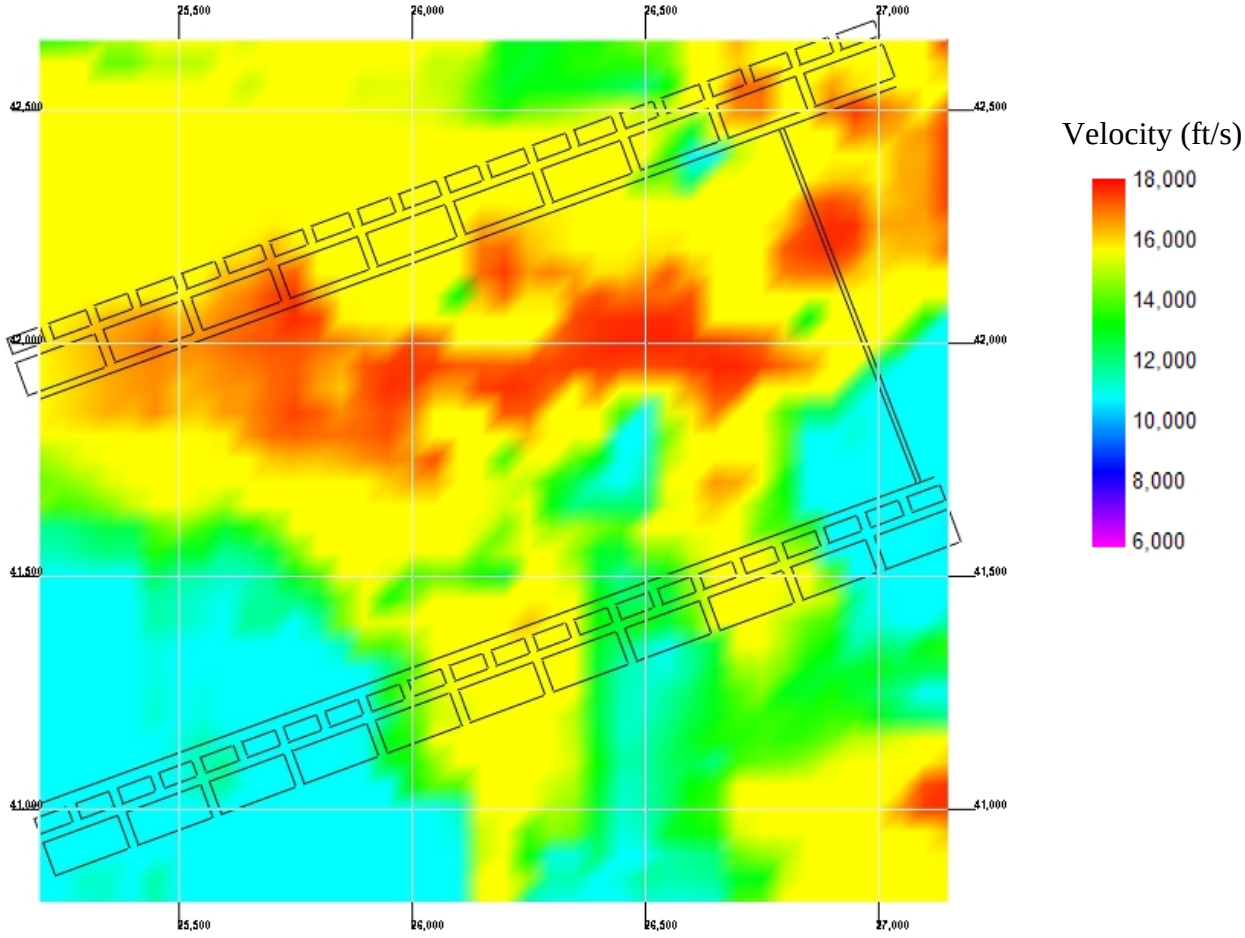

Figure B.1. Velocity tomogram at Z = 5,400 feet

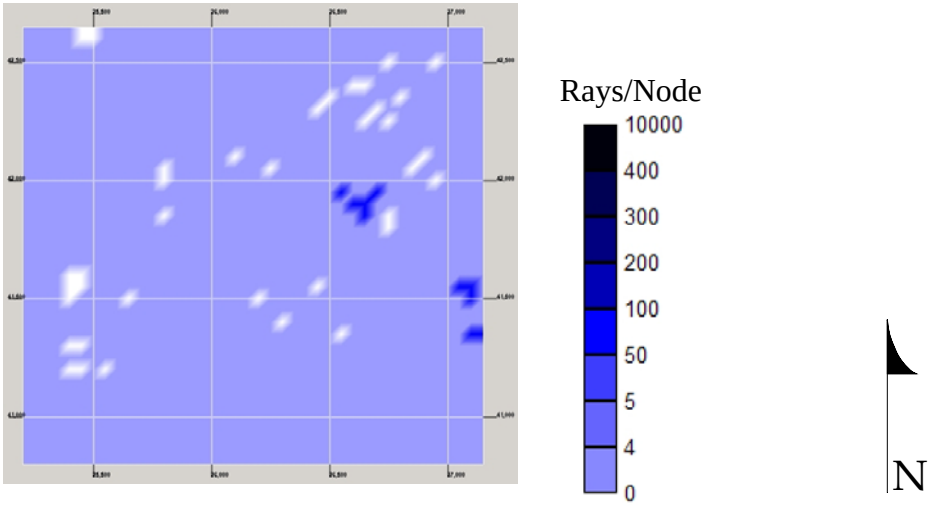

Figure B.2. Ray density plot at Z = 5,400 feet.

07-21-97
Plan View at Z = 5,400 feet (Floor Level)

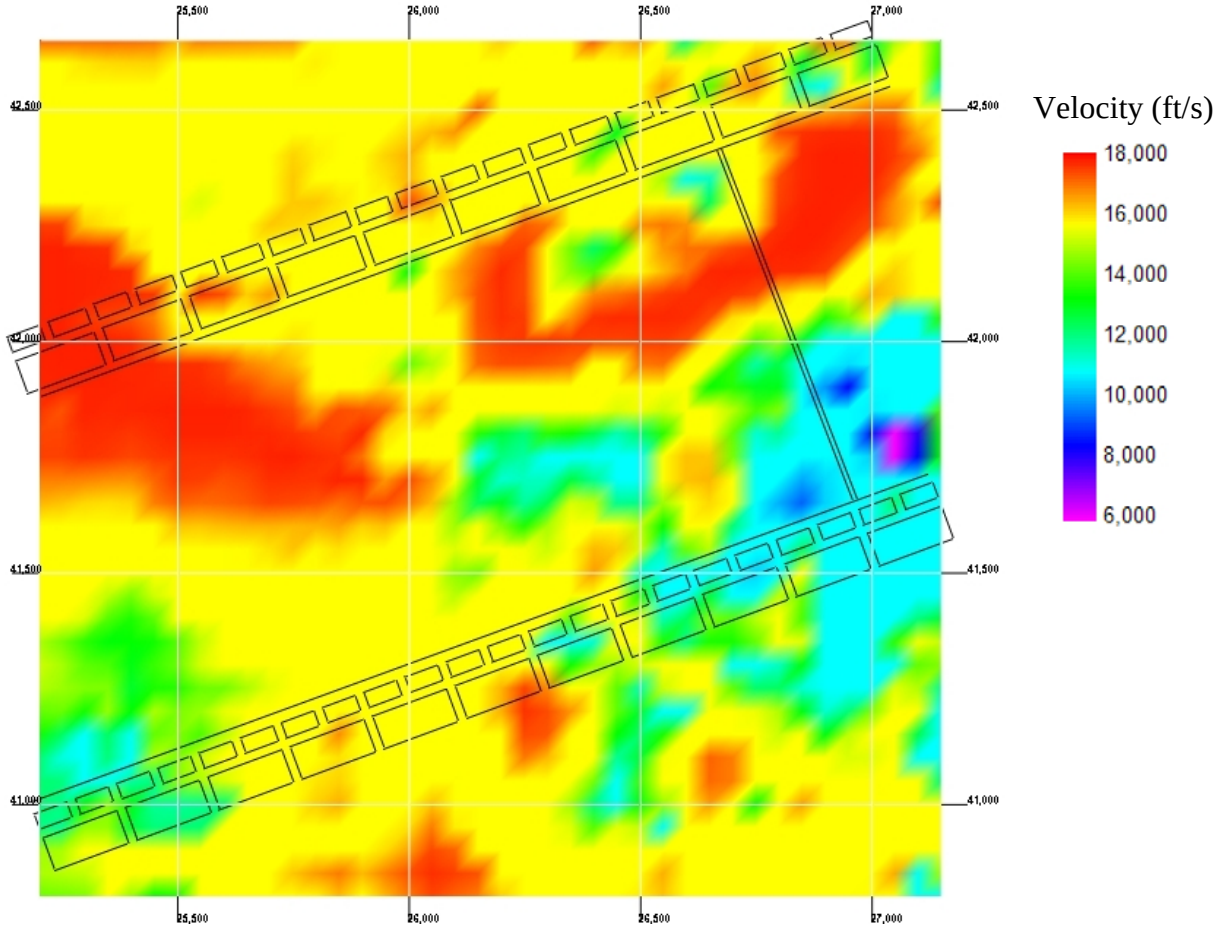

Figure B.3. Velocity tomogram at Z = 5,400 feet

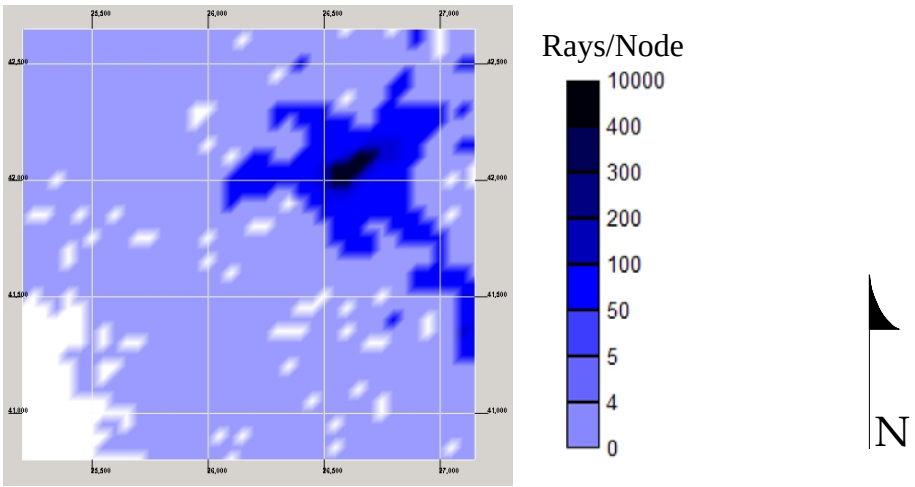

Figure B.4. Ray density plot at Z = 5,400 feet.

07-22-97
Plan View at Z = 5,400 feet (Floor Level)

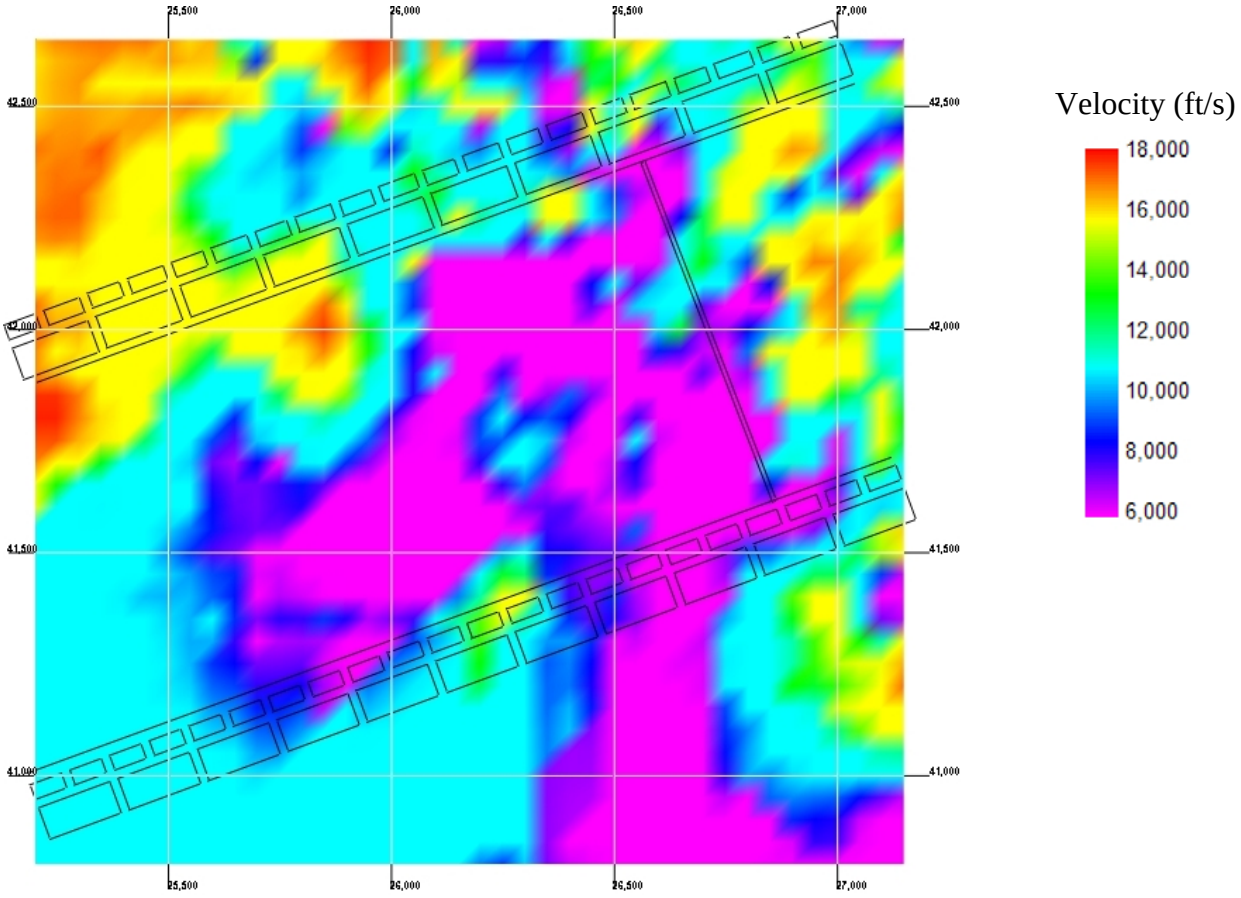

Figure B.5. Velocity tomogram at Z = 5,400 feet.

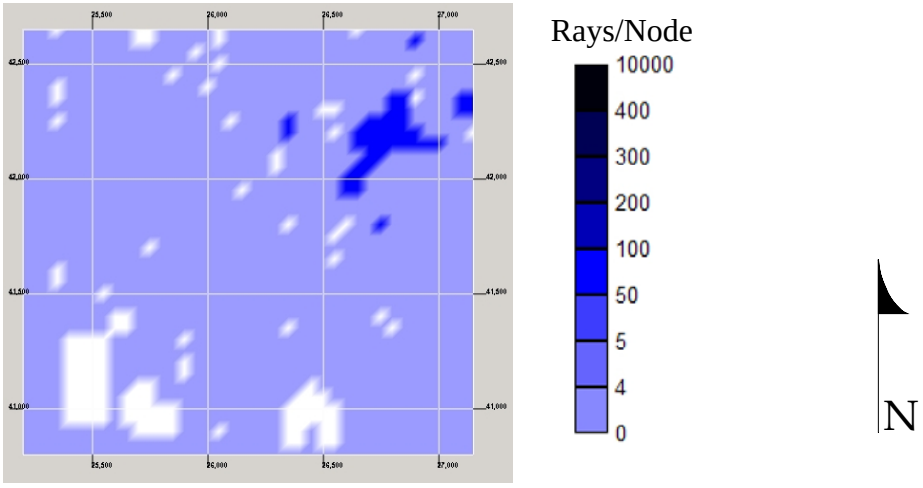

Figure B.6. Ray density plot at Z = 5,400 feet.

07-23-97
Plan View at Z = 5,400 feet (Floor Level)

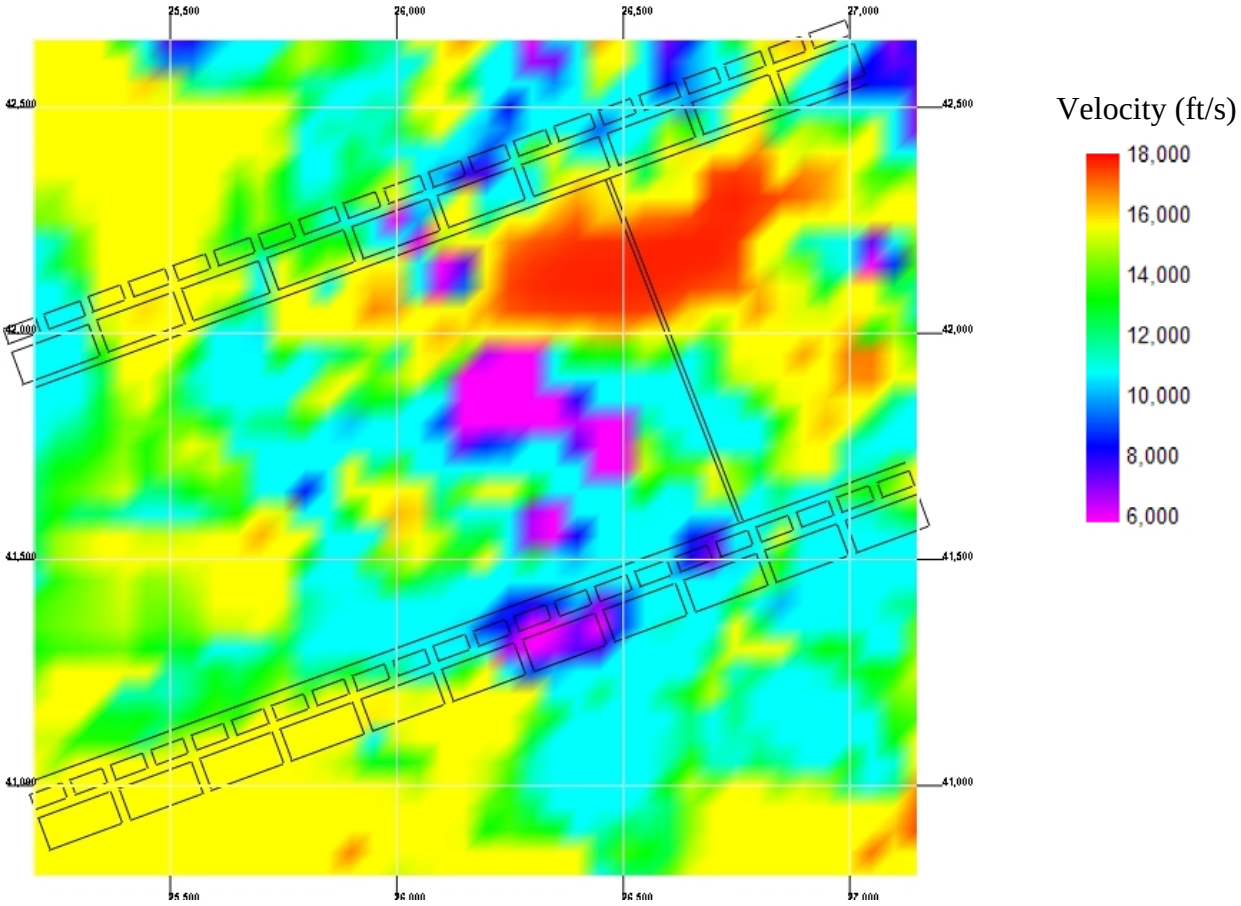

Figure B.7. Velocity tomogram at Z = 5,400 feet.

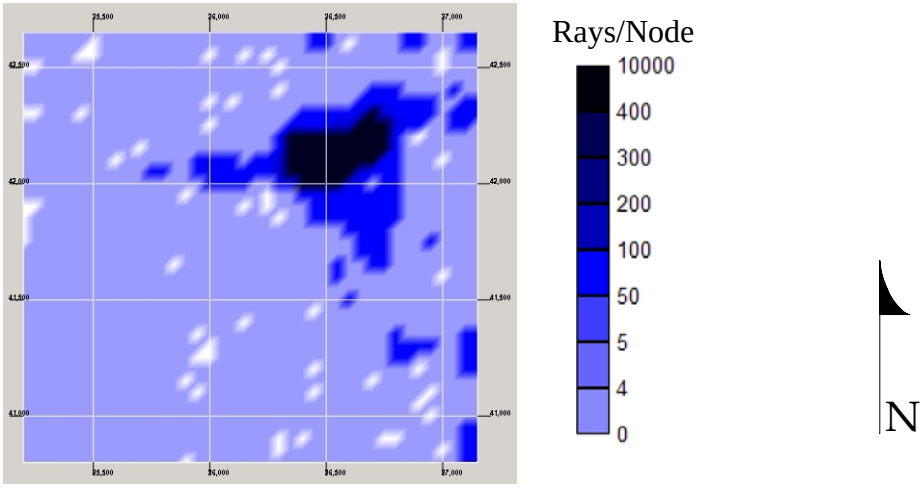

Figure B.8. Ray density plot at Z = 5,400 feet.

07-24-97
Plan View at Z = 5,400 feet (Floor Level)

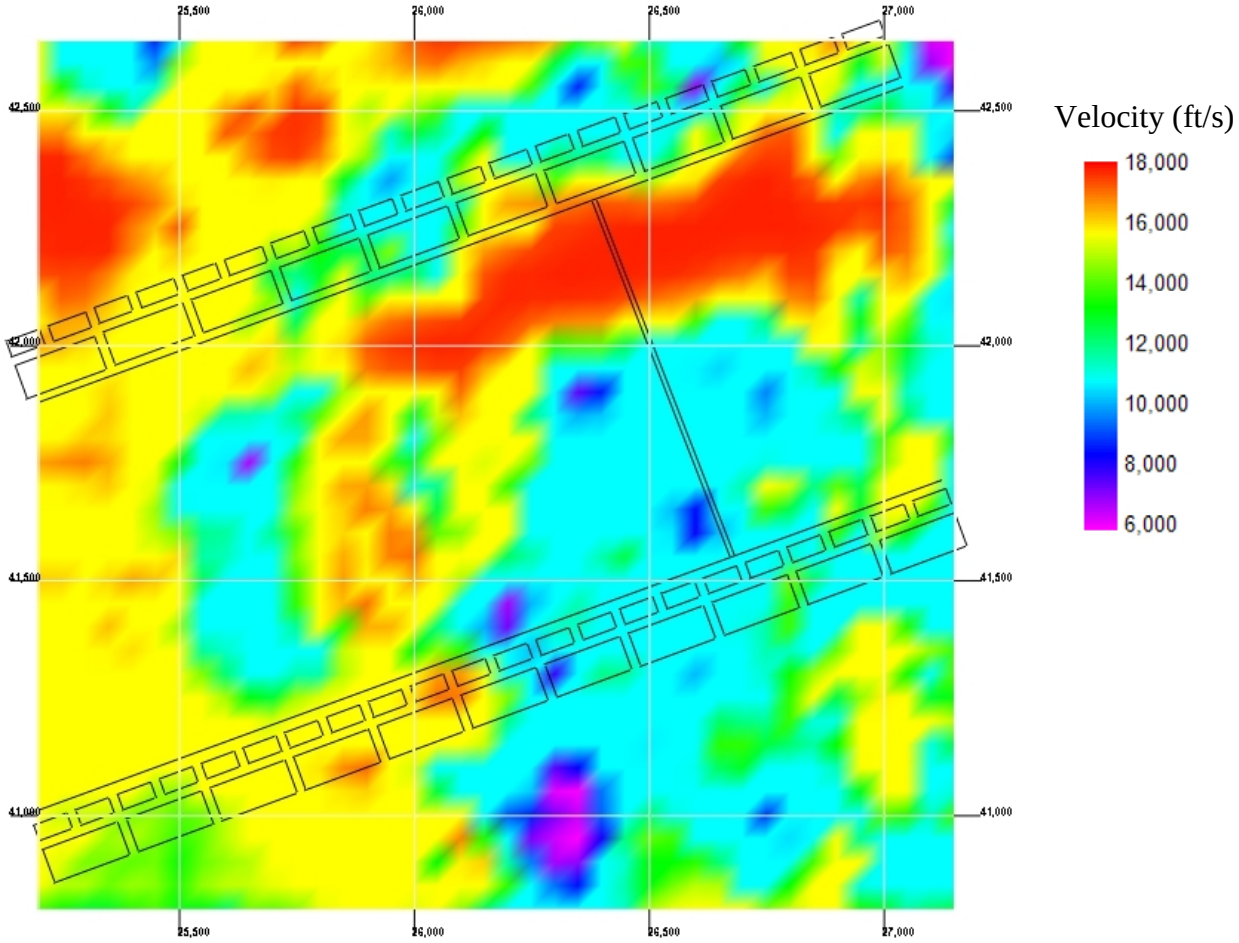

Figure B.9. Velocity tomogram at Z = 5,400 feet.

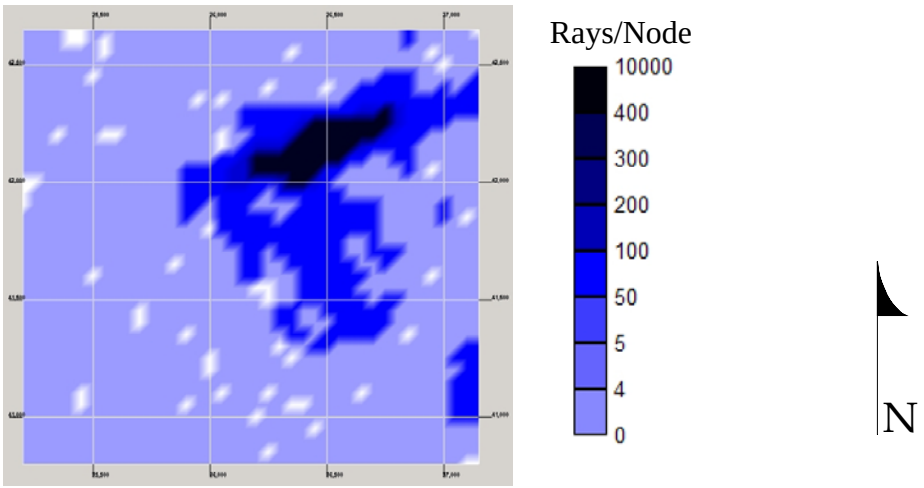

Figure B.10. Ray density plot at Z = 5,400 feet.

07-25-97
Plan View at Z = 5,400 feet (Floor Level)

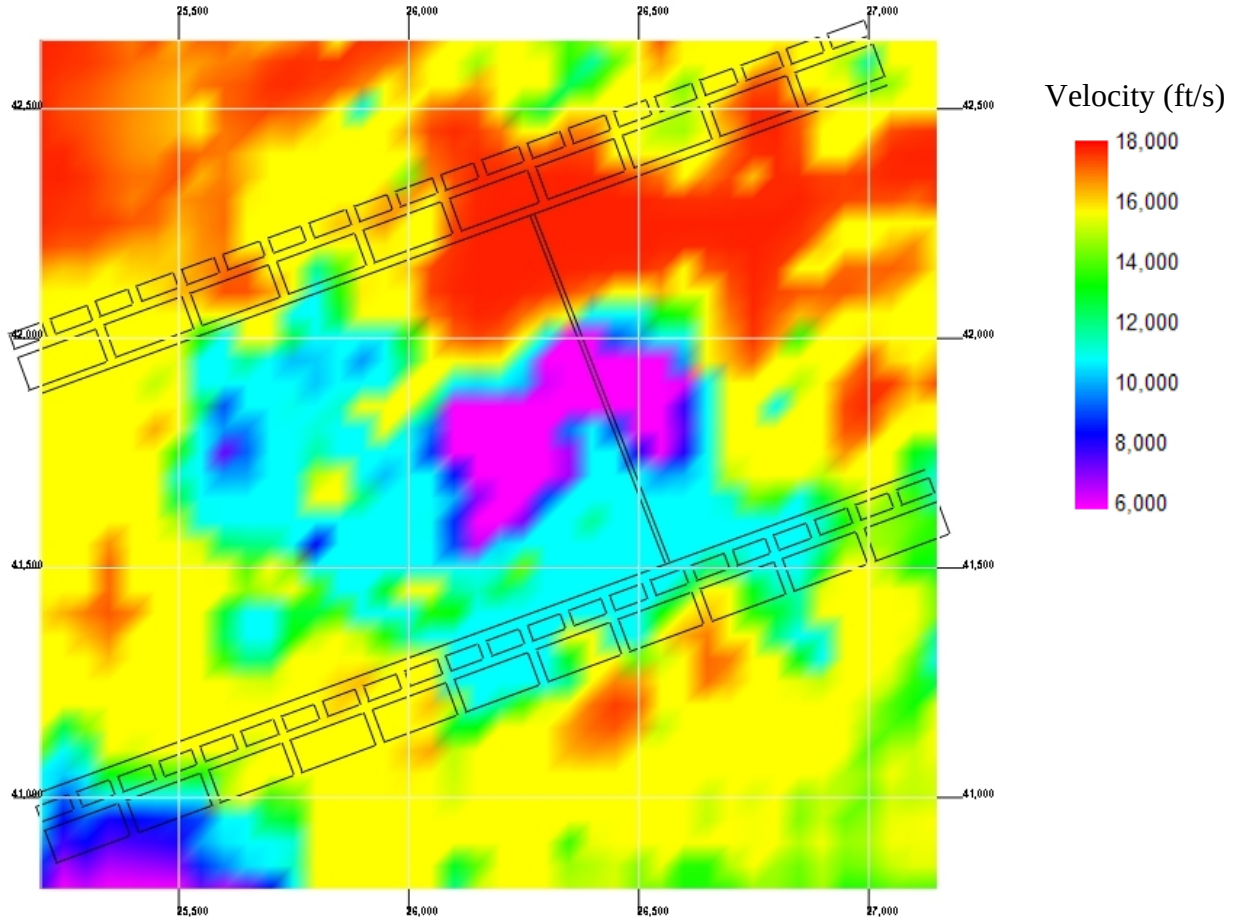

Figure B.11. Velocity tomogram at Z = 5,400 feet.

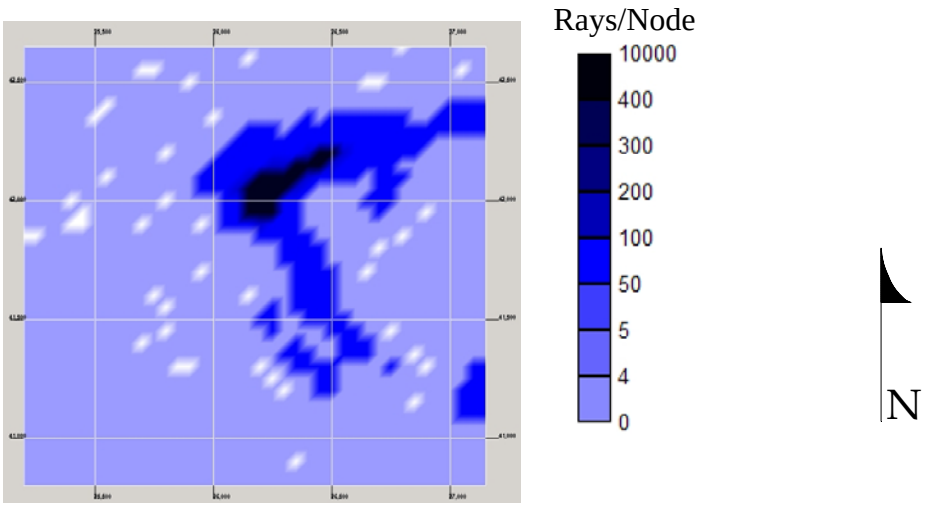

Figure B.12. Ray density plot at Z = 5,400 feet.

07-26-97

Plan View at Z = 5,400 feet (Floor Level)

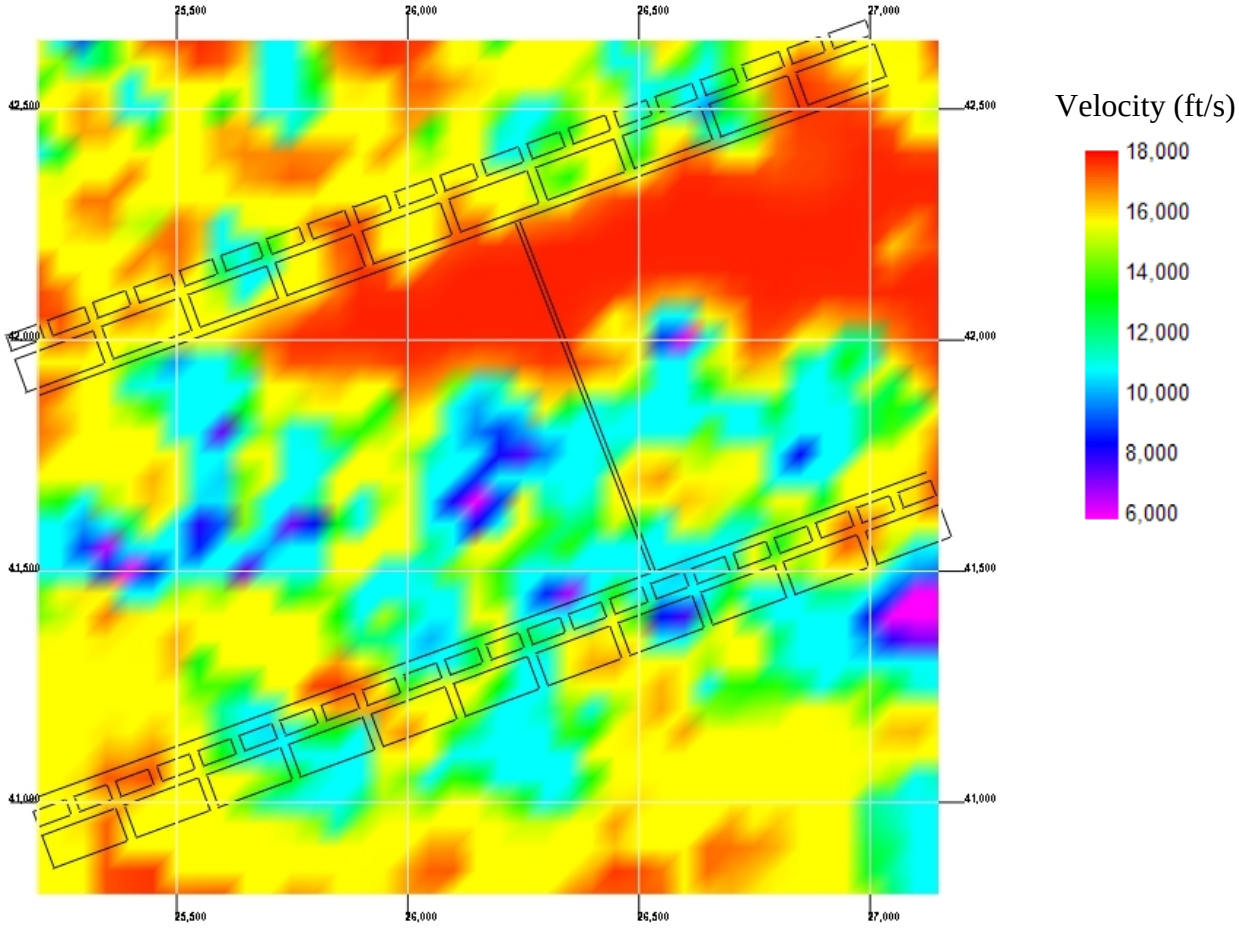

Figure B.13. Velocity tomogram at Z = 5,400 feet.

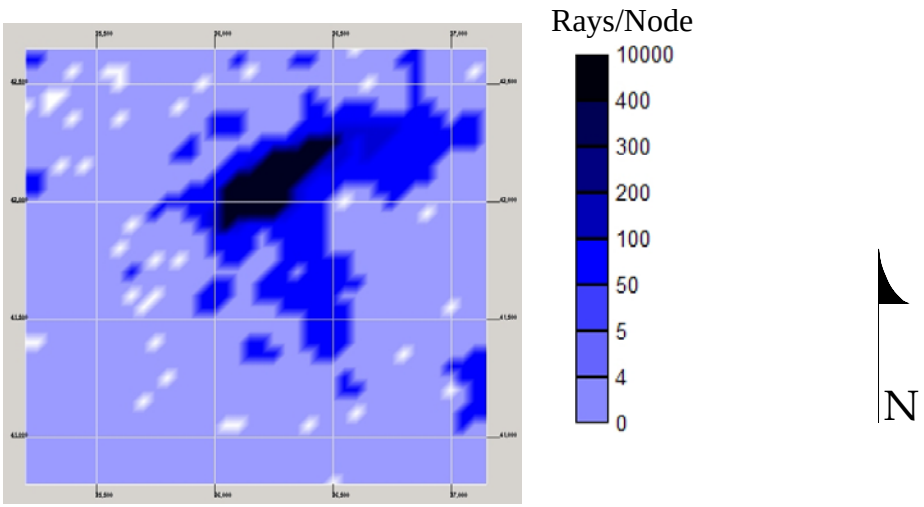

Figure B.14. Ray density plot at Z = 5,400 feet.

07-27-97
Plan View at Z = 5,400 feet (Floor Level)

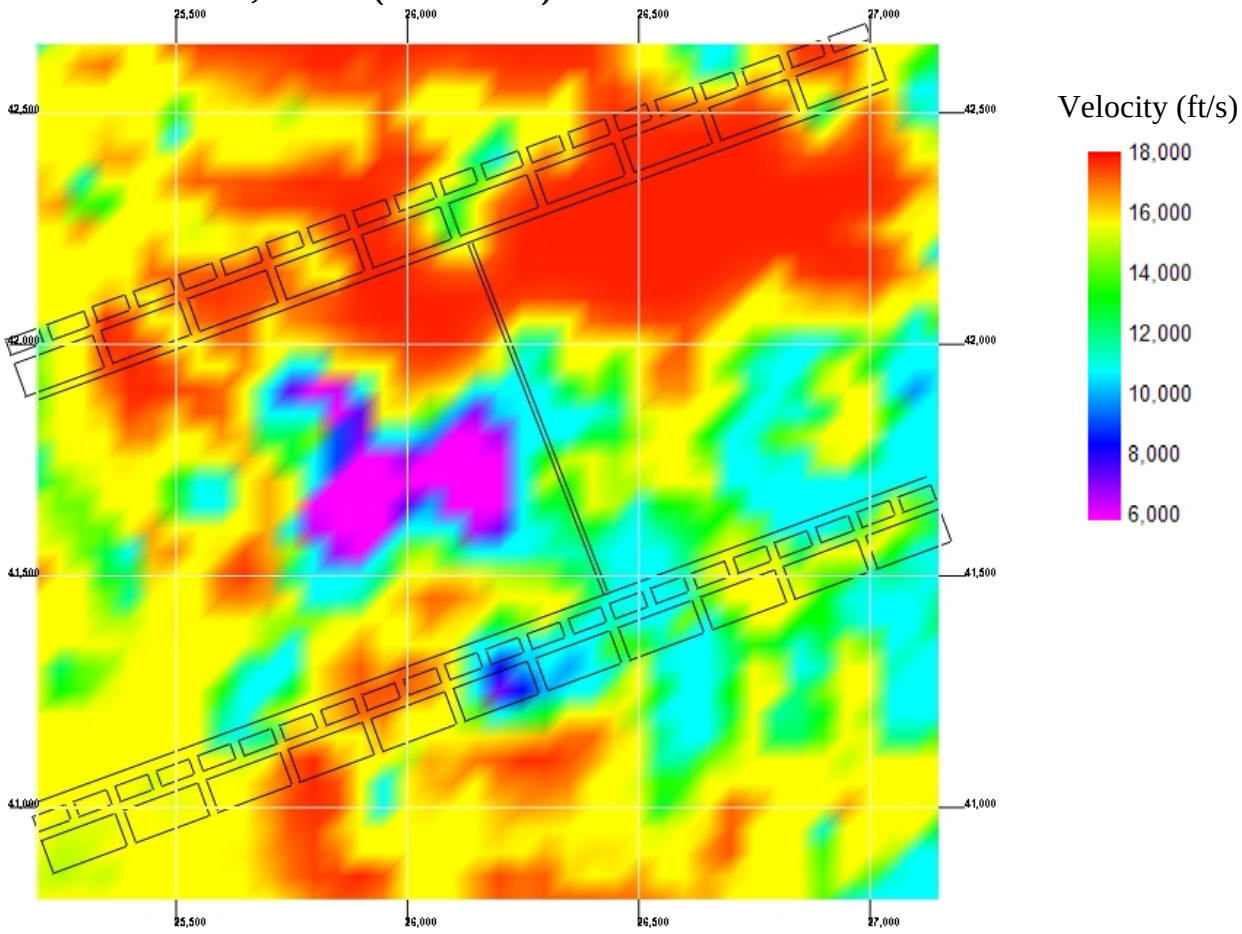

Figure B.15. Velocity tomogram at Z = 5,400 feet.

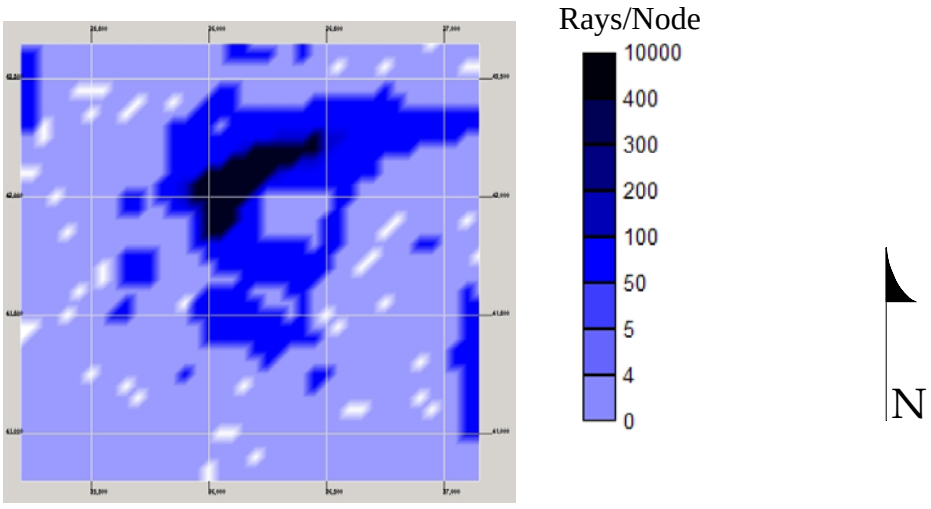

Figure B.16. Ray density plot at Z = 5,400 feet.

07-28-97

Plan View at Z = 5,400 feet (Floor Level)

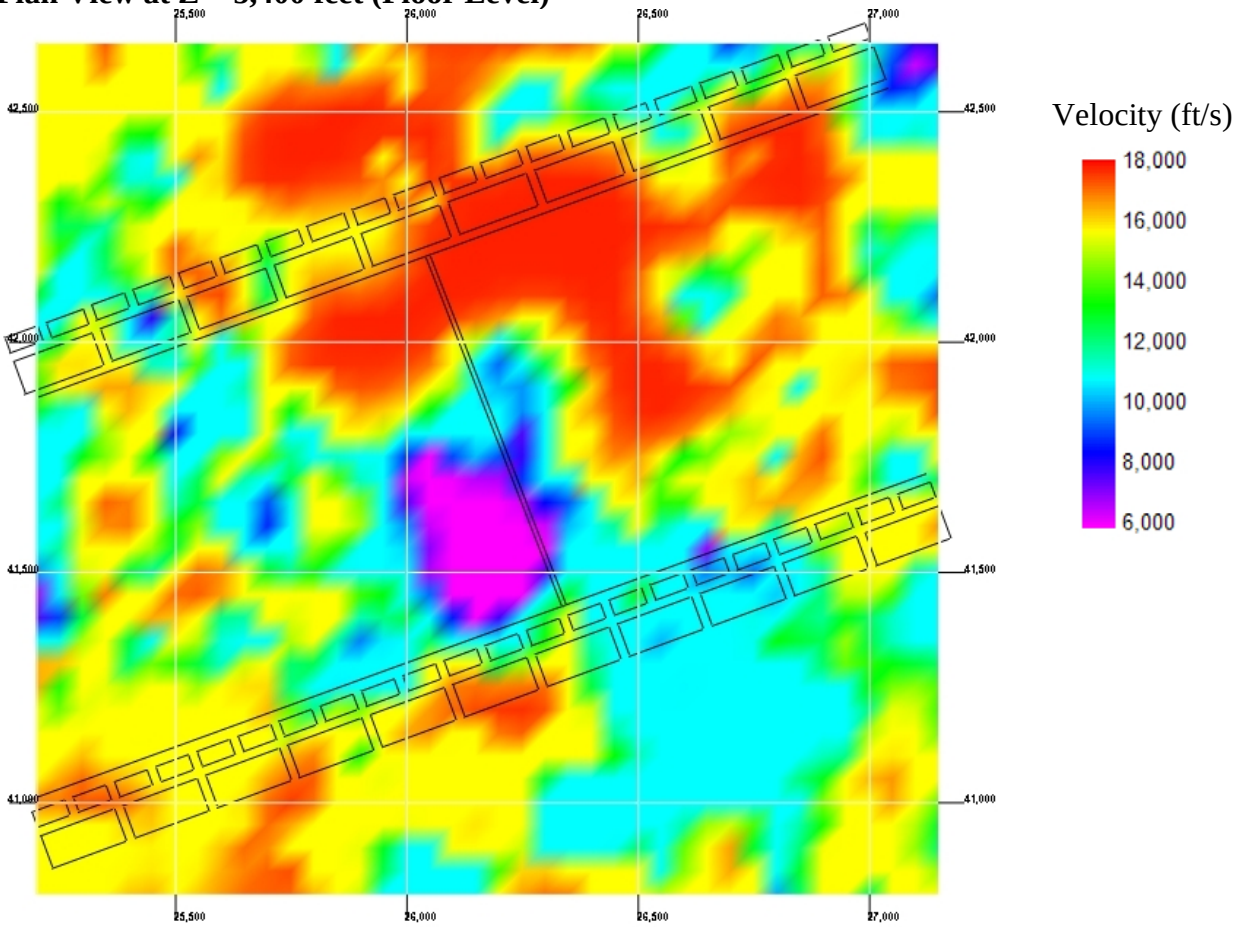

Figure B.17. Velocity tomogram at Z = 5,400 feet.

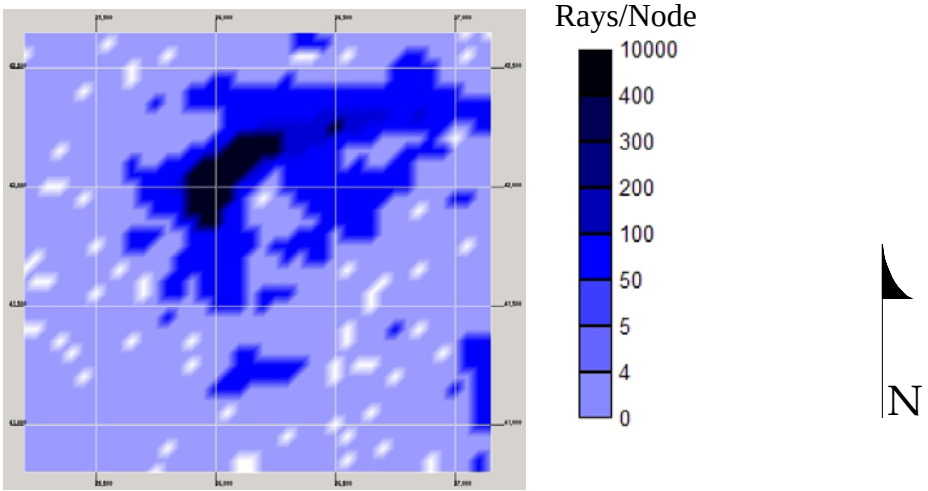

Figure B.18. Ray density plot at Z = 5,400 feet.

07-30-97

Plan View at Z = 5,400 feet (Floor Level)

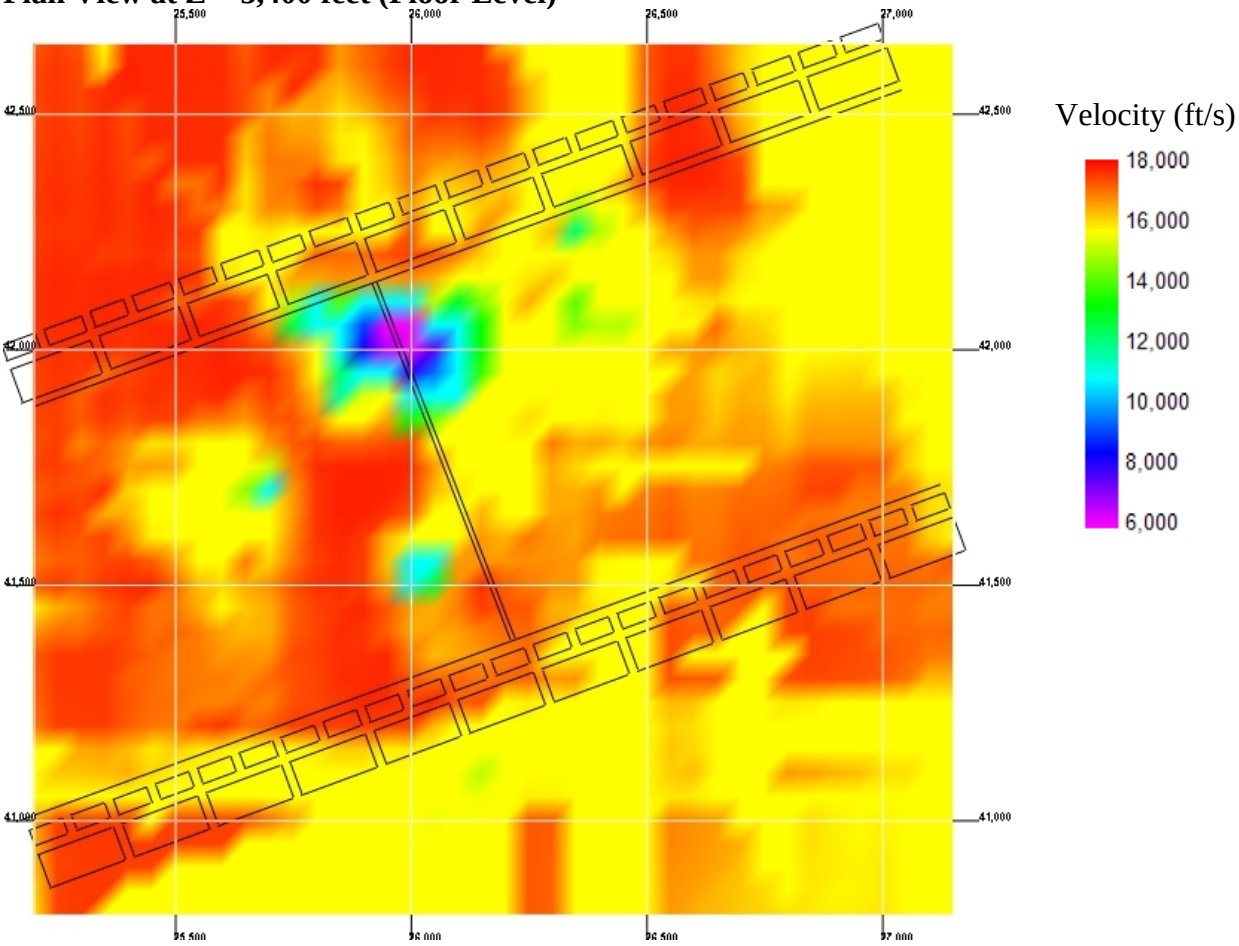

Figure B.19. Velocity tomogram at Z = 5,400 feet.

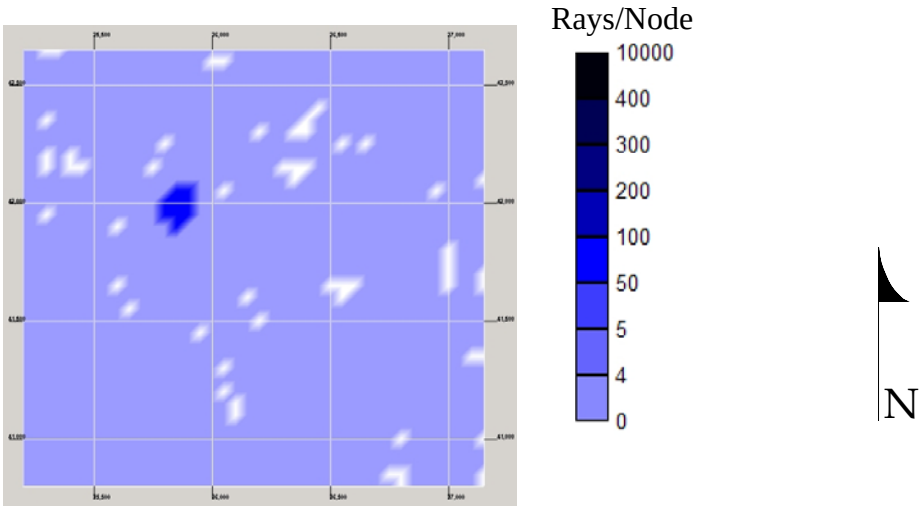

Figure B.20. Ray density plot at Z = 5,400 feet.

07-31-97
Plan View at Z = 5,400 feet (Floor Level)

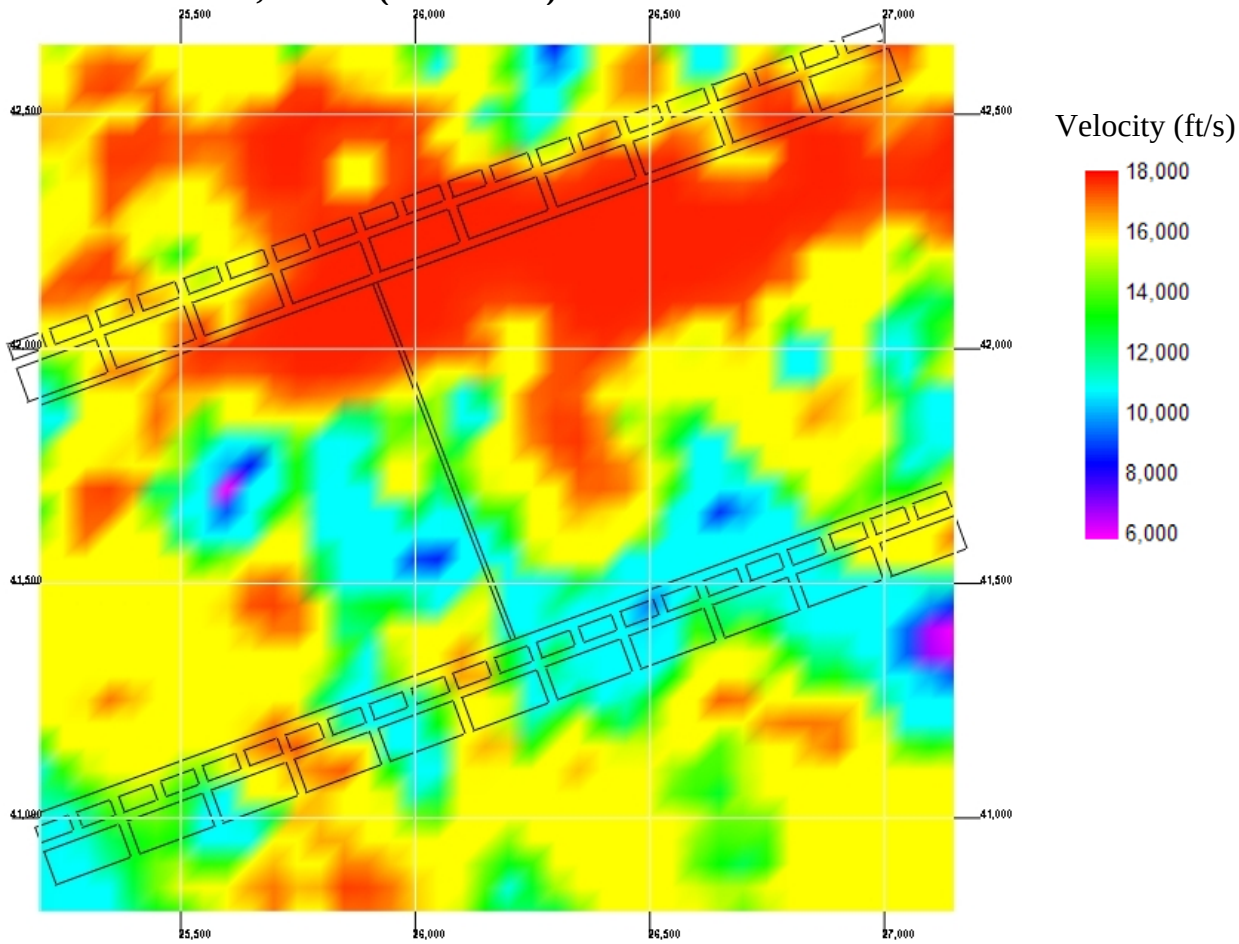

Figure B.21. Velocity tomogram at Z = 5,400 feet.

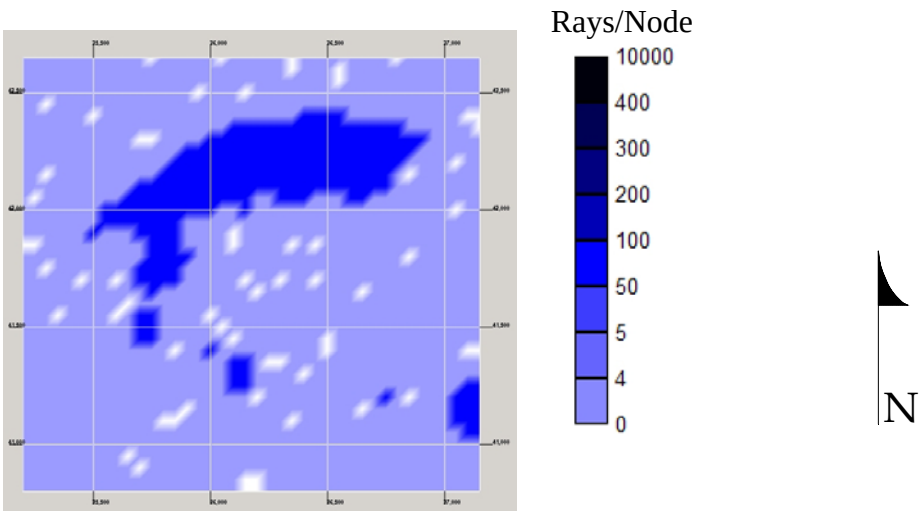

Figure B.22. Ray density plot at Z = 5,400 feet.

08-01-97

Plan View at Z = 5,400 feet (Floor Level)

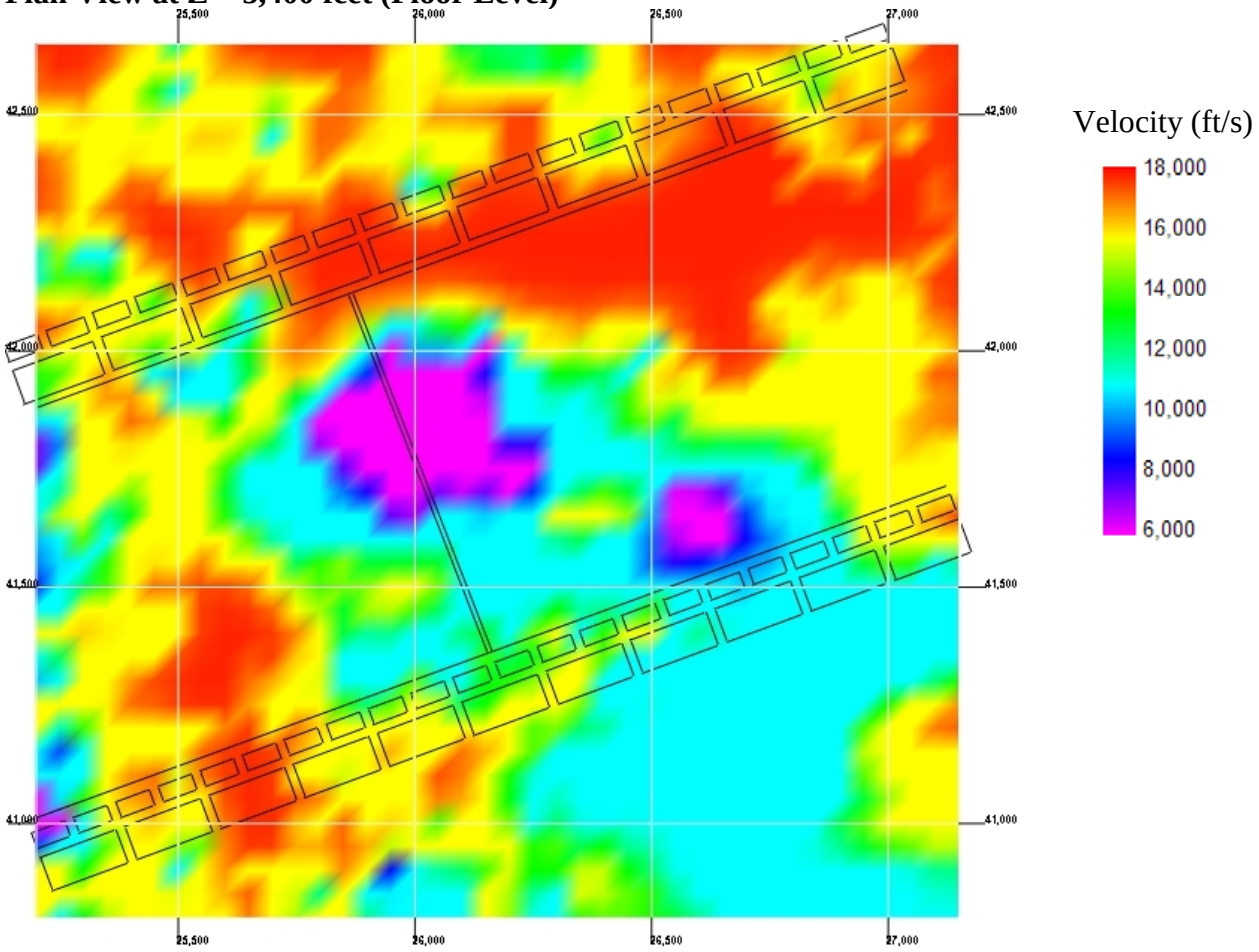

Figure B.23. Velocity tomogram at Z = 5,400 feet.

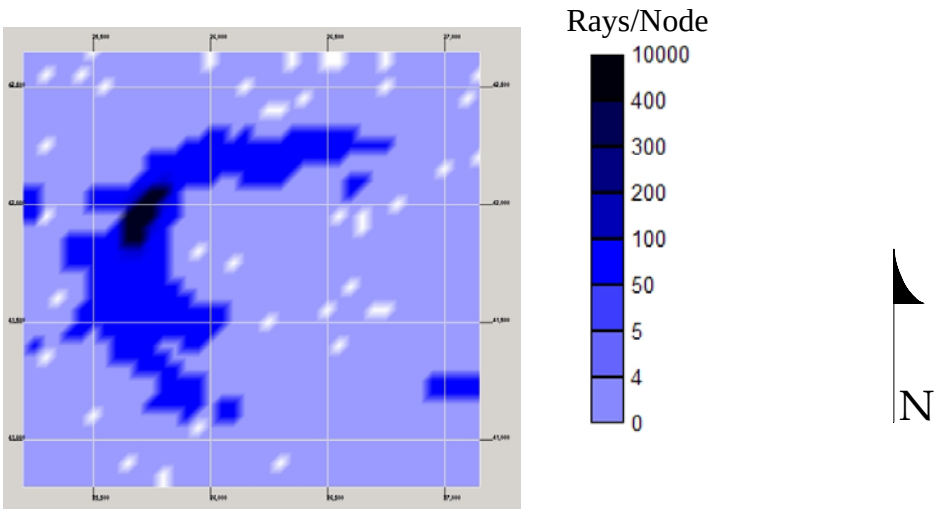

Figure B.24. Ray density plot at Z = 5,400 feet.

08-02-97

Plan View at Z = 5,400 feet (Floor Level)

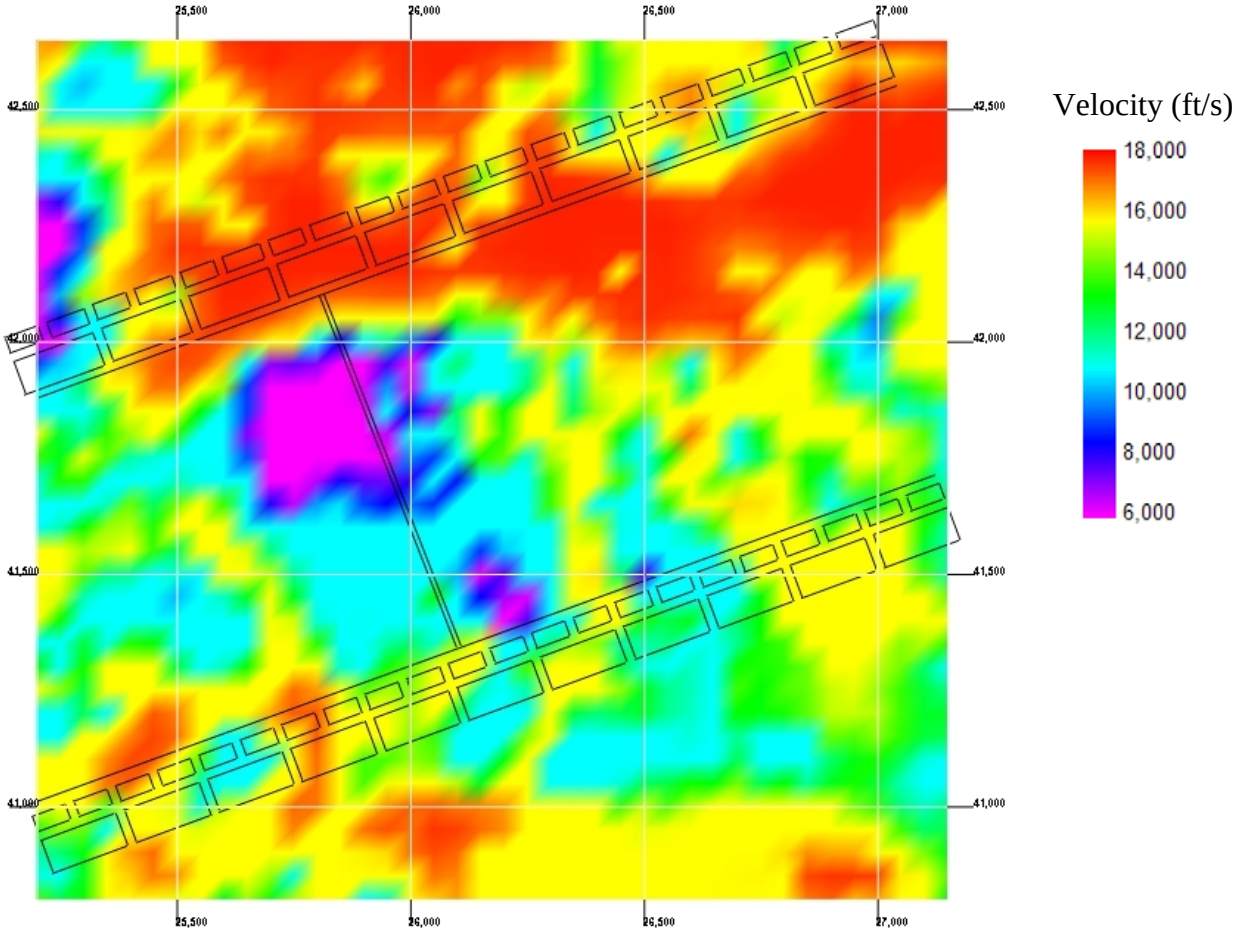

Figure B.25. Velocity tomogram at Z = 5,400 feet.

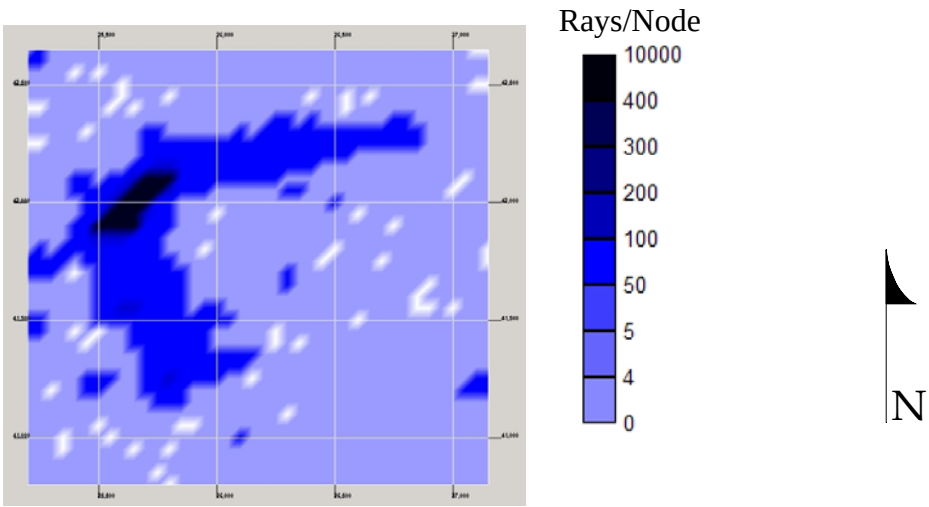

Figure B.26. Ray density plot at Z = 5,400 feet.

08-03-97

Plan View at Z = 5,400 feet (Floor Level)

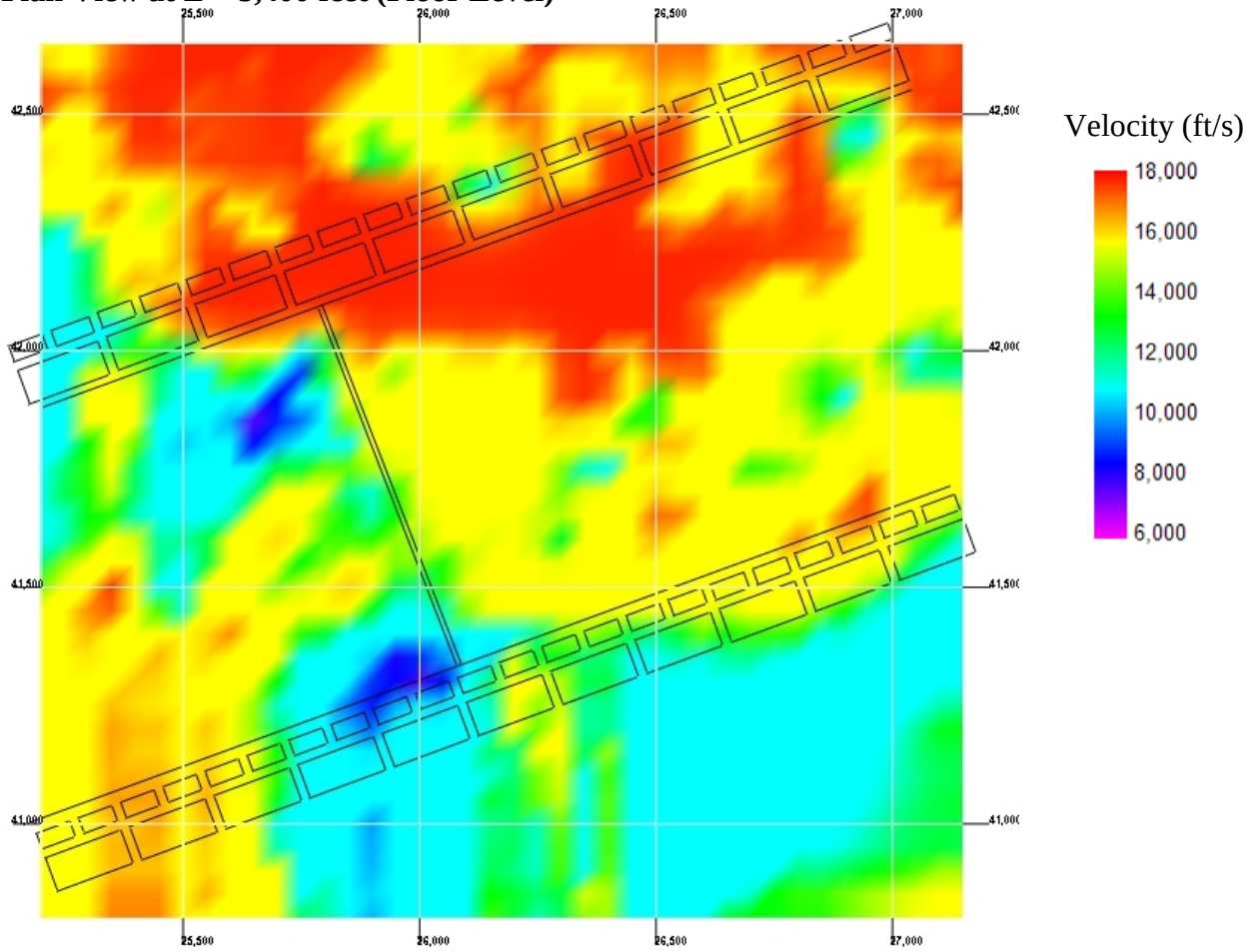

Figure B.27. Velocity tomogram at Z = 5,400 feet.

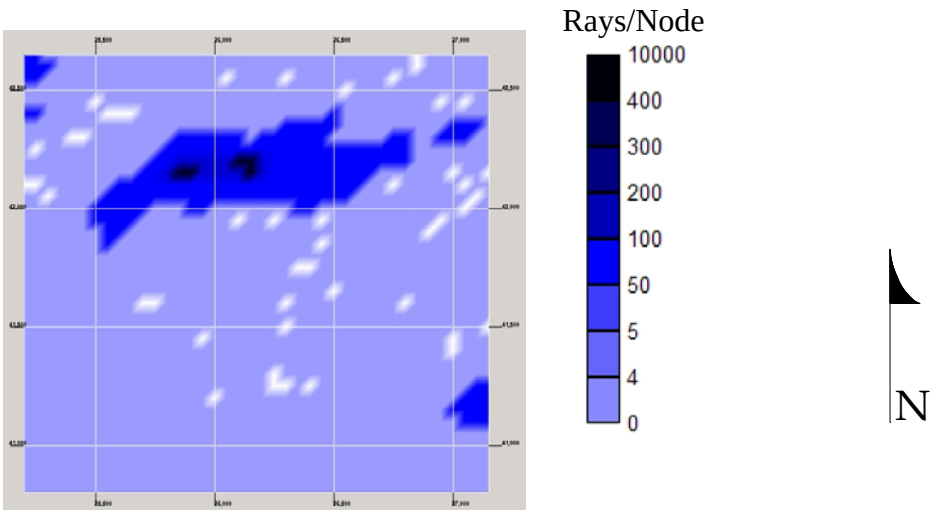

Figure B.28. Ray density plot at Z = 5,400 feet.

08-04-97

Plan View at Z = 5,400 feet (Floor Level)

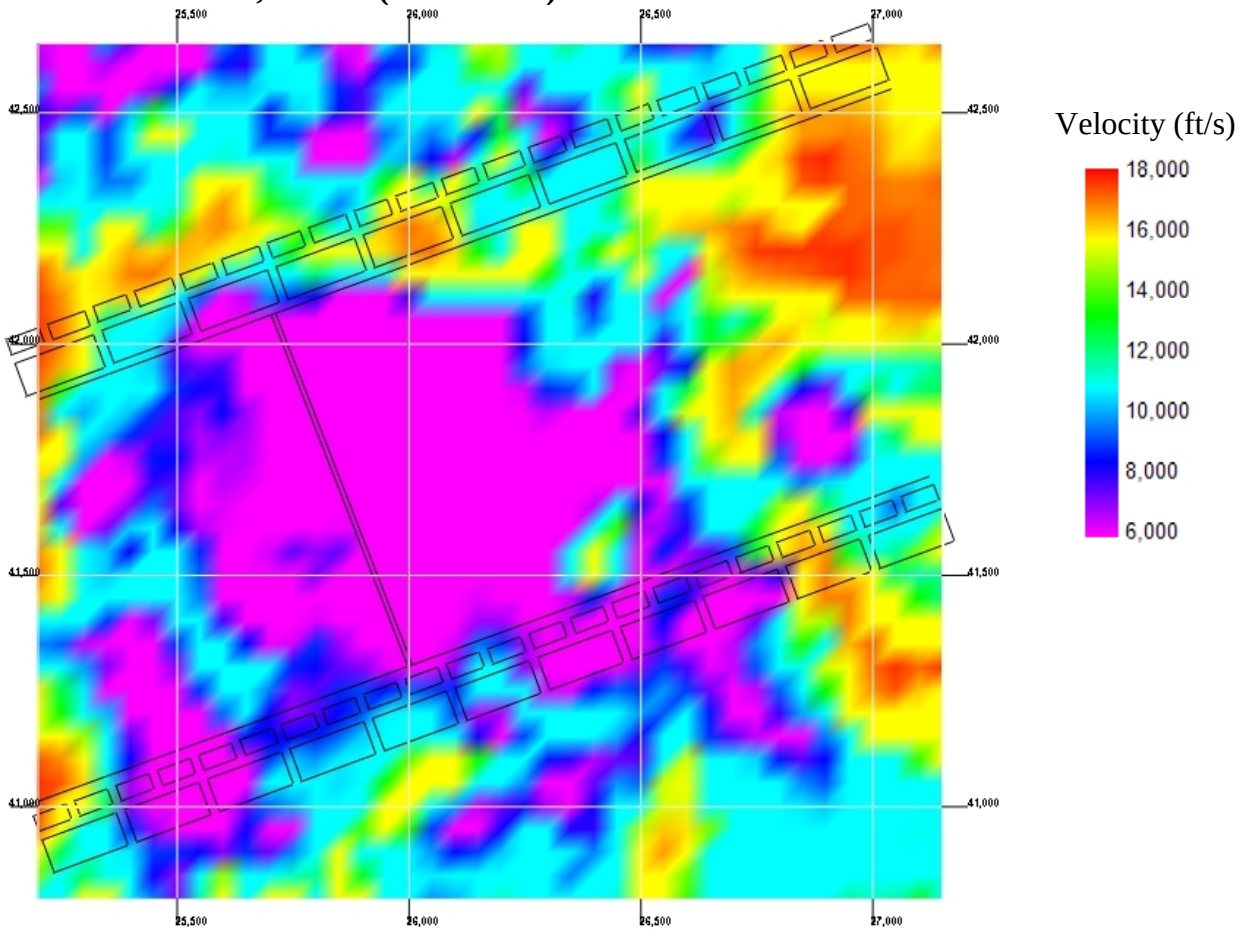

Figure B.29. Velocity tomogram at Z = 5,400 feet.

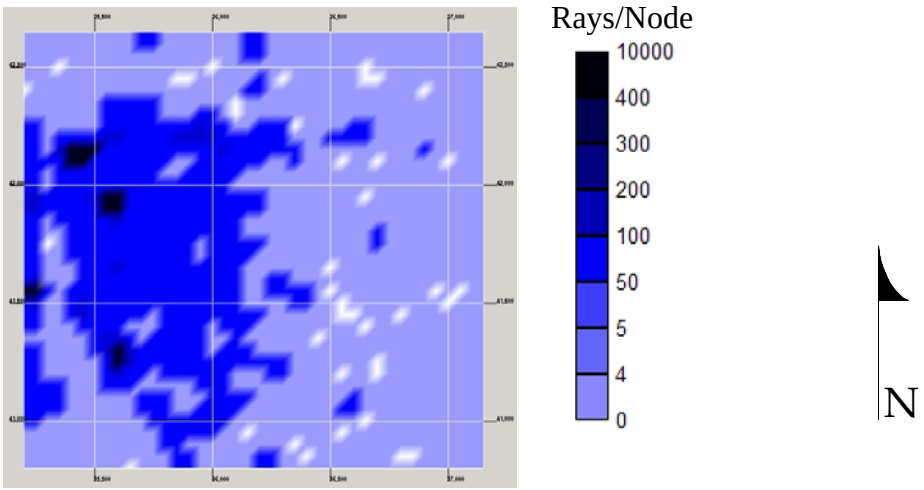

Figure B.30. Ray density plot at Z = 5,400 feet.

08-05-97

Plan View at Z = 5,400 feet (Floor Level)

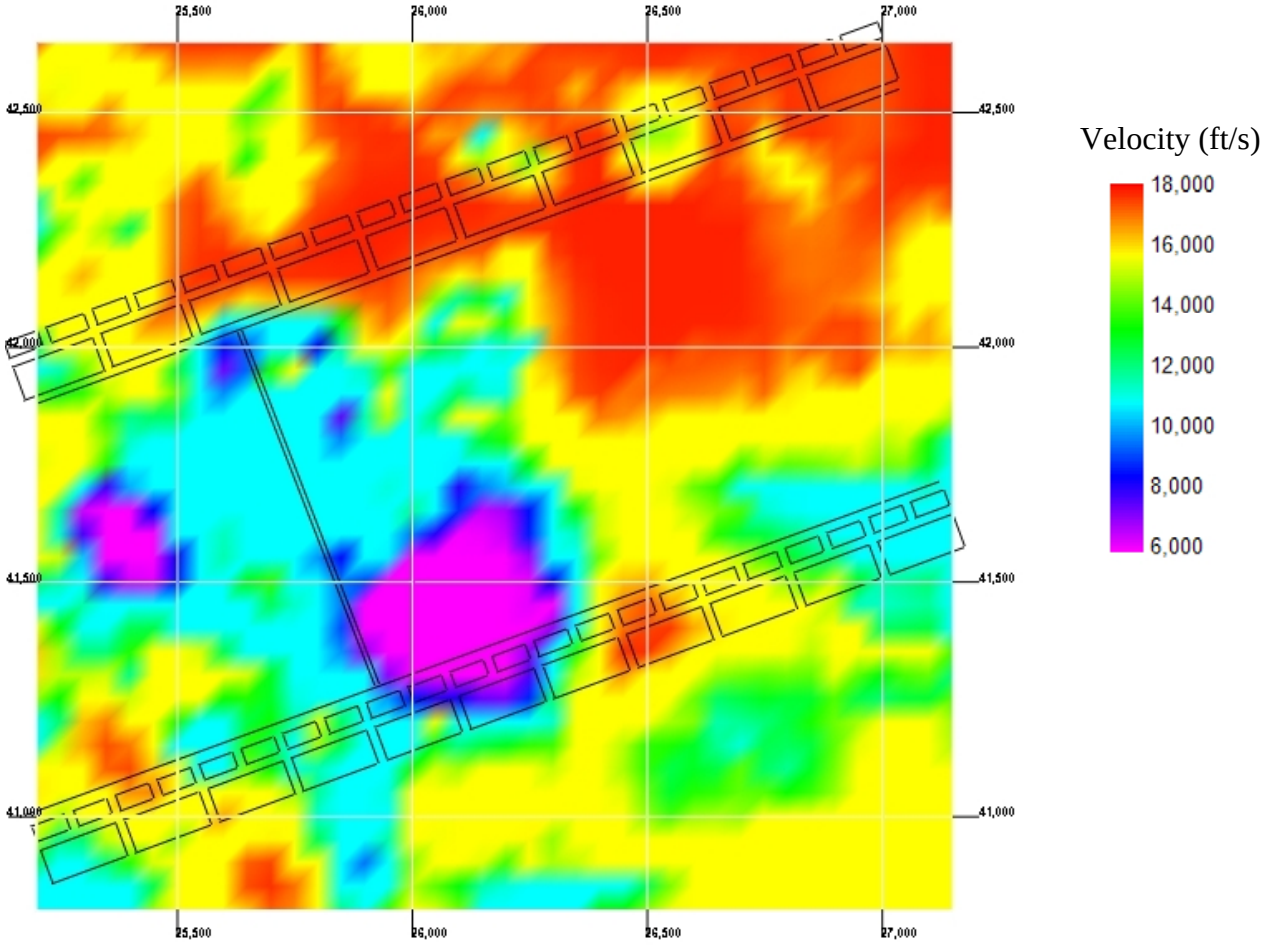

Figure B.31. Velocity tomogram at Z = 5,400 feet.

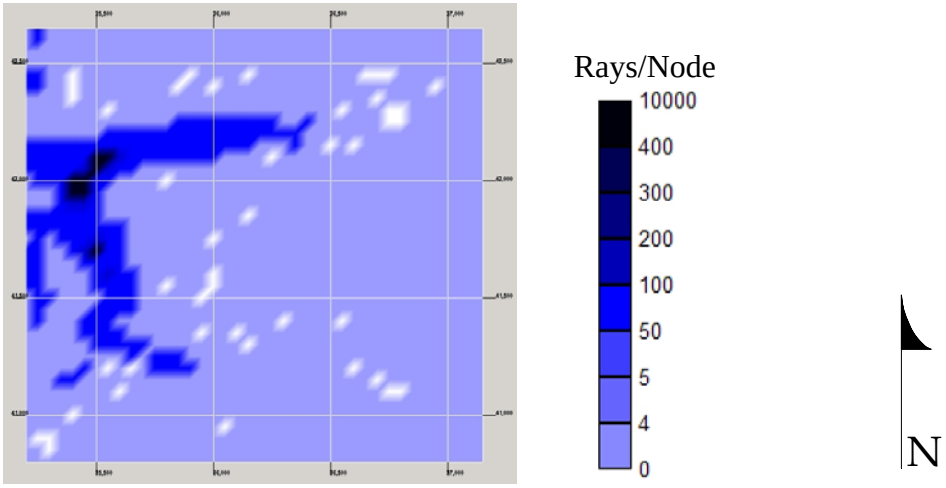

Figure B.32. Ray density plot at Z = 5,400 feet.

08-06-97

Plan View at Z = 5,400 feet (Floor Level)

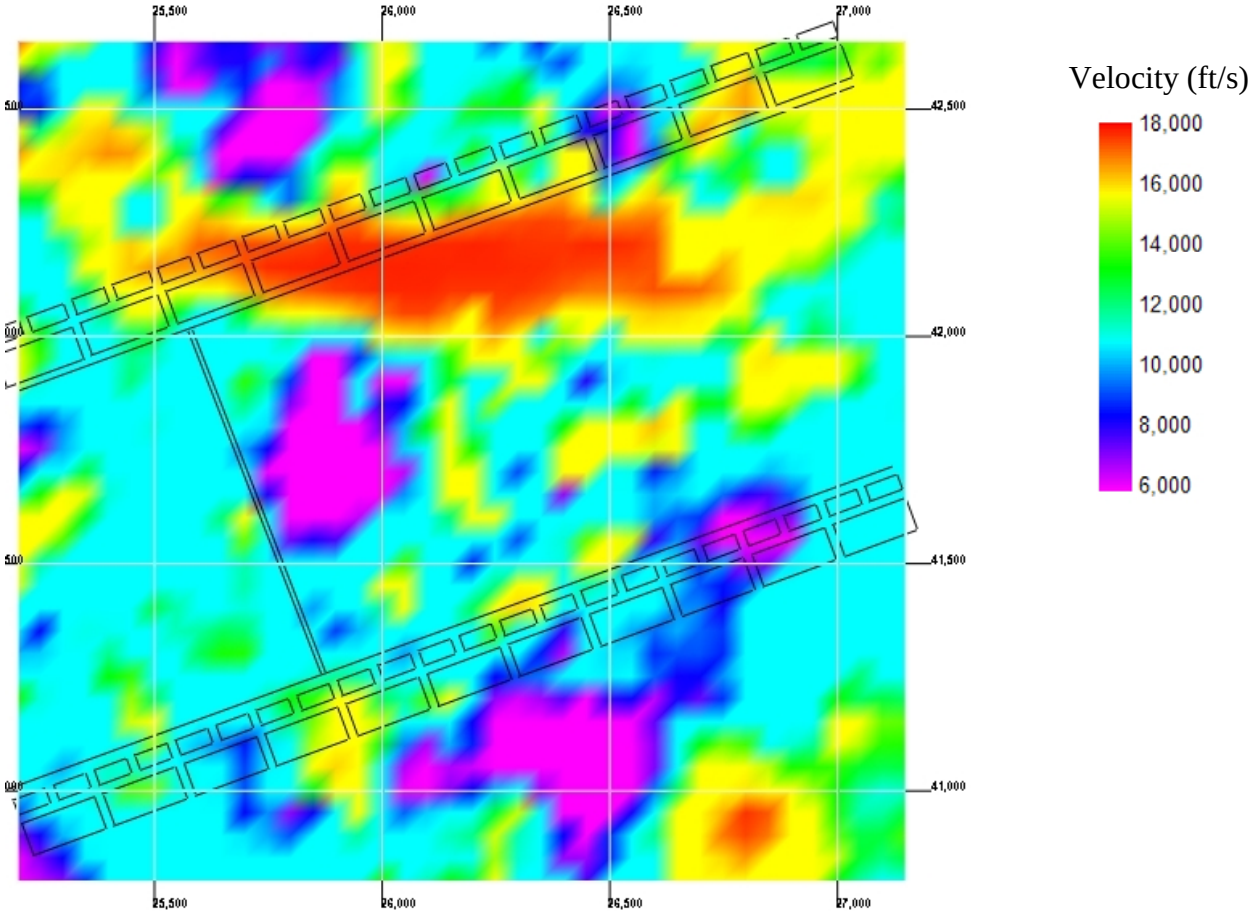

Figure B.33. Velocity tomogram at Z = 5,400 feet.

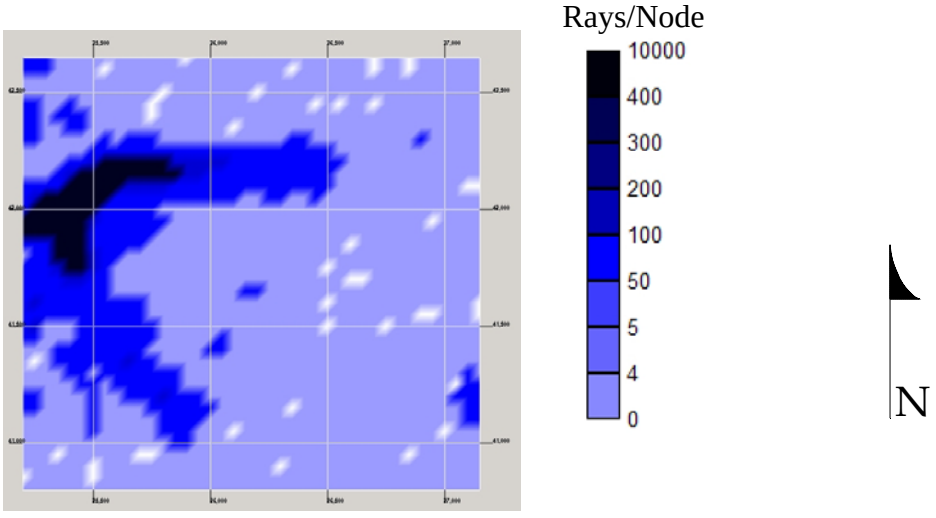

Figure B.34. Ray density plot at Z = 5,400 feet.

08-07-97

Plan View at Z = 5,400 feet (Floor Level)

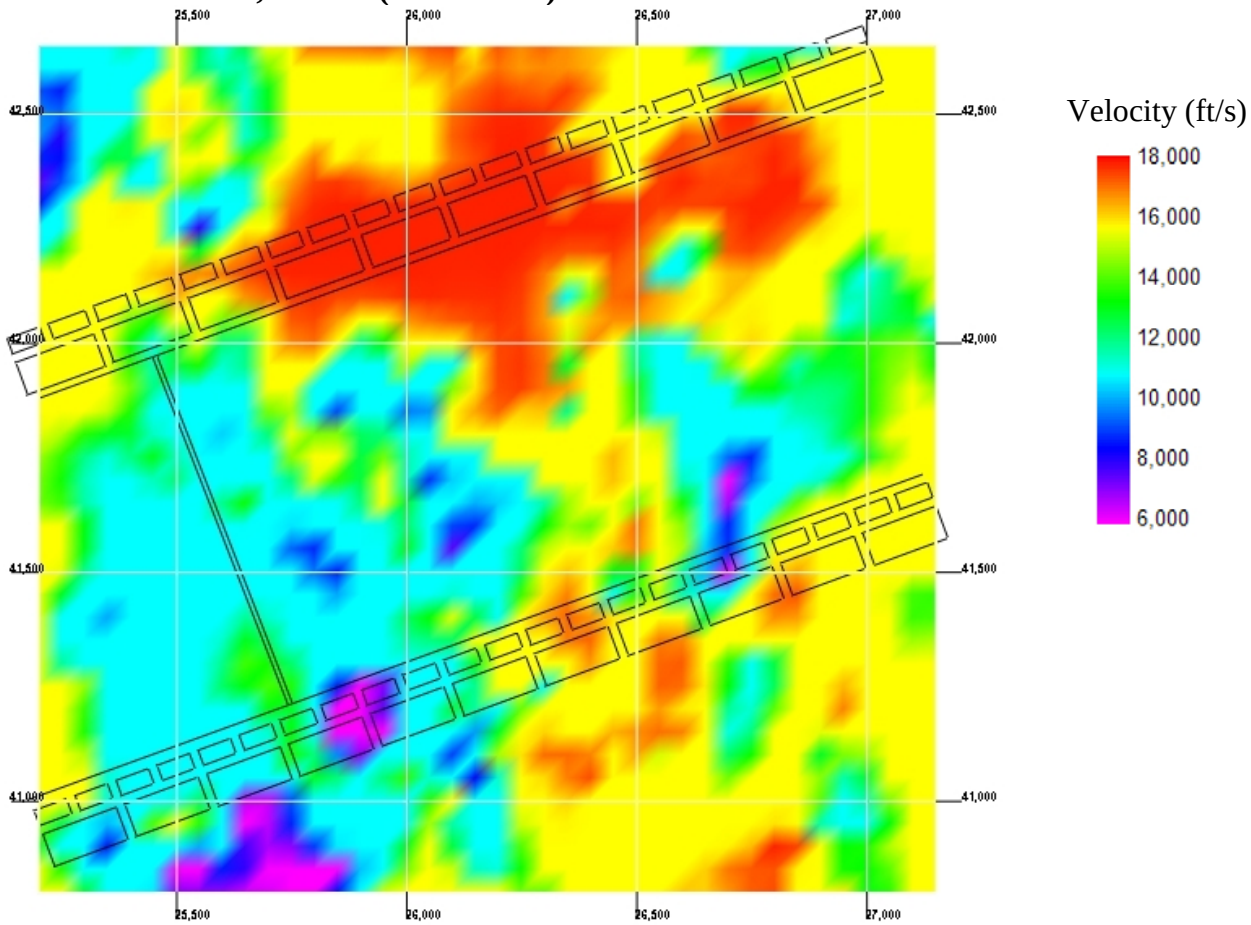

Figure B.35. Velocity tomogram at Z = 5,400 feet.

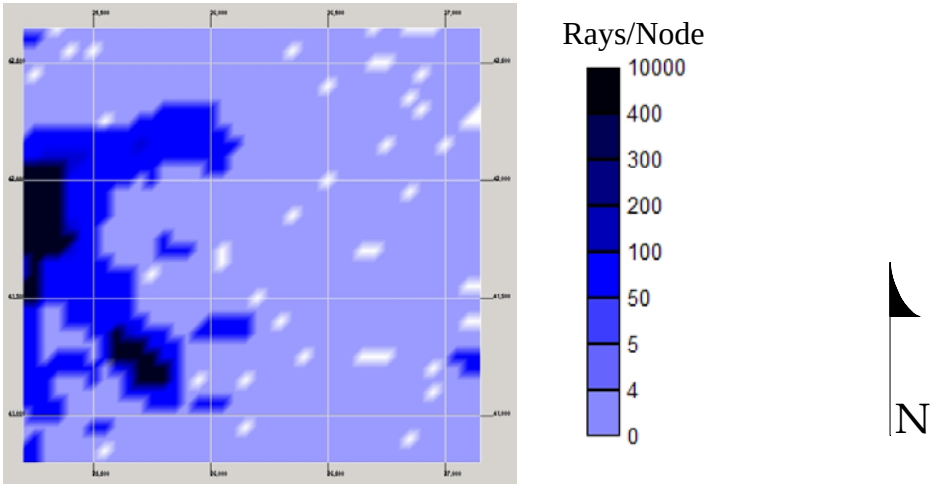

Figure B.36. Ray density plot at Z = 5,400 feet.

APPENDIX C

Velocity Tomograms & Ray Density Plots

SEAM LEVEL
Z = 5, 550 FEET

07-20-97

Plan View at Z = 5,550 feet (Seam Level)

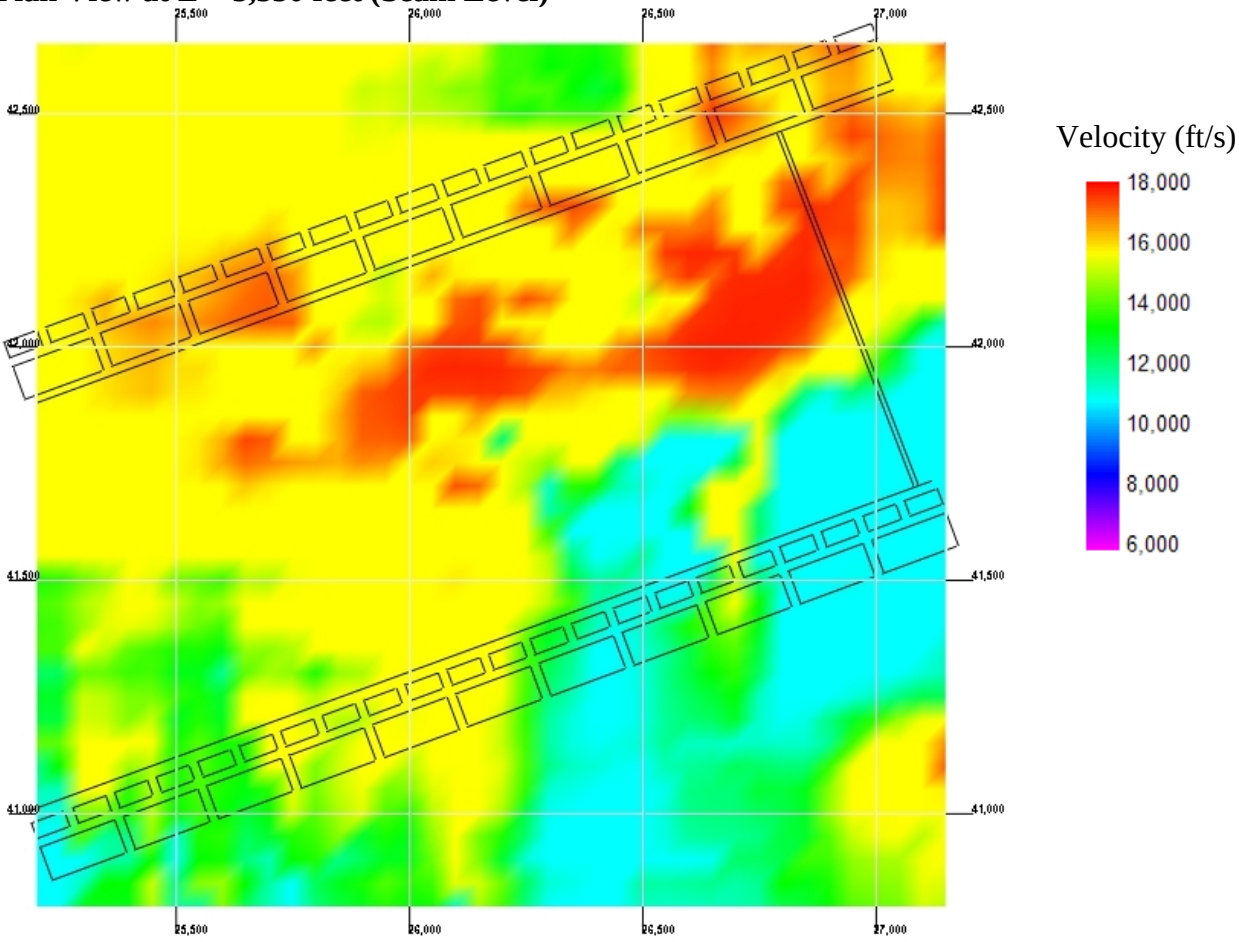

Figure C.1. Velocity tomogram at Z = 5,550 feet.

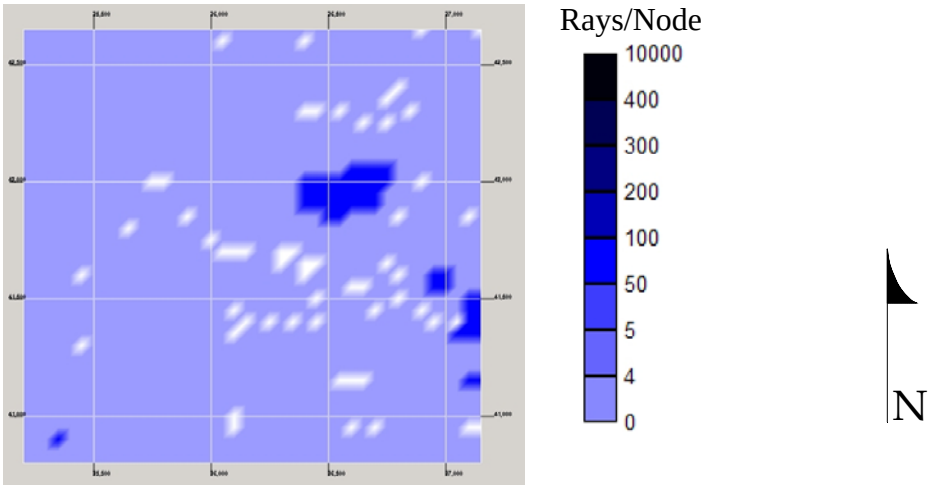

Figure C.2. Ray density plot at Z = 5,550 feet.

07-21-97
Plan View at Z = 5,550 feet (Seam Level)

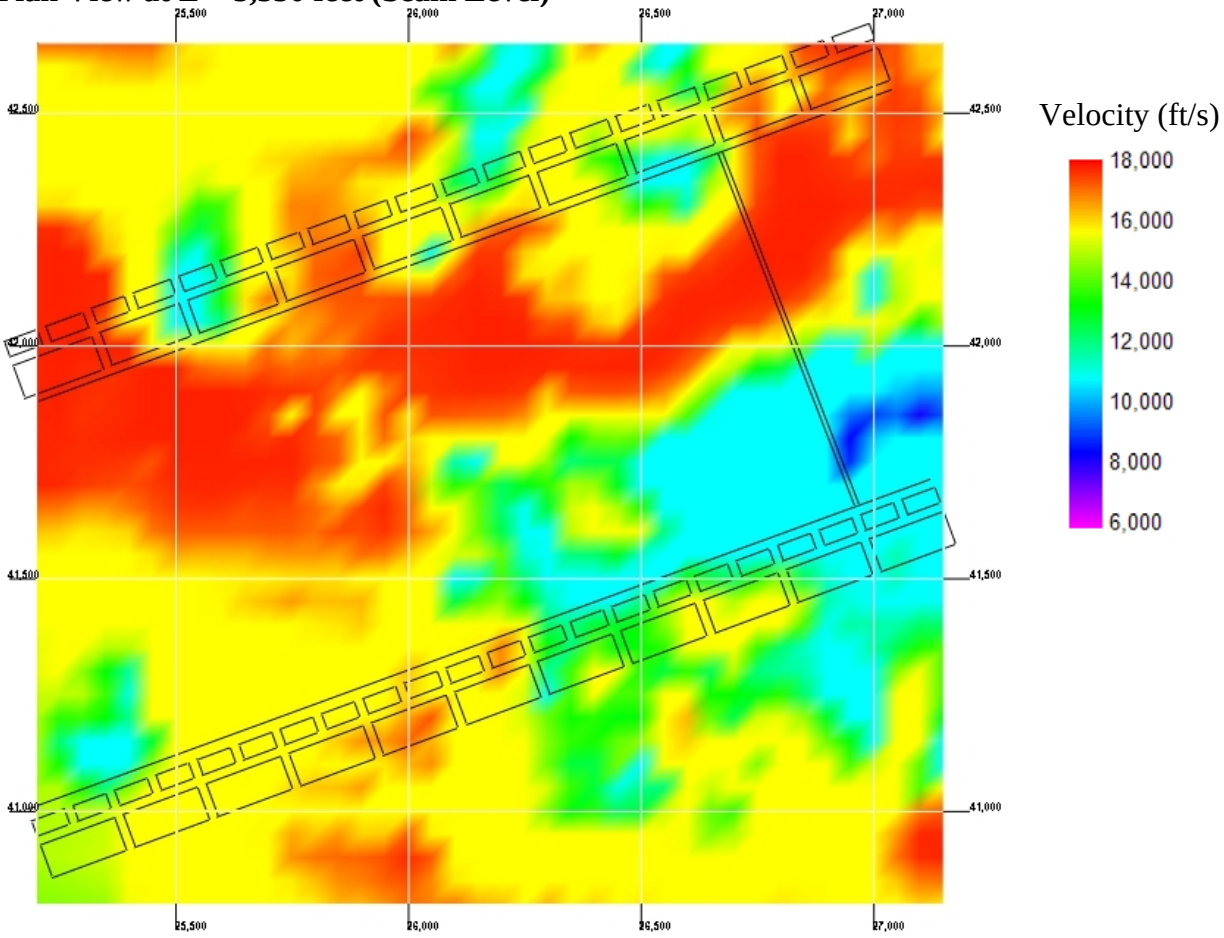

Figure C.3. Velocity tomogram at Z = 5,550 feet.

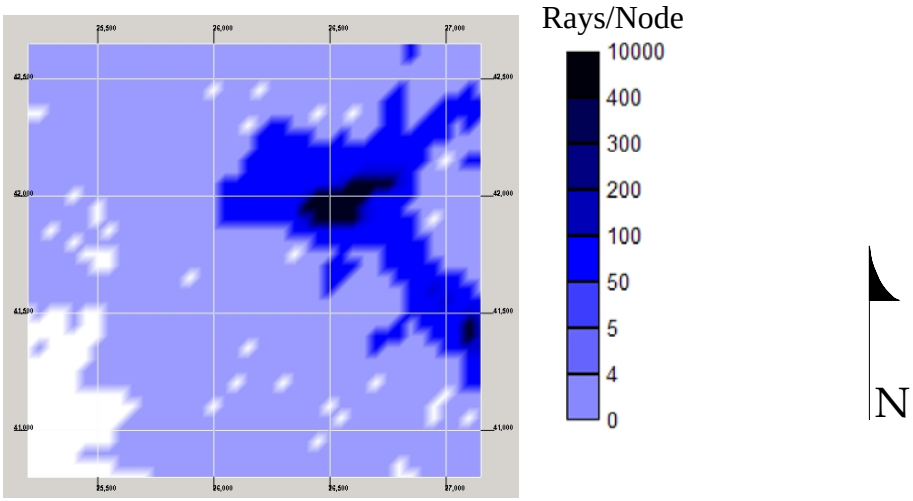

Figure C.4. Ray density plot at Z = 5,550 feet.

07-22-97

Plan View at Z = 5,550 feet (Seam Level)

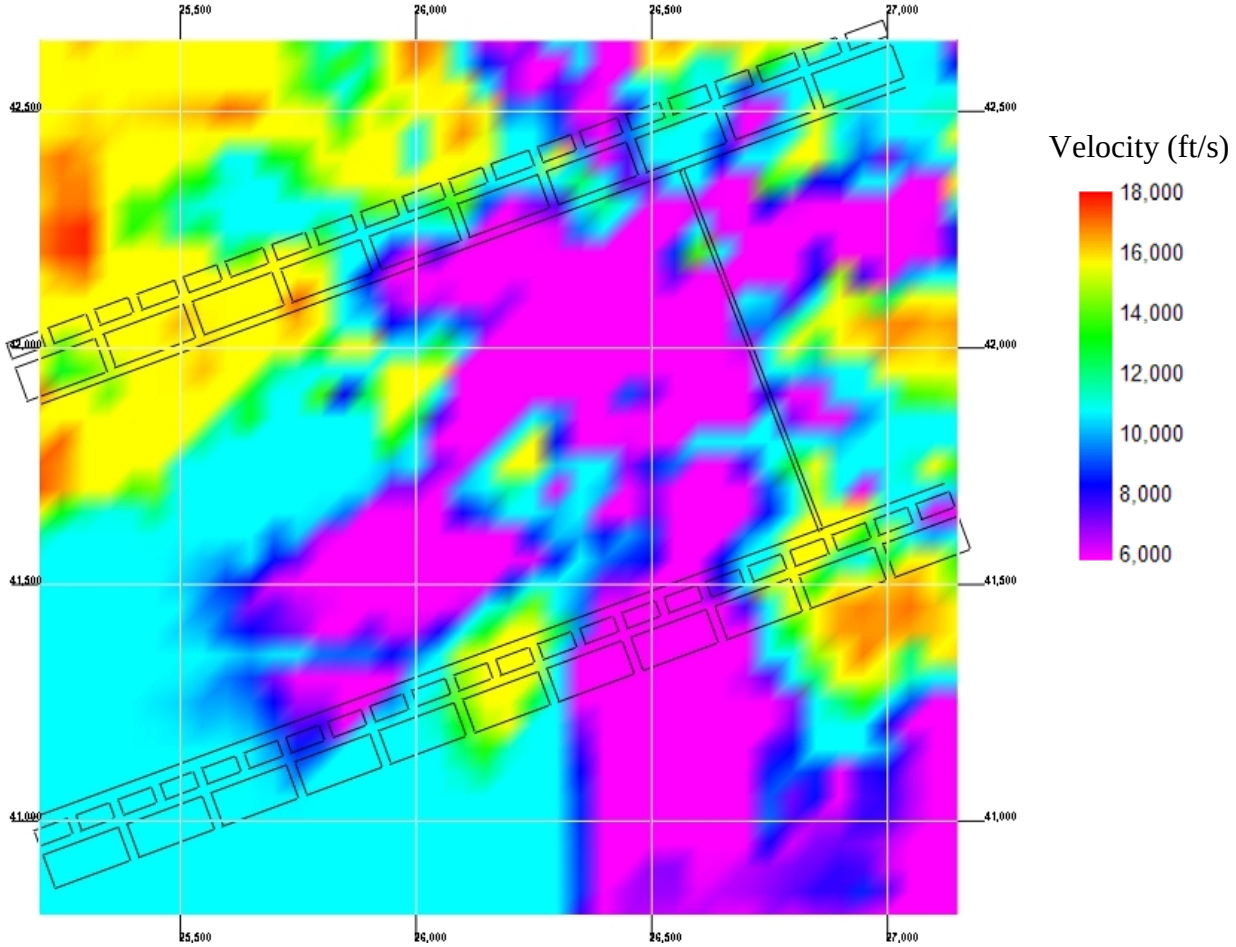

Figure C.5. Velocity tomogram at Z = 5,550 feet.

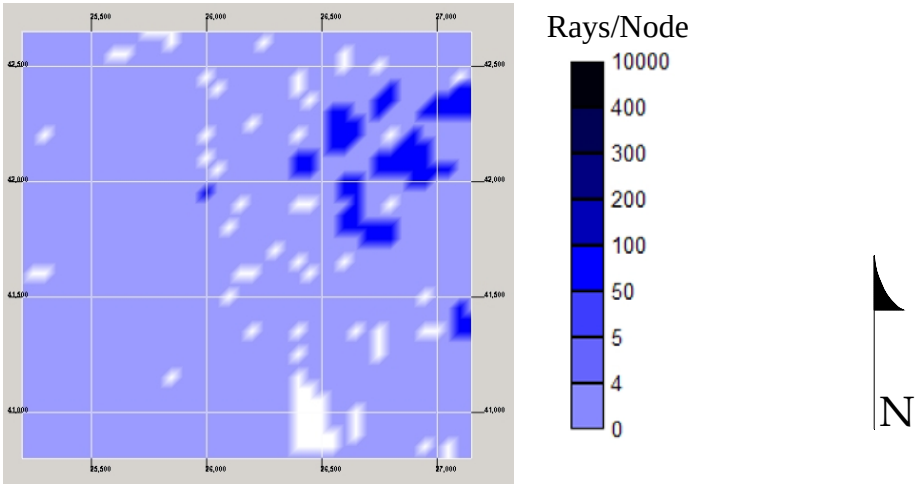

Figure C.6. Ray density plot at Z = 5,550 feet.

07-23-97
Plan View at Z = 5,550 feet (Seam Level)

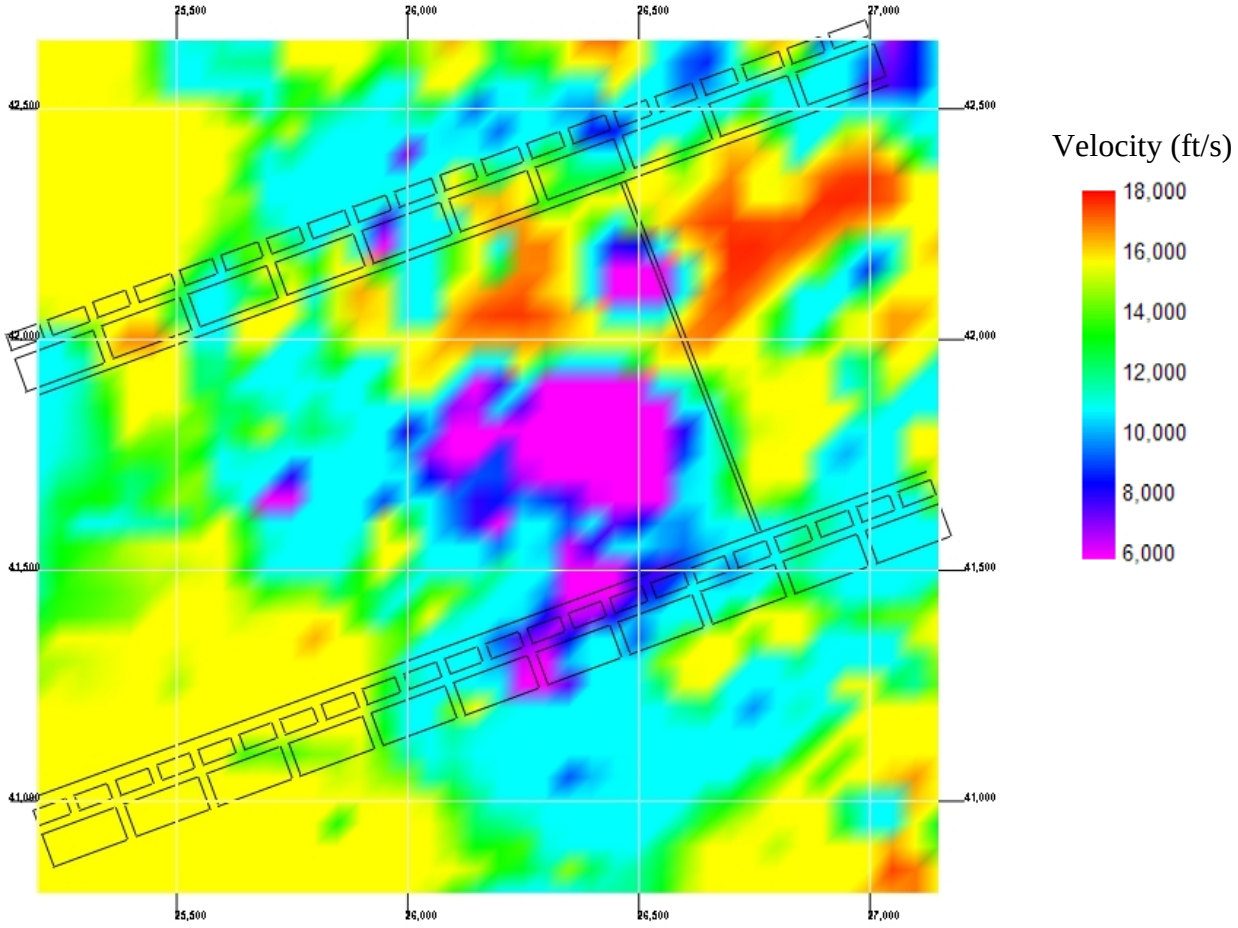

Figure C.7. Velocity tomogram at Z = 5,550 feet.

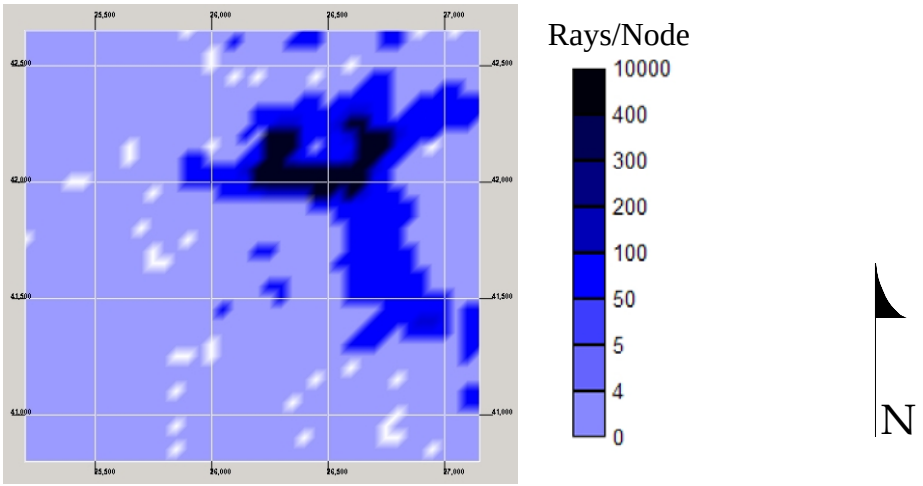

Figure C.8. Ray density plot at Z = 5,550 feet.

07-24-97
Plan View at Z = 5,550 feet (Seam Level)

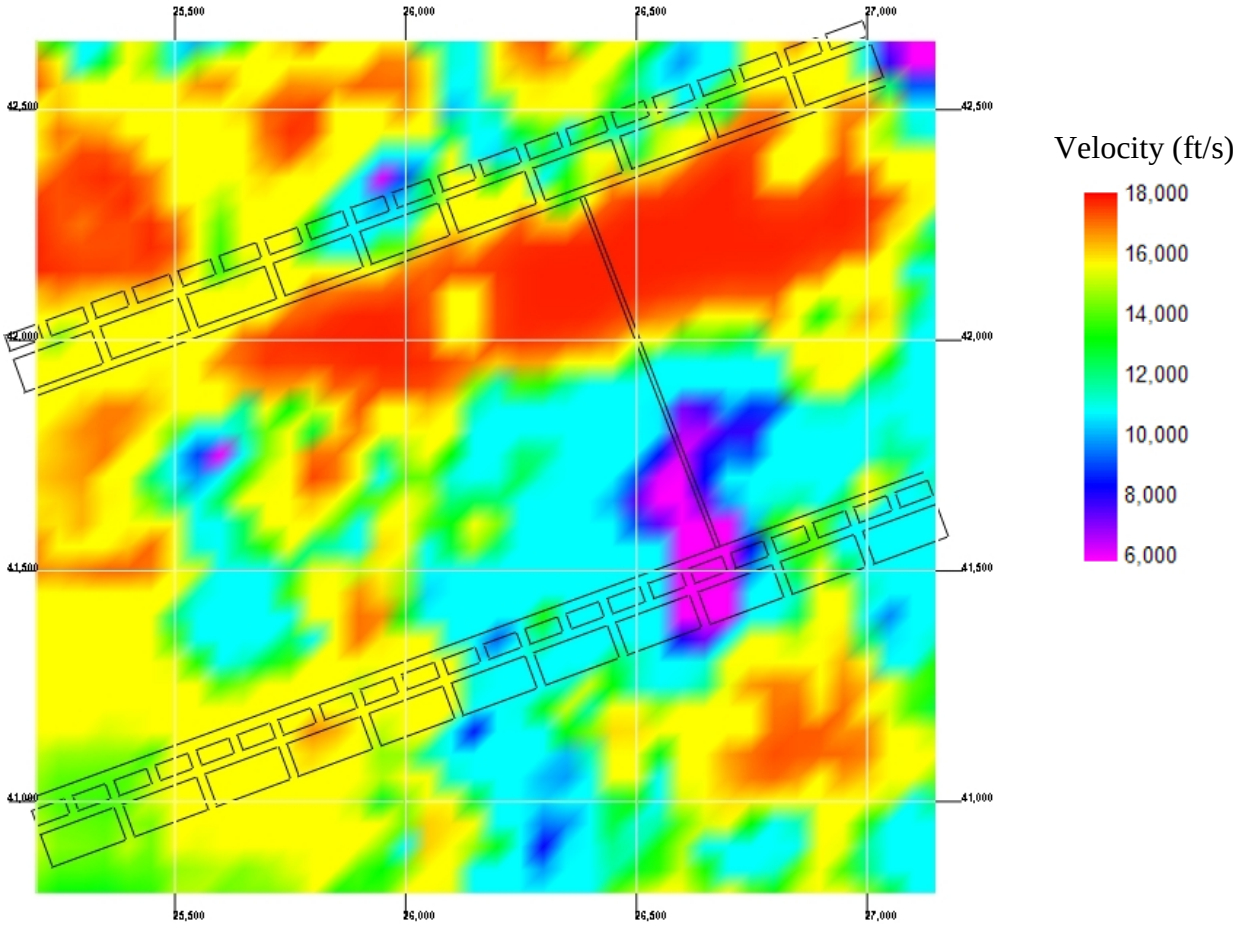

Figure C.9. Velocity tomogram at Z = 5,550 feet.

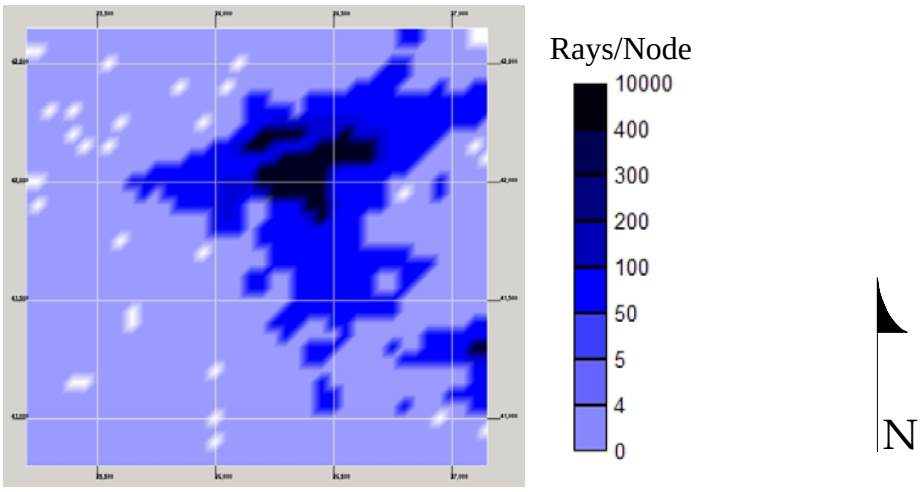

Figure C.10. Ray density plot at Z = 5,550 feet.

07-25-97

Plan View at Z = 5,550 feet (Seam Level)

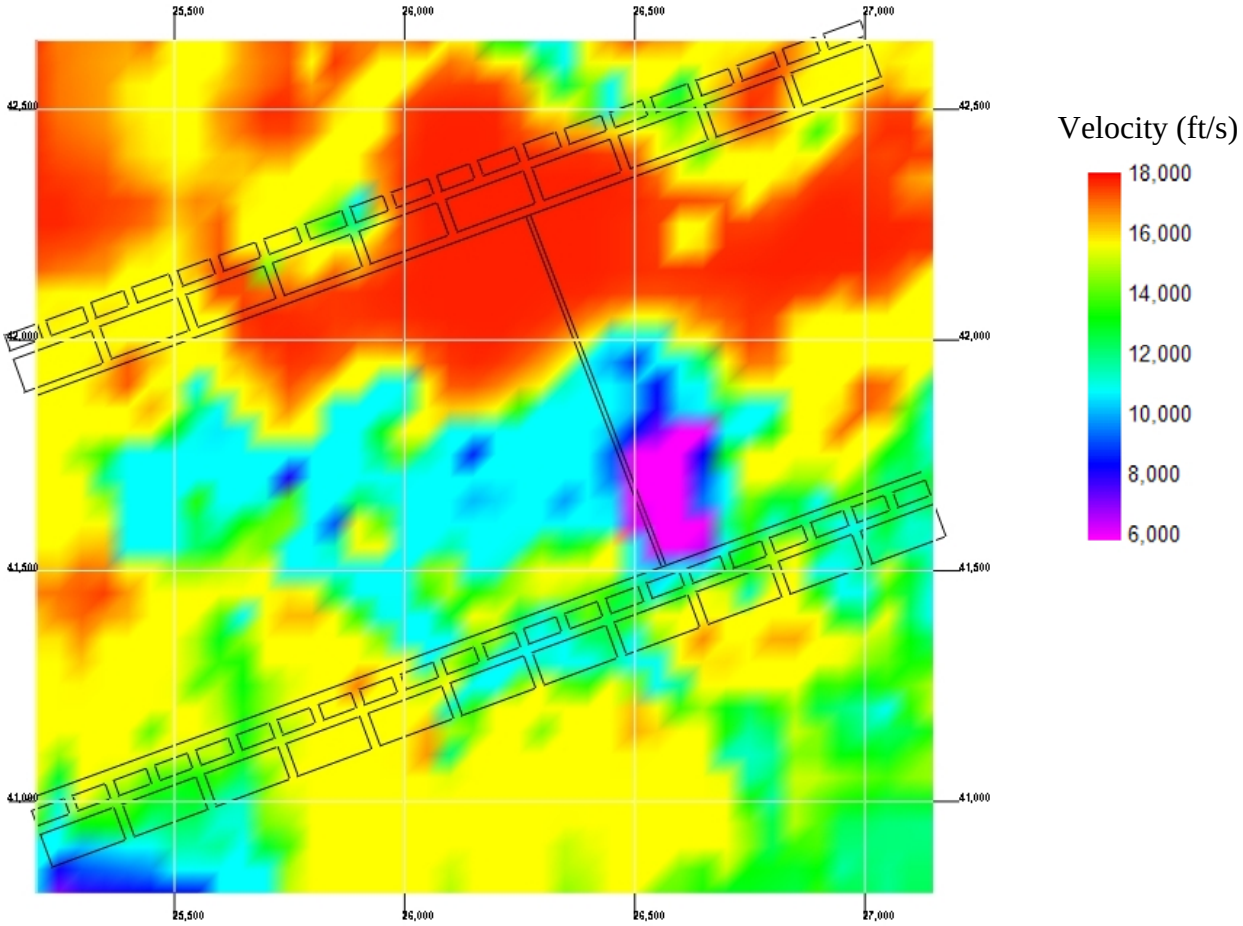

Figure C.11. Velocity tomogram at Z = 5,550 feet.

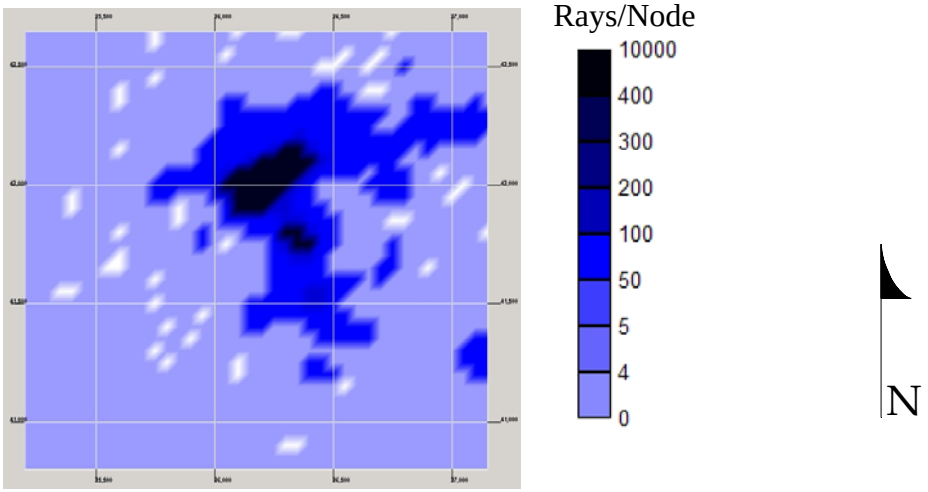

Figure C.12. Ray density plot at Z = 5,550 feet.

07-26-97
Plan View at Z = 5,550 feet (Seam Level)

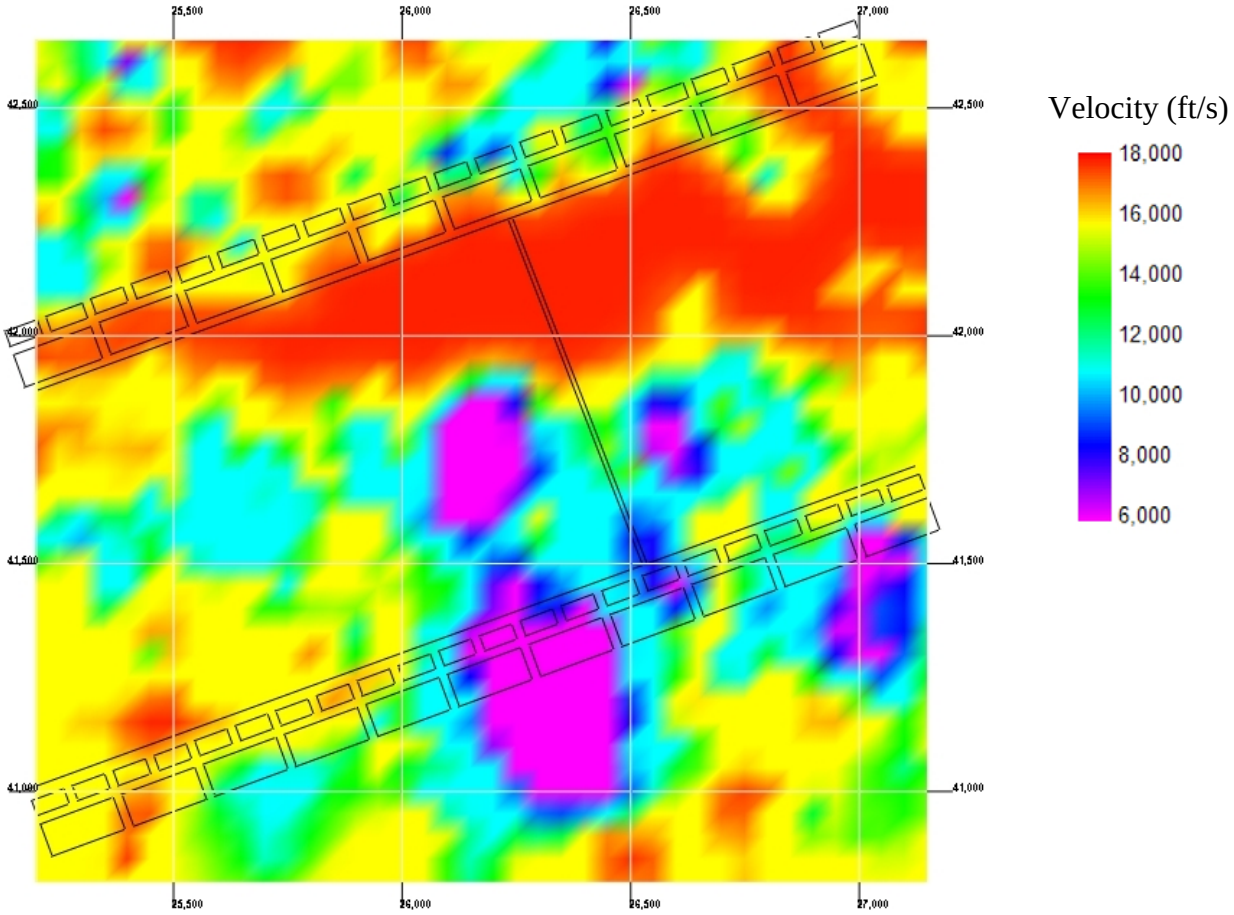

Figure C.13. Velocity tomogram at Z = 5,550 feet.

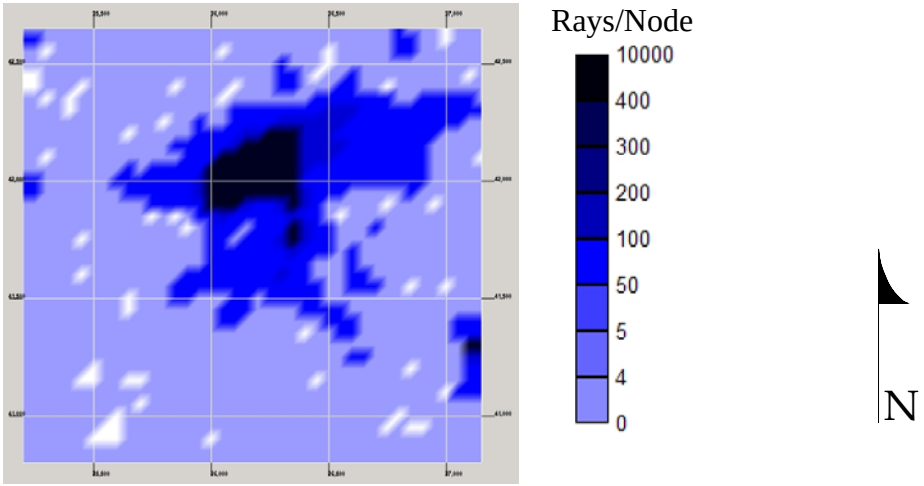

Figure C.14. Ray density plot at Z = 5,550 feet.

07-27-97
Plan View at Z = 5,550 feet (Seam Level)

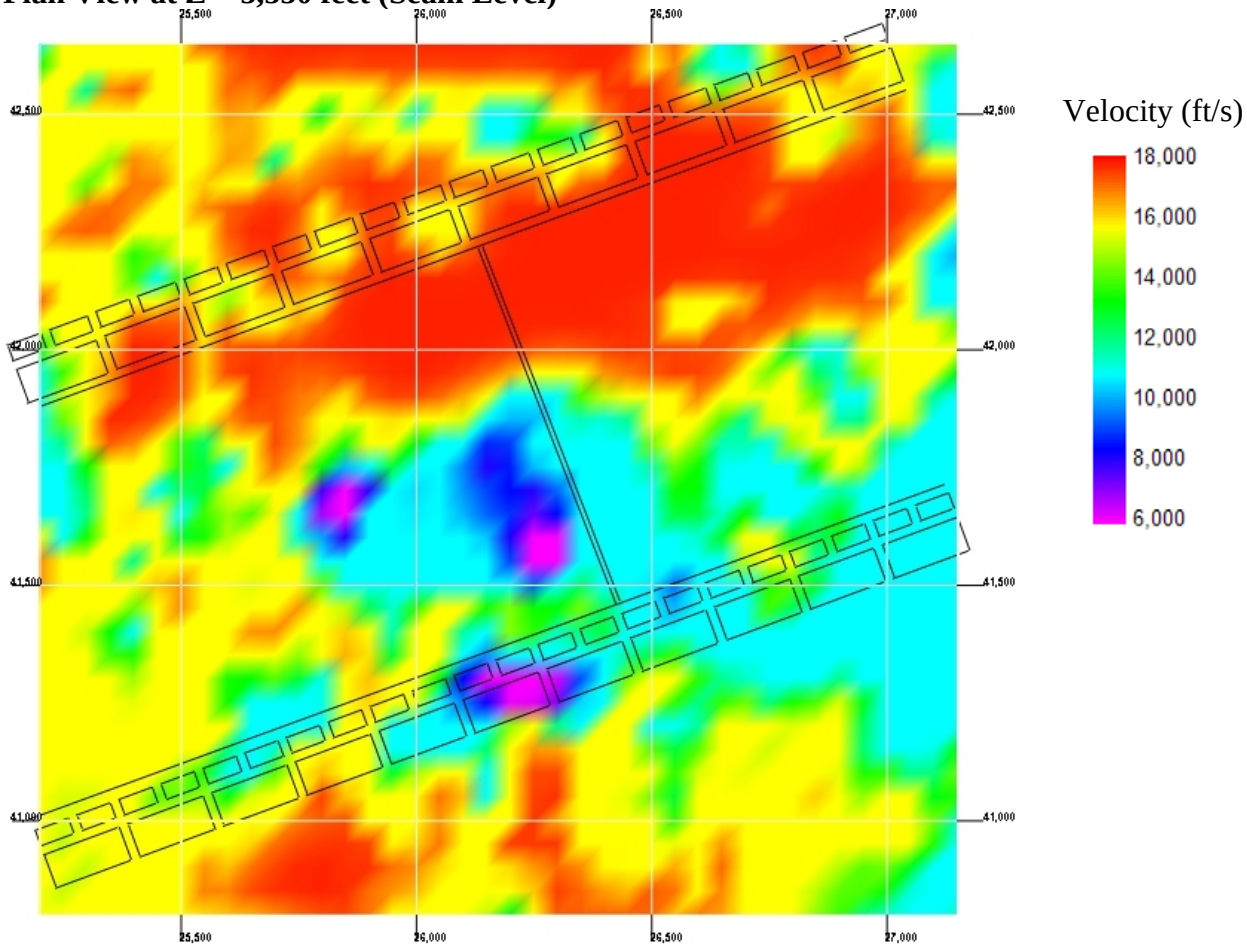

Figure C.15. Velocity tomogram at Z = 5,550 feet.

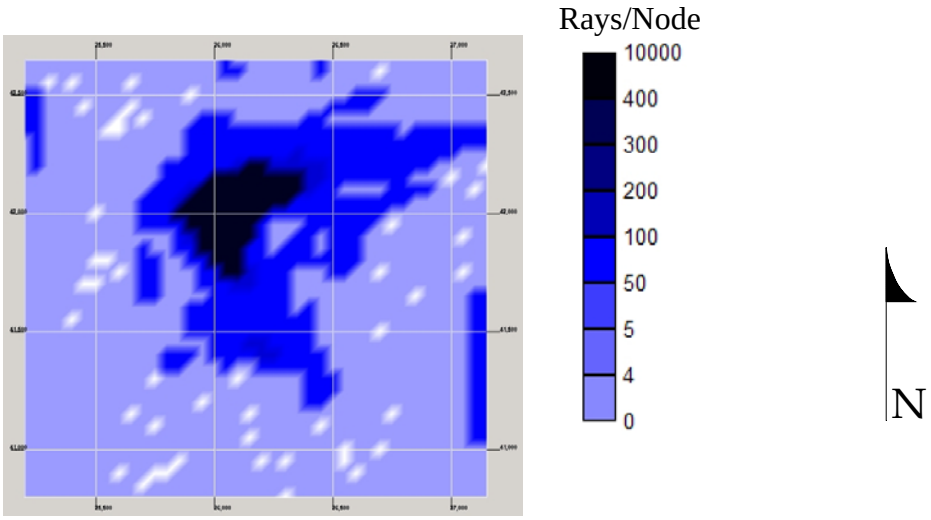

Figure C.16. Ray density plot at Z = 5,550 feet.

07-28-97
Plan View at Z = 5,550 feet (Seam Level)

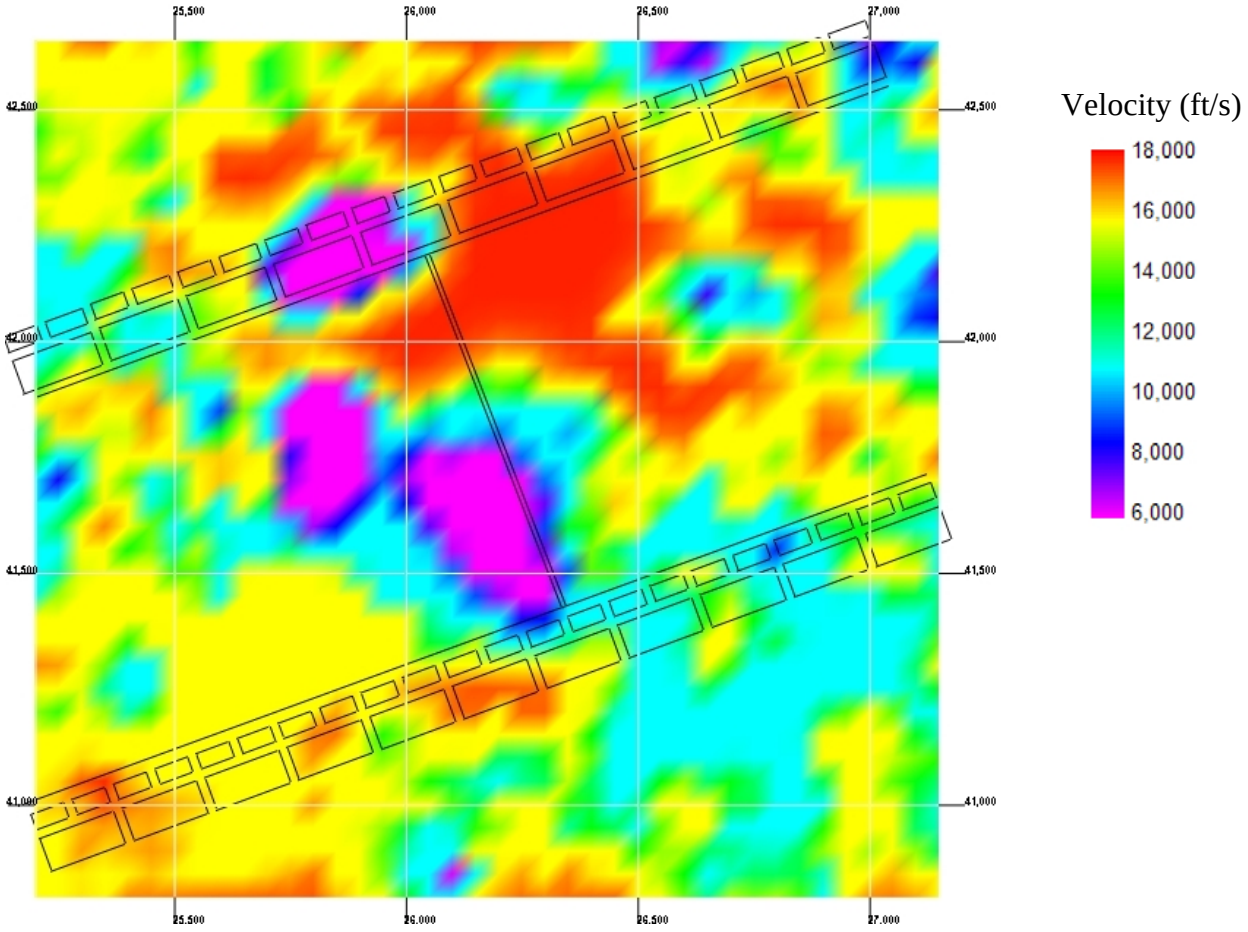

Figure C.17. Velocity tomogram at Z = 5,550 feet.

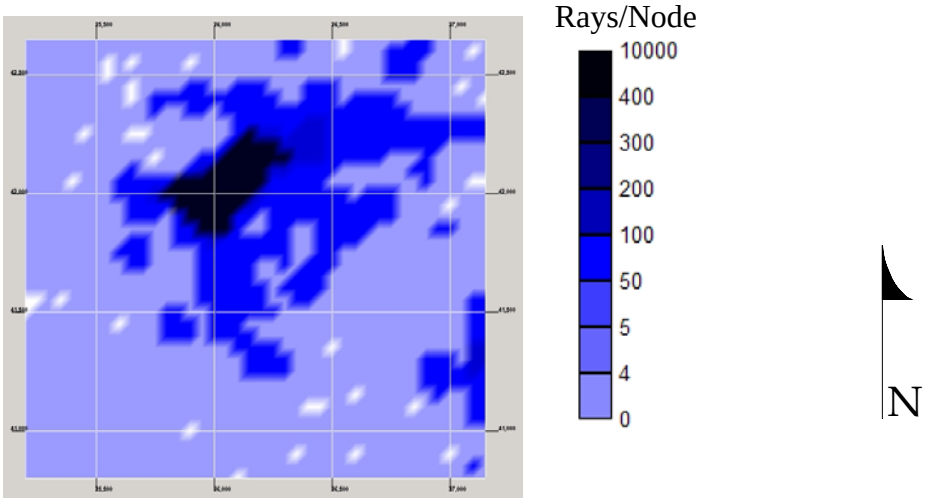

Figure C.18. Ray density plot at Z = 5,550 feet.

07-30-97

Plan View at Z = 5,550 feet (Seam Level)

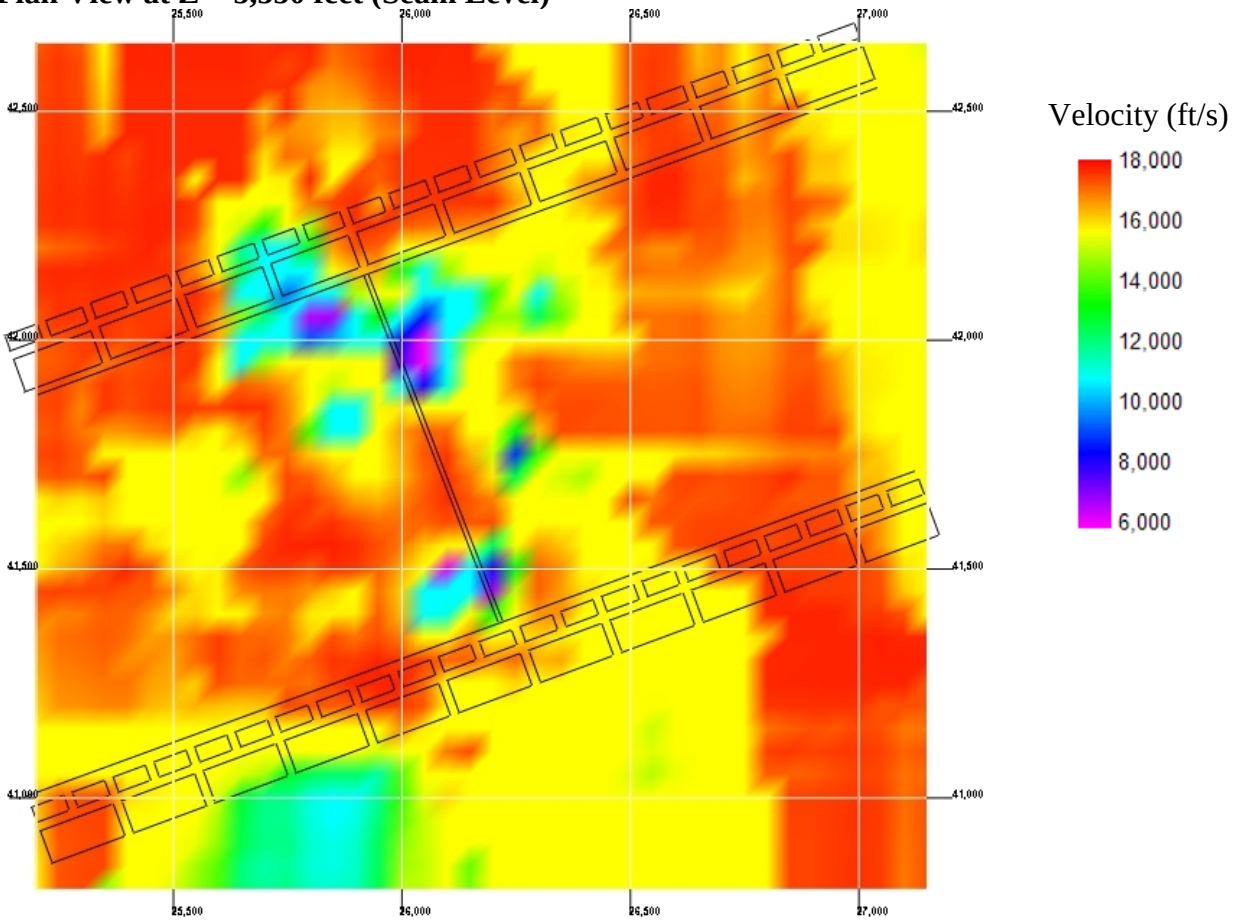

Figure C.19. Velocity tomogram at Z = 5,550 feet.

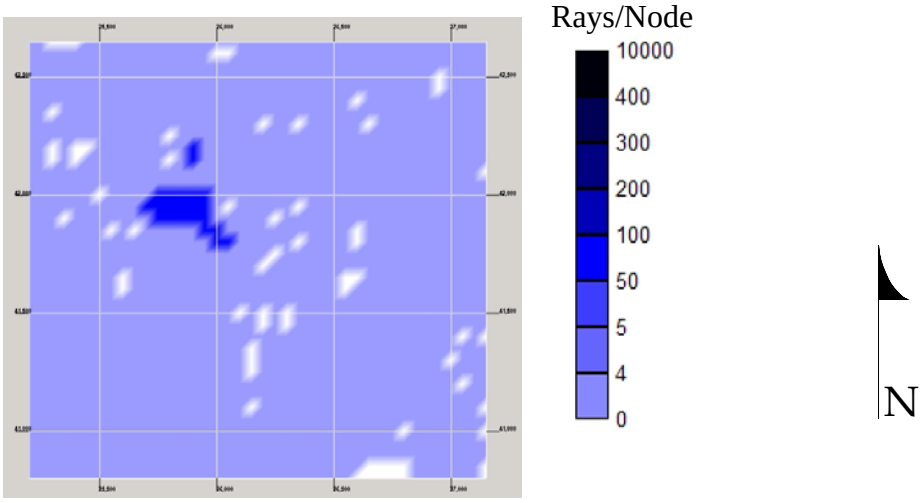

Figure C.20. Ray density plot at Z = 5,550 feet.

07-31-97

Plan View at Z = 5,550 feet (Seam Level)

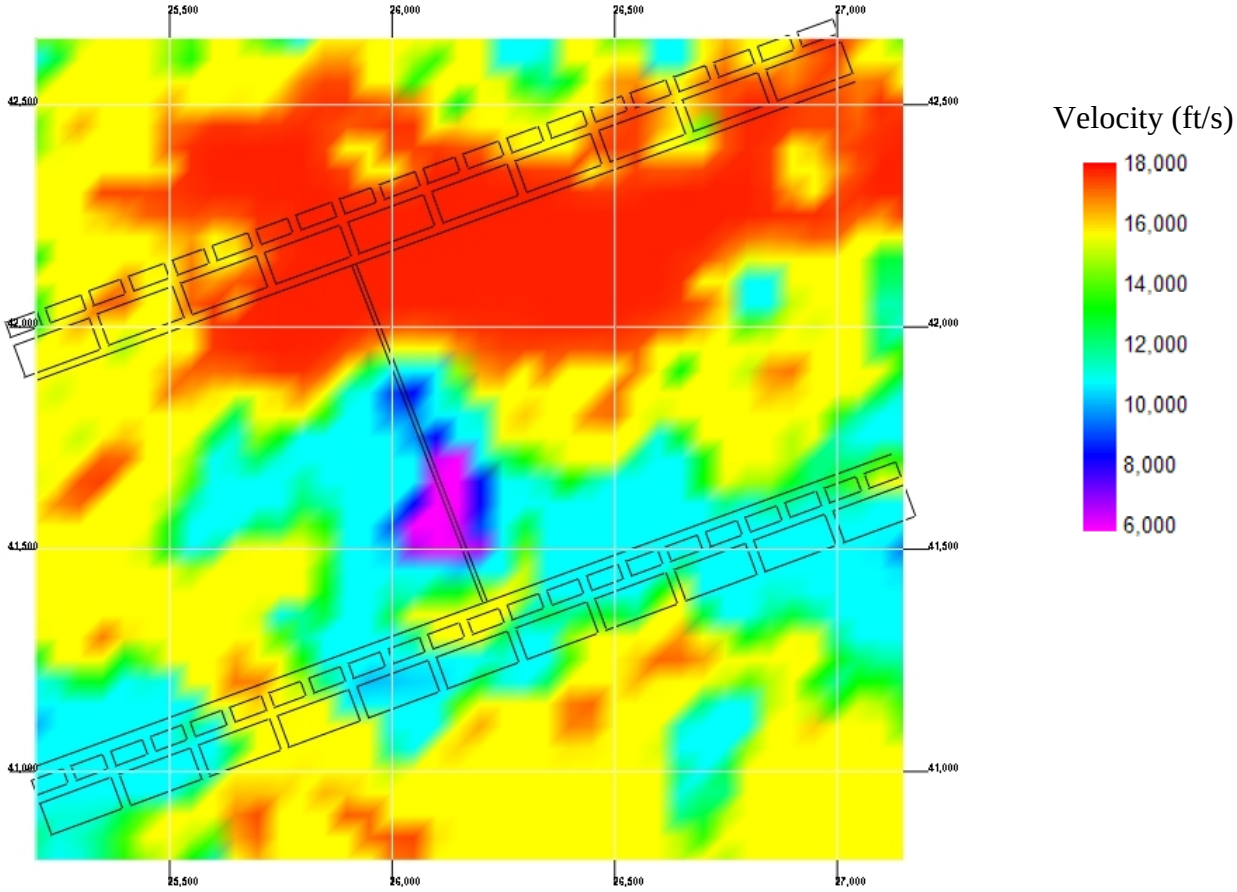

Figure C.21. Velocity tomogram at Z = 5,550 feet.

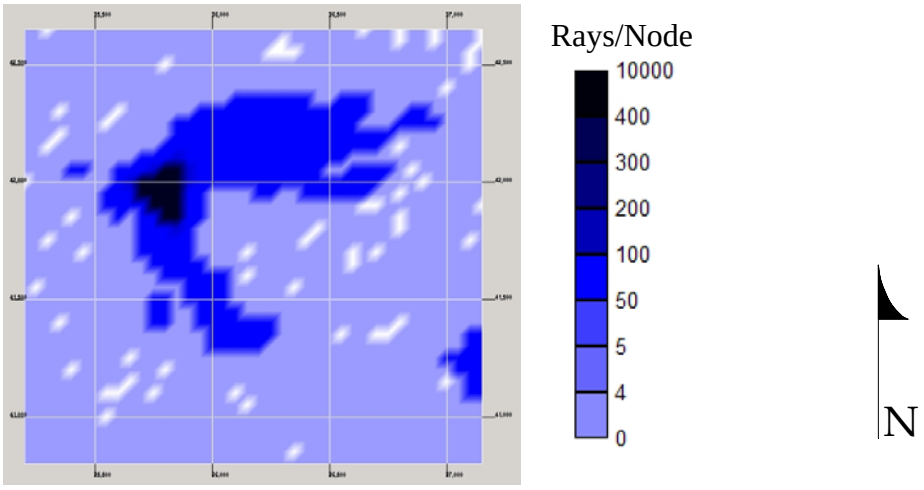

Figure C.22. Ray density plot at Z = 5,550 feet.

08-01-97

Plan View at Z = 5,550 feet (Seam Level)

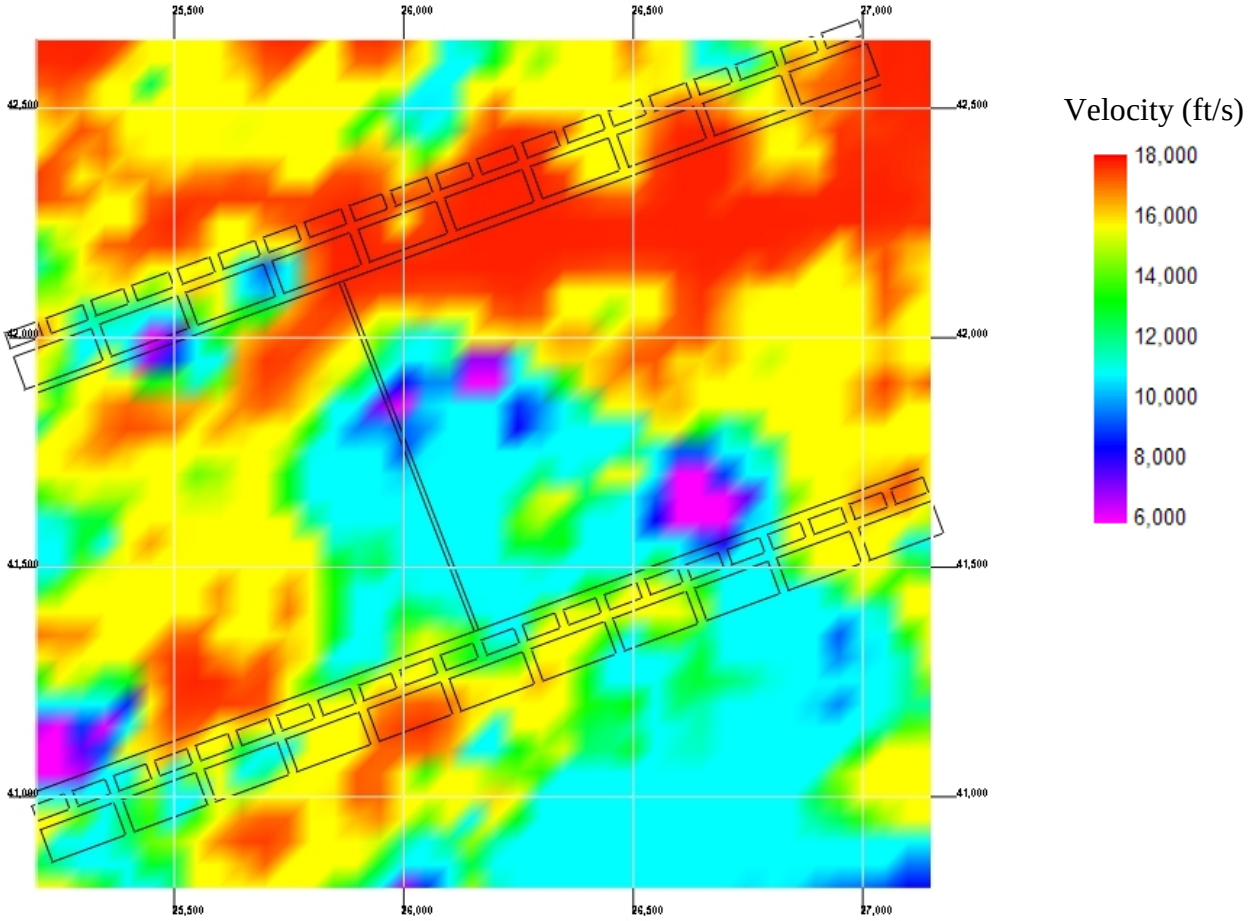

Figure C.23. Velocity tomogram at Z = 5,550 feet.

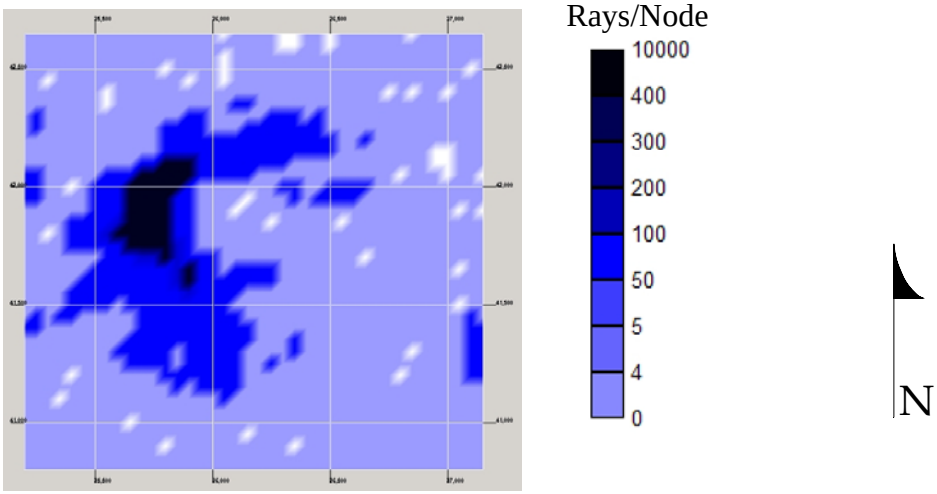

Figure C.24. Ray density plot at Z = 5,550 feet.

08-02-97

Plan View at Z = 5,550 feet (Seam Level)

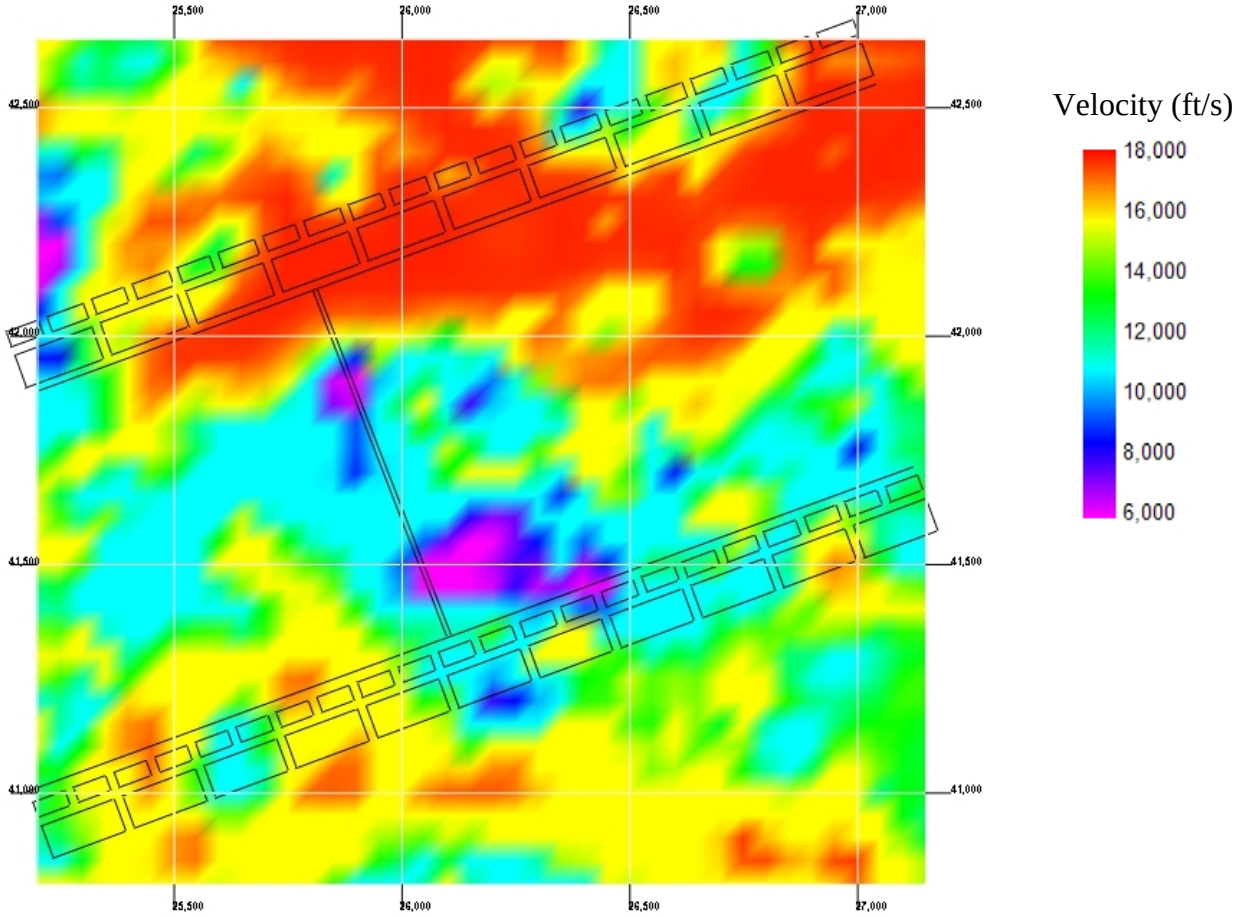

Figure C.25. Velocity tomogram at Z = 5,550 feet.

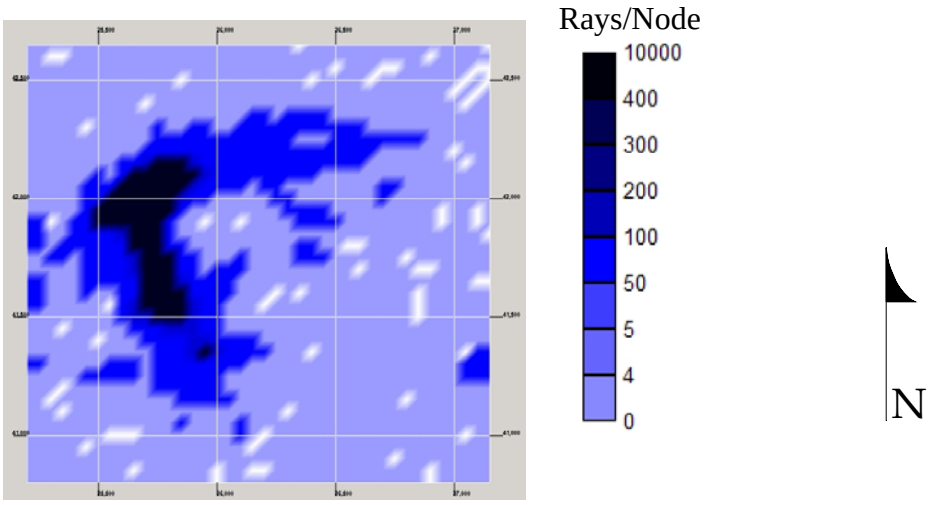

Figure C.26. Ray density plot at Z = 5,550 feet.

08-03-97

Plan View at Z = 5,550 feet (Seam Level)

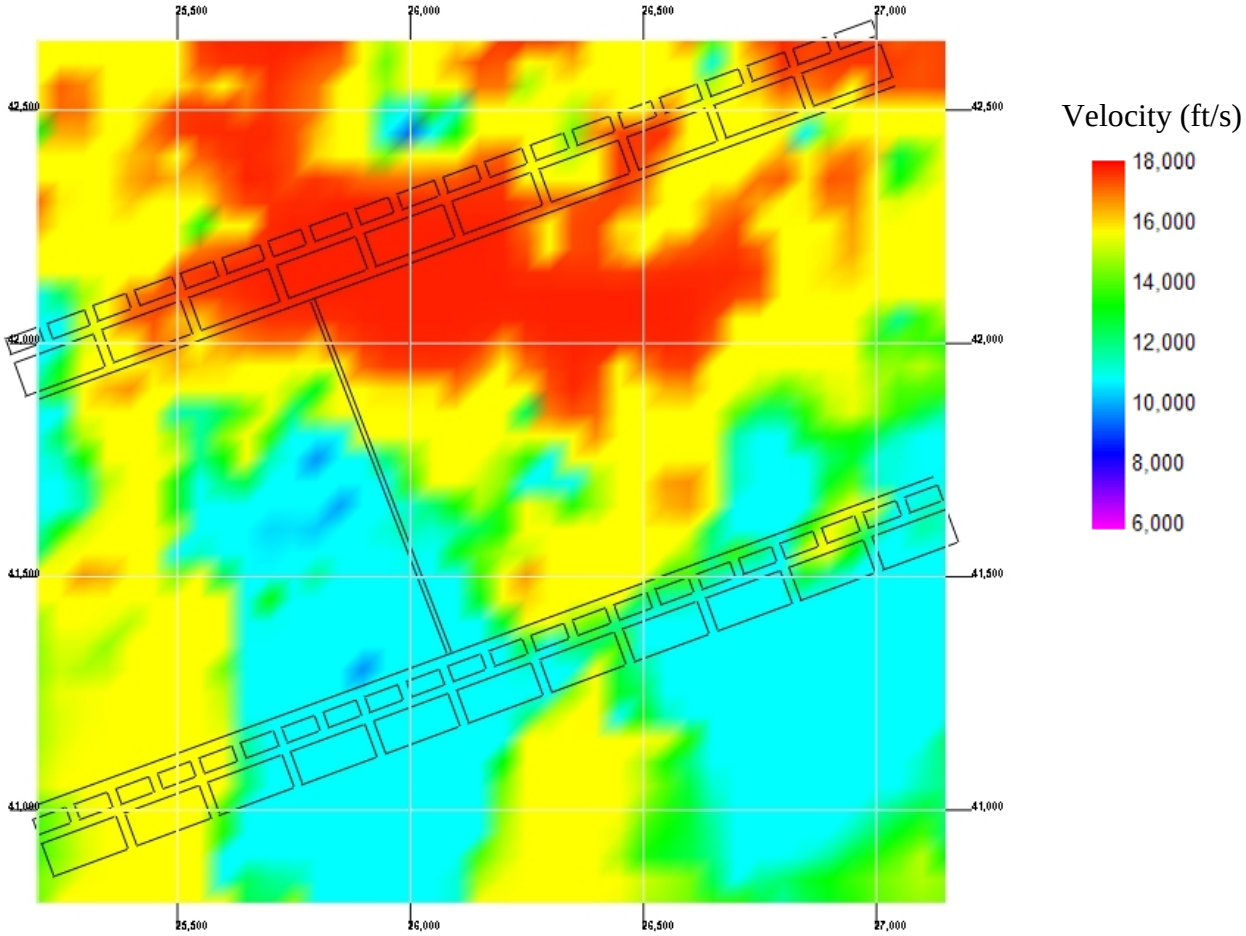

Figure C.27. Velocity tomogram at Z = 5,550 feet.

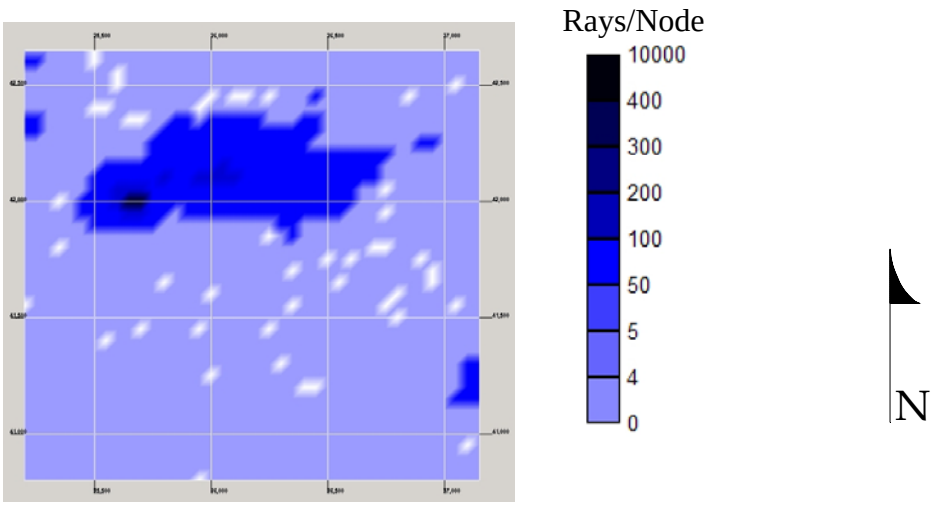

Figure C.28. Ray density plot at Z = 5,550 feet.

08-04-97

Plan View at Z = 5,550 feet (Seam Level)

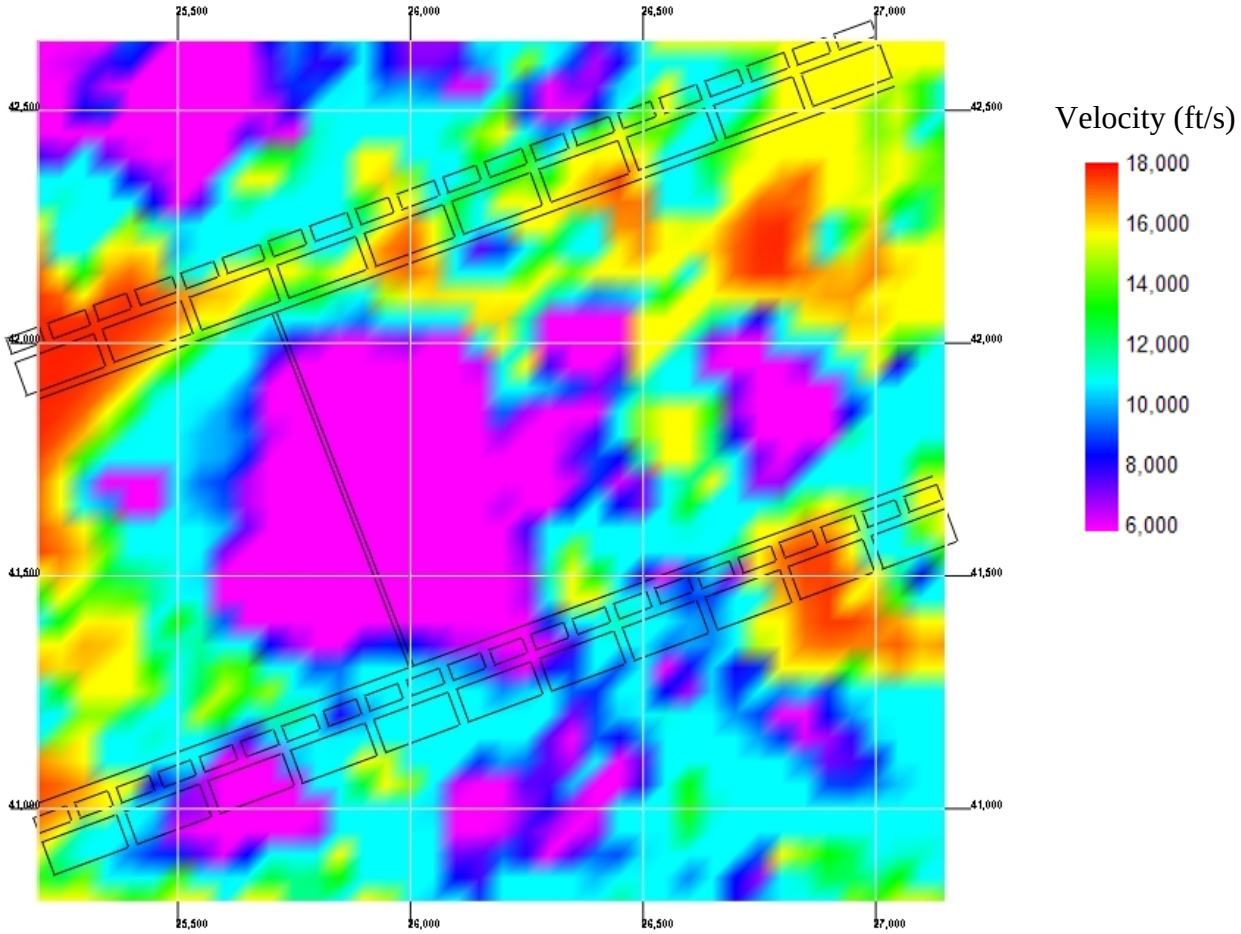

Figure C.29. Velocity tomogram at Z = 5,550 feet.

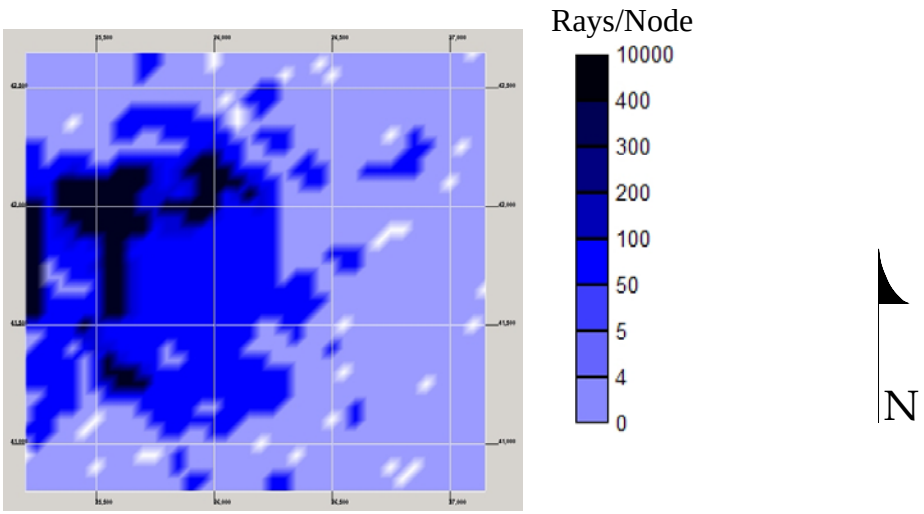

Figure C.30. Ray density plot at Z = 5,550 feet.

08-05-97

Plan View at Z = 5,550 feet (Seam Level)

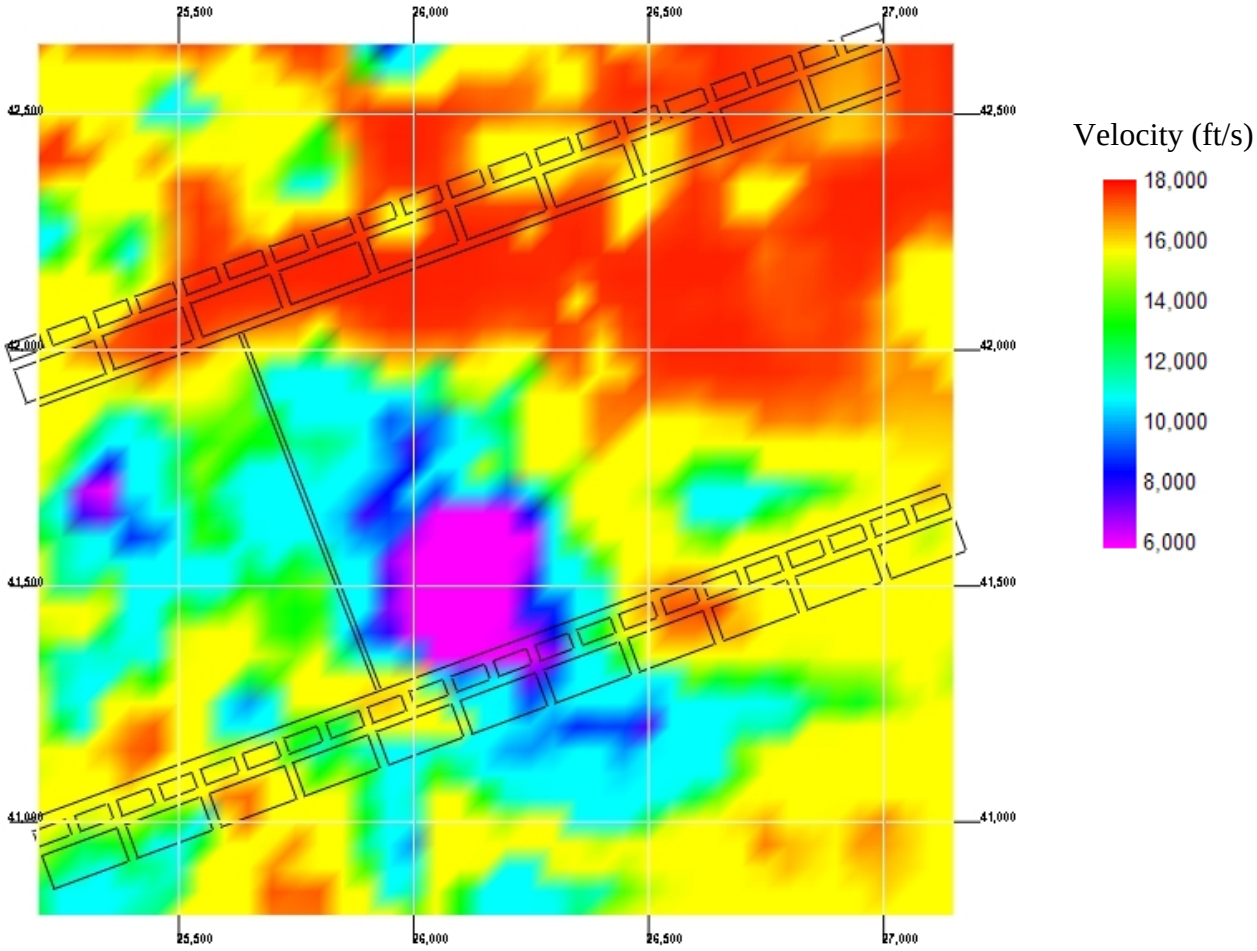

Figure C.31. Velocity tomogram at Z = 5,550 feet.

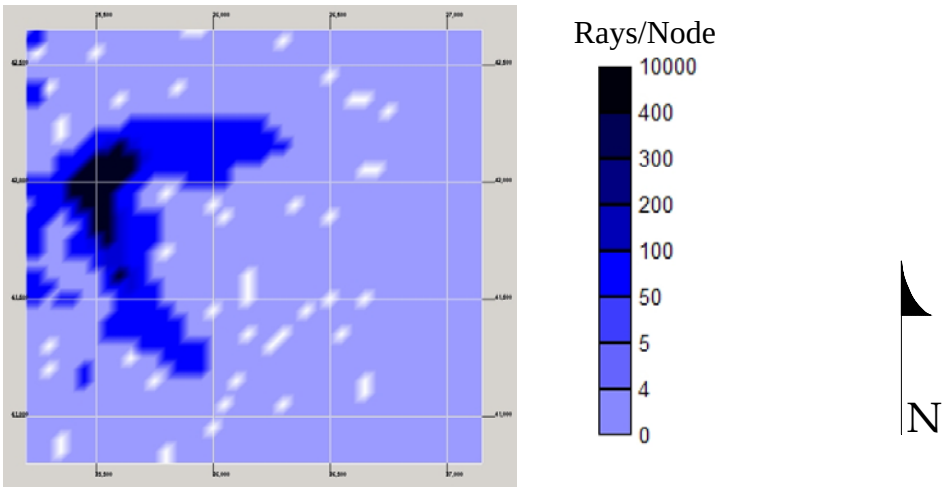

Figure C.32. Ray density plot at Z = 5,550 feet.

08-06-97

Plan View at Z = 5,550 feet (Seam Level)

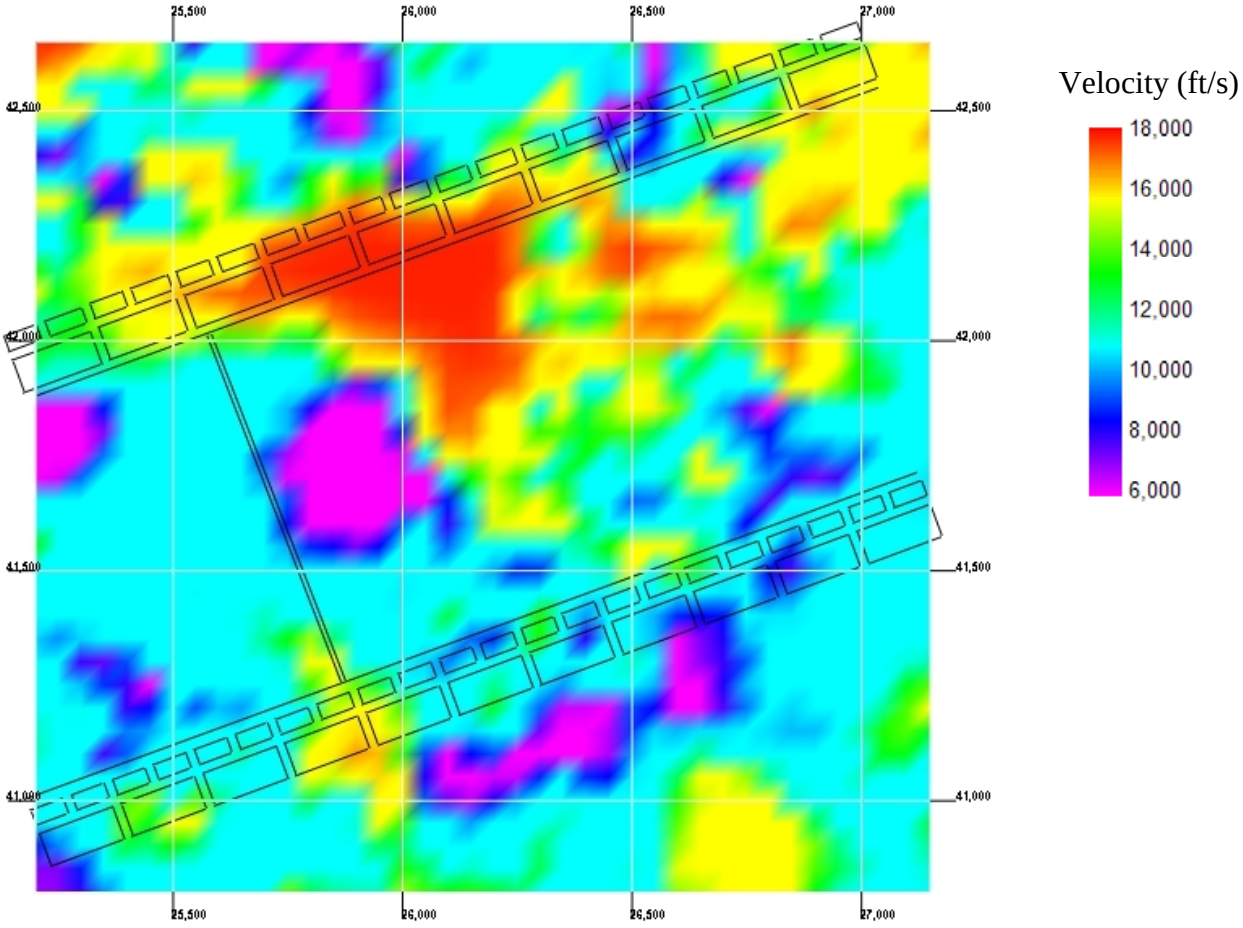

Figure C.33. Velocity tomogram at Z = 5,550 feet.

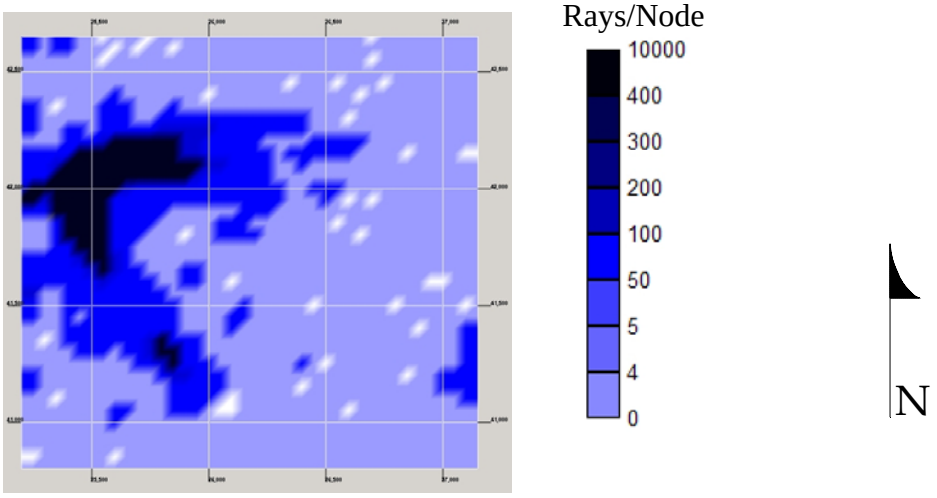

Figure C.34. Ray density plot at Z = 5,550 feet.

08-07-97

Plan View at Z = 5,550 feet (Seam Level)

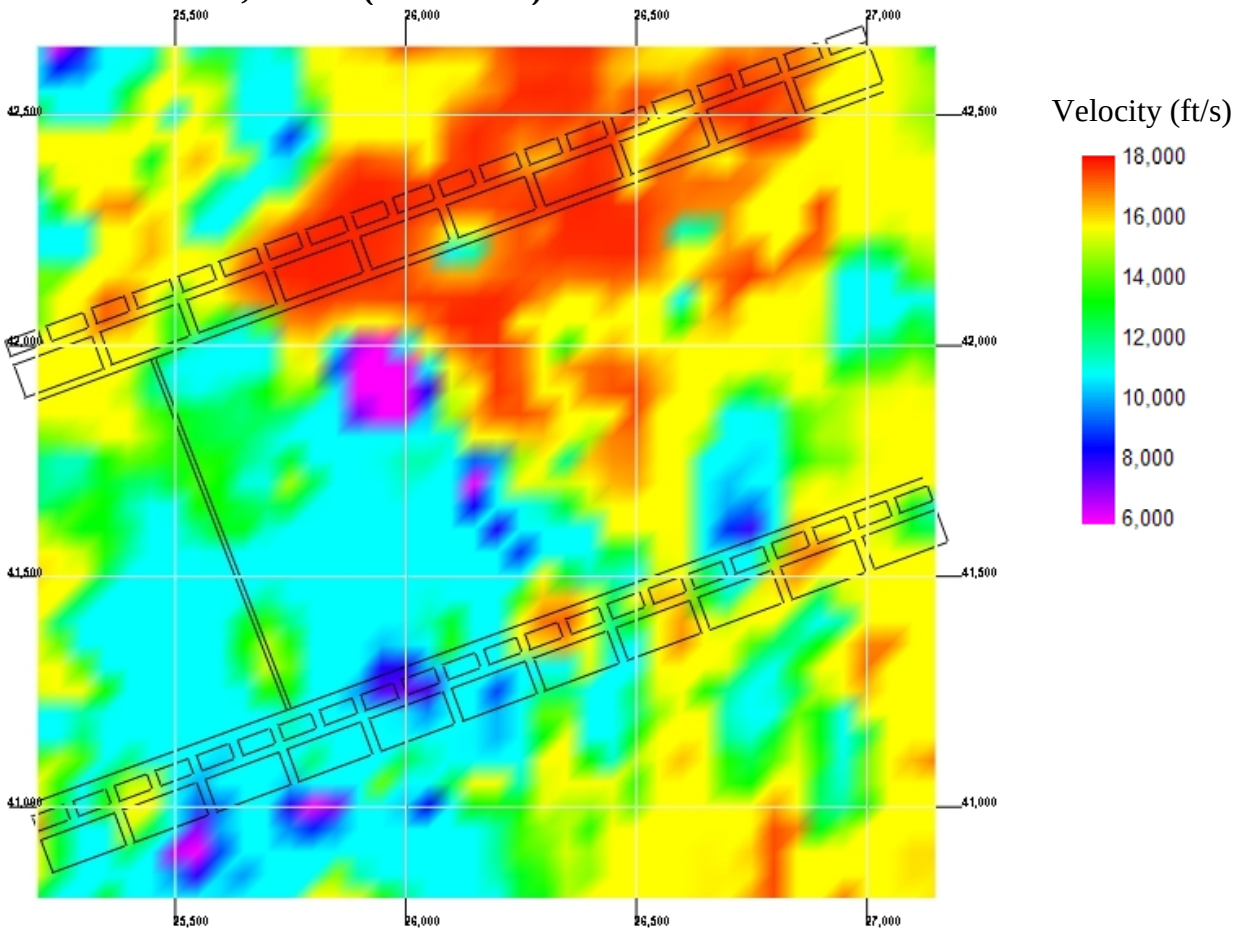

Figure C.35. Velocity tomogram at Z = 5,550 feet.

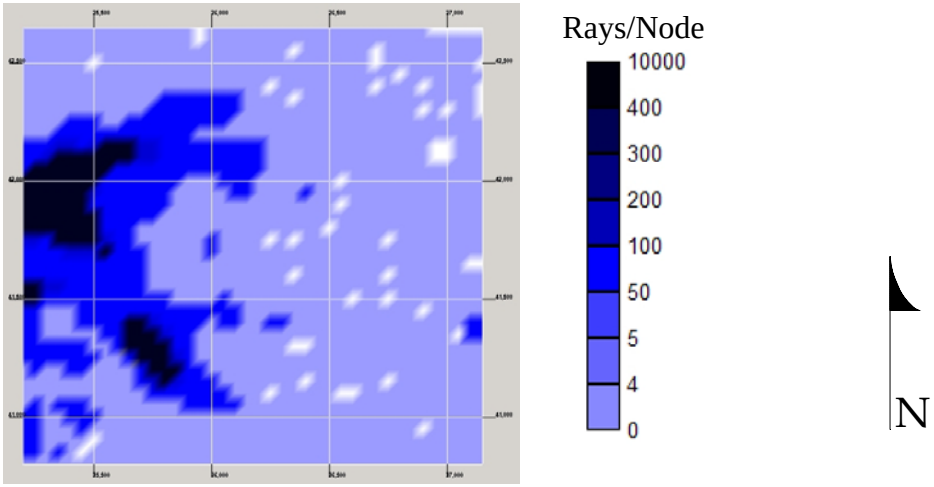

Figure C.36. Ray density plot at Z = 5,550 feet.

APPENDIX D

Velocity Tomograms & Ray Density Plots

ROOF LEVEL
Z = 5, 700 FEET

07-20-97
Plan View at Z = 5,700 feet (Roof Level)

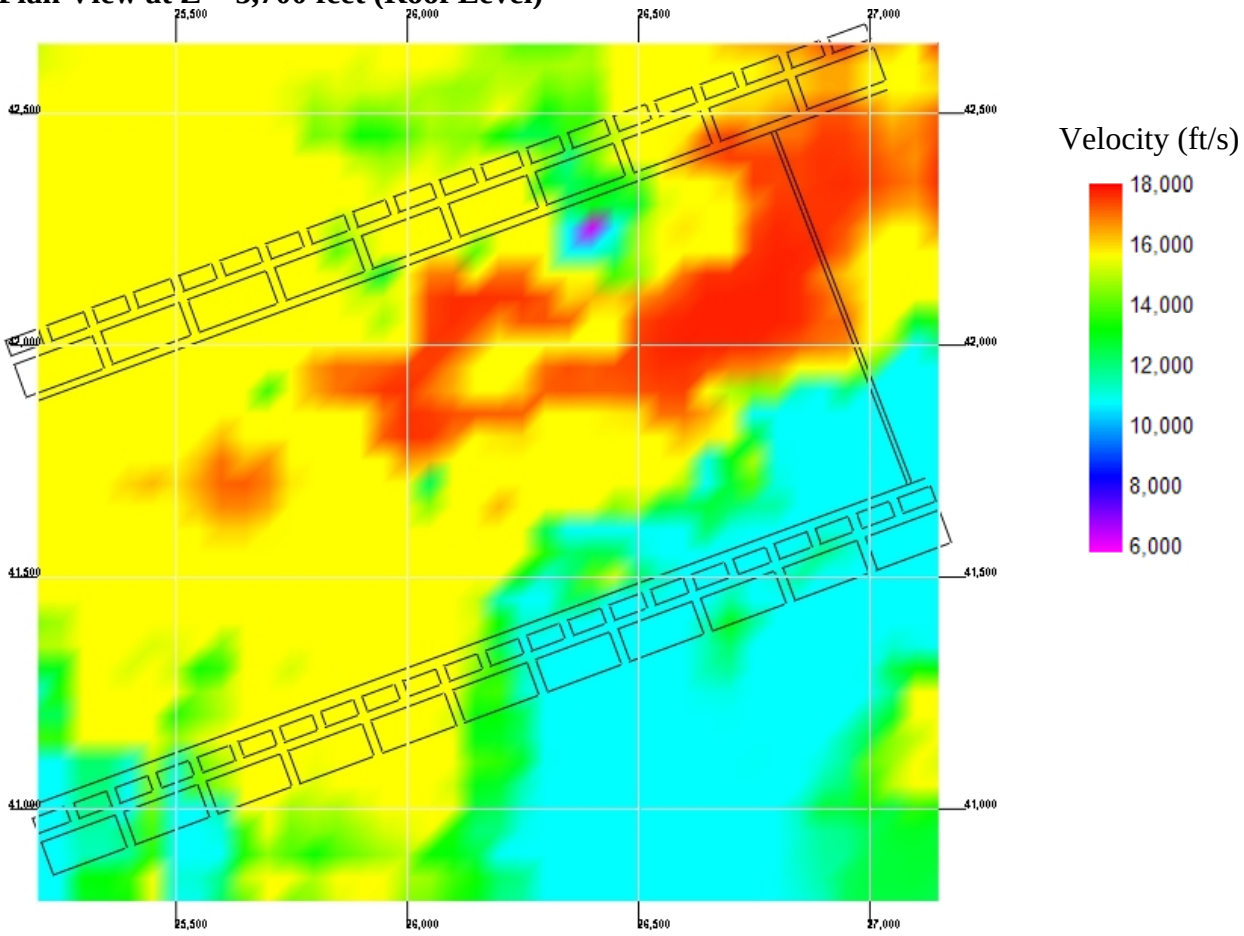

Figure D.1. Velocity tomogram at Z = 5,700 feet.

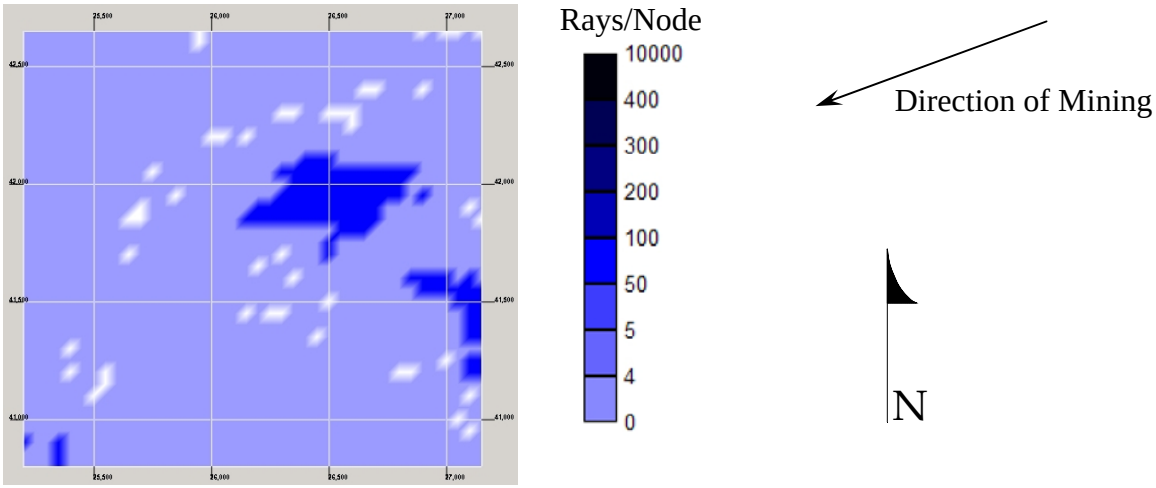

Figure D.2. Ray density plot at Z = 5,700 feet.

07-21-97

Plan View at Z = 5,700 feet (Roof Level)

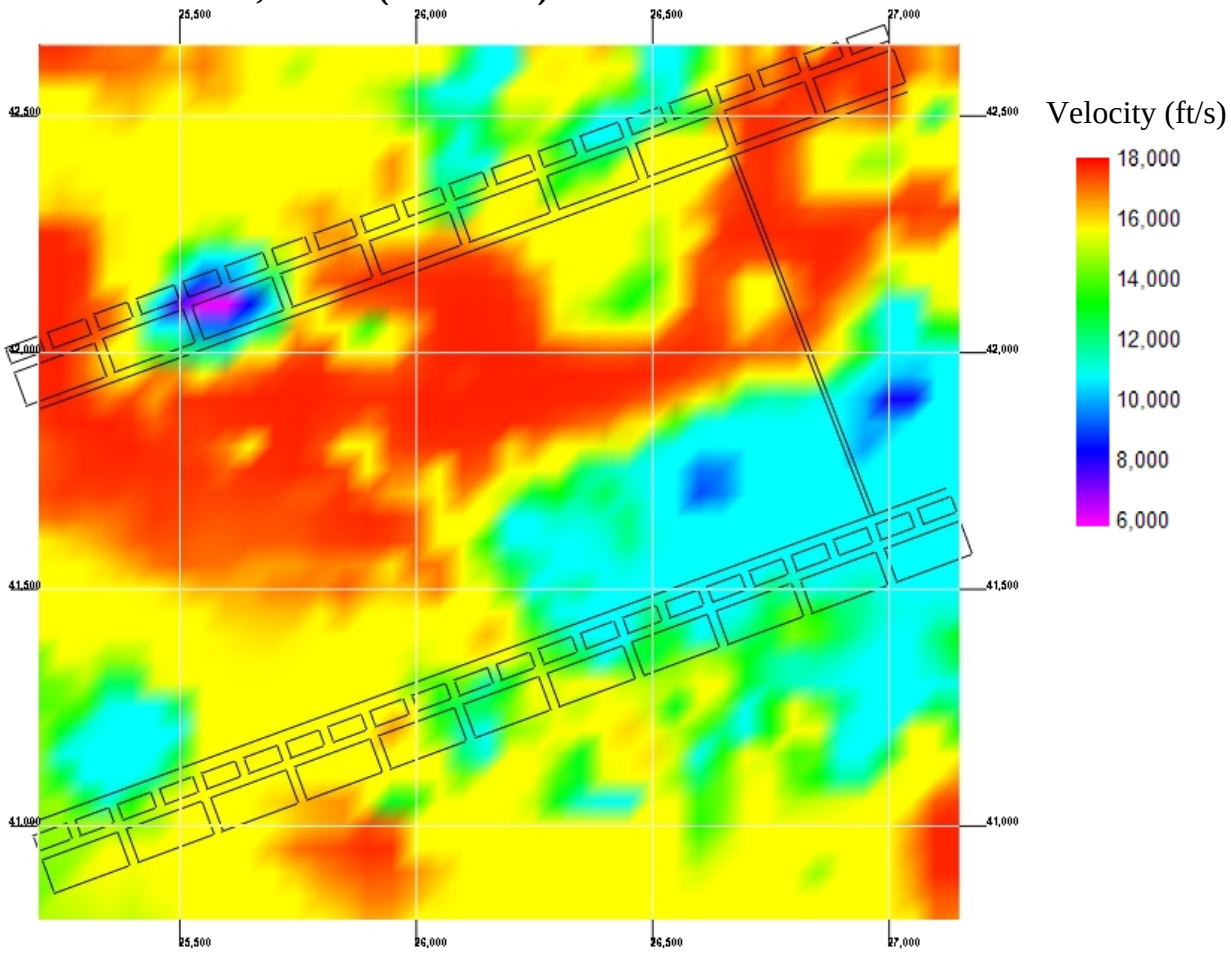

Figure D.3. Velocity tomogram at Z = 5,700 feet.

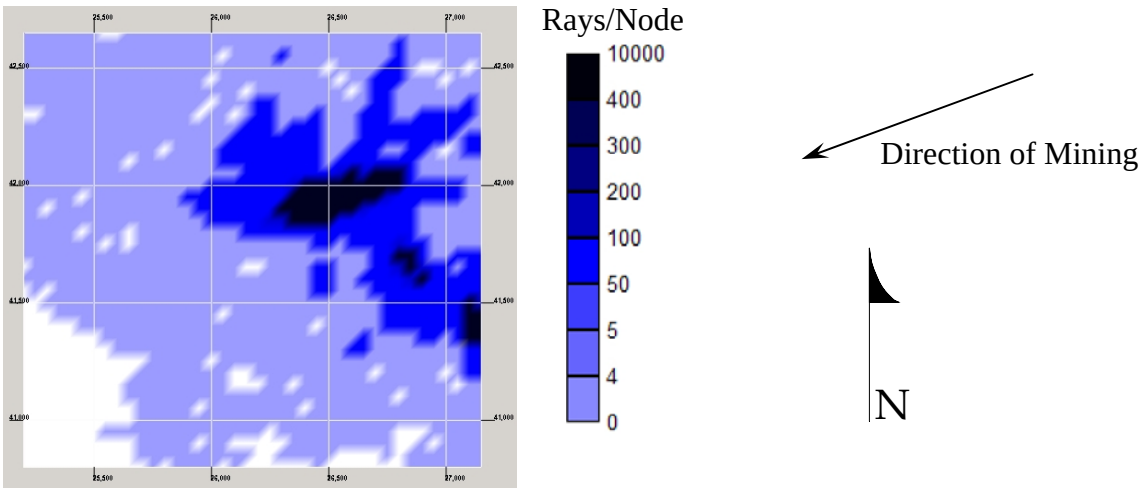

Figure D.4. Ray density plot at Z = 5,700 feet.

07-22-97
Plan View at Z = 5,700 feet (Roof Level)

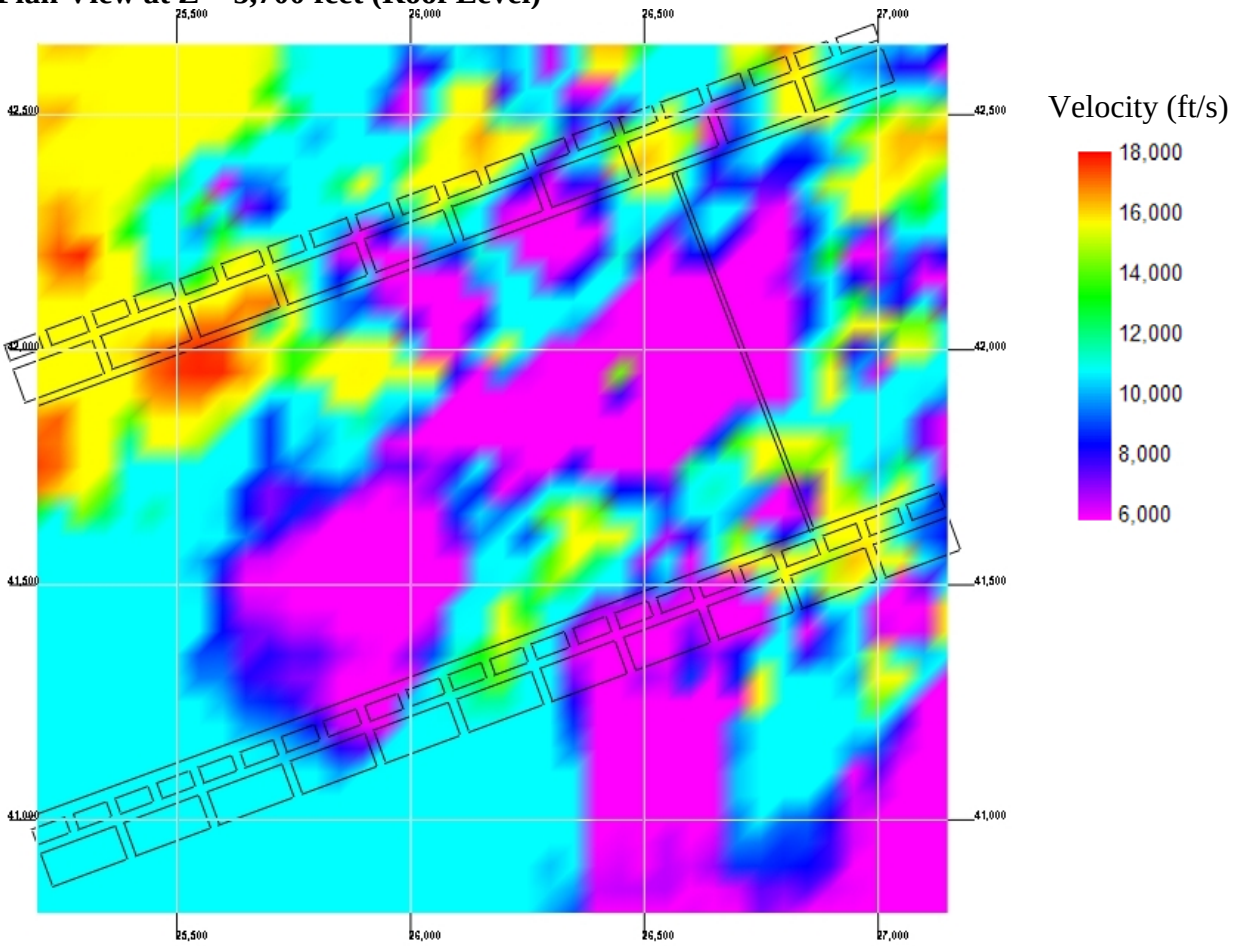

Figure D.5. Velocity tomogram at Z = 5,700 feet.

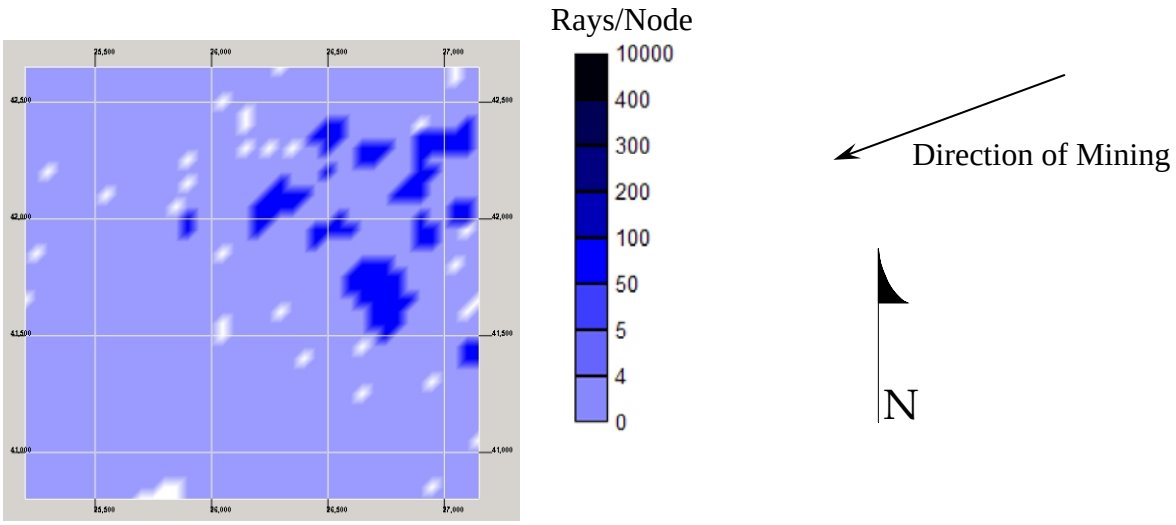

Figure D.6. Ray density plot at Z = 5,700 feet.

07-23-97
Plan View at Z = 5,700 feet (Roof Level)

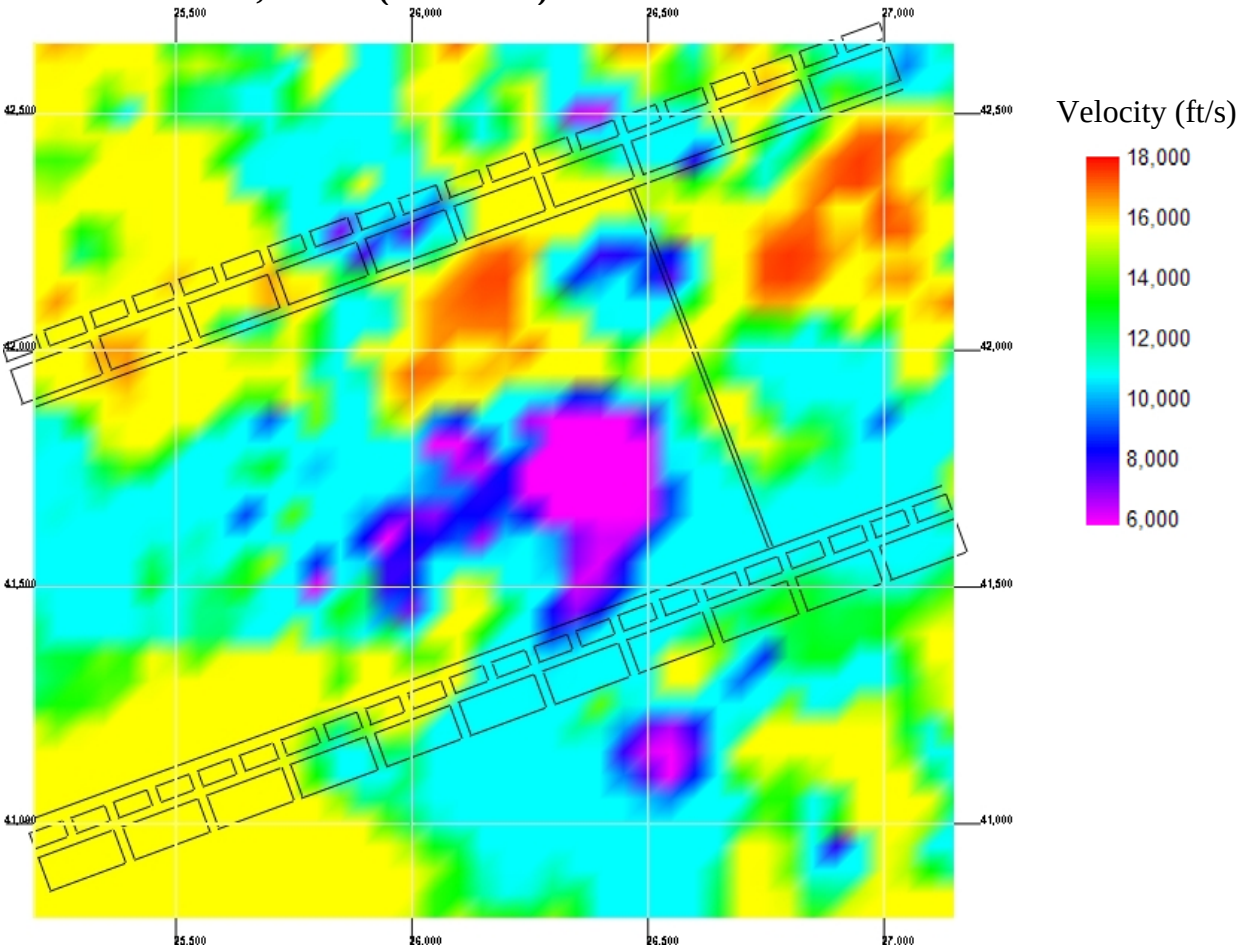

Figure D.7. Velocity tomogram at Z = 5,700 feet.

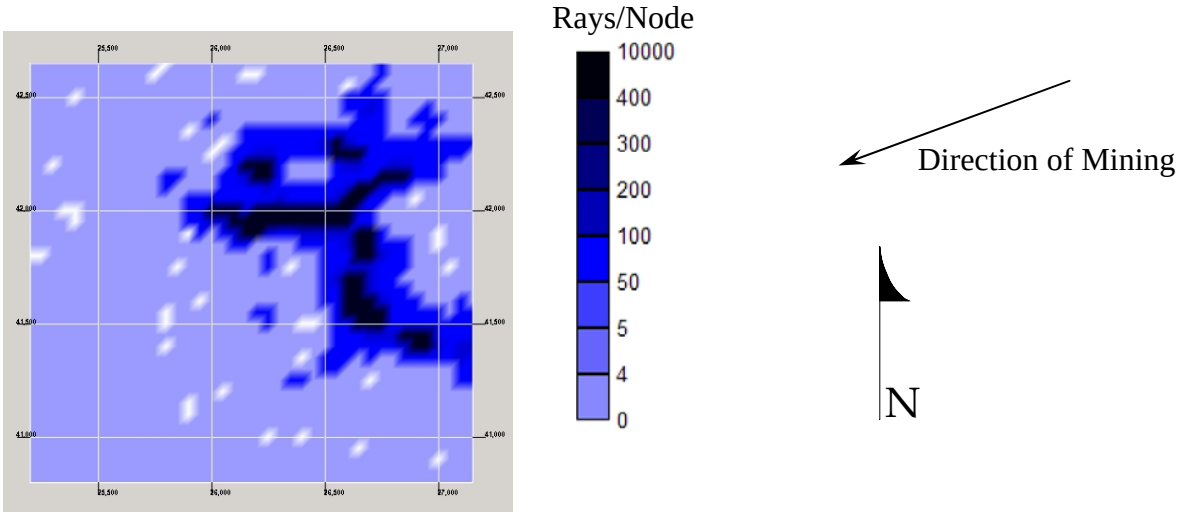

Figure D.8. Ray density plot at Z = 5,700 feet.

07-24-97
Plan View at Z = 5,700 feet (Roof Level)

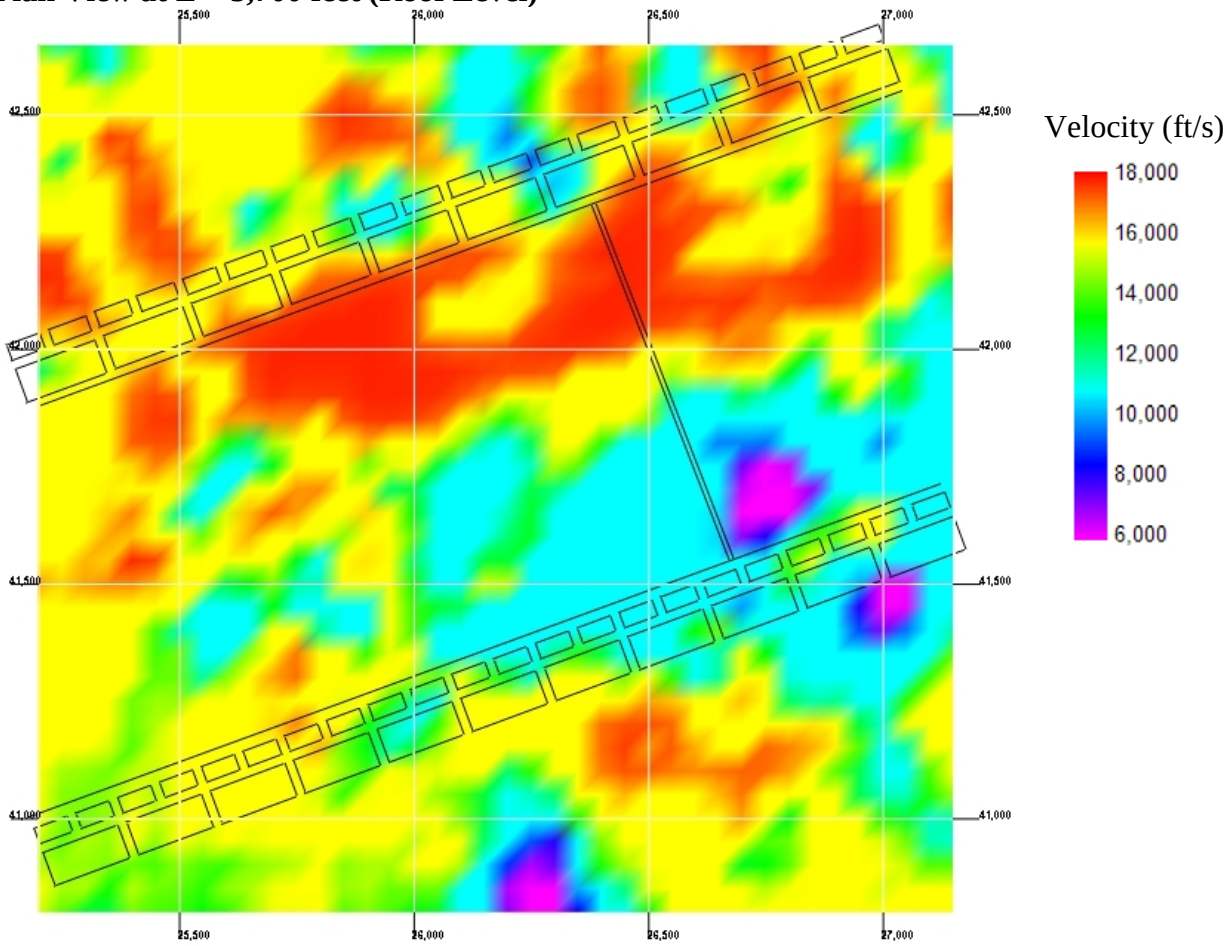

Figure D.9. Velocity tomogram at Z = 5,700 feet.

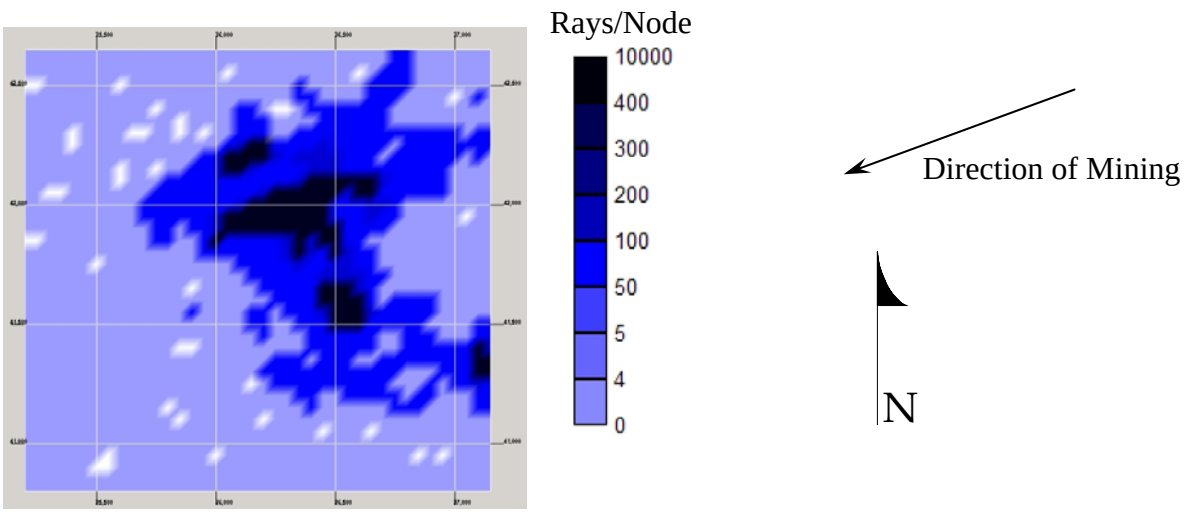

Figure D.10. Ray density plot at Z = 5,700 feet.

07-25-97
Plan View at Z = 5,700 feet (Roof Level)

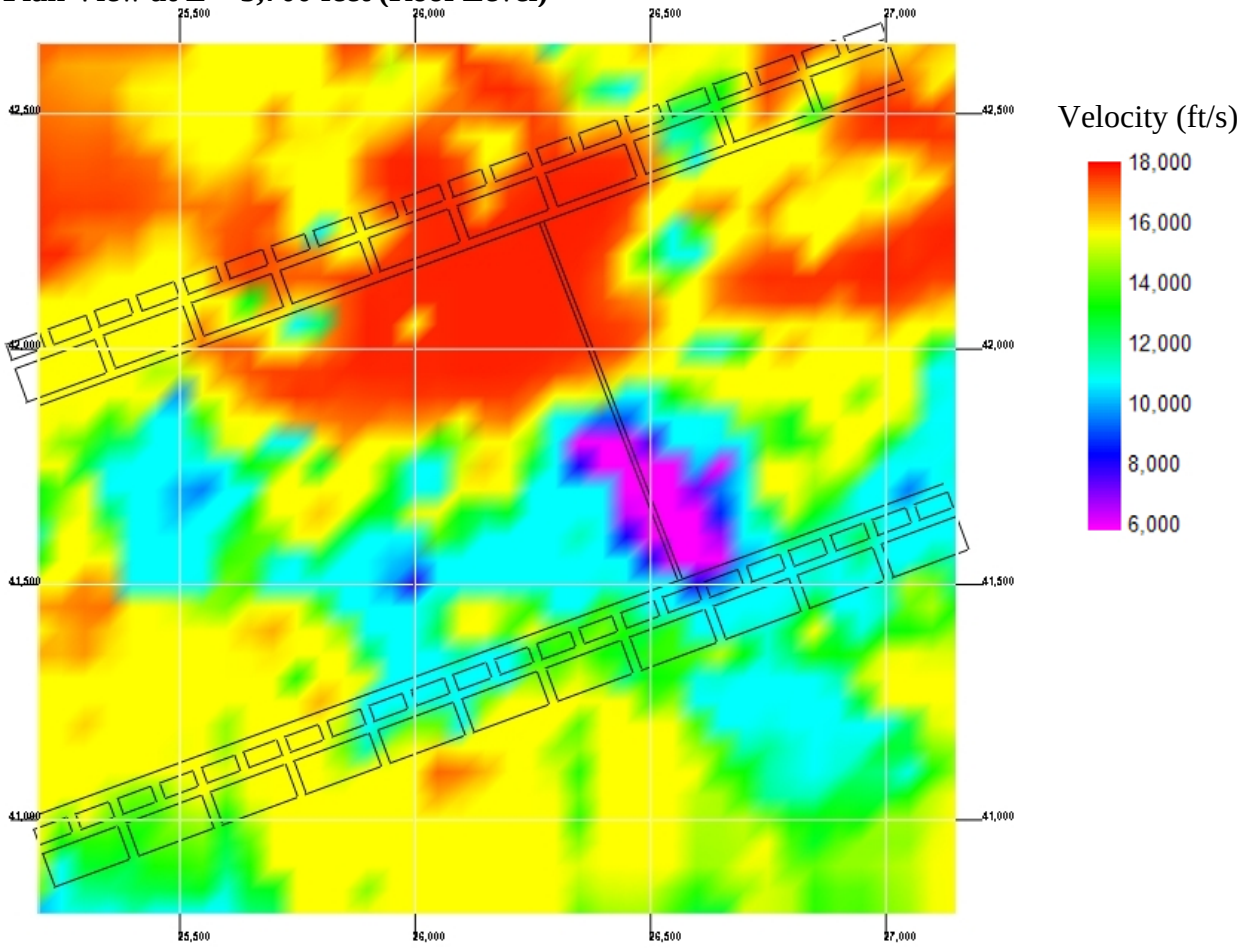

Figure D.11. Velocity tomogram at Z = 5,700 feet.

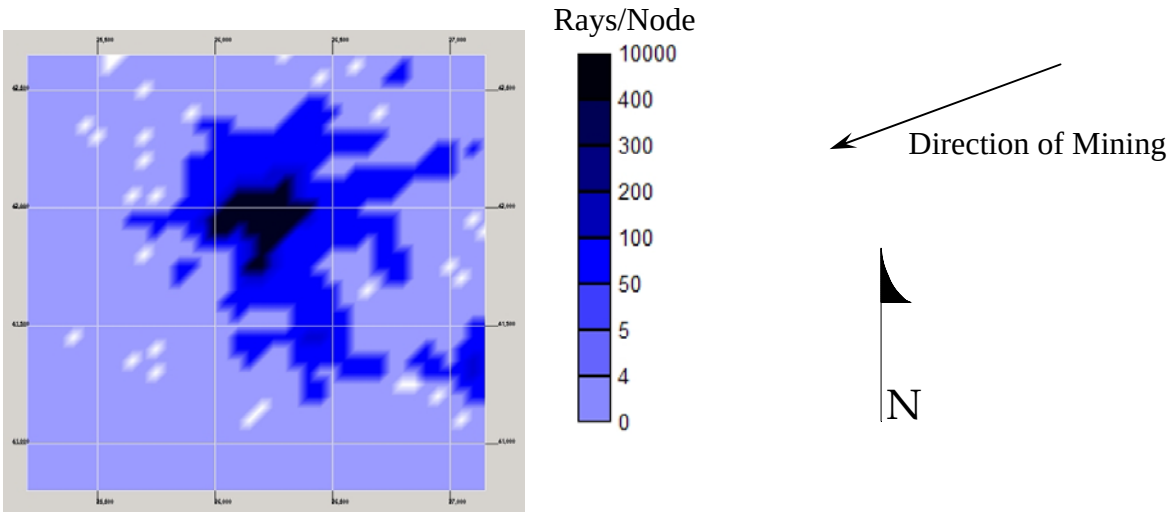

Figure D.12. Ray density plot at Z = 5,700 feet.

07-26-97
Plan View at Z = 5,700 feet (Roof Level)

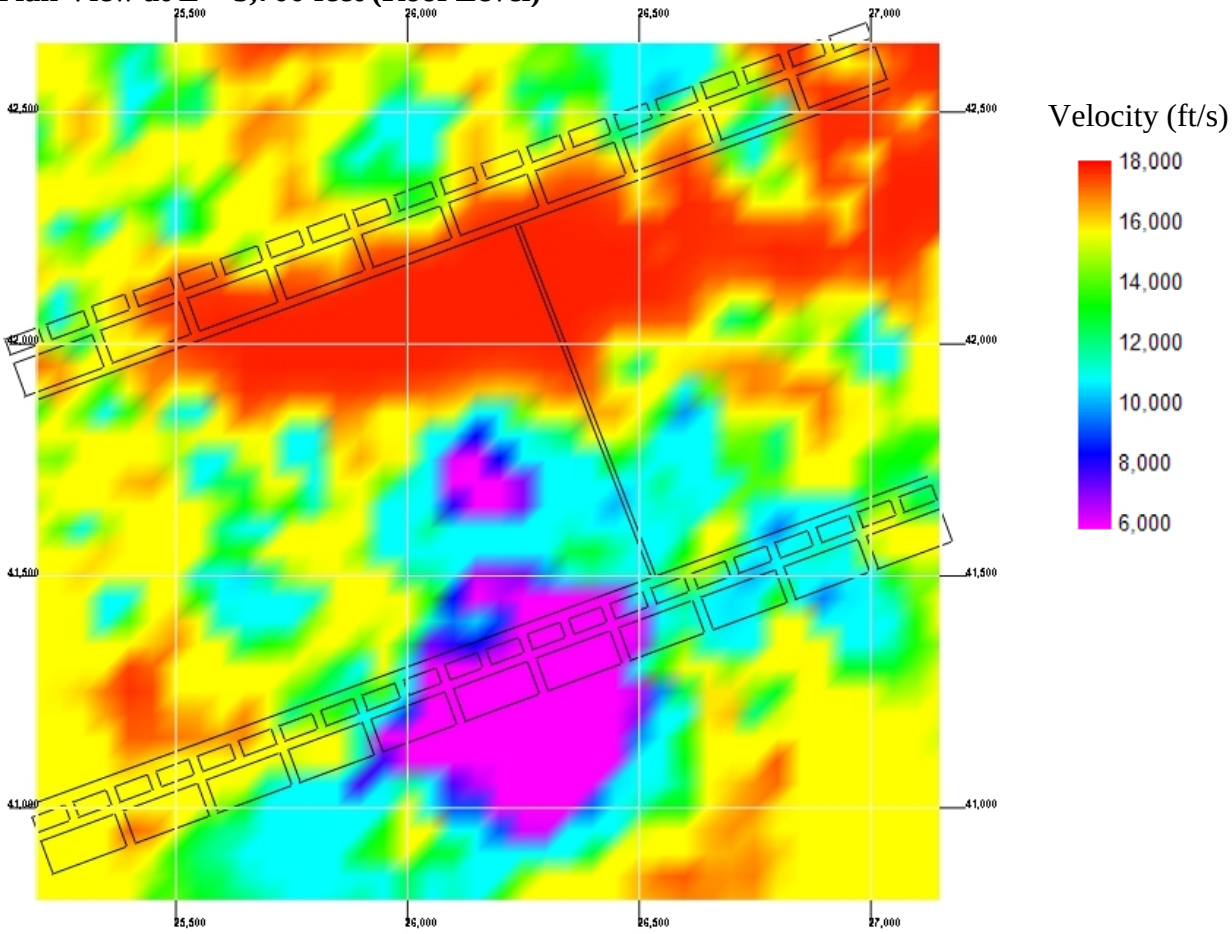

Figure D.13. Velocity tomogram at Z = 5,700 feet.

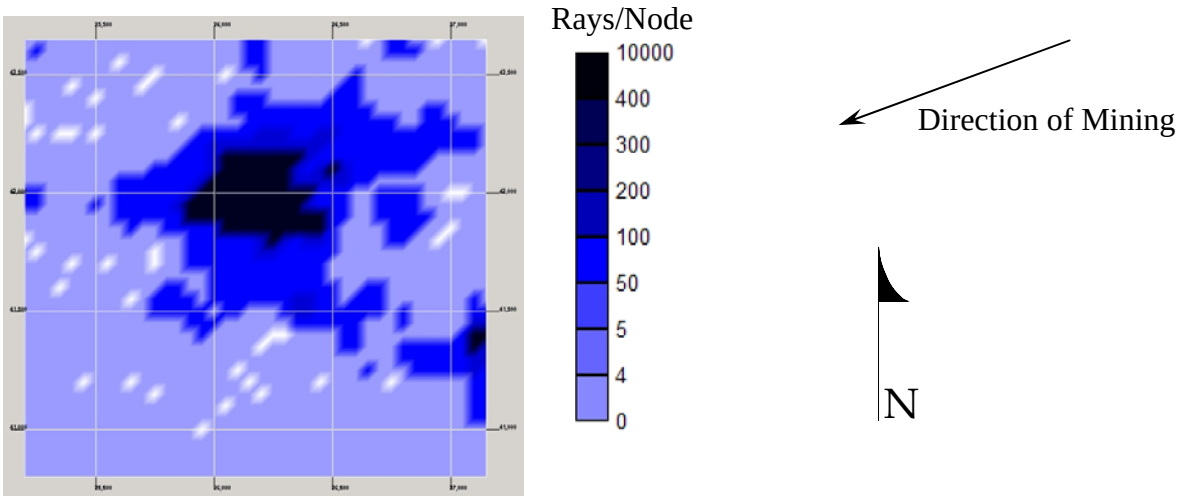

Figure D.14. Ray density plot at Z = 5,700 feet.

07-27-97
Plan View at Z = 5,700 feet (Roof Level)

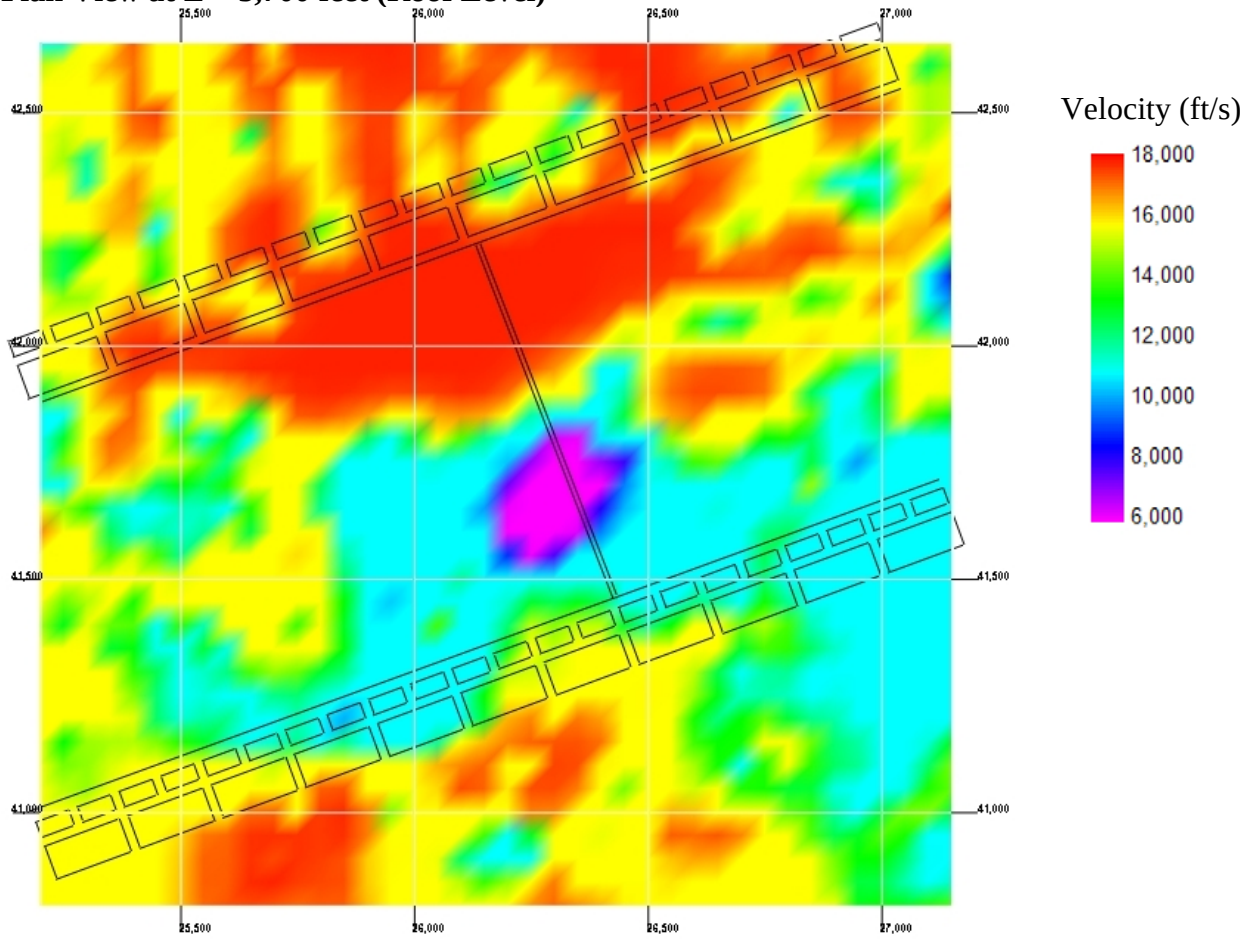

Figure D.15. Velocity tomogram at Z = 5,700 feet.

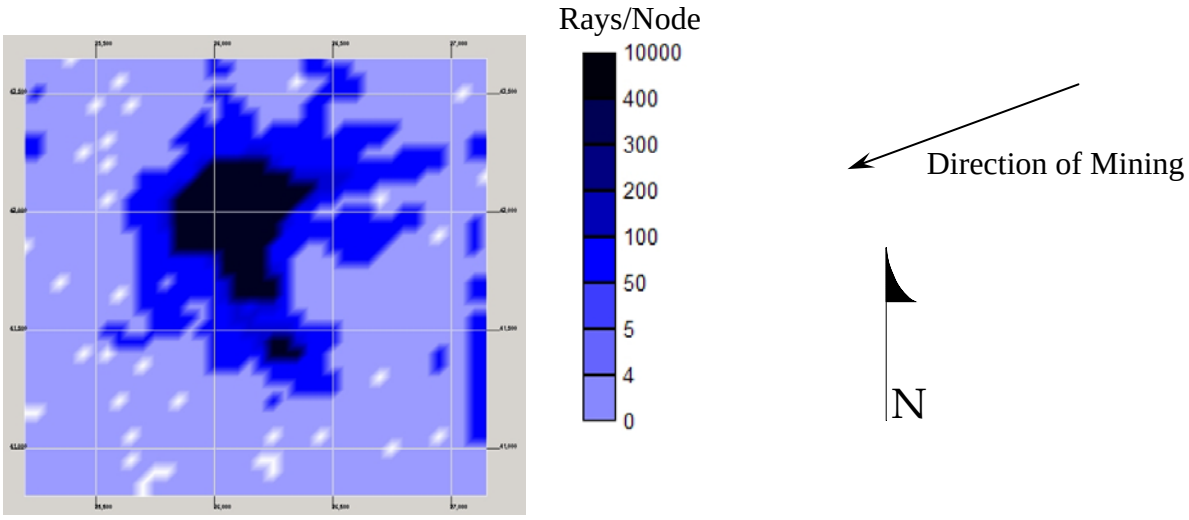

Figure D.16. Ray density plot at Z = 5,700 feet.

07-28-97
Plan View at Z = 5,700 feet (Roof Level)

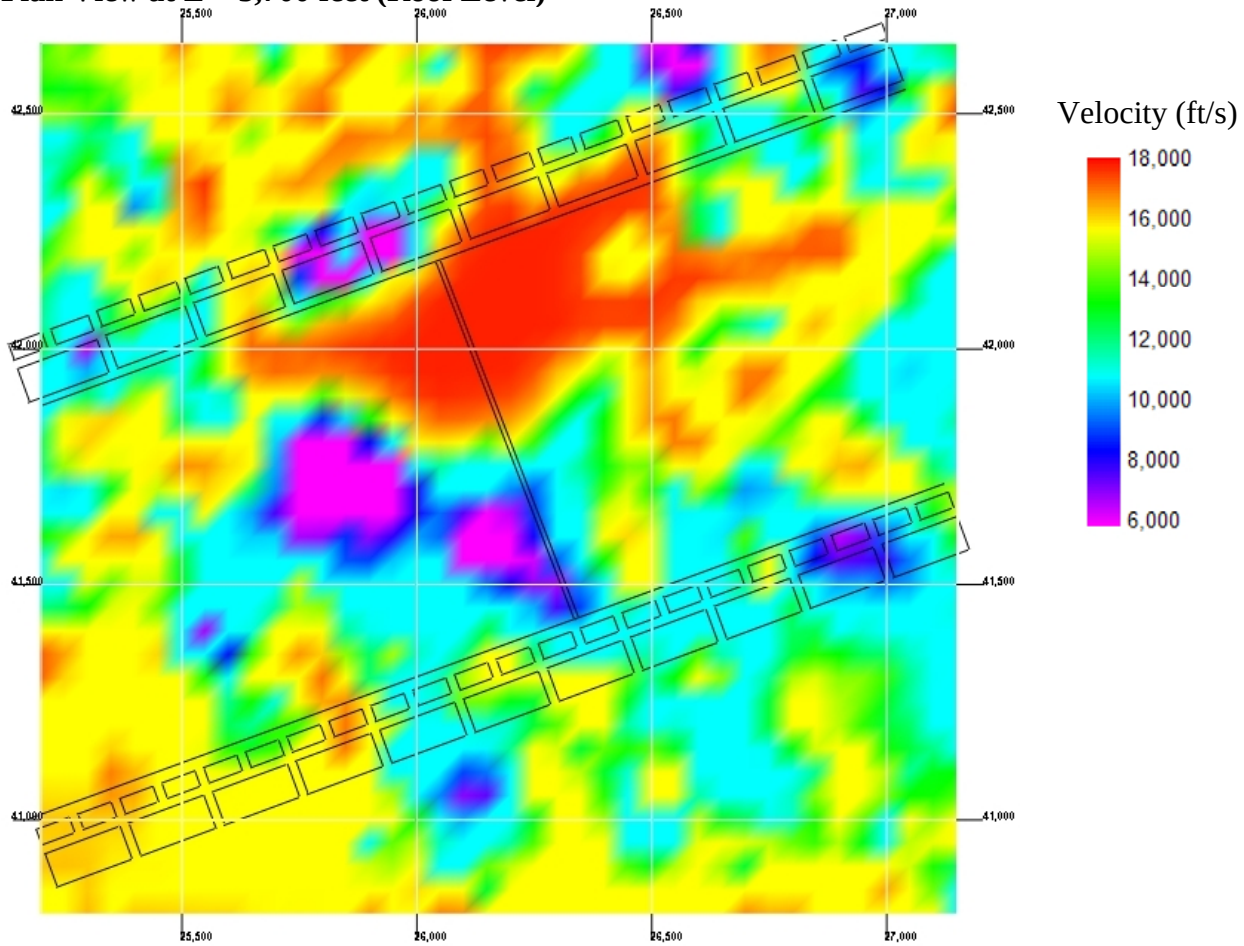

Figure D.17. Velocity tomogram at Z = 5,700 feet.

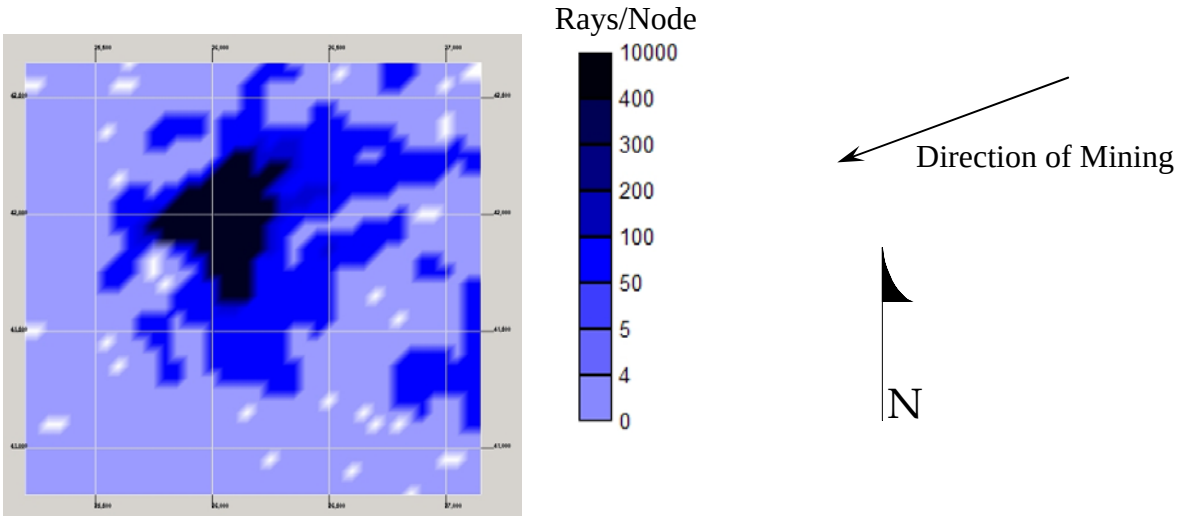

Figure D.18. Ray density plot at Z = 5,700 feet.

07-30-97

Plan View at Z = 5,700 feet (Roof Level)

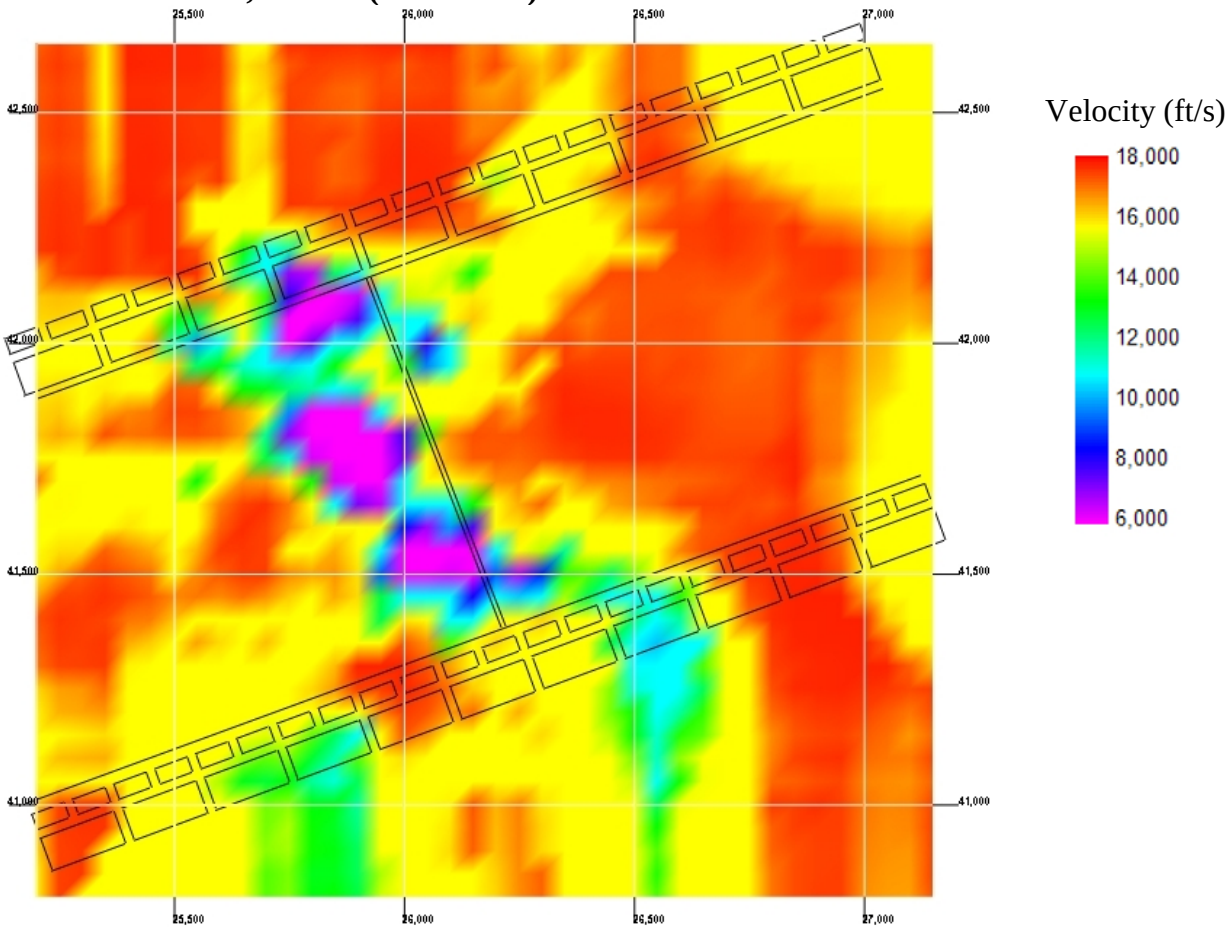

Figure D.19. Velocity tomogram at Z = 5,700 feet.

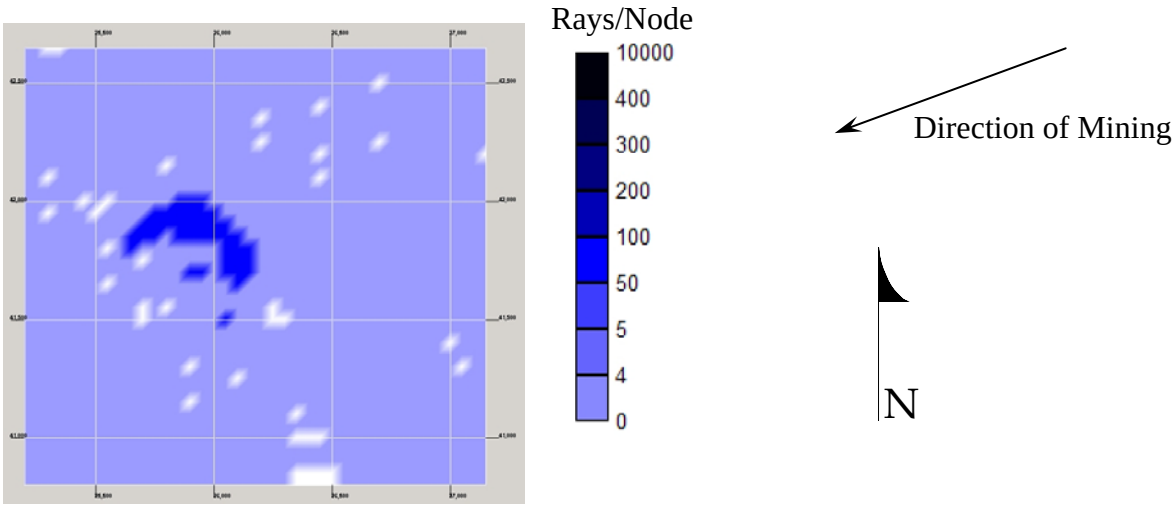

Figure D.20. Ray density plot at Z = 5,700 feet.

07-31-97
Plan View at Z = 5,700 feet (Roof Level)

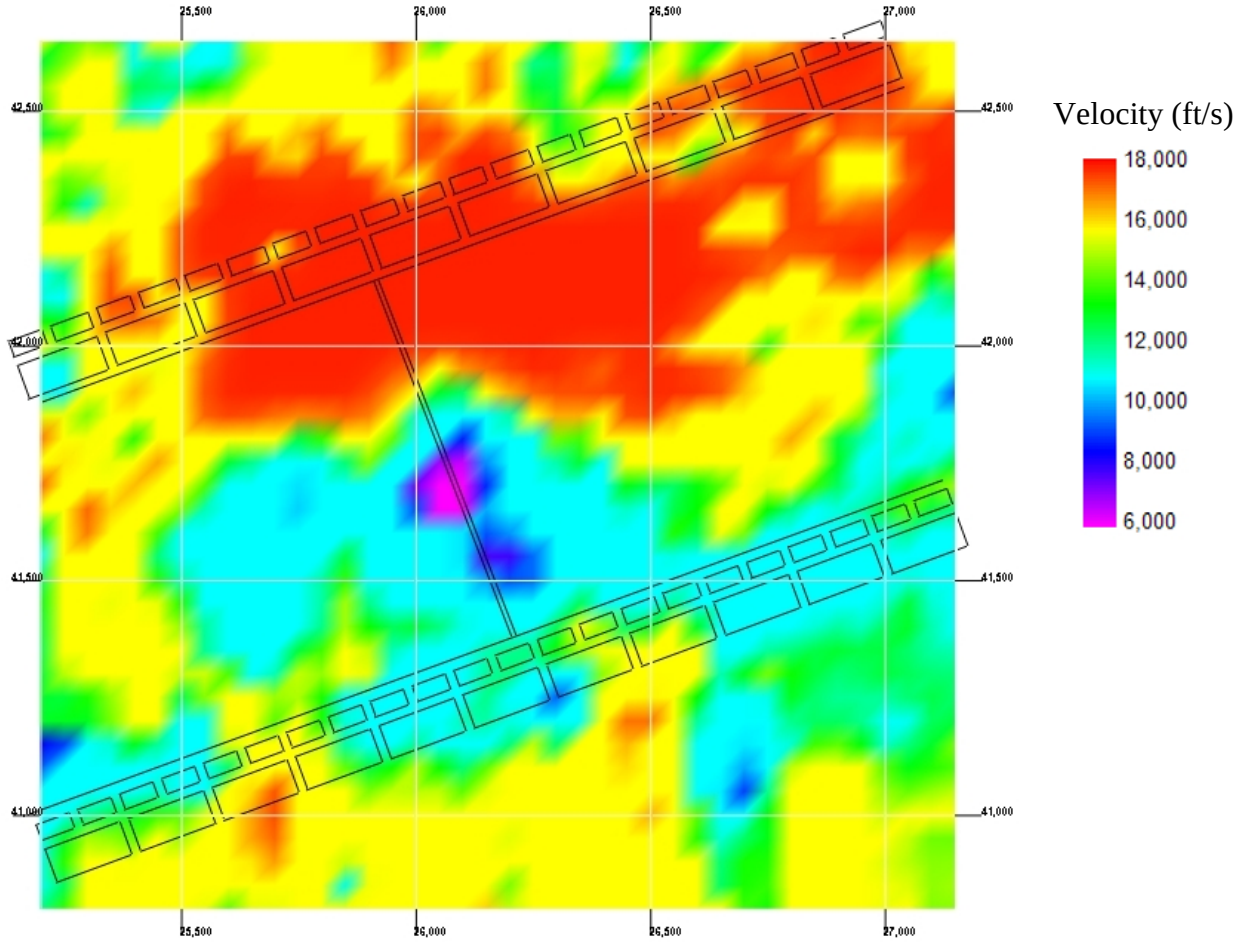

Figure D.21. Velocity tomogram at Z = 5,700 feet.

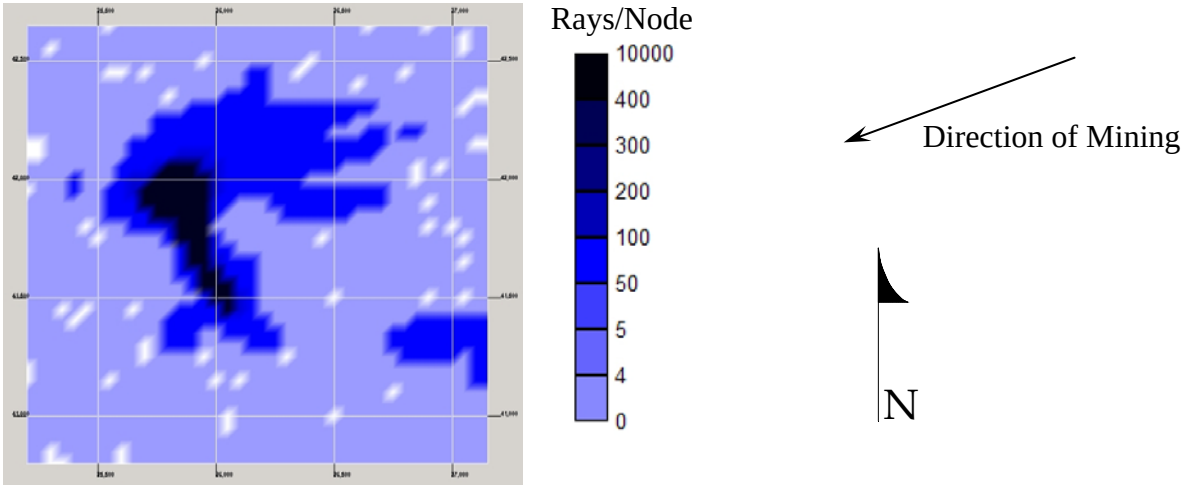

Figure D.22. Ray density plot at Z = 5,700 feet.

08-01-97

Plan View at Z = 5,700 feet (Roof Level)

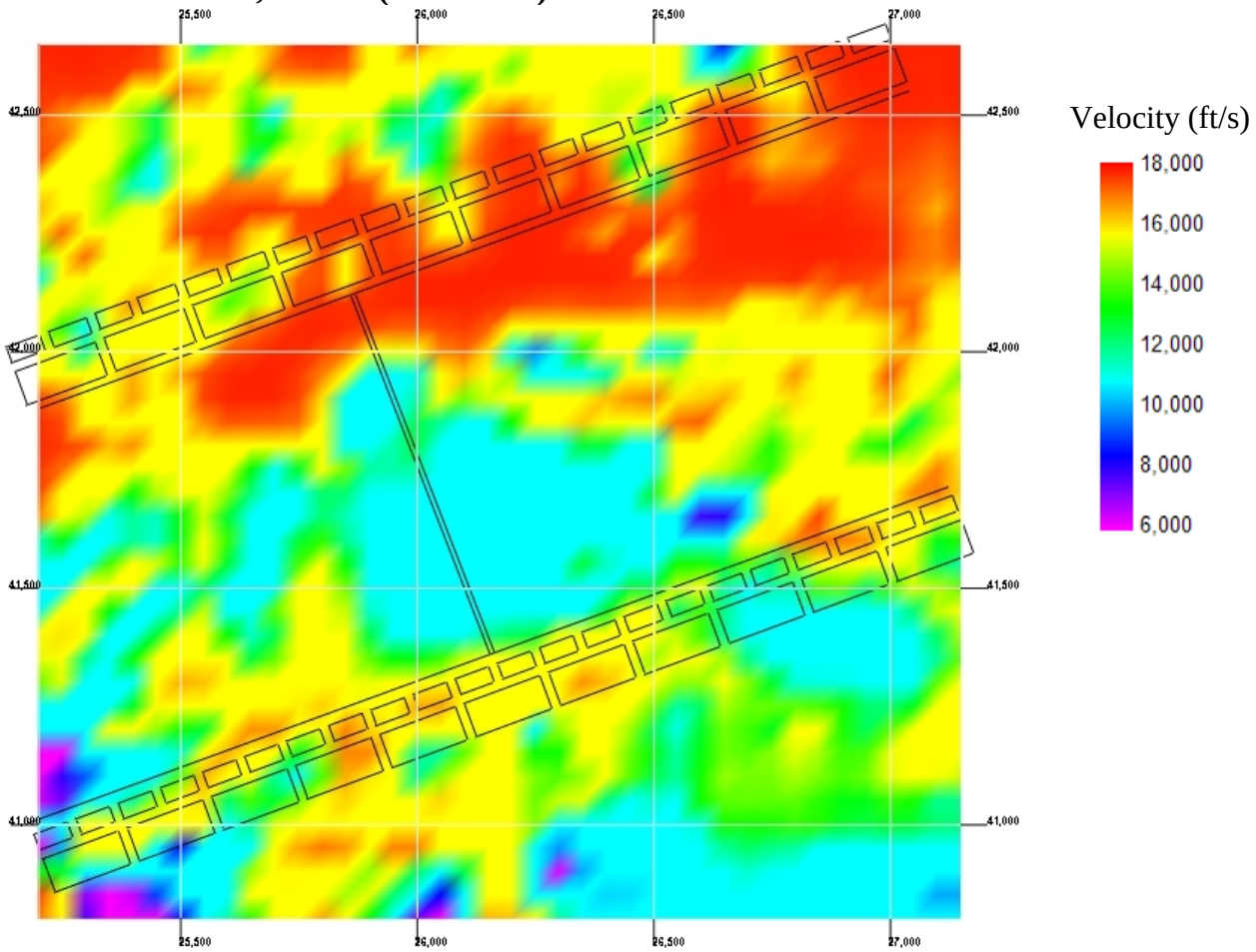

Figure D.23. Velocity tomogram at Z = 5,700 feet.

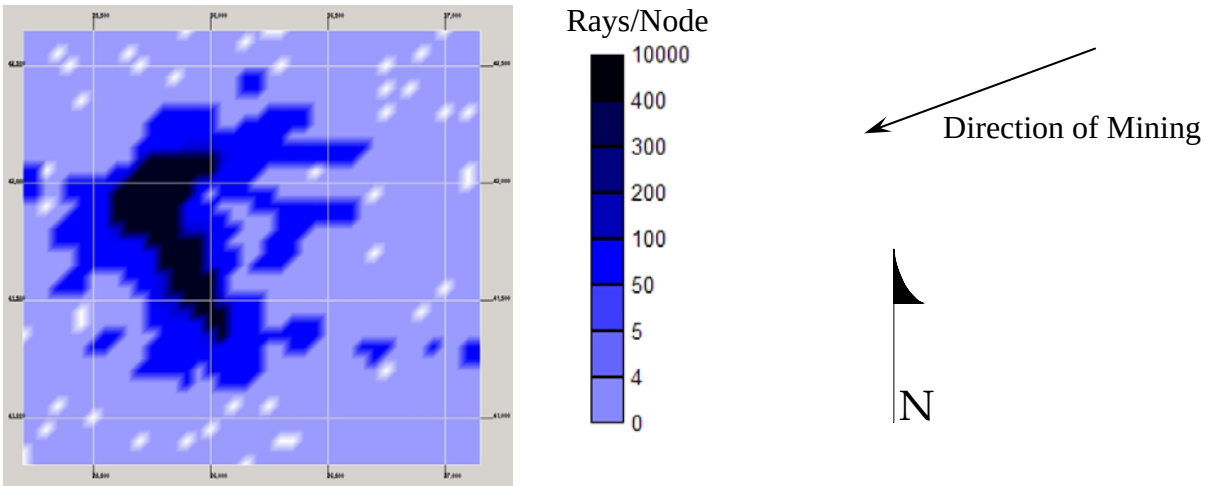

Figure D.24. Ray density plot at Z = 5,700 feet.

08-02-97

Plan View at Z = 5,700 feet (Roof Level)

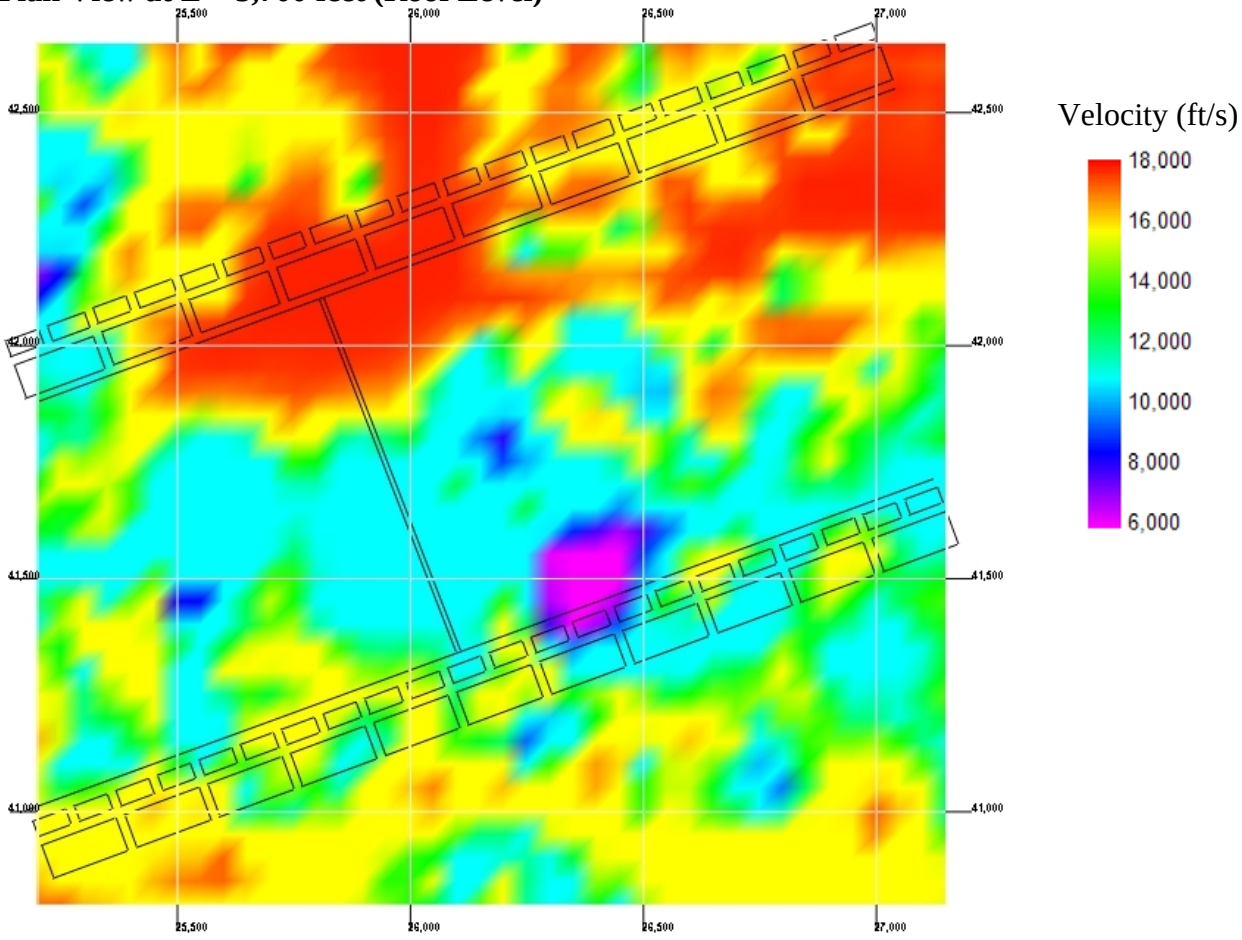

Figure D.25. Velocity tomogram at Z = 5,700 feet.

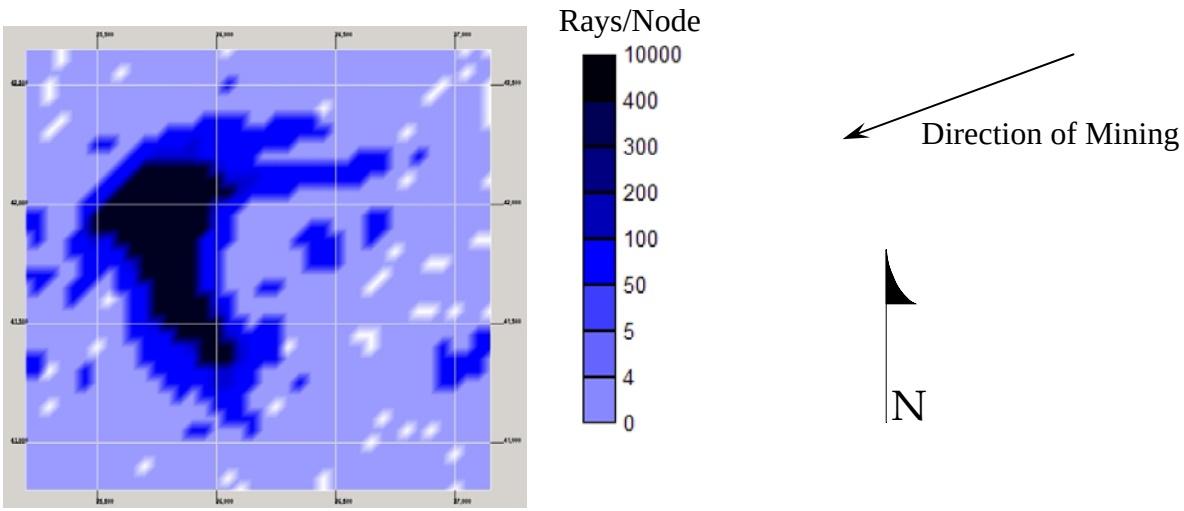

Figure D.26. Ray density plot at Z = 5,700 feet.

08-03-97

Plan View at Z = 5,700 feet (Roof Level)

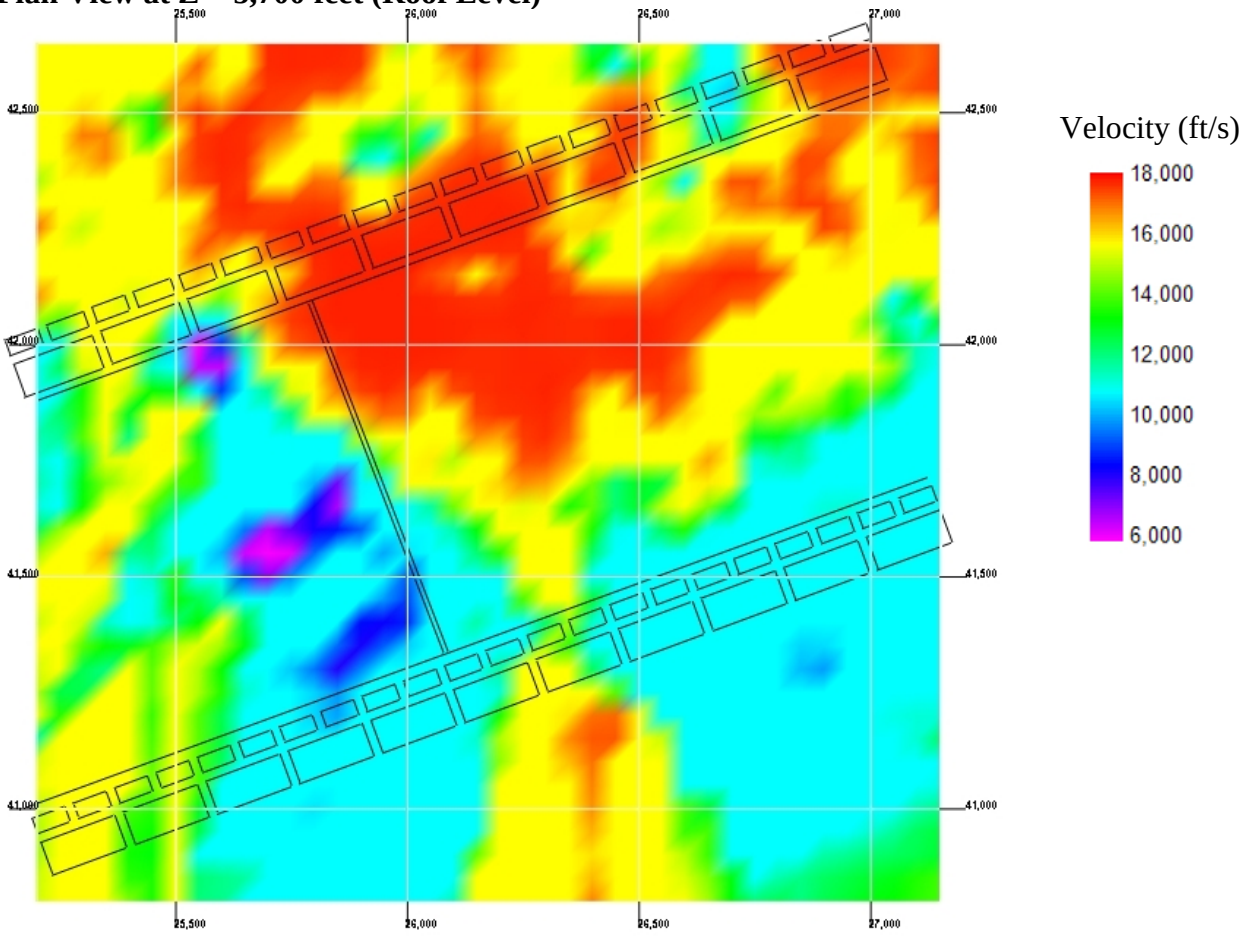

Figure D.27. Velocity tomogram at Z = 5,700 feet.

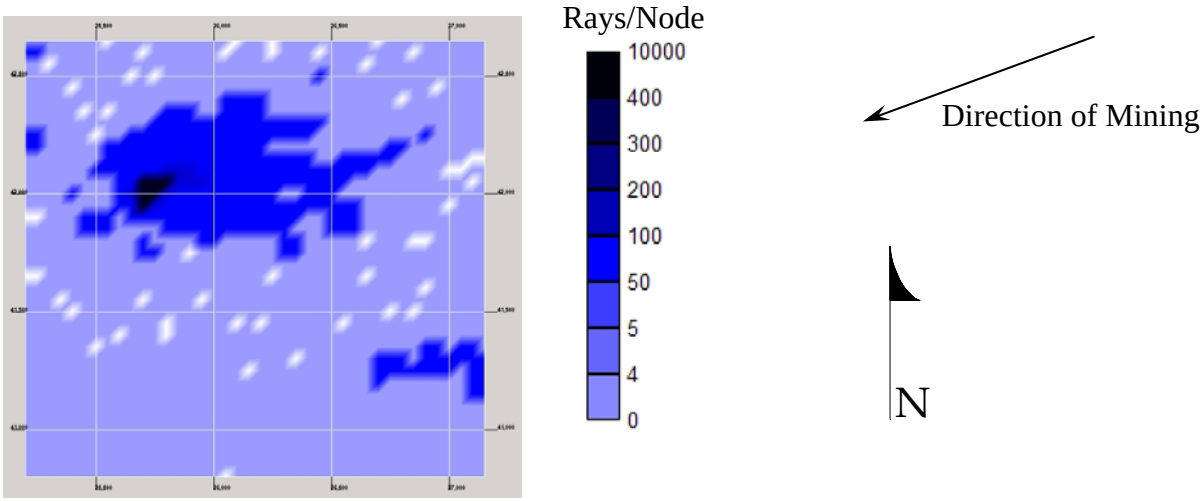

Figure D.28. Ray density plot at Z = 5,700 feet.

08-04-97

Plan View at Z = 5,700 feet (Roof Level)

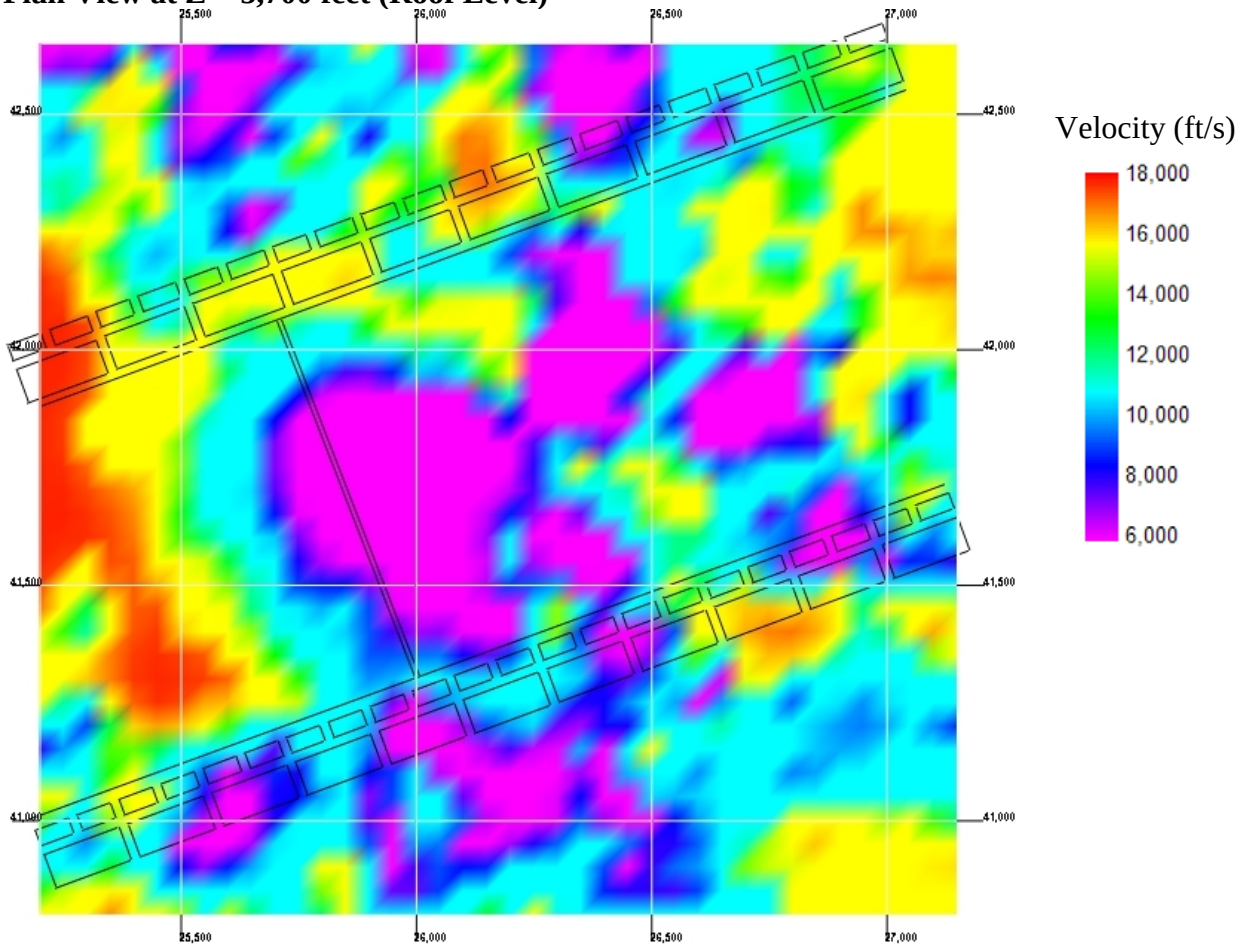

Figure D.29. Velocity tomogram at Z = 5,700 feet.

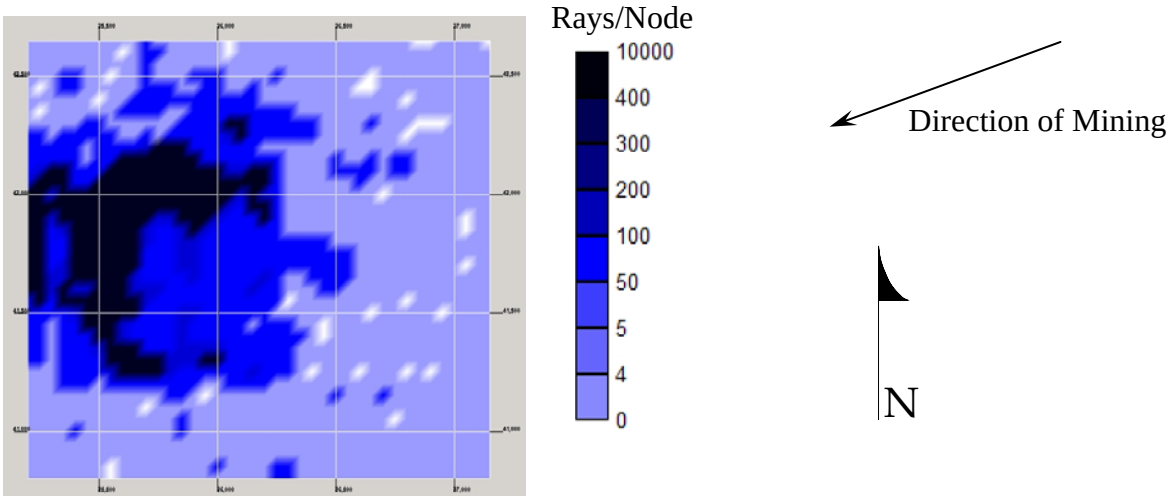

Figure D.30. Ray density plot at Z = 5,700 feet.

08-05-97
Plan View at Z = 5,700 feet (Roof Level)

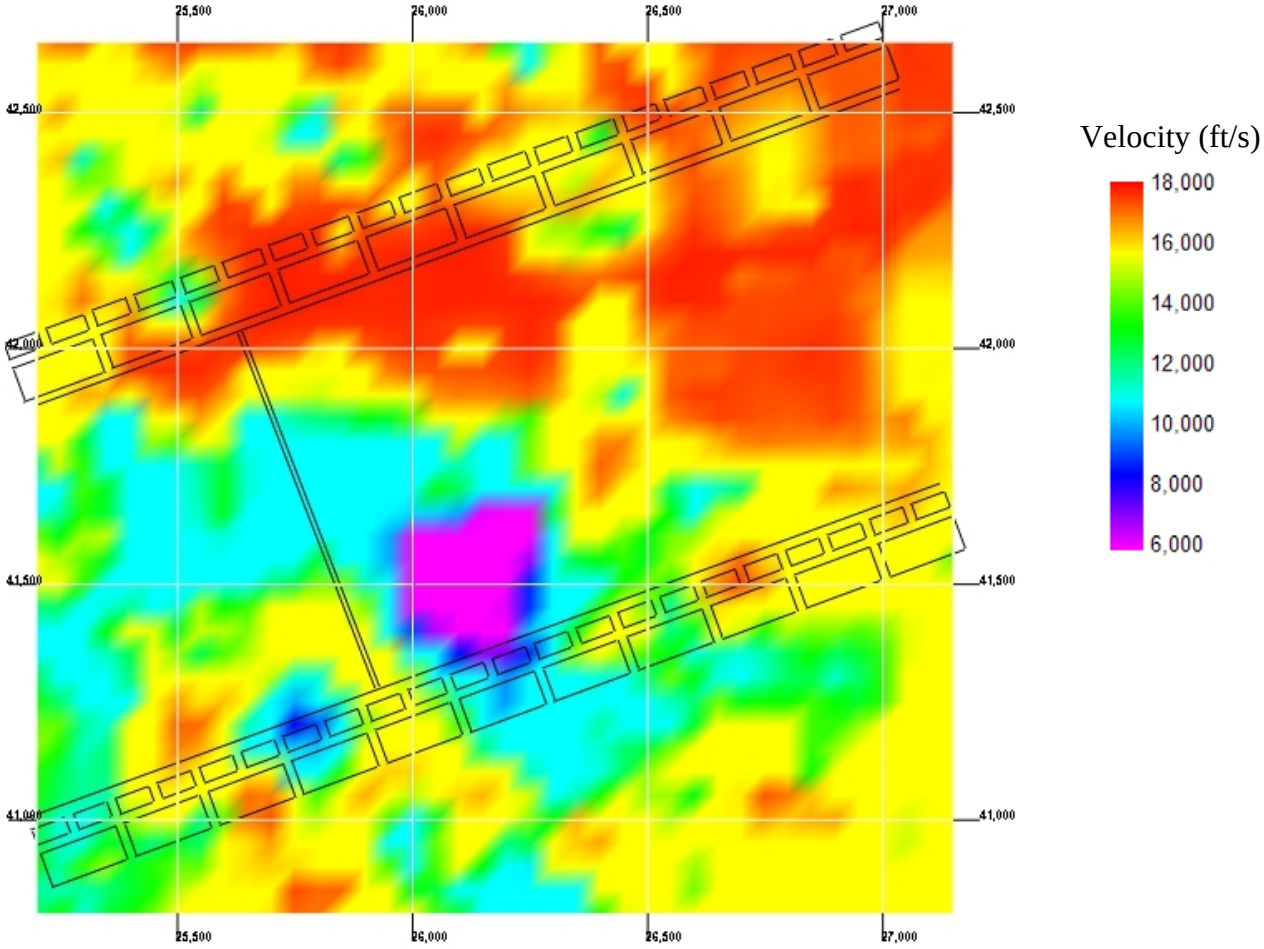

Figure D.31. Velocity tomogram at Z = 5,700 feet.

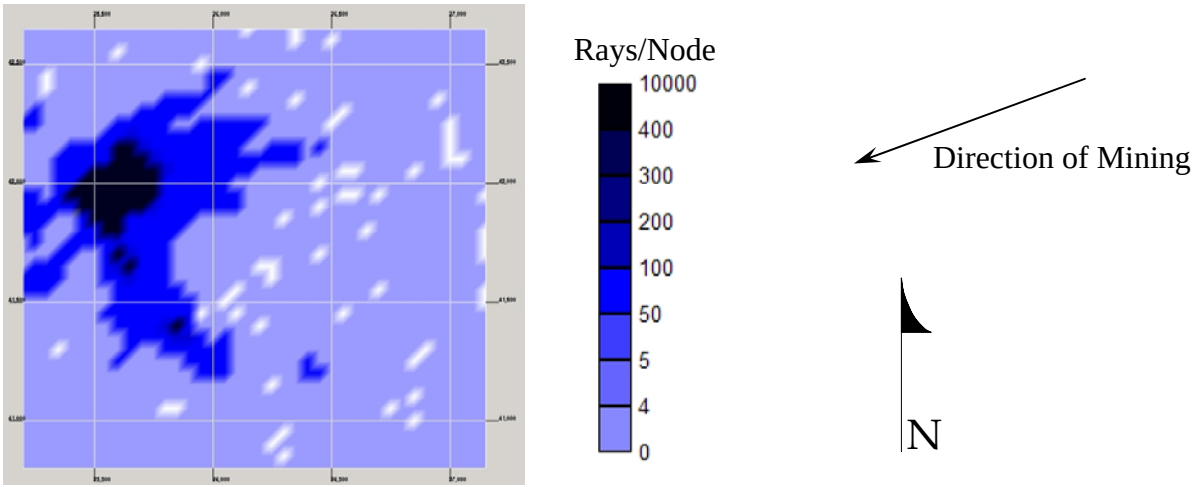

Figure D.32. Ray density plot at Z = 5,700 feet.

08-06-97

Plan View at Z = 5,700 feet (Roof Level)

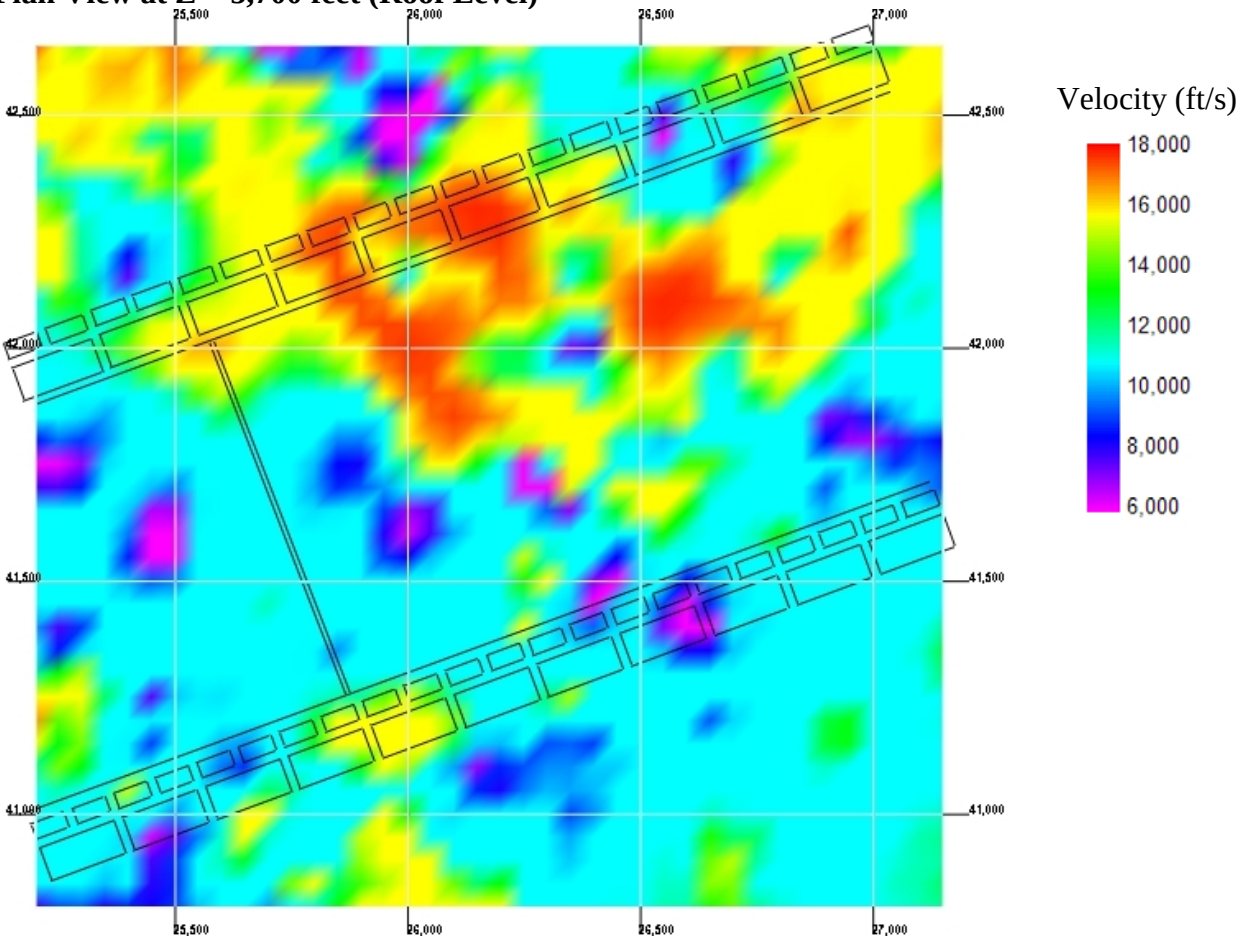

Figure D.33. Velocity tomogram at Z = 5,700 feet.

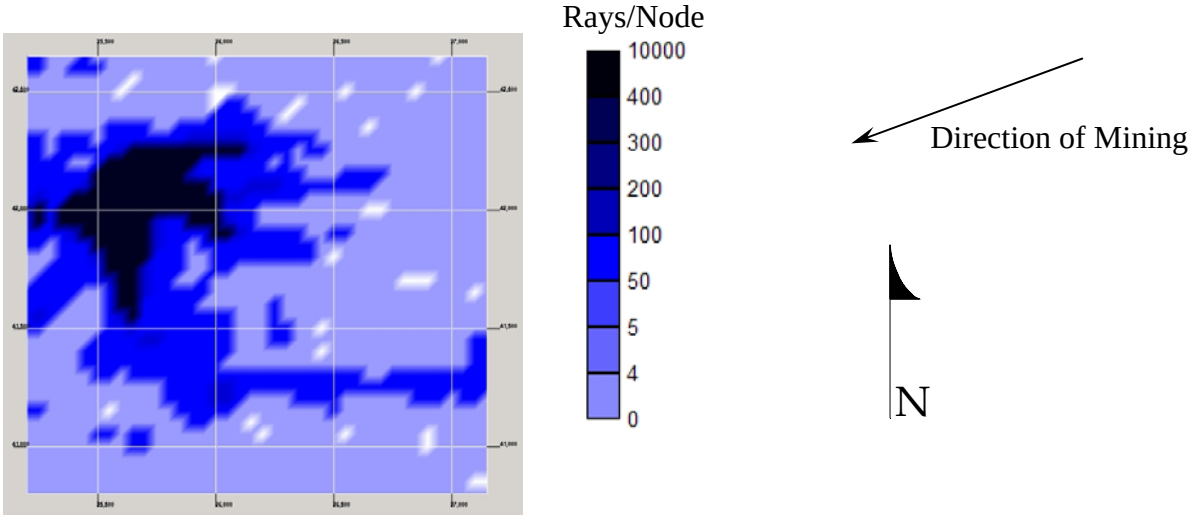

Figure D.34. Ray density plot at Z = 5,700 feet.

08-07-97
Plan View at Z = 5,700 feet (Roof Level)

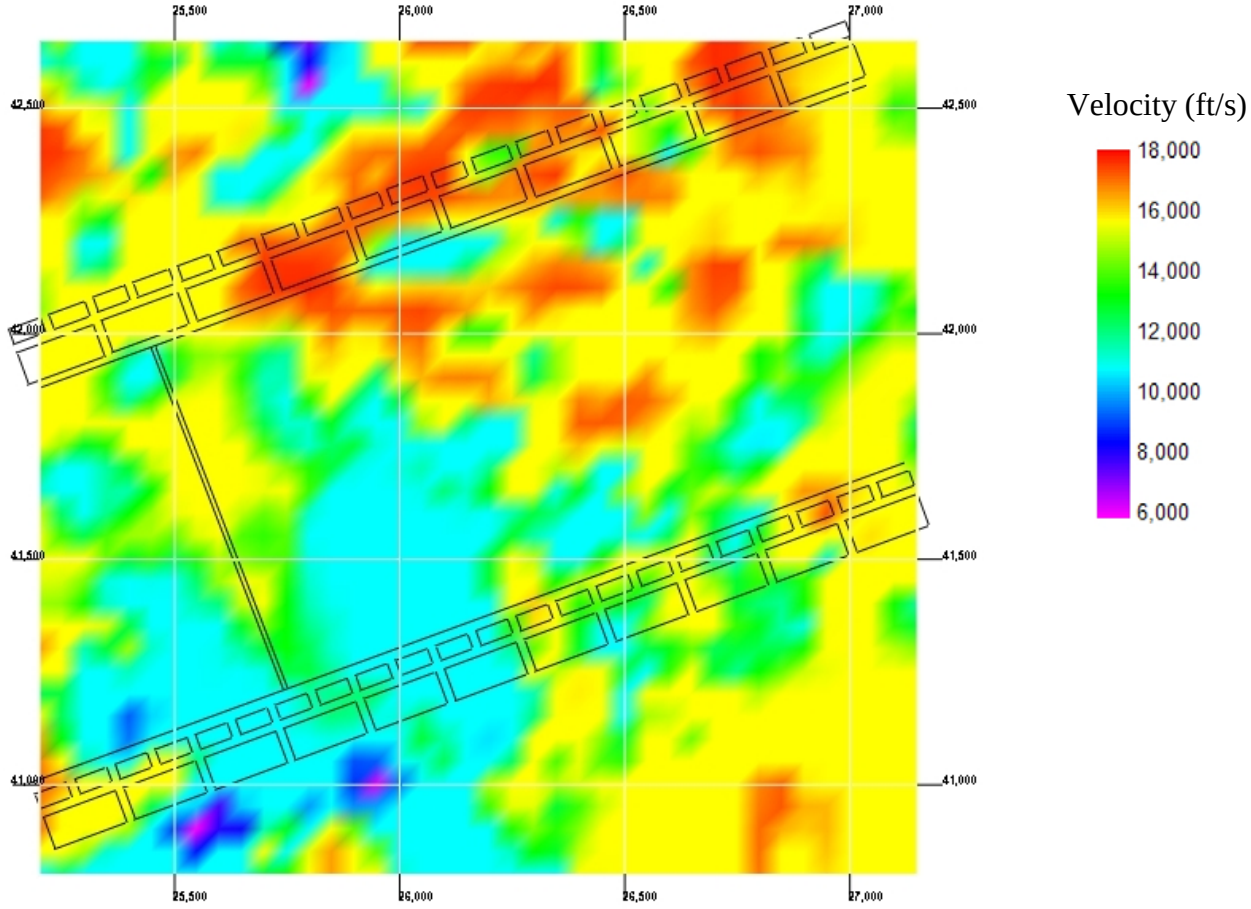

Figure D.35. Velocity tomogram at Z = 5,700 feet.

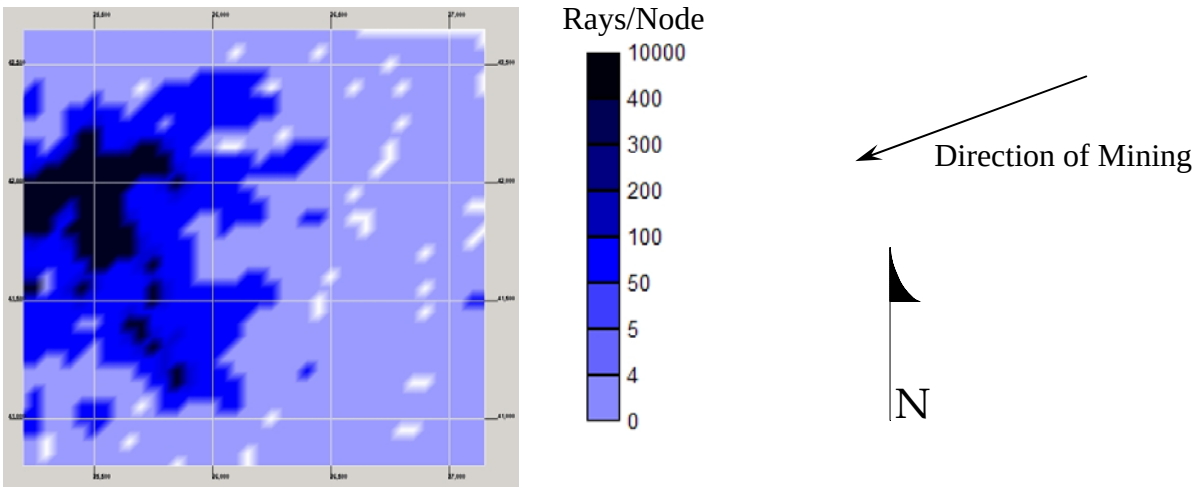

Figure D.36. Ray density plot at Z = 5,700 feet.

APPENDIX E

Velocity Tomograms and Ray Density Plots

VERTICAL PROFILE - MIDFACE
Y = 41, 800 FEET

07-20-97
Section View at Y = 41,800 feet (Midface)

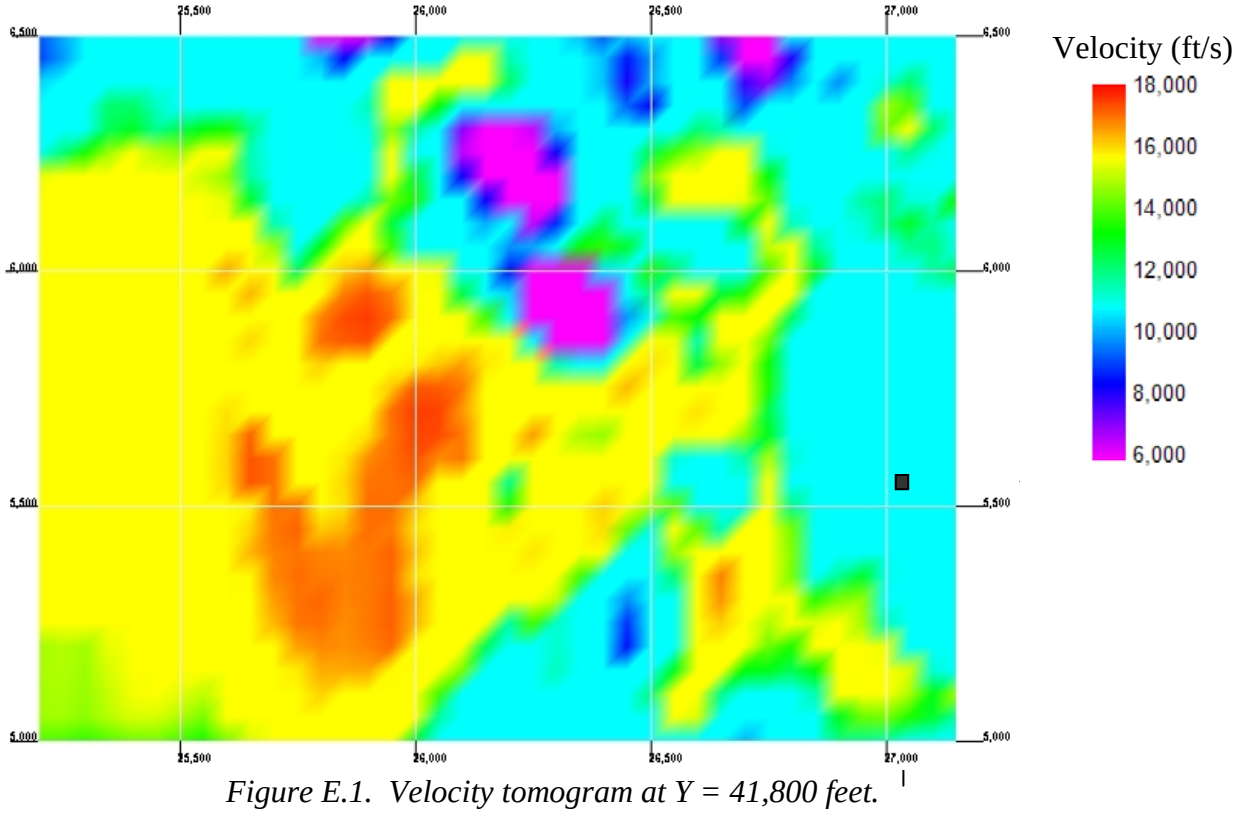

Figure E.1. Velocity tomogram at Y = 41,800 feet.

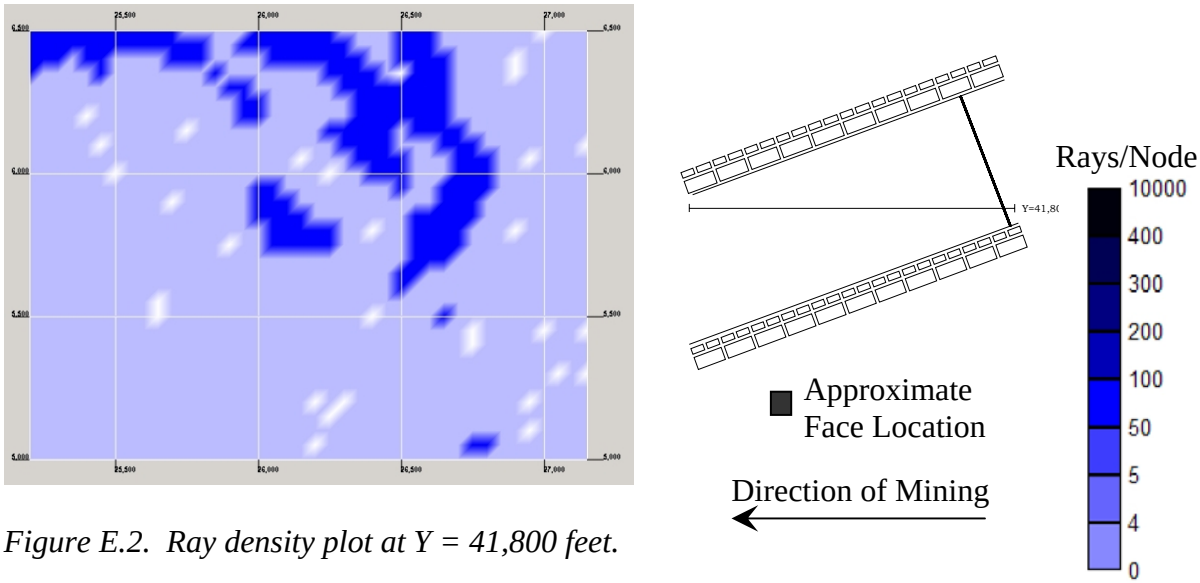

Figure E.2. Ray density plot at Y = 41,800 feet.

07-21-97
Section View at Y = 41,800 feet (Midface)

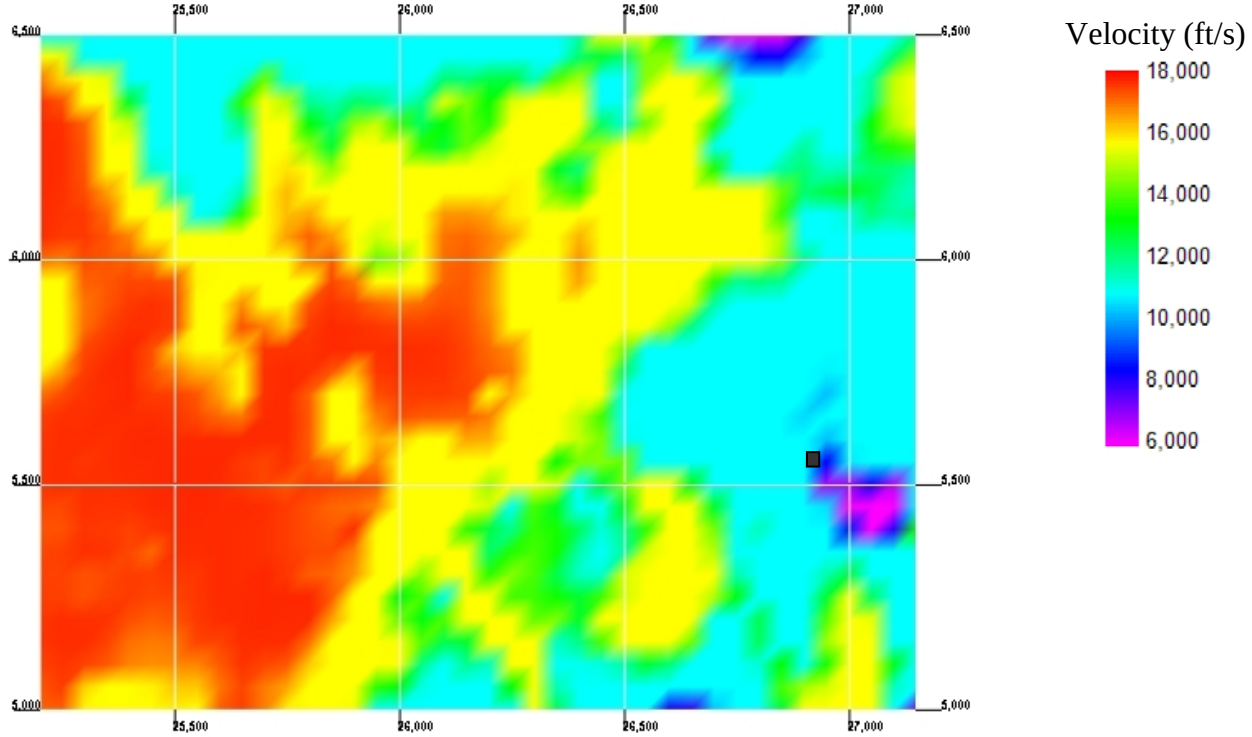

Figure E.3. Velocity tomogram at Y = 41,800 feet.

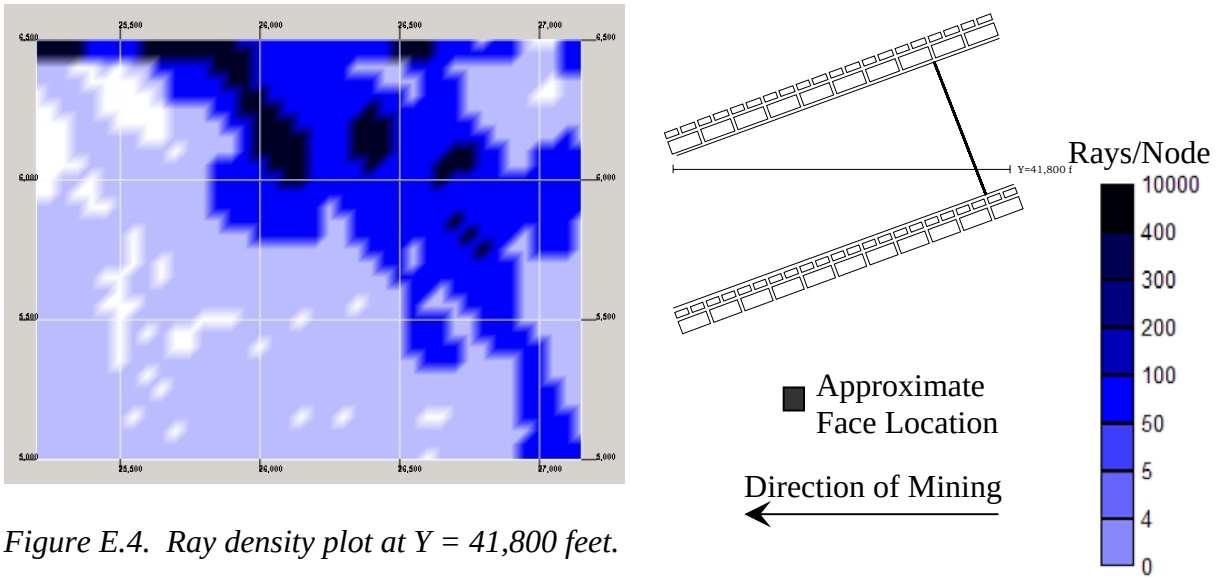

Figure E.4. Ray density plot at Y = 41,800 feet.

07-22-97
Section View at Y = 41,800 feet (Midface)

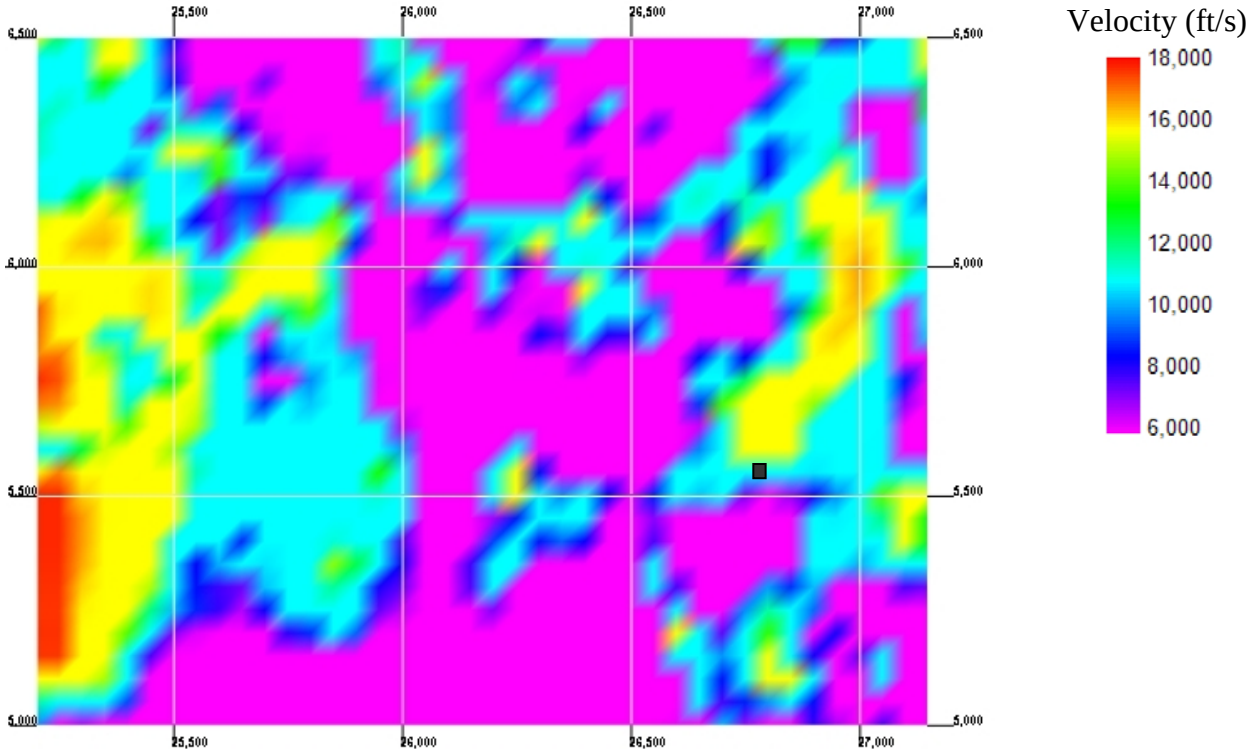

Figure E.5. Velocity tomogram at Y = 41,800 feet.

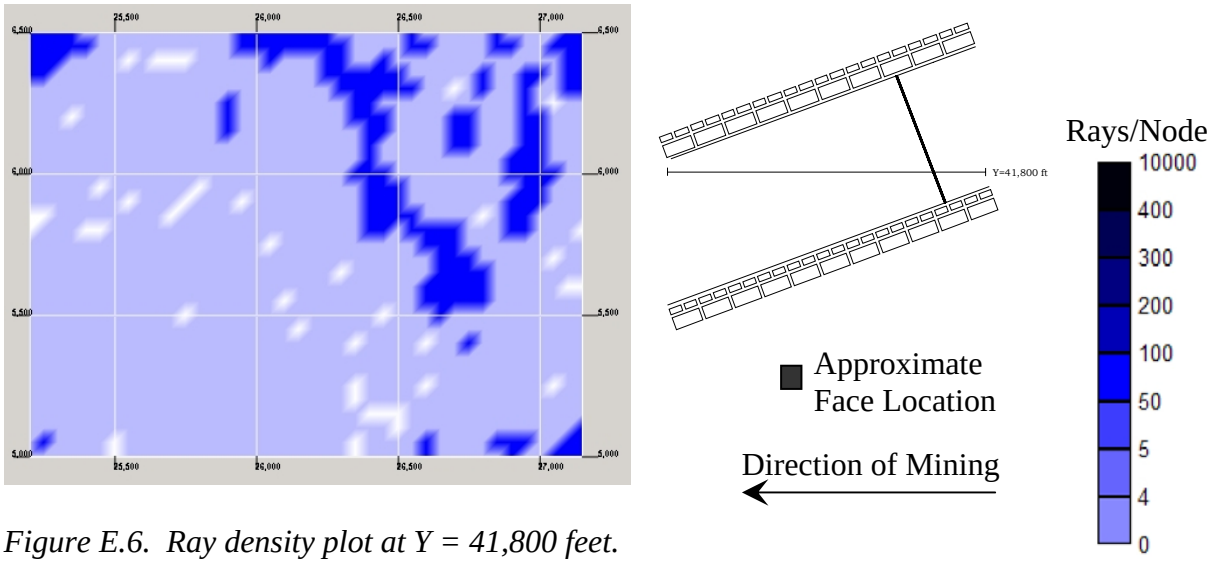

Figure E.6. Ray density plot at Y = 41,800 feet.

07-23-97
Section View at Y = 41,800 feet (Midface)

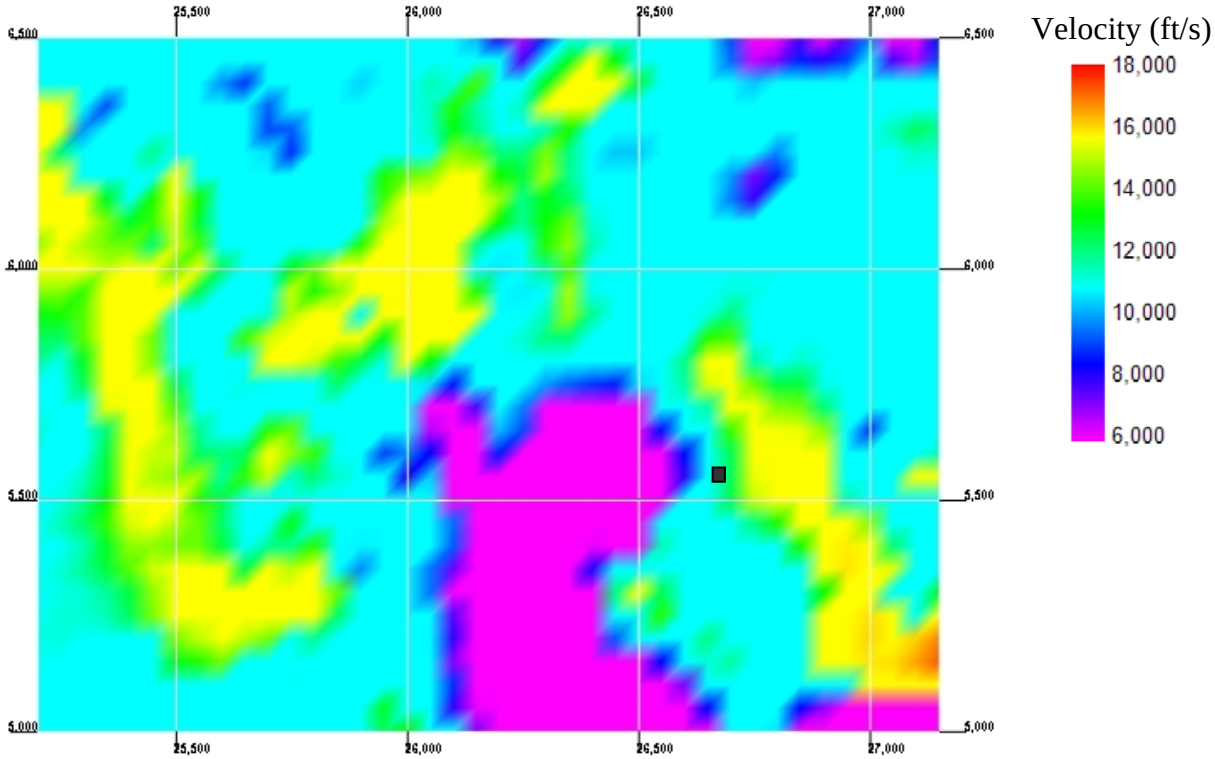

Figure E.7. Velocity tomogram at Y = 41,800 feet.

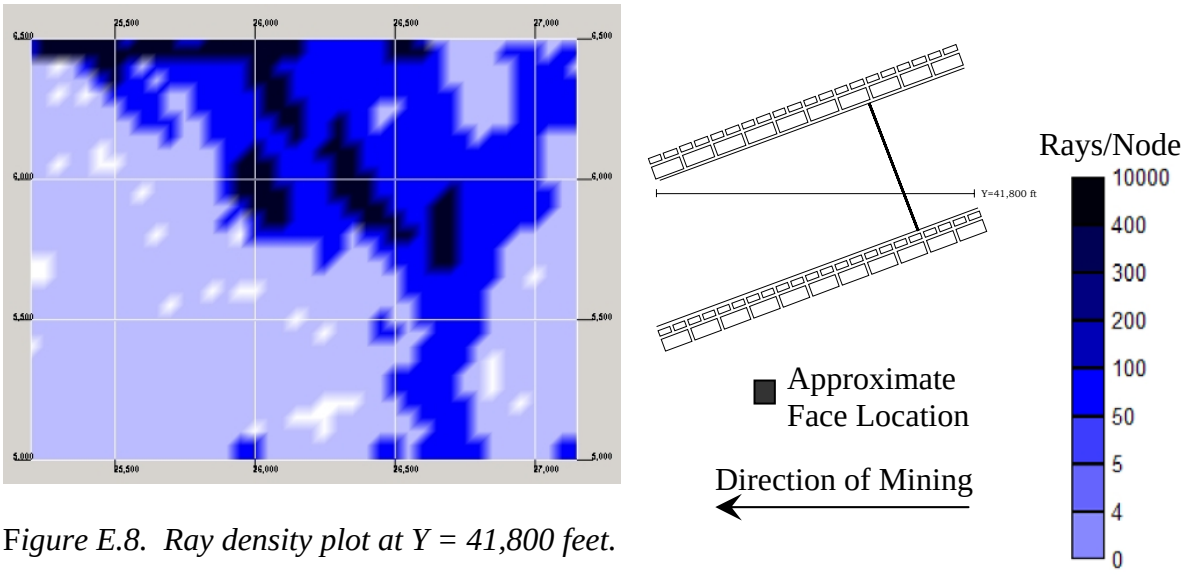

Figure E.8. Ray density plot at Y = 41,800 feet.

07-24-97
Section View at Y = 41,800 feet (Midface)

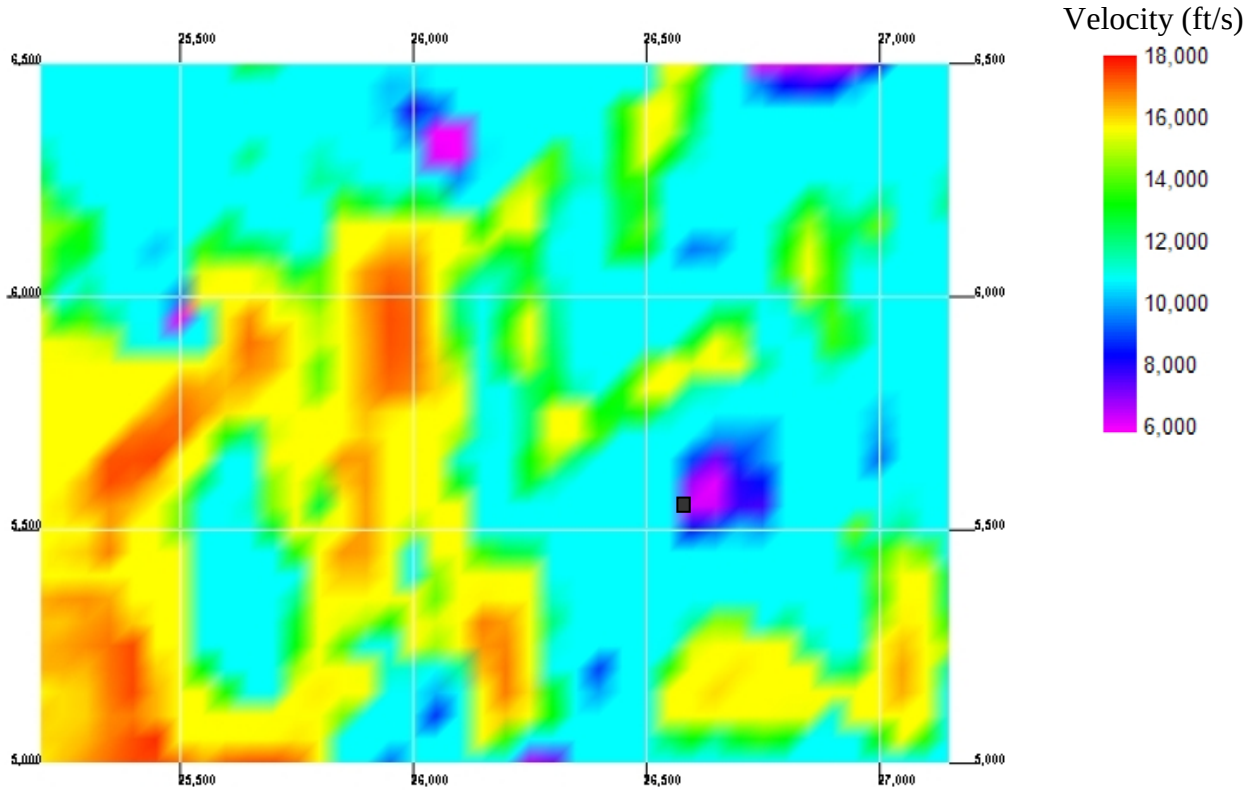

Figure E.9. Velocity tomogram at Y = 41,800 feet.

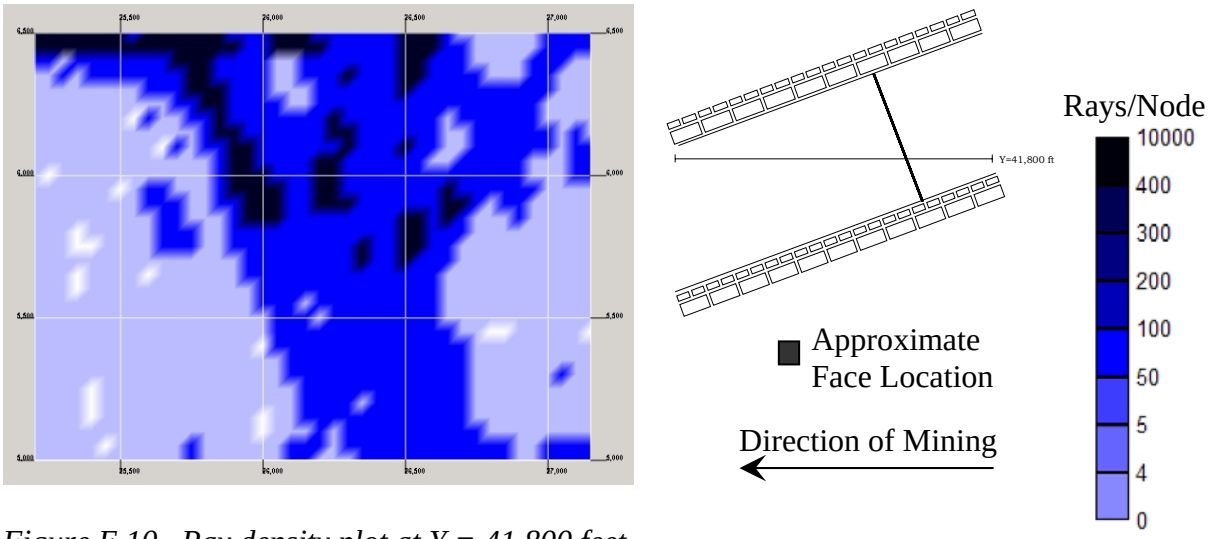

Figure E.10. Ray density plot at Y = 41,800 feet.

07-25-97
Section View at Y = 41,800 feet (Midface)

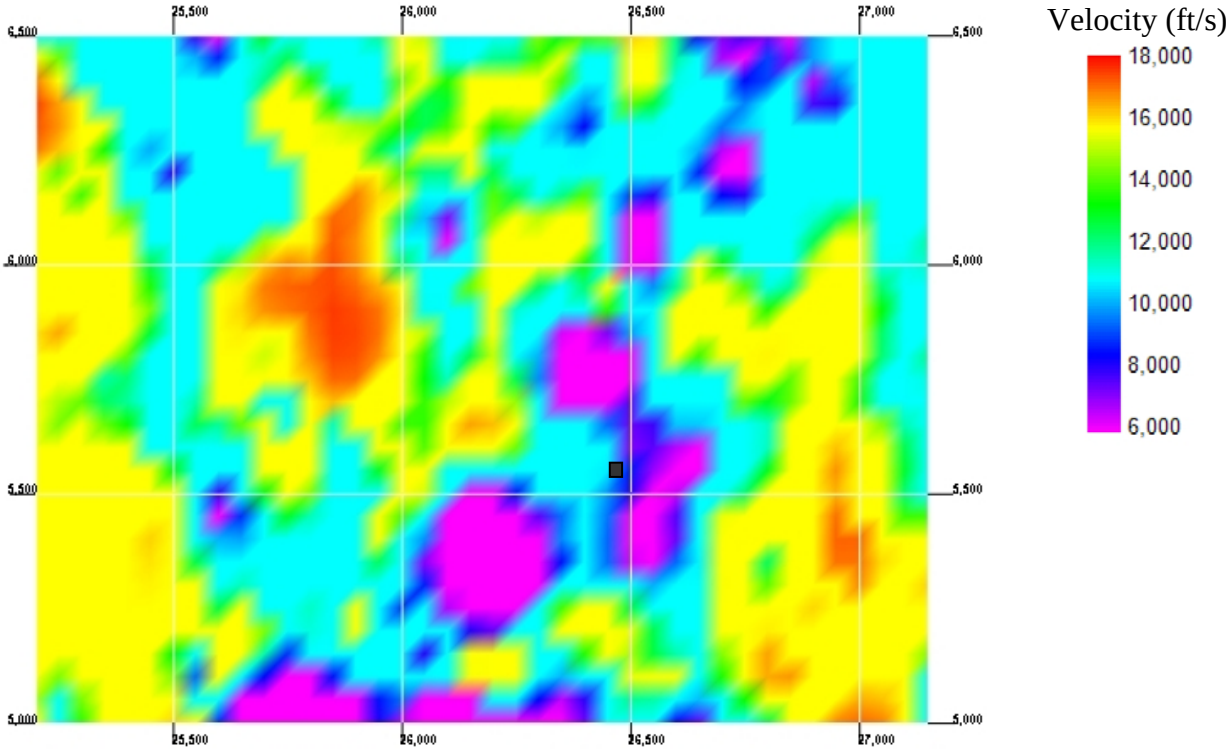

Figure E.11. Velocity tomogram at Y = 41,800 feet.

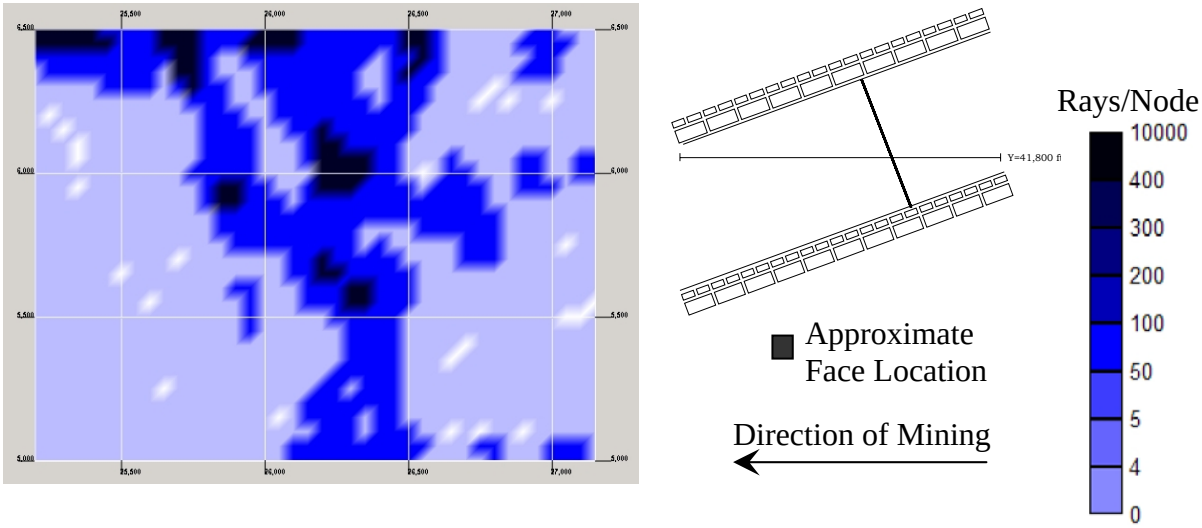

Figure E.12. Ray density plot at Y = 41,800 feet.

07-26-97
Section View at Y = 41,800 feet (Midface)

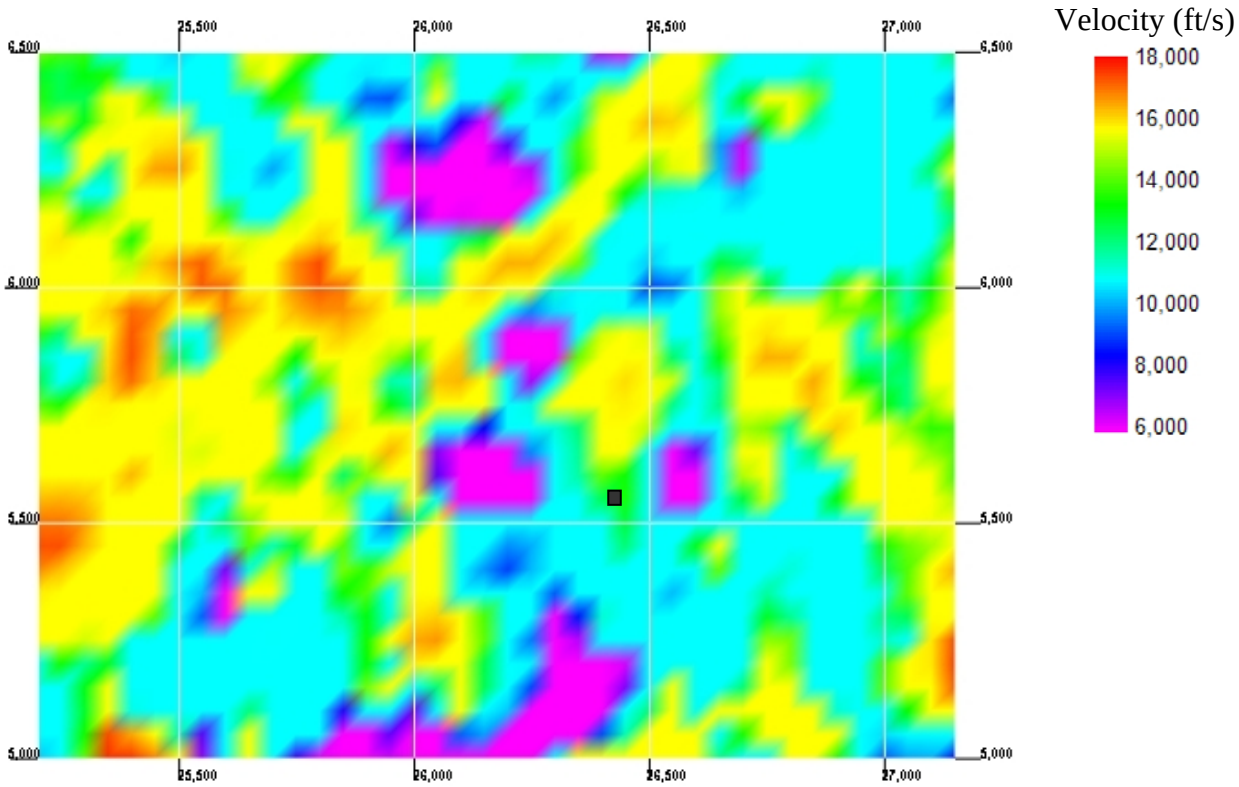

Figure F.13. Velocity tomogram at Y = 41,800 feet.

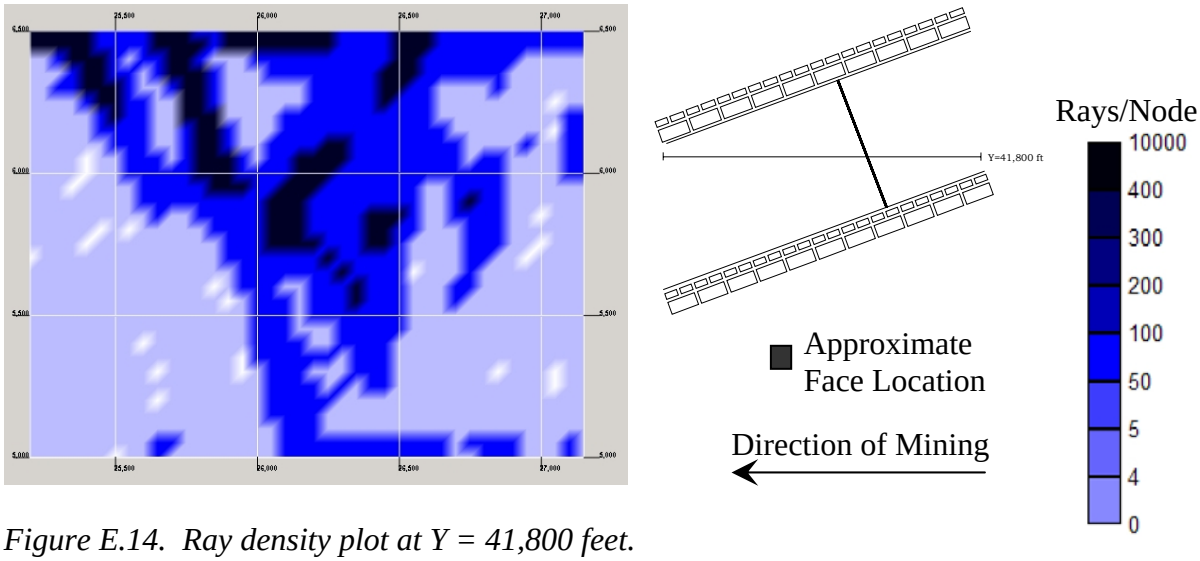

Figure E.14. Ray density plot at Y = 41,800 feet.

07-27-97
Section View at Y = 41,800 feet (Midface)

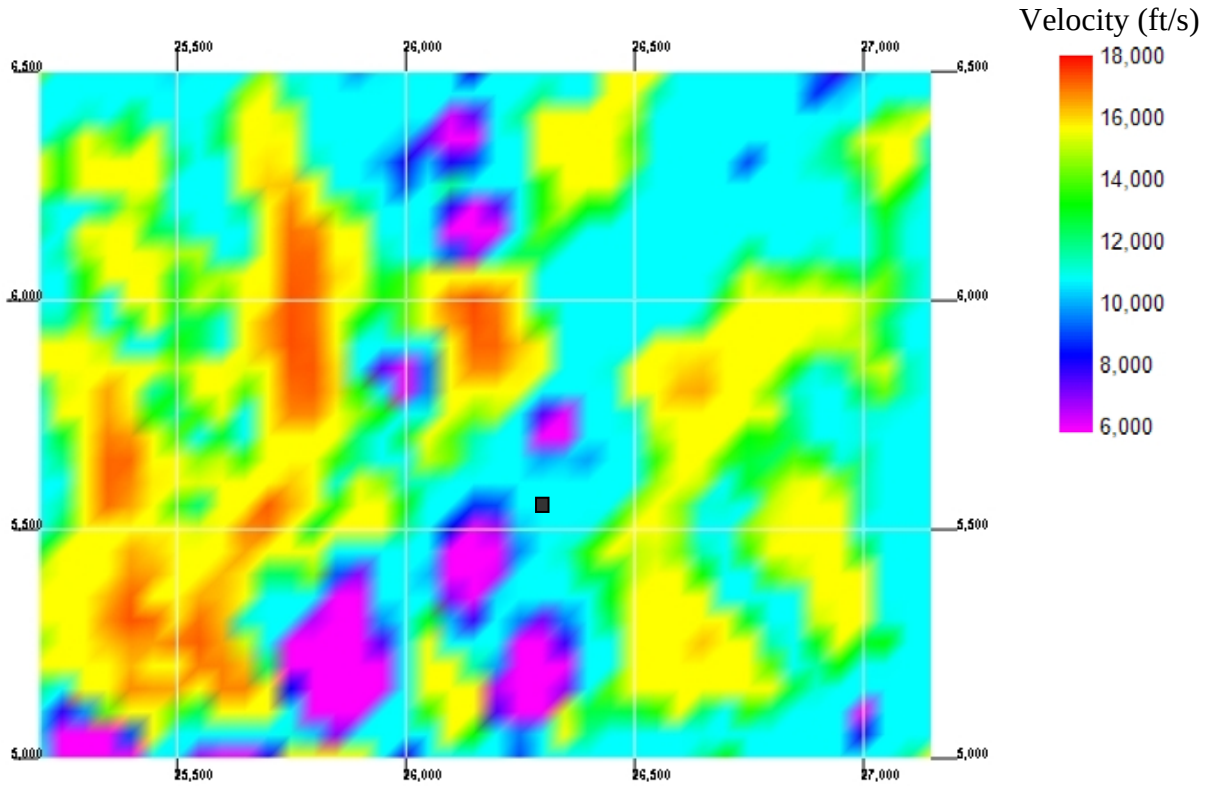

Figure F.15. Velocity tomogram at Y = 41,800 feet.

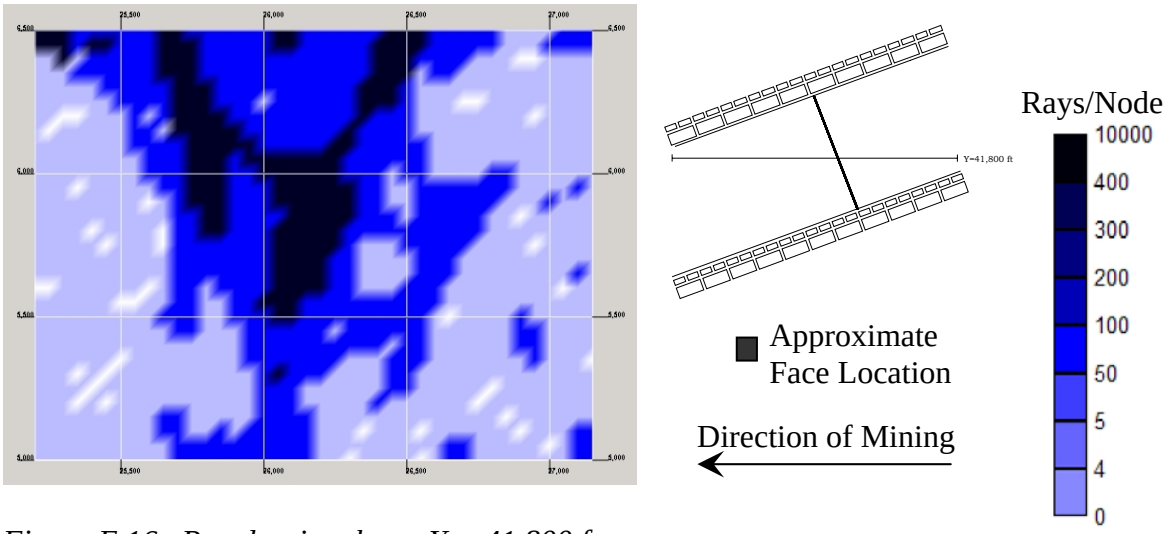

Figure E.16. Ray density plot at Y = 41,800 feet.

07-28-97
Section View at Y = 41,800 feet (Midface)

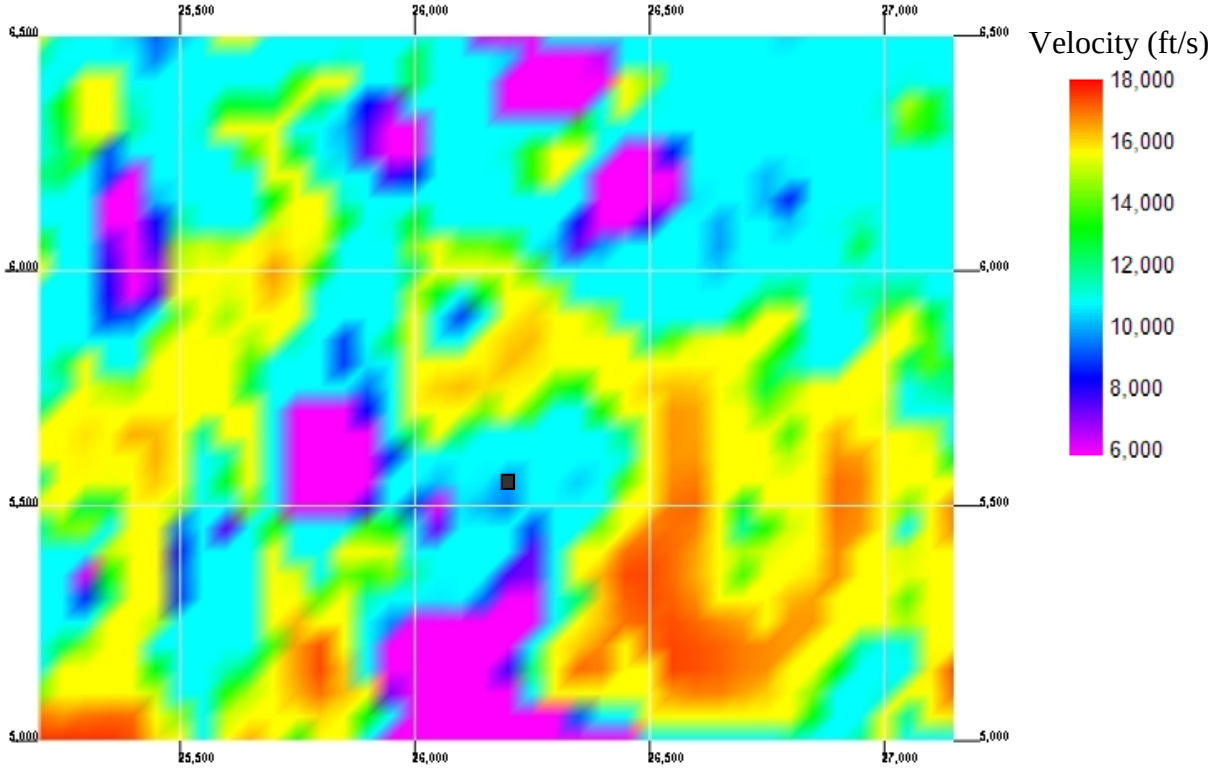

Figure F.17. Velocity tomogram at Y = 41,800 feet.

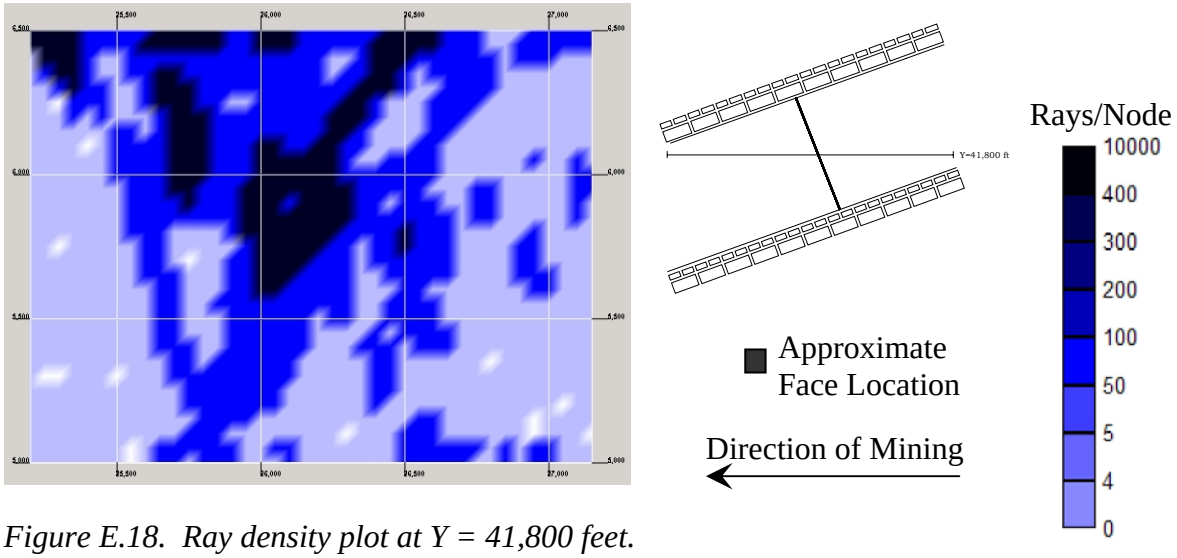

Figure E.18. Ray density plot at Y = 41,800 feet.

07-30-97
Section View at Y = 41,800 feet (Midface)

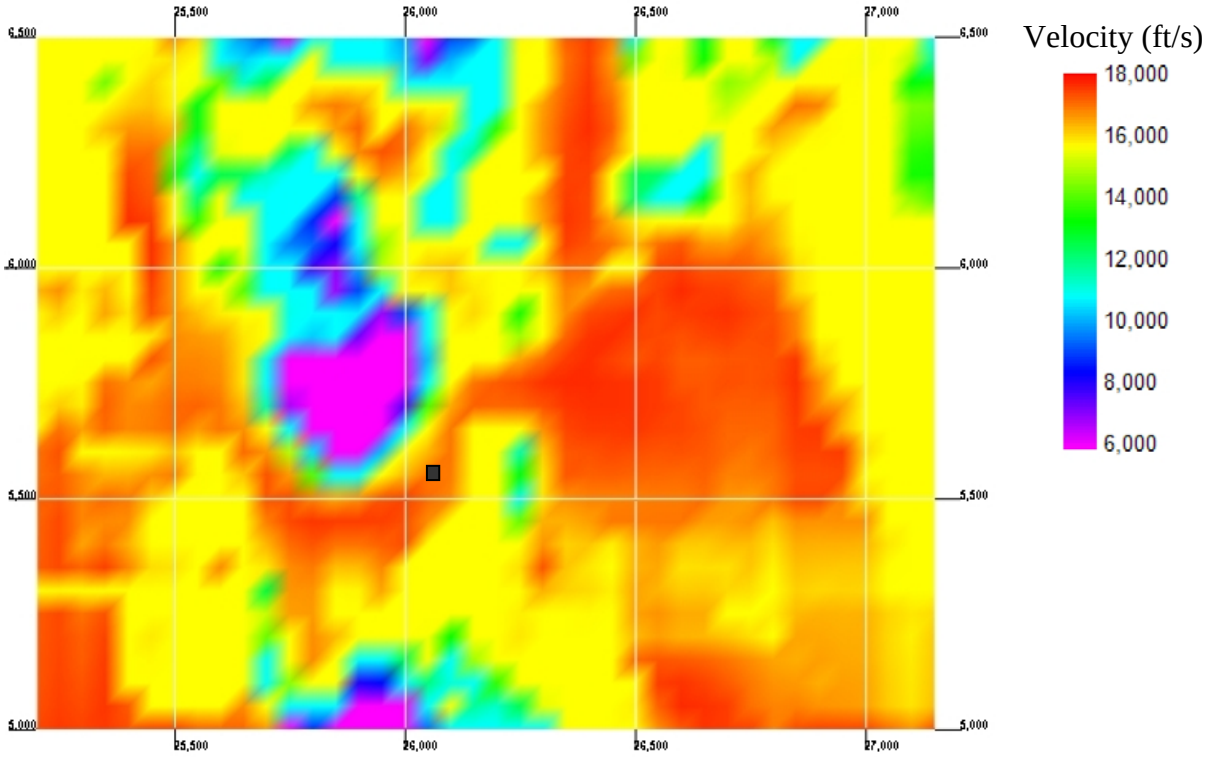

Figure E.19. Velocity tomogram at Y = 41,800 feet.

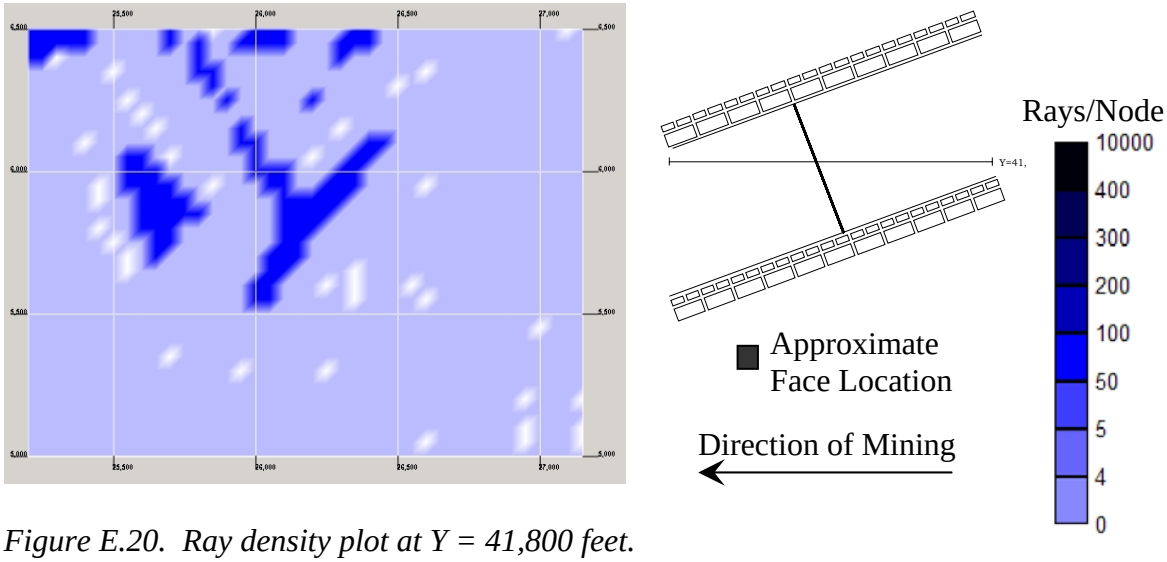

Figure E.20. Ray density plot at Y = 41,800 feet.

07-31-97
Section View at Y = 41,800 feet (Midface)

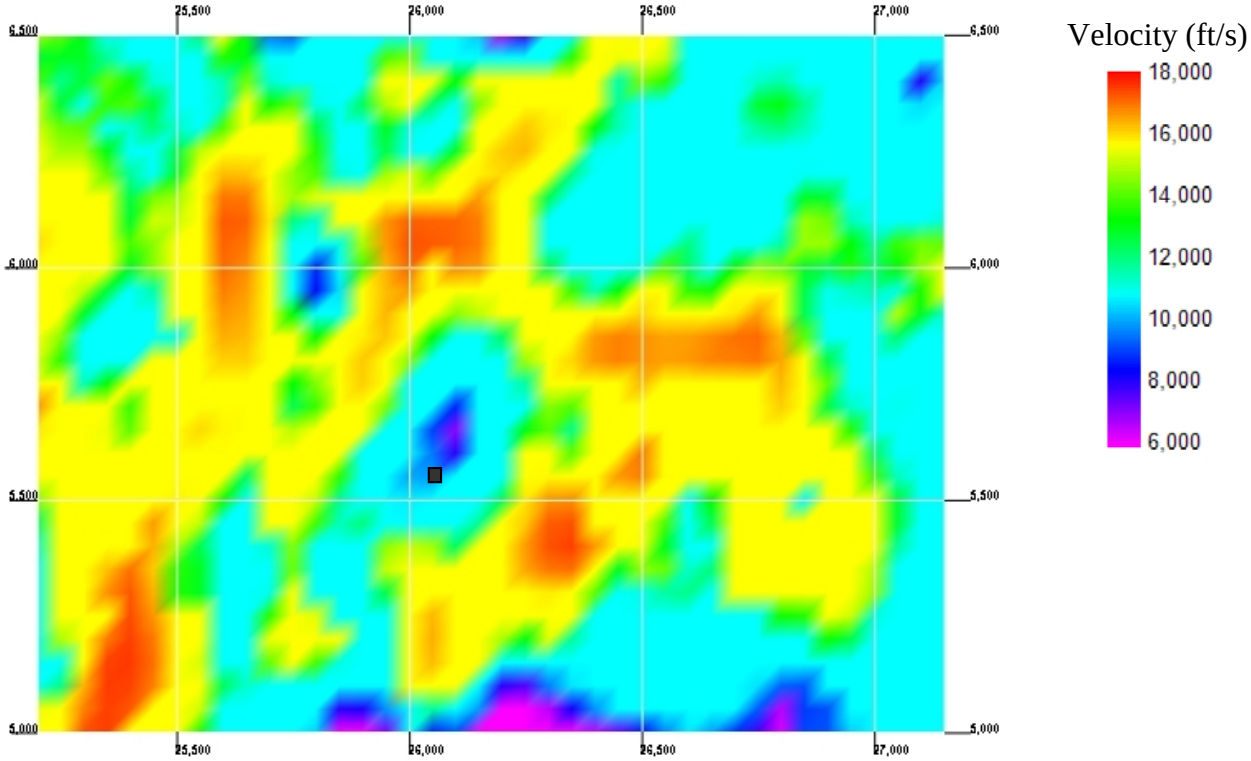

Figure E.21. Velocity tomogram at Y = 41,800 feet.

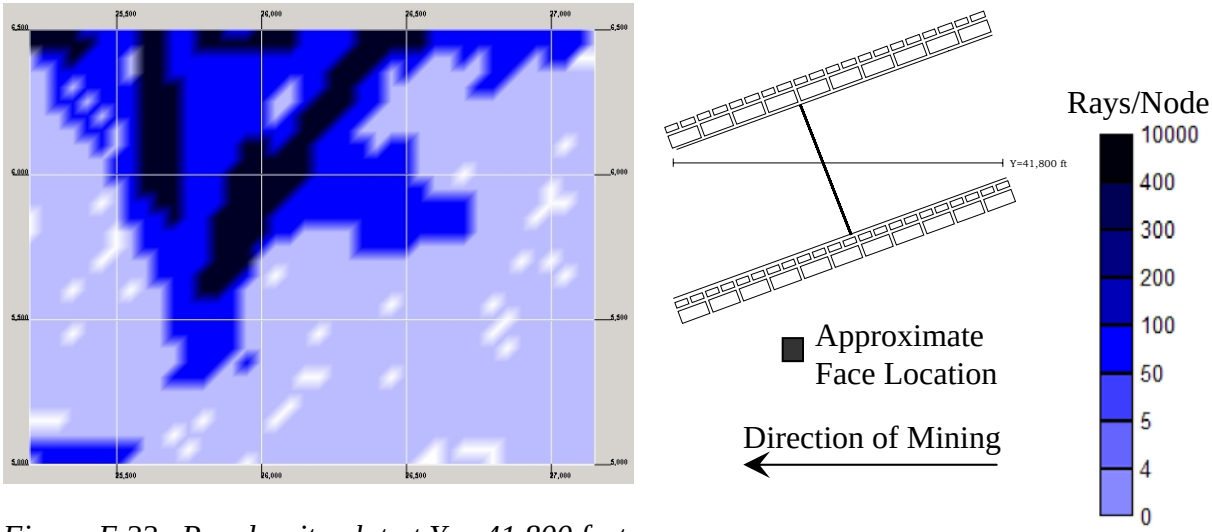

Figure E.22. Ray density plot at Y = 41,800 feet.

08-01-97
Section View at Y = 41,800 feet (Midface)

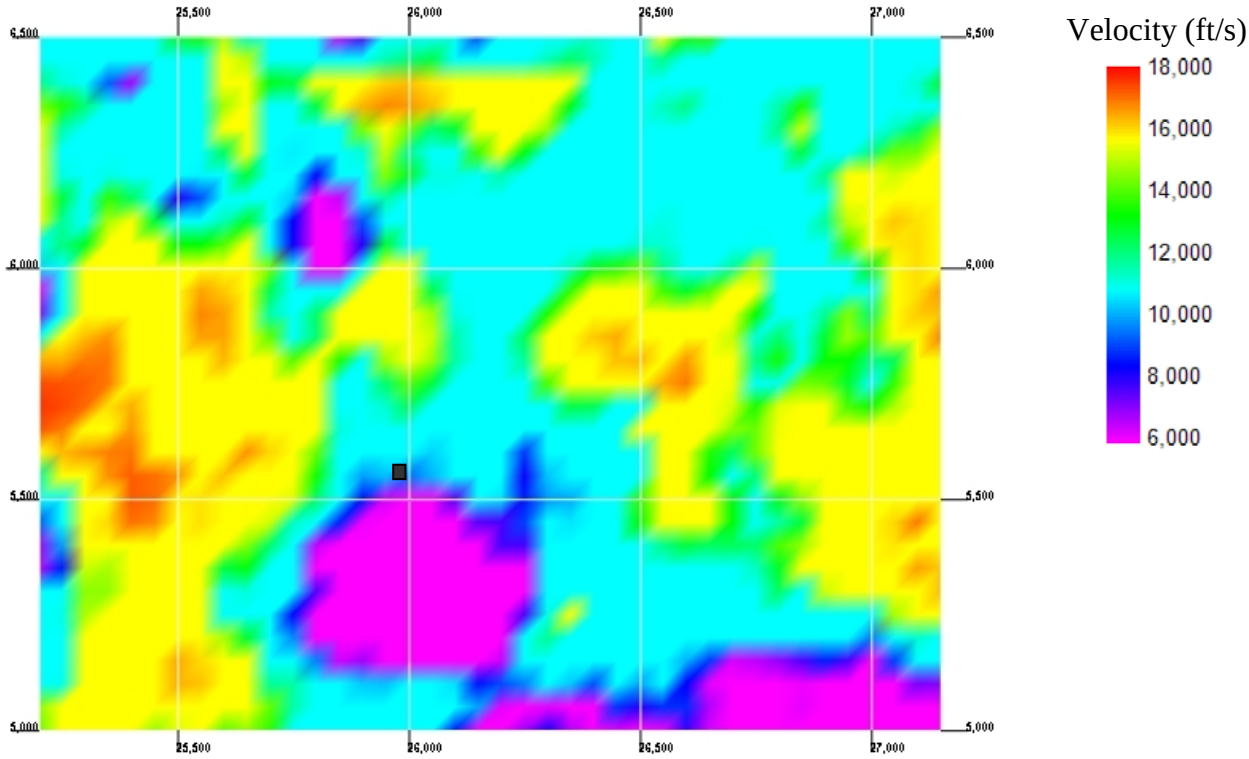

Figure E.23. Velocity tomogram at Y = 41,800 feet.

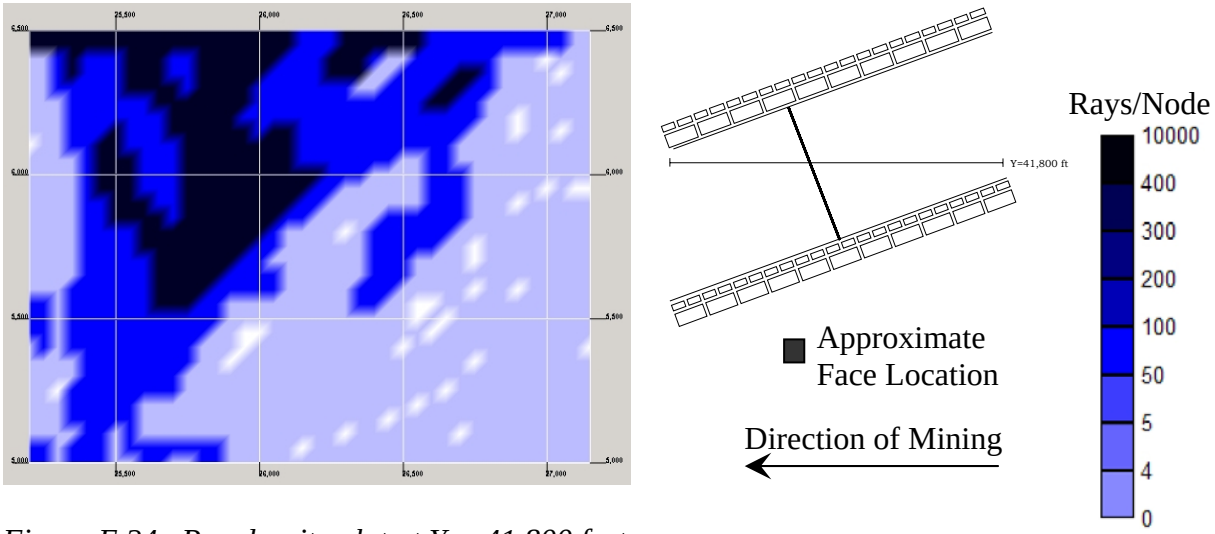

Figure E.24. Ray density plot at Y = 41,800 feet.

08-02-97
Section View at Y = 41,800 feet (Midface)

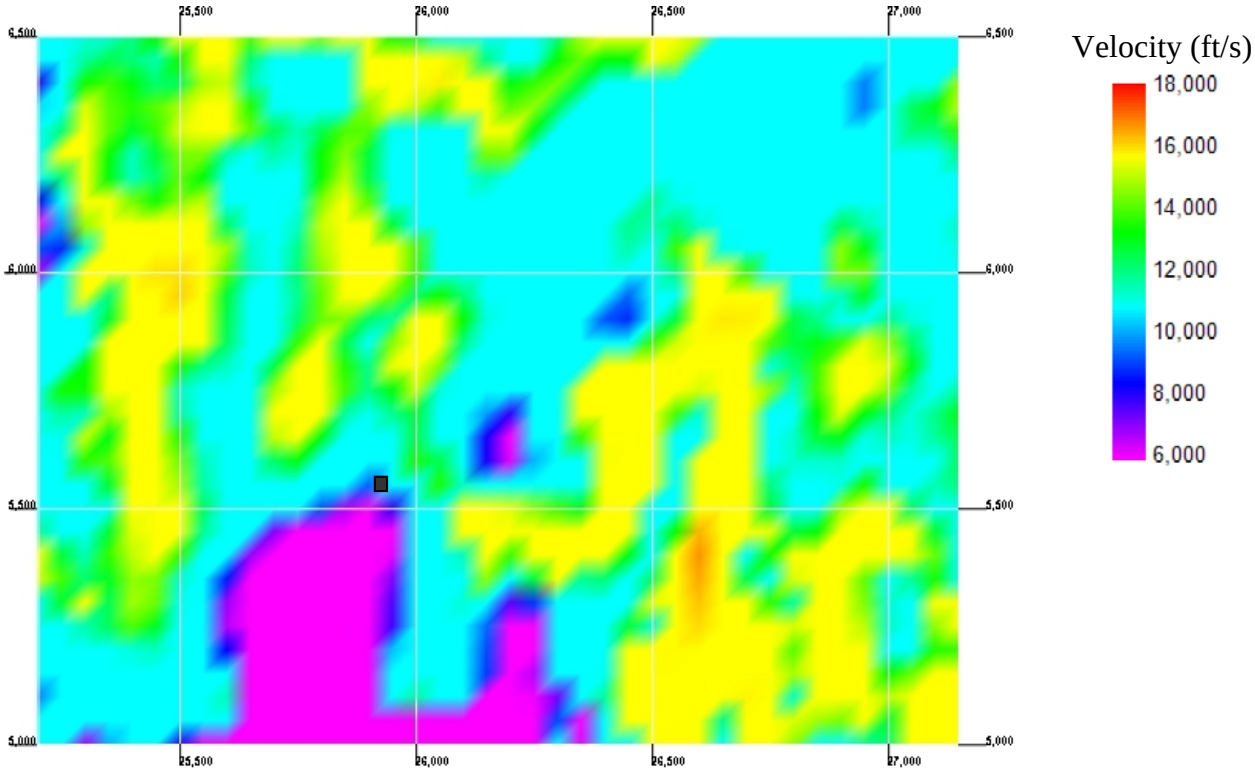

Figure E.25. Velocity tomogram at Y = 41,800 feet.

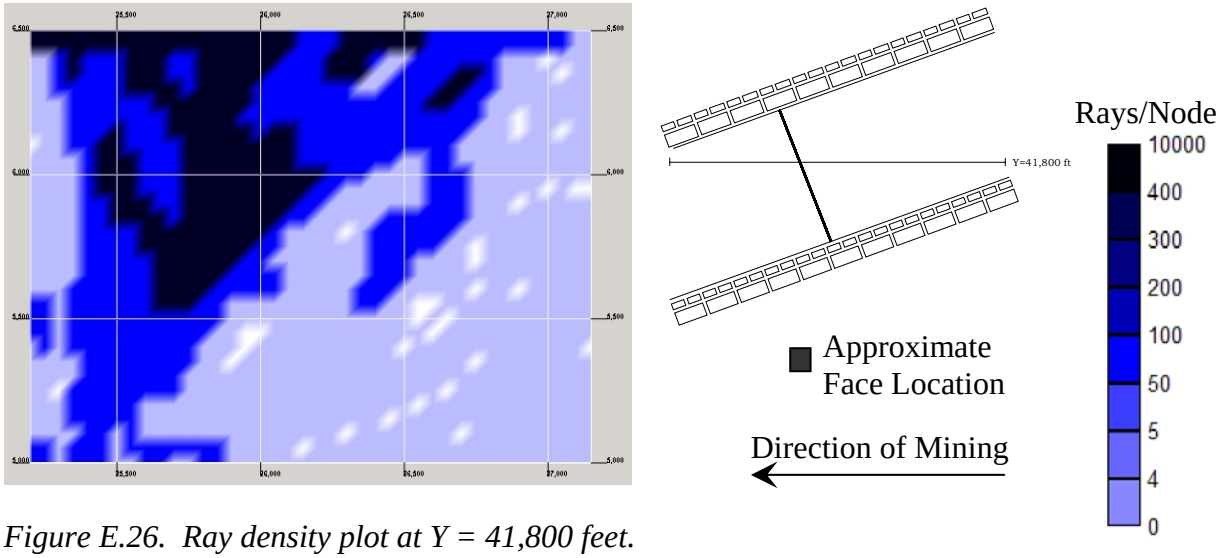

Figure E.26. Ray density plot at Y = 41,800 feet.

08-03-97
Section View at Y = 41,800 feet (Midface)

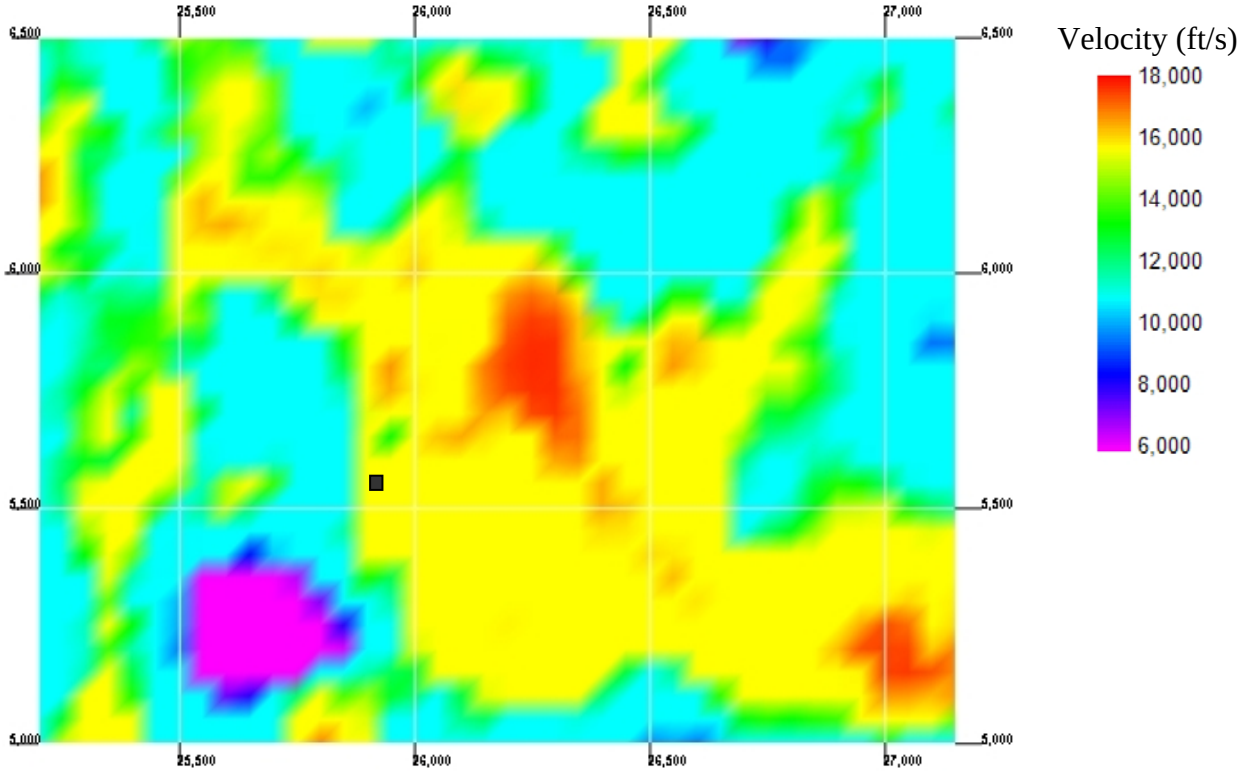

Figure E.27. Velocity tomogram at Y = 41,800 feet.

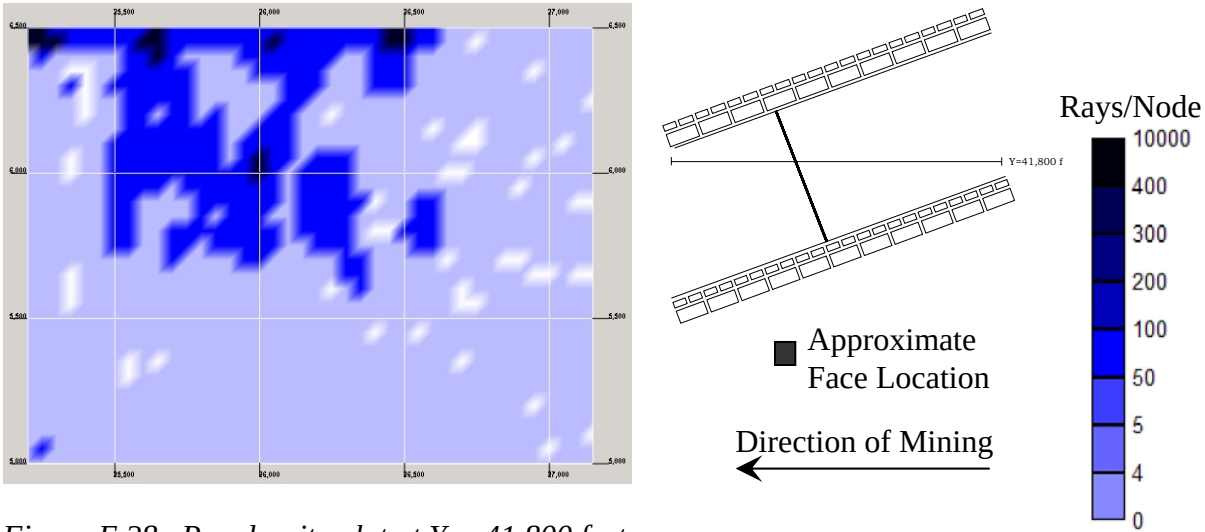

Figure E.28. Ray density plot at Y = 41,800 feet.

08-04-97
Section View at Y = 41,800 feet (Midface)

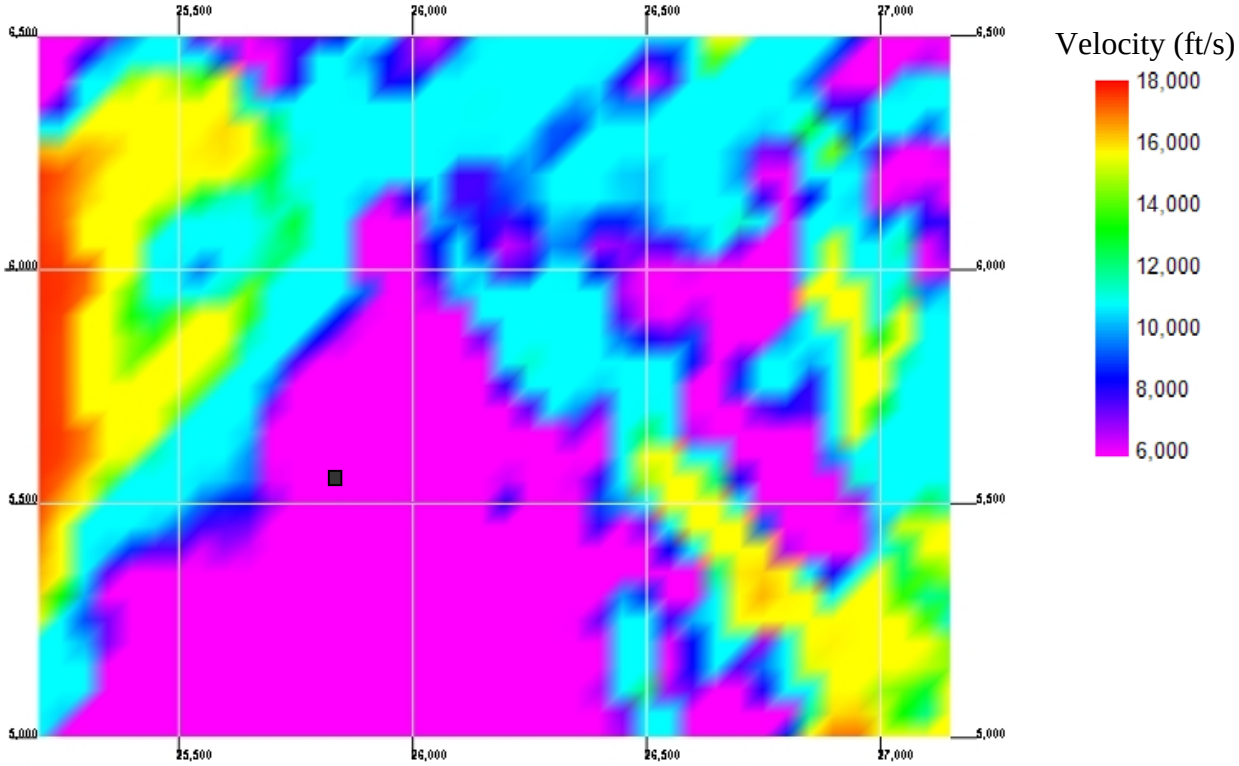

Figure E.29. Velocity tomogram at Y = 41,800 feet.

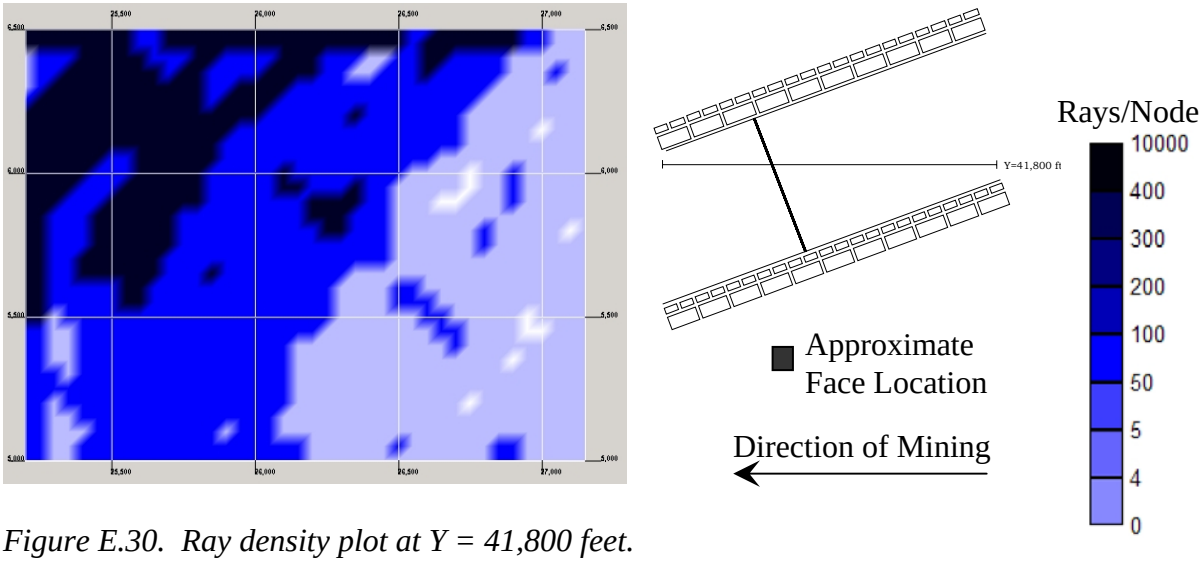

Figure E.30. Ray density plot at Y = 41,800 feet.

08-05-97
Section View at Y = 41,800 feet (Midface)

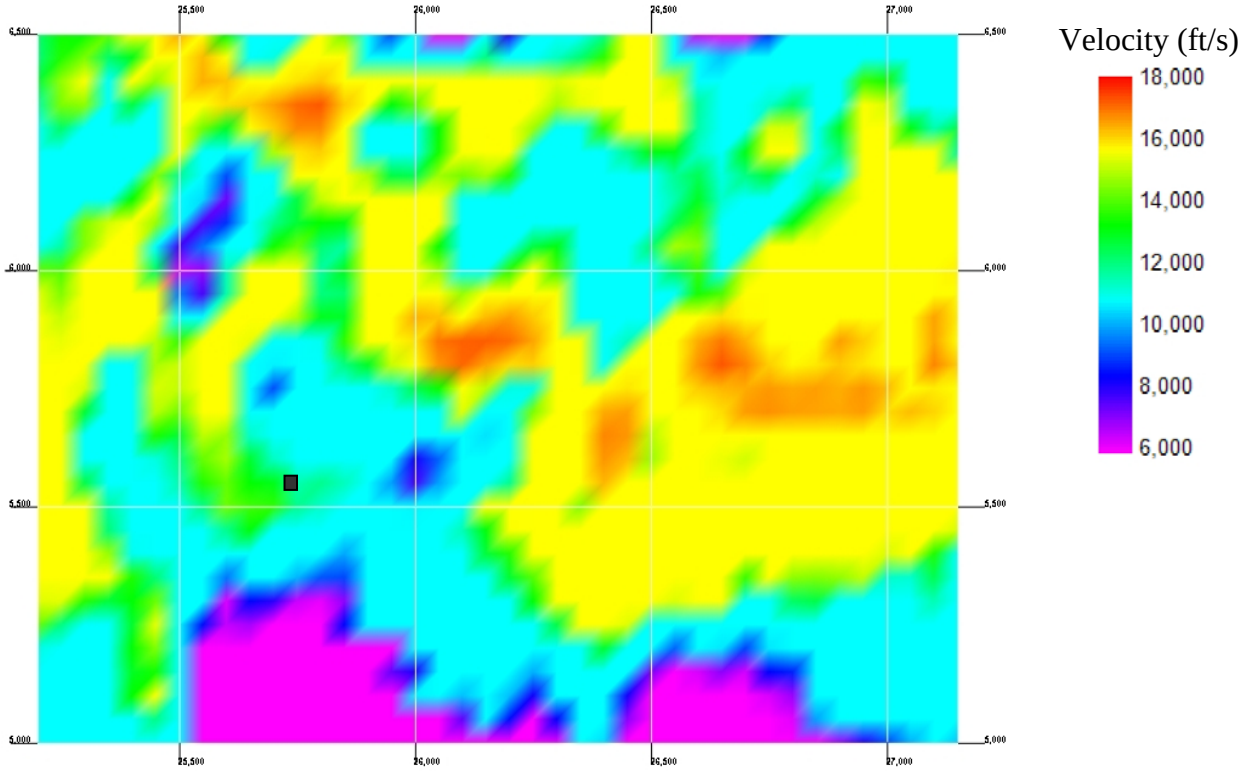

Figure E.31. Velocity tomogram at Y = 41,800 feet.

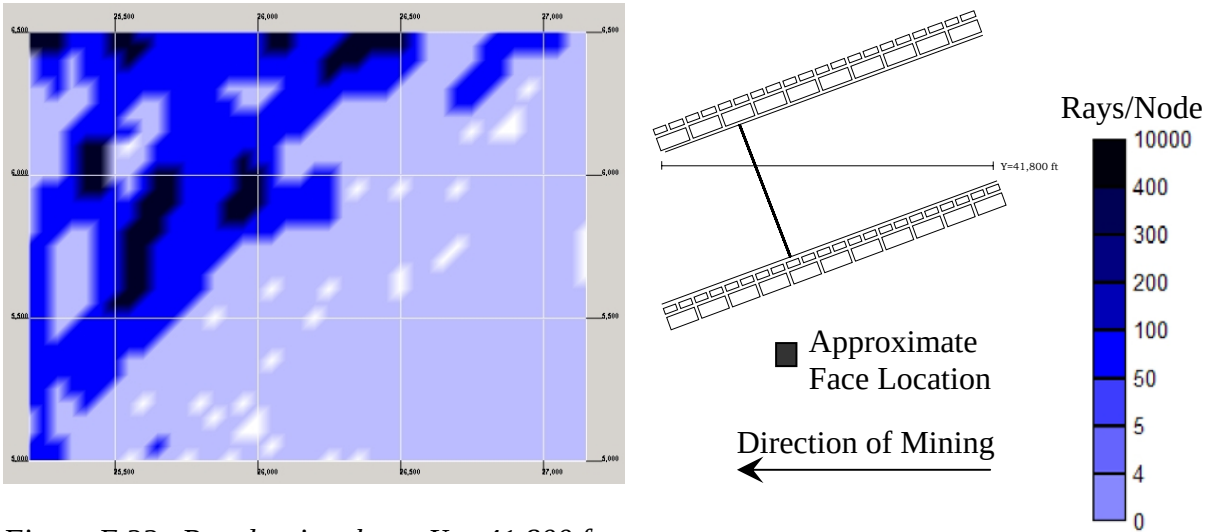

Figure E.32. Ray density plot at Y = 41,800 feet.

08-06-97
Section View at Y = 41,800 feet (Midface)

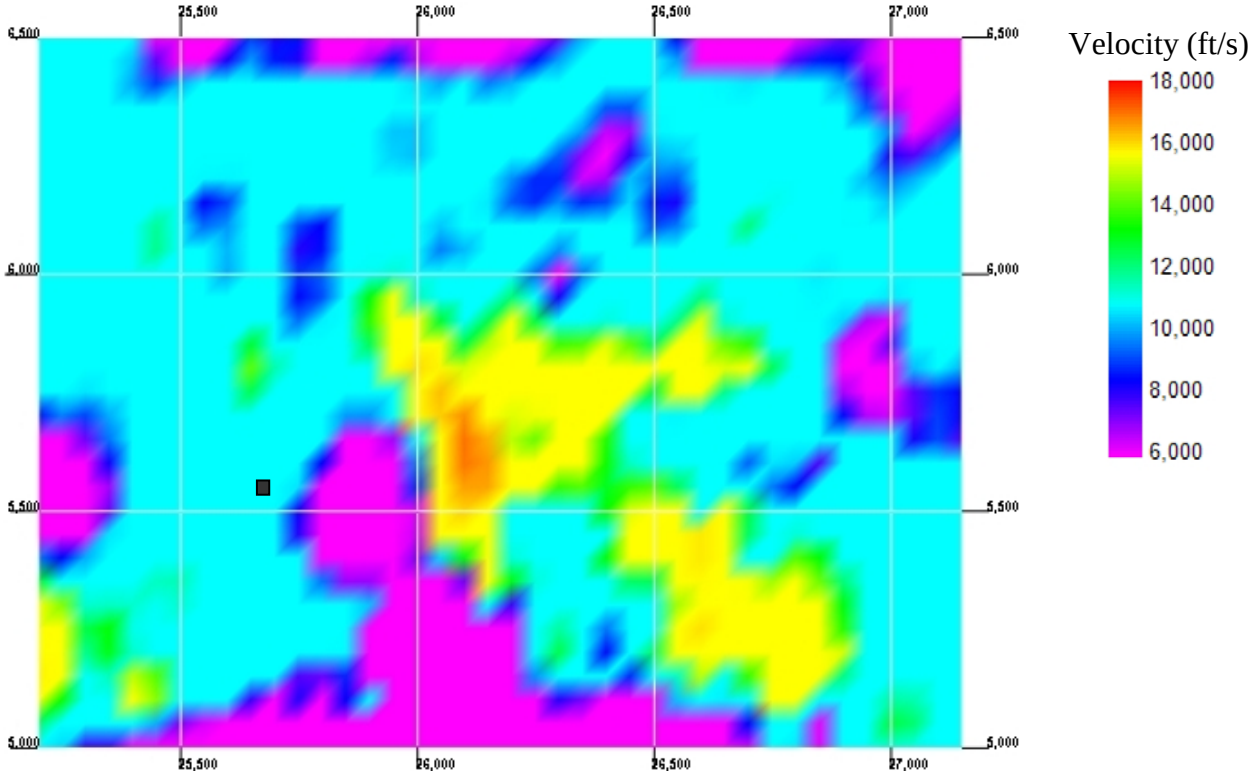

Figure E.33. Velocity tomogram at Y = 41,800 feet.

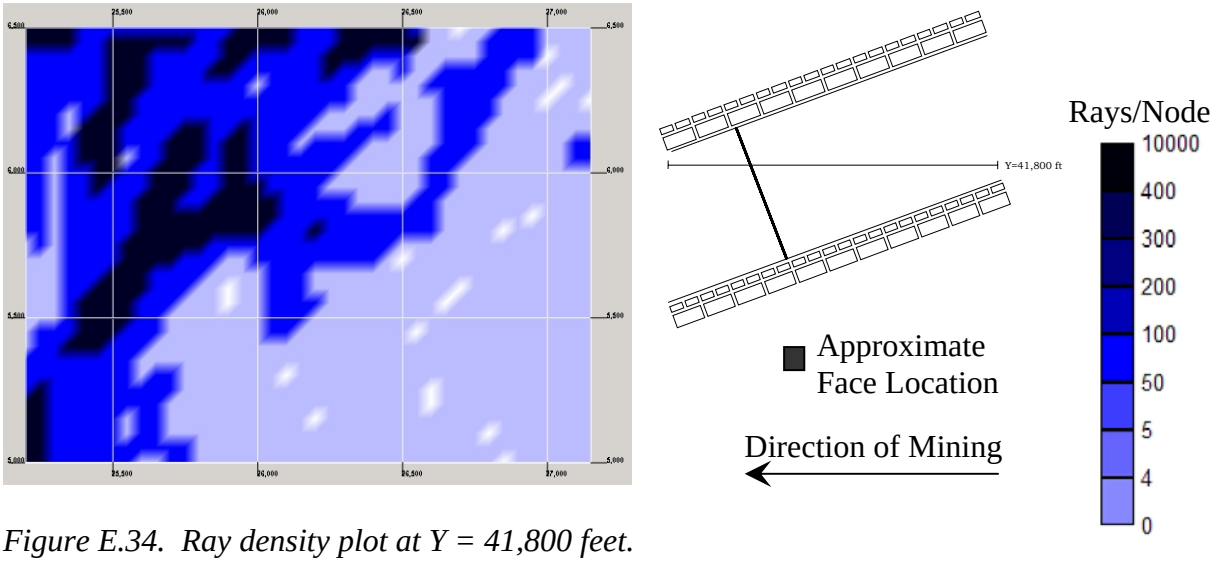

Figure E.34. Ray density plot at Y = 41,800 feet.

08-07-97
Section View at Y = 41,800 feet (Midface)

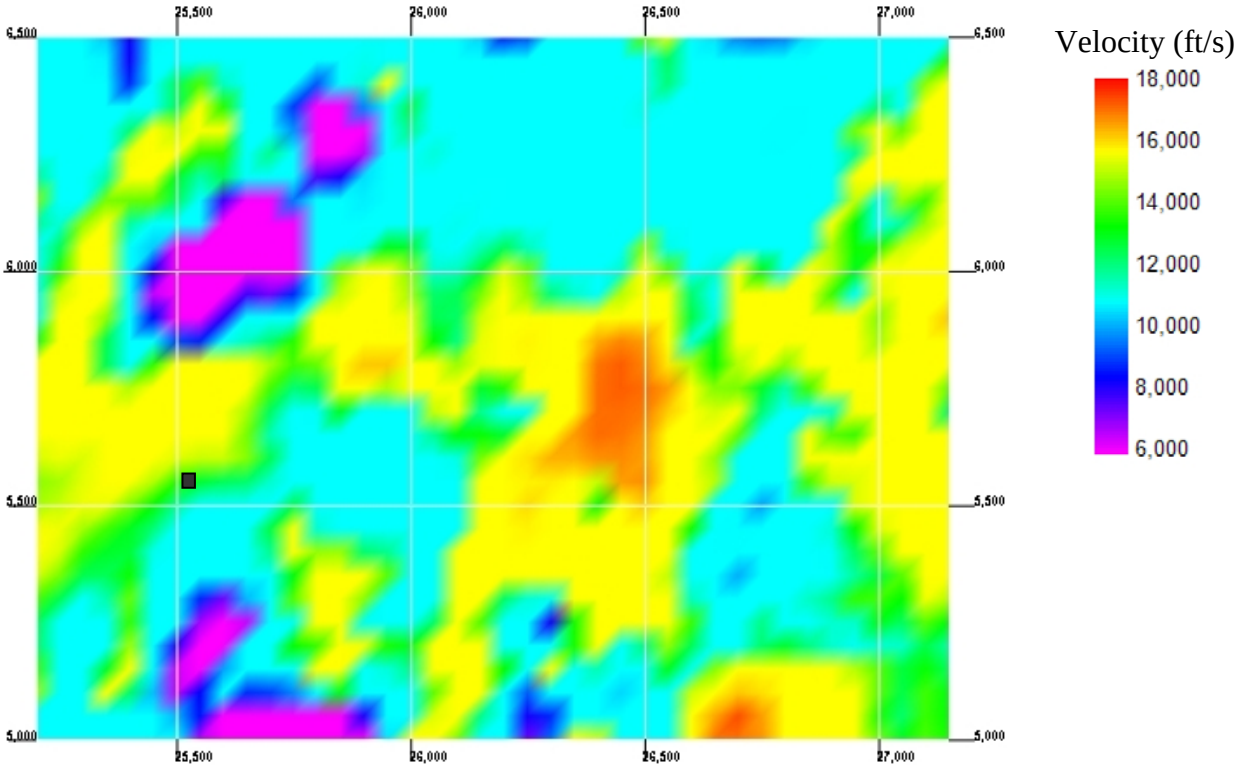

Figure E.35. Velocity tomogram at Y = 41,800 feet.

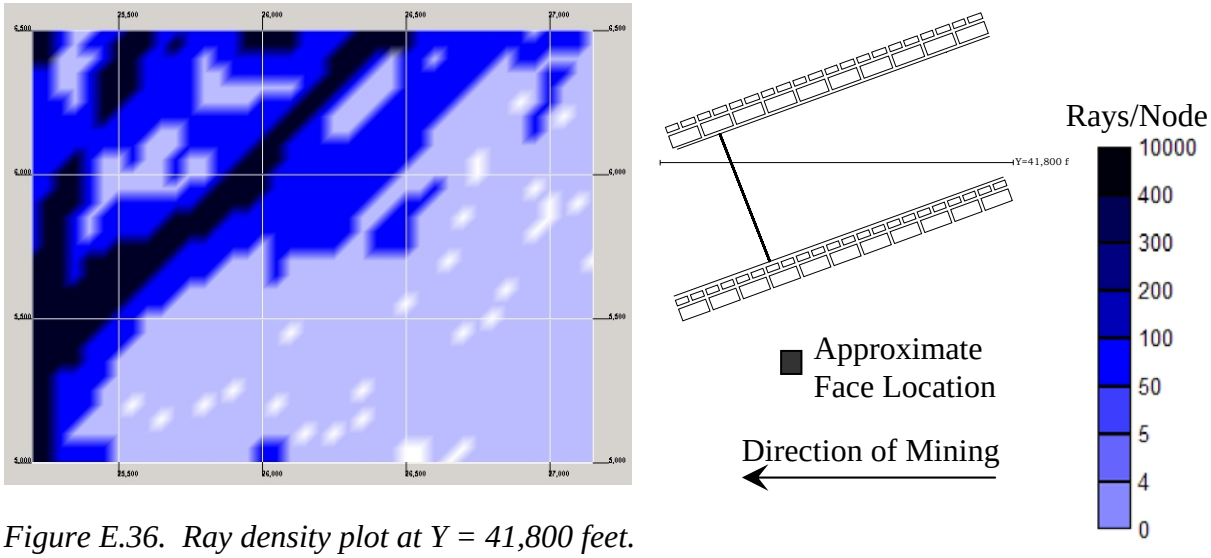

Figure E.36. Ray density plot at Y = 41,800 feet.

APPENDIX F

Velocity Tomograms and Microseismic Events

SEAM LEVEL
Z = 5, 550 FEET

07-20-97
Plan View at Z = 5,550 feet (Seam Level)

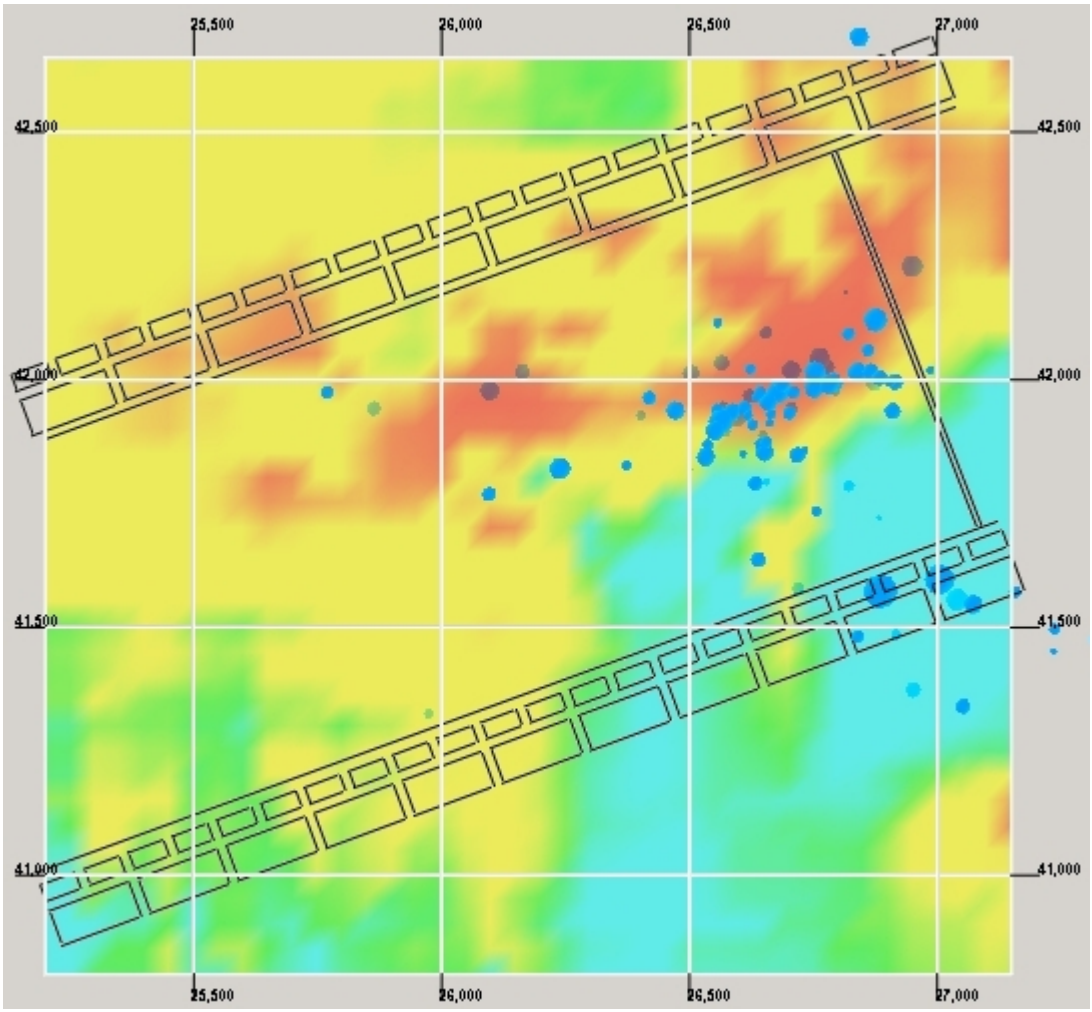

Figure F.1. Velocity Tomogram at Z = 5,550 feet.

Velocity (ft/s)

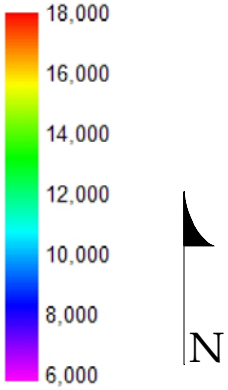

Microseismic Events are represented by blue spheres. The spheres are scaled according to relative magnitude. The layer displayed, at 5,550 feet, is set to 55% transparency so that microseismic events under the seam can be viewed.

07-21-97
Plan View at Z = 5,550 feet (Seam Level)

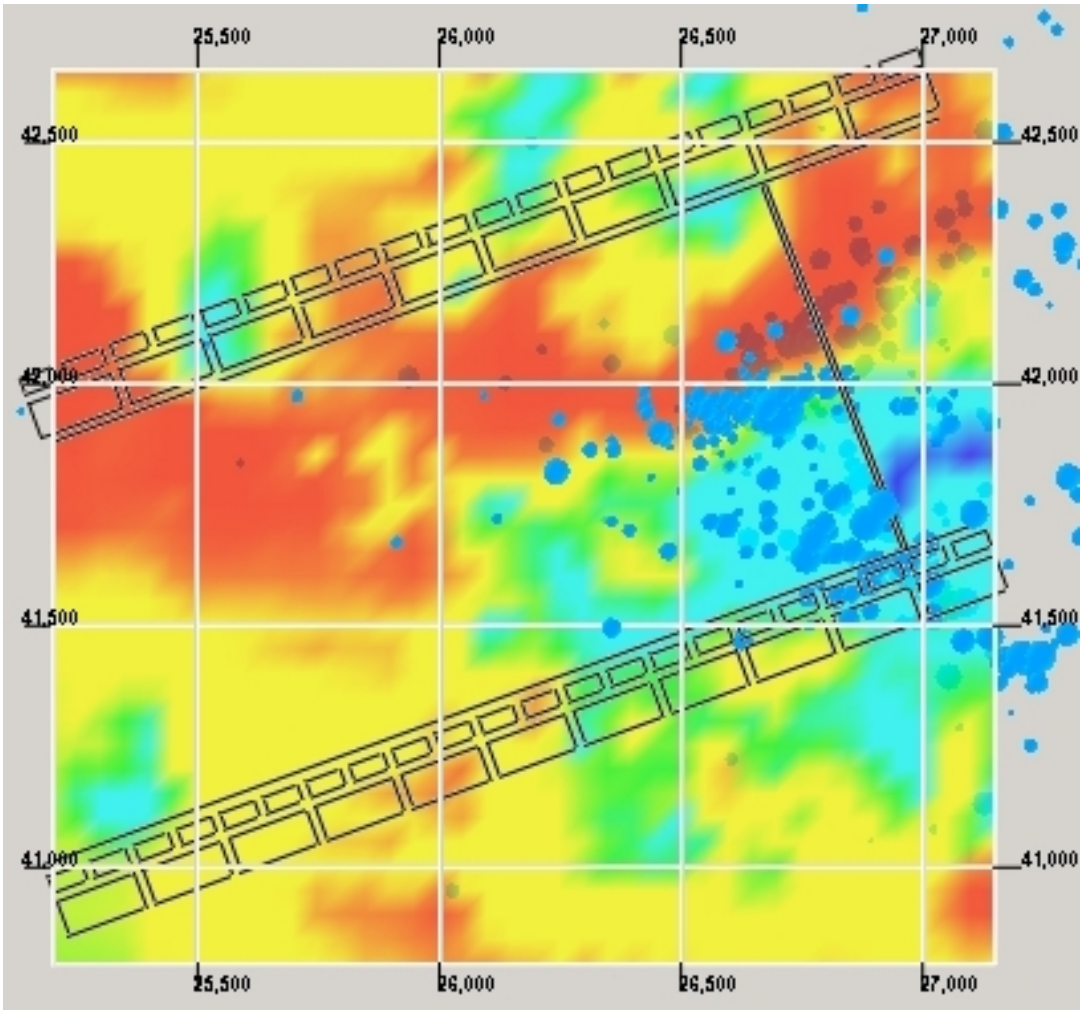

Figure F.2. Velocity Tomogram at Z = 5,550 feet.

Velocity (ft/s)

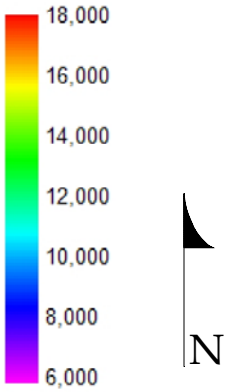

Microseismic Events are represented by blue spheres. The spheres are scaled according to relative magnitude. The layer displayed, at 5,550 feet, is set to 55% transparency so that microseismic events under the seam can be viewed.

07-22-97
Plan View at Z = 5,550 feet (Seam Level)

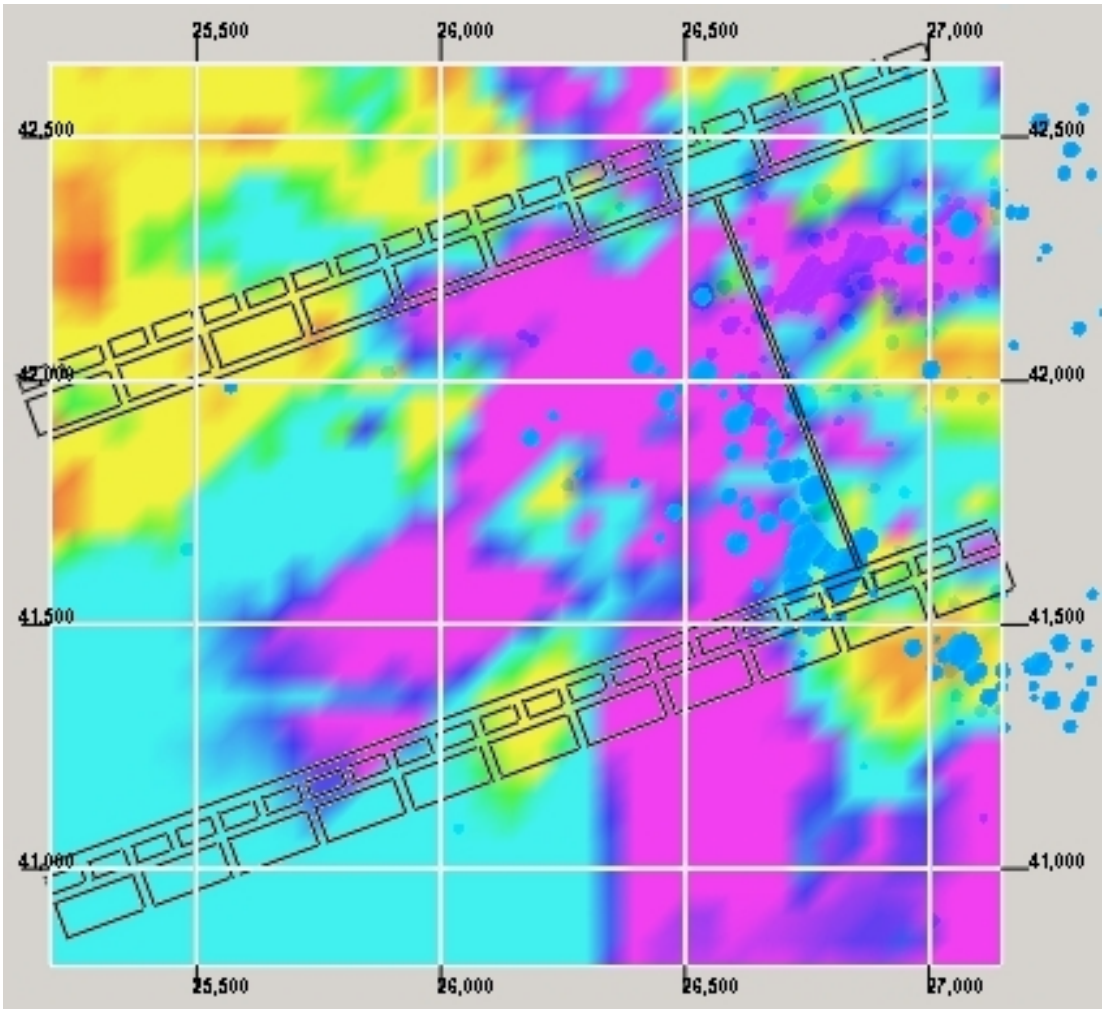

Figure F.3. Velocity Tomogram at Z = 5,550 feet.

Velocity (ft/s)

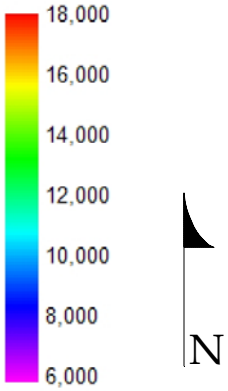

Microseismic Events are represented by blue spheres. The spheres are scaled according to relative magnitude. The layer displayed, at 5,550 feet, is set to 55% transparency so that microseismic events under the seam can be viewed.

07-23-97
Plan View at Z = 5,550 feet (Seam Level)

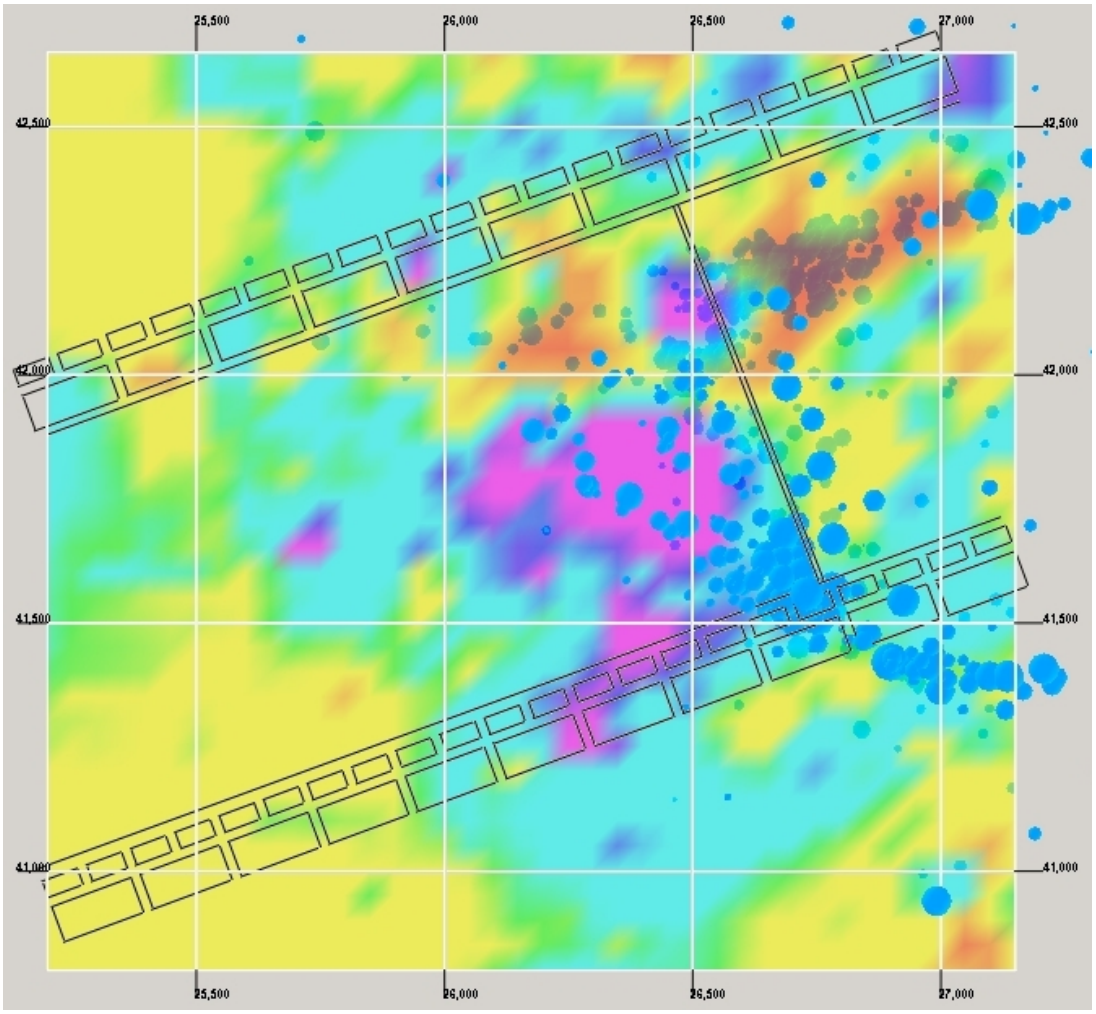

Figure F.4. Velocity Tomogram at Z = 5,550 feet.

Velocity (ft/s)

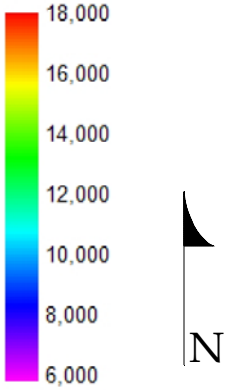

Microseismic Events are represented by blue spheres. The spheres are scaled according to relative magnitude. The layer displayed, at 5,550 feet, is set to 55% transparency so that microseismic events under the seam can be viewed.

07-24-97
Plan View at Z = 5,550 feet (Seam Level)

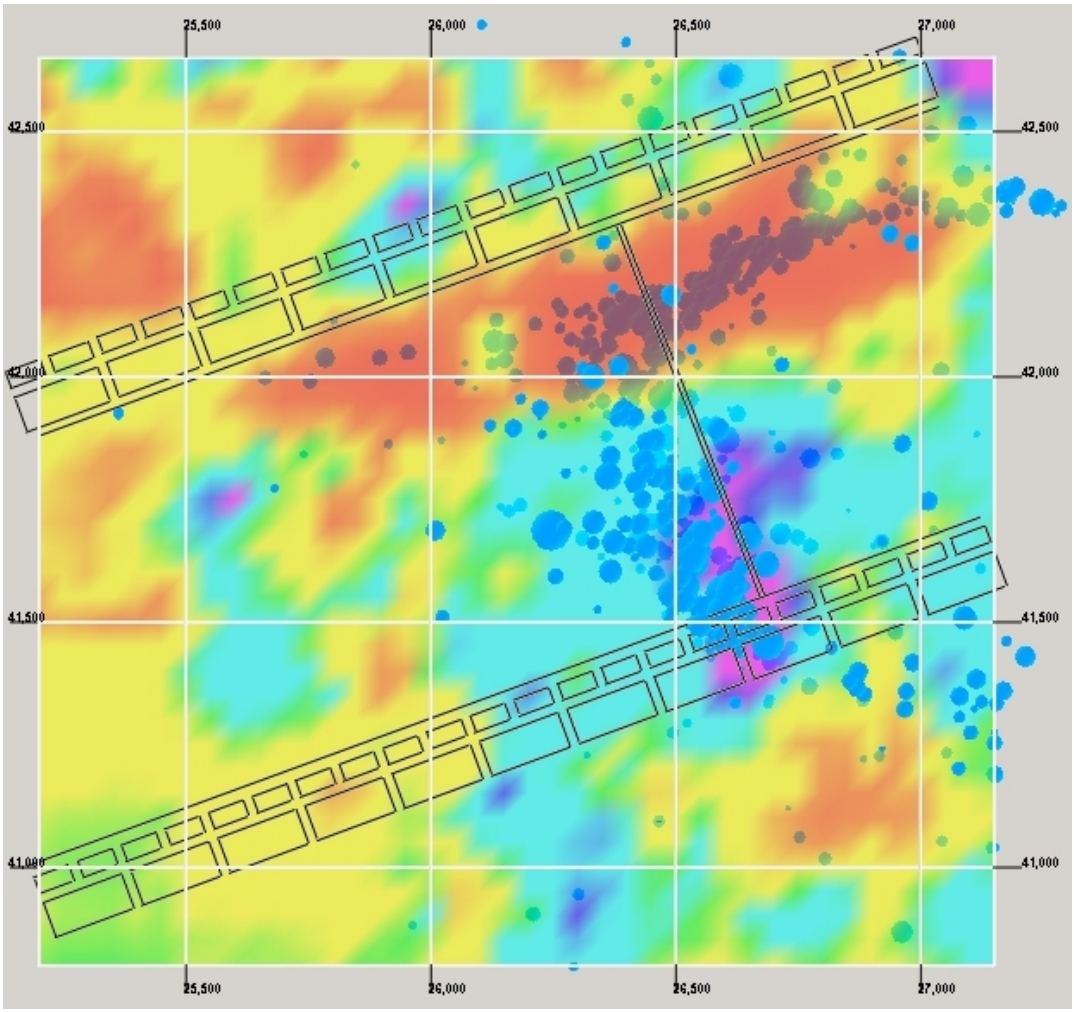

Figure F.5. Velocity Tomogram at Z = 5,550 feet.

Velocity (ft/s)

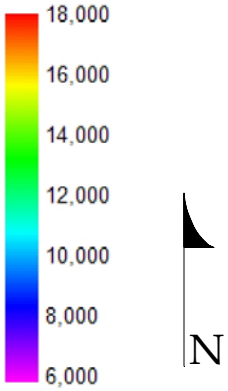

Microseismic Events are represented by blue spheres. The spheres are scaled according to relative magnitude. The layer displayed, at 5,550 feet, is set to 55% transparency so that microseismic events under the seam can be viewed.

07-25-97
Plan View at Z = 5,550 feet (Seam Level)

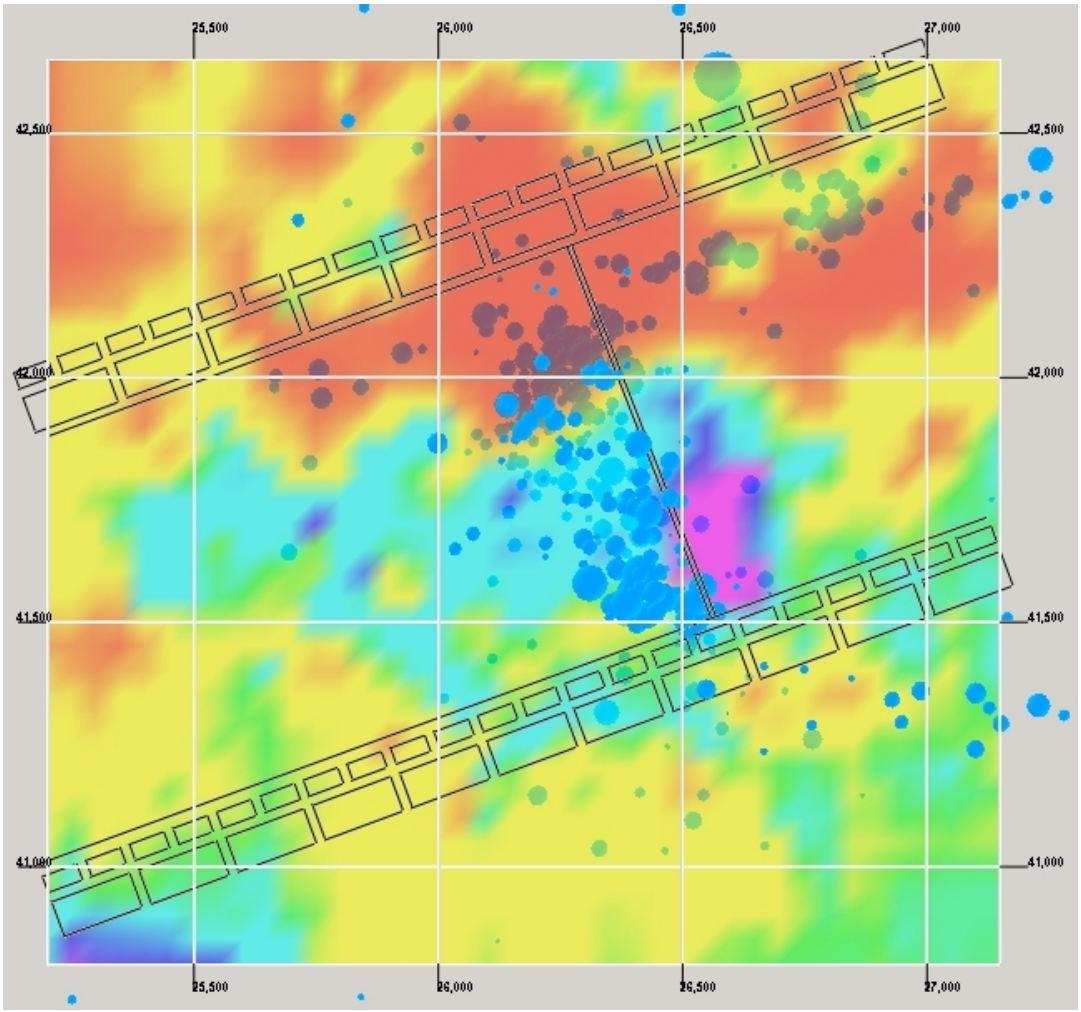

Figure F.6. Velocity Tomogram at Z = 5,550 feet.

Velocity (ft/s)

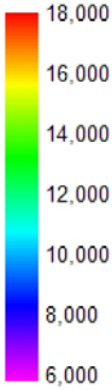

Microseismic Events are represented by blue spheres. The spheres are scaled according to relative magnitude. The layer displayed, at 5,550 feet, is set to 55% transparency so that microseismic events under the seam can be viewed.

07-26-97
Plan View at Z = 5,550 feet (Seam Level)

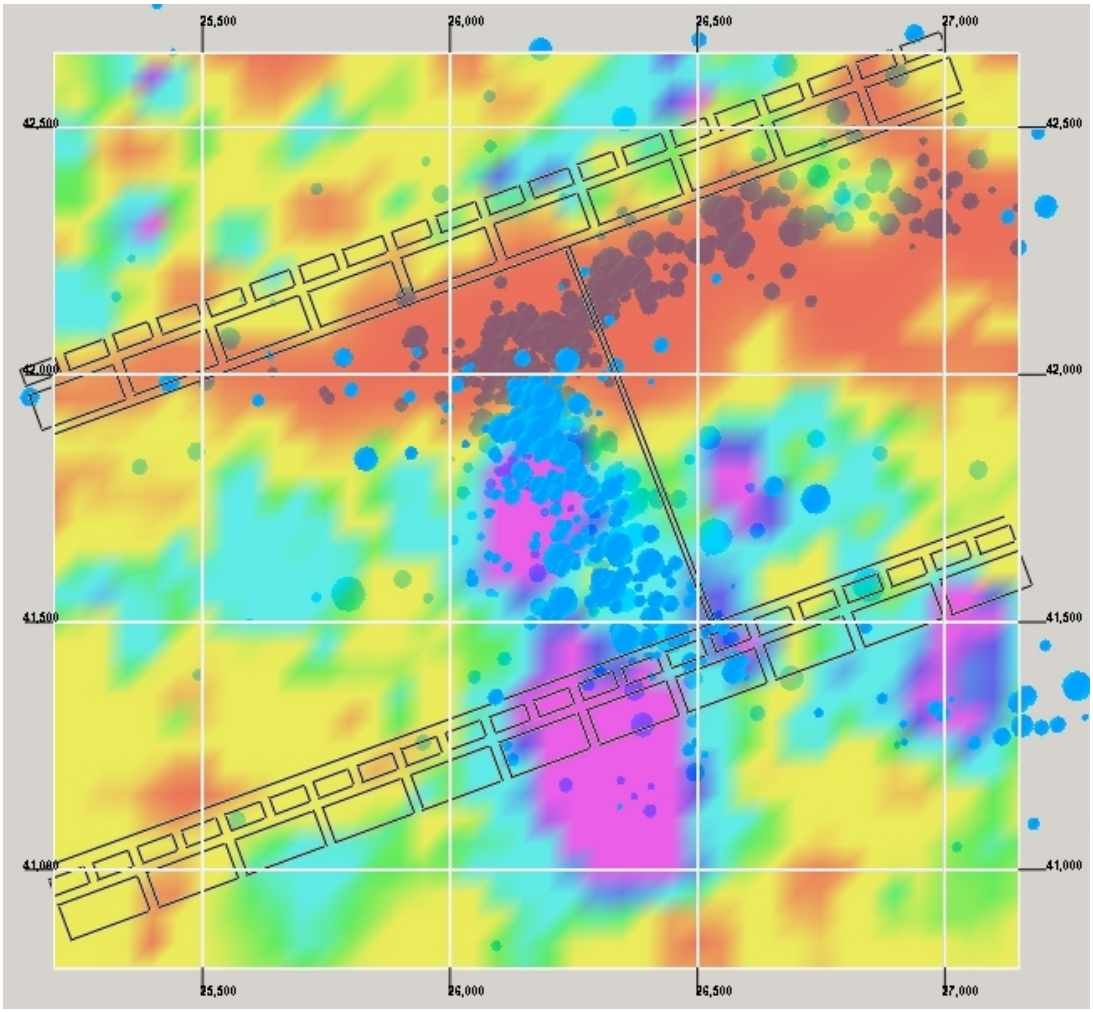

Figure F.7. Velocity Tomogram at Z z = 5,550 feet.

Velocity (ft/s)

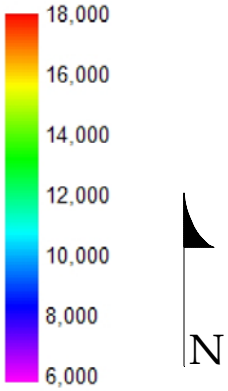

Microseismic Events are represented by blue spheres. The spheres are scaled according to relative magnitude. The layer displayed, at 5,550 feet, is set to 55% transparency so that microseismic events under the seam can be viewed.

07-27-97
Plan View at Z = 5,550 feet (Seam Level)

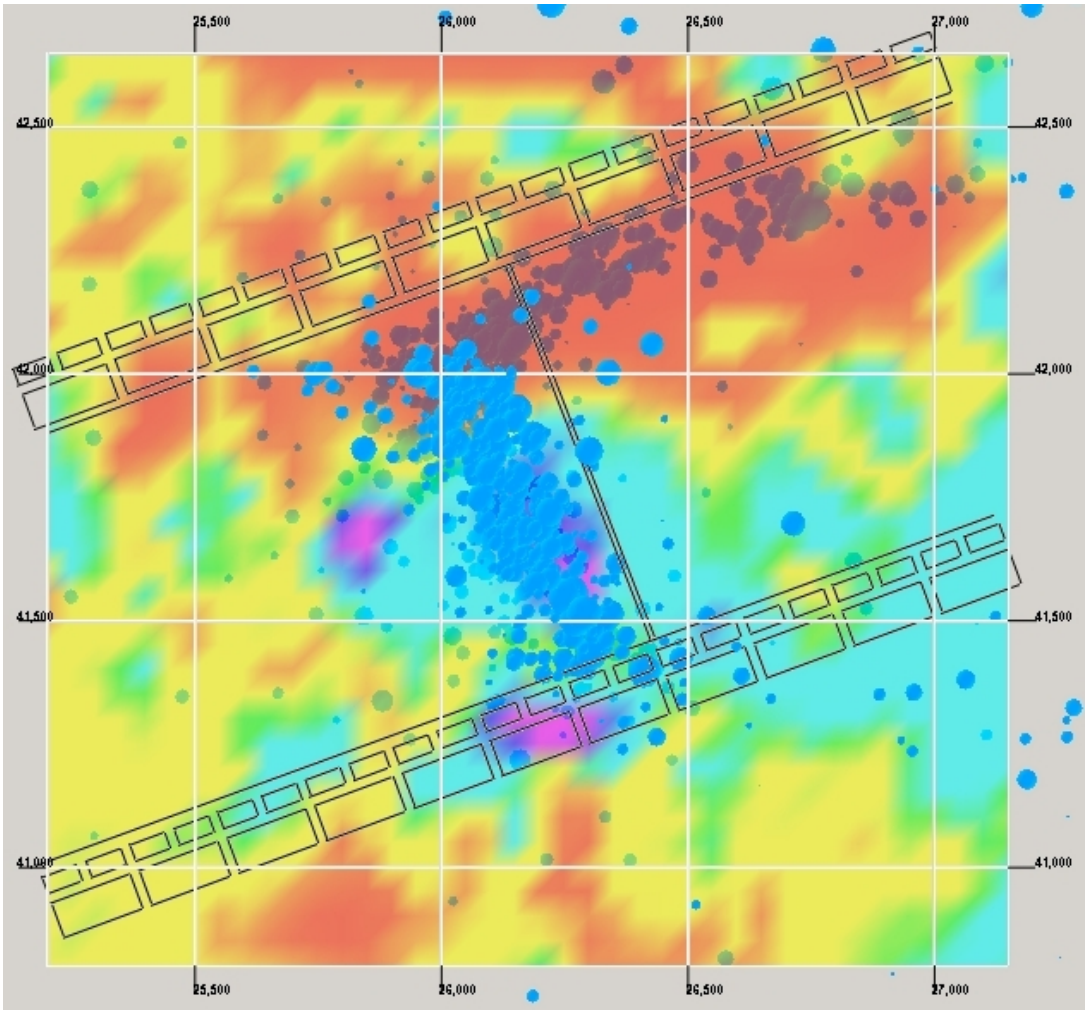

Figure F.8. Velocity Tomogram at Z = 5,550 feet.

Velocity (ft/s)

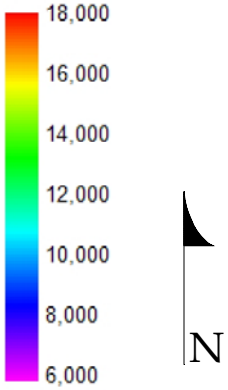

Microseismic Events are represented by blue spheres. The spheres are scaled according to relative magnitude. The layer displayed, at 5,550 feet, is set to 55% transparency so that microseismic events under the seam can be viewed.

07-28-97
Plan View at Z = 5,550 feet (Seam Level)

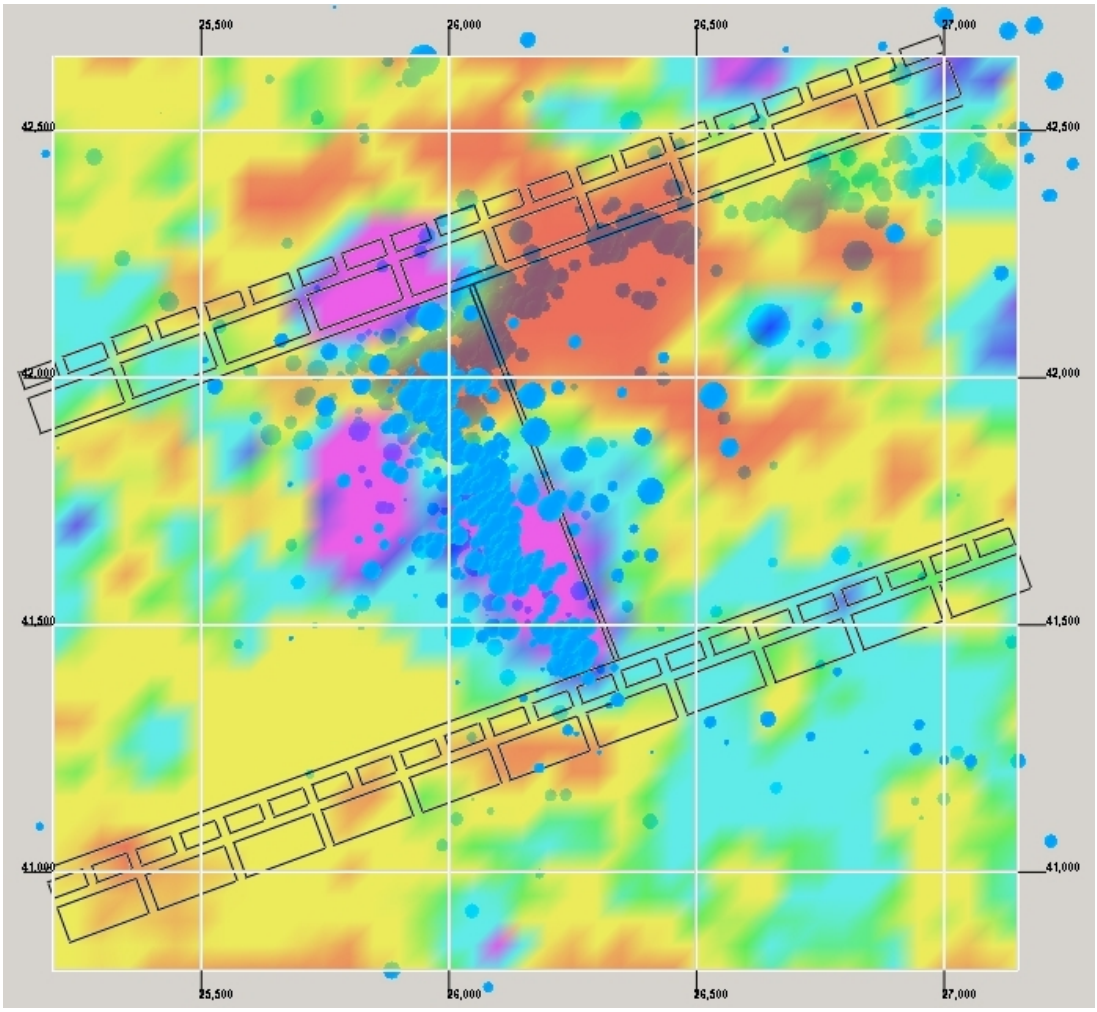

Figure F.9. Velocity Tomogram at Z = 5,550 feet.

Velocity (ft/s)

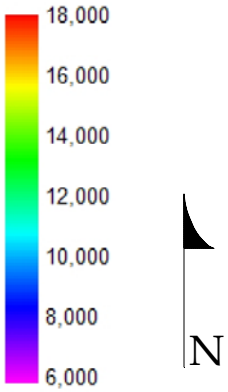

Microseismic Events are represented by blue spheres. The spheres are scaled according to relative magnitude. The layer displayed, at 5,550 feet, is set to 55% transparency so that microseismic events under the seam can be viewed.

07-30-97
Plan View at Z = 5,550 feet (Seam Level)

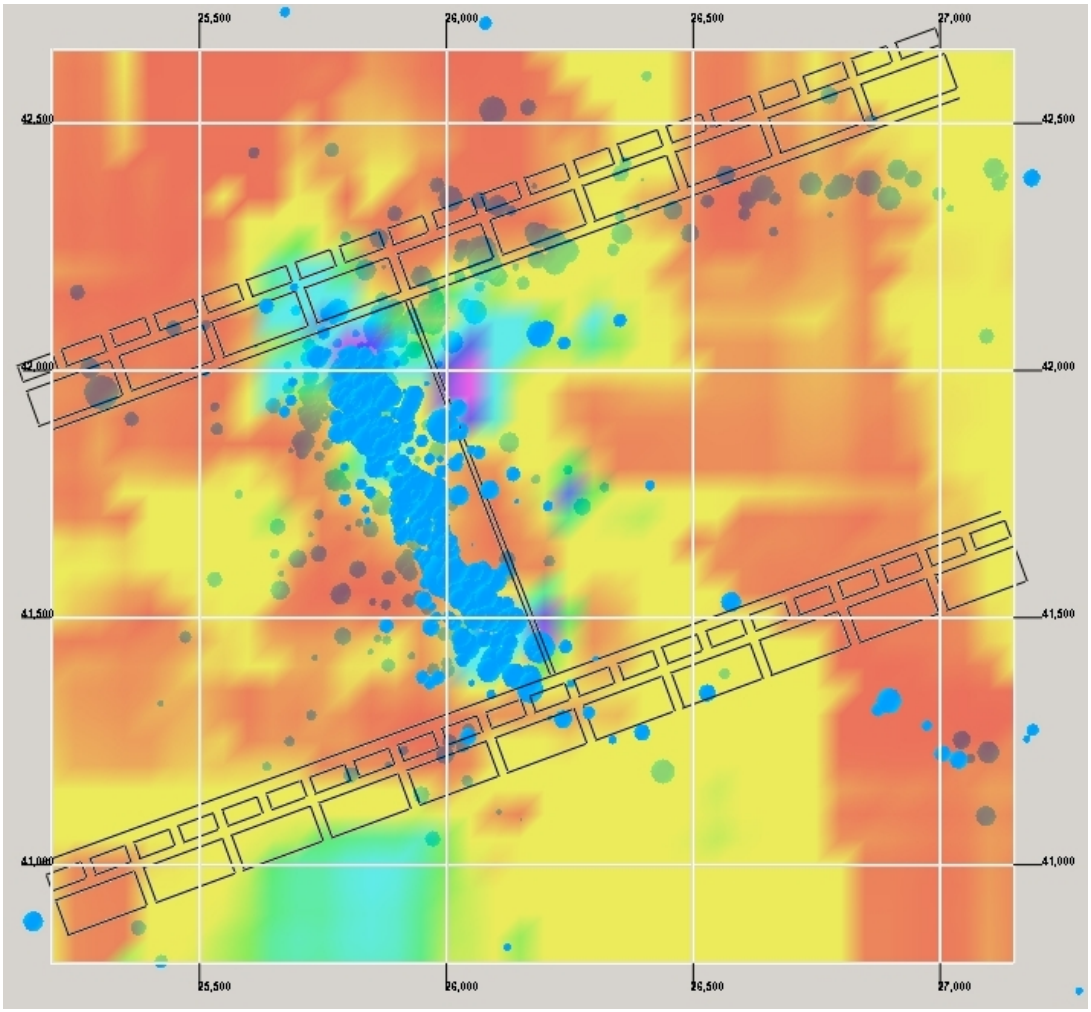

Figure F.10. Velocity Tomogram at Z = 5,550 feet.

Velocity (ft/s)

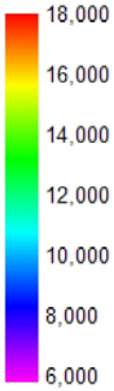

Microseismic Events are represented by blue spheres. The spheres are scaled according to relative magnitude. The layer displayed, at 5,550 feet, is set to 55% transparency so that microseismic events under the seam can be viewed.

07-31-97
Plan View at Z = 5,550 feet (Seam Level)

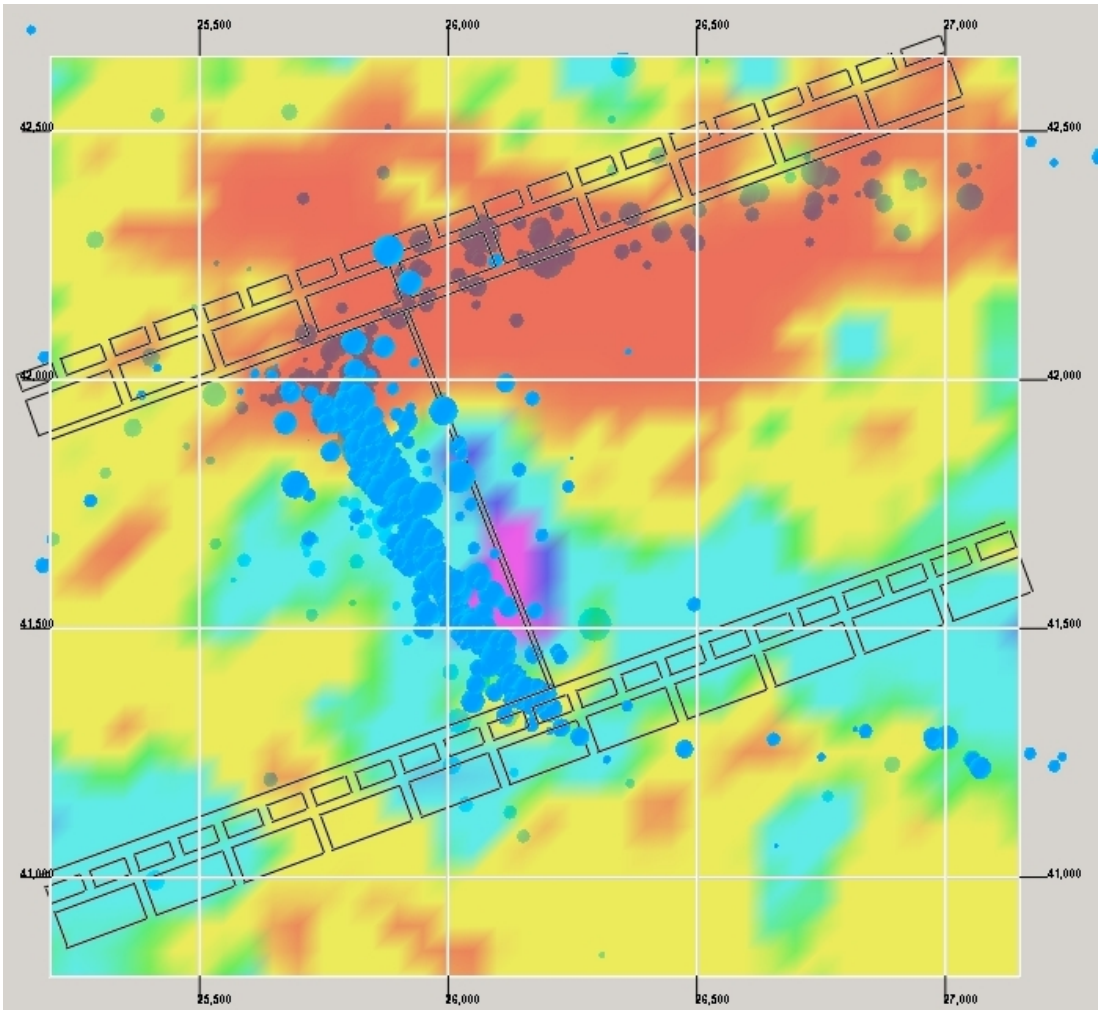

Figure F.11. Velocity Tomogram at Z = 5,550 feet.

Velocity (ft/s)

18,000
16,000
14,000
12,000
10,000
8,000
6,000

N

Microseismic Events are represented by blue spheres. The spheres are scaled according to relative magnitude. The layer displayed, at 5,550 feet, is set to 55% transparency so that microseismic events under the seam can be viewed.

08-01-97
Plan View at Z = 5,550 feet (Seam Level)

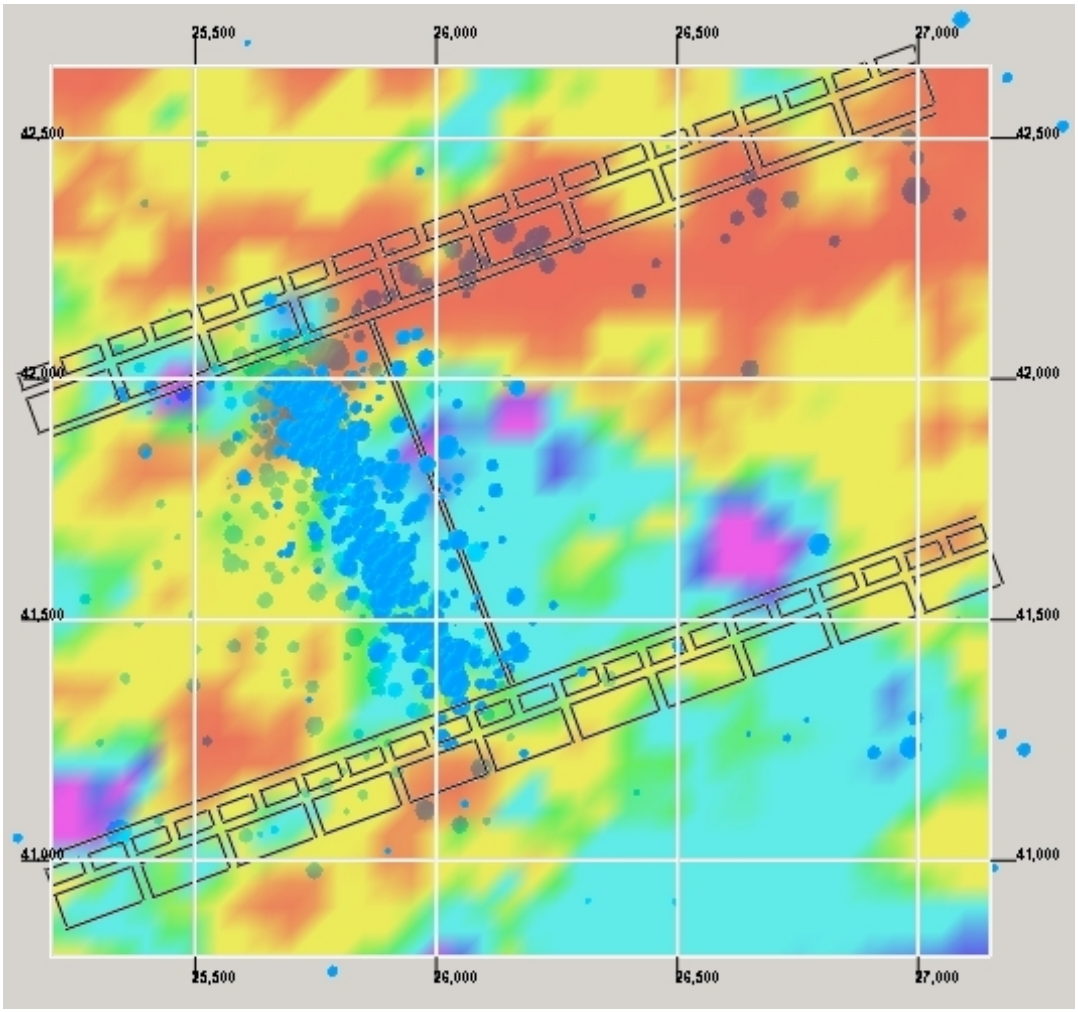

Figure F.12. Velocity Tomogram at Z = 5,550 feet.

Velocity (ft/s)

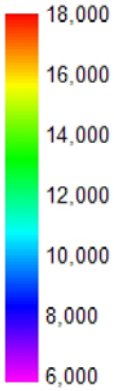

Microseismic Events are represented by blue spheres. The spheres are scaled according to relative magnitude. The layer displayed, at 5,550 feet, is set to 55% transparency so that microseismic events under the seam can be viewed.

08-02-97
Plan View at Z = 5,550 feet (Seam Level)

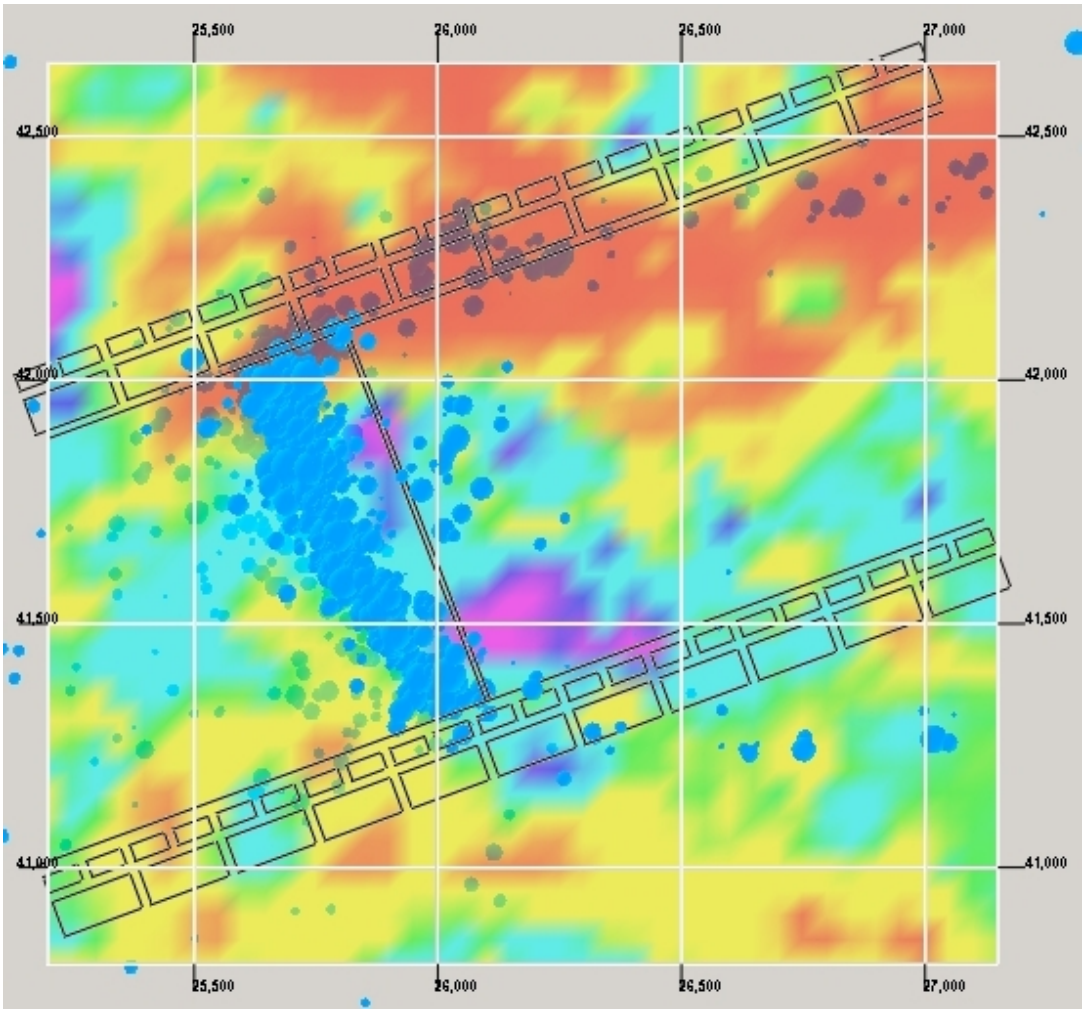

Figure F.13. Velocity Tomogram at Z = 5,550 feet.

Velocity (ft/s)

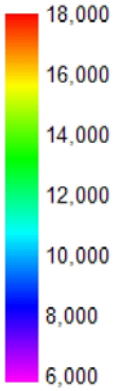

Microseismic Events are represented by blue spheres. The spheres are scaled according to relative magnitude. The layer displayed, at 5,550 feet, is set to 55% transparency so that microseismic events under the seam can be viewed.

08-03-97
Plan View at Z = 5,550 feet (Seam Level)

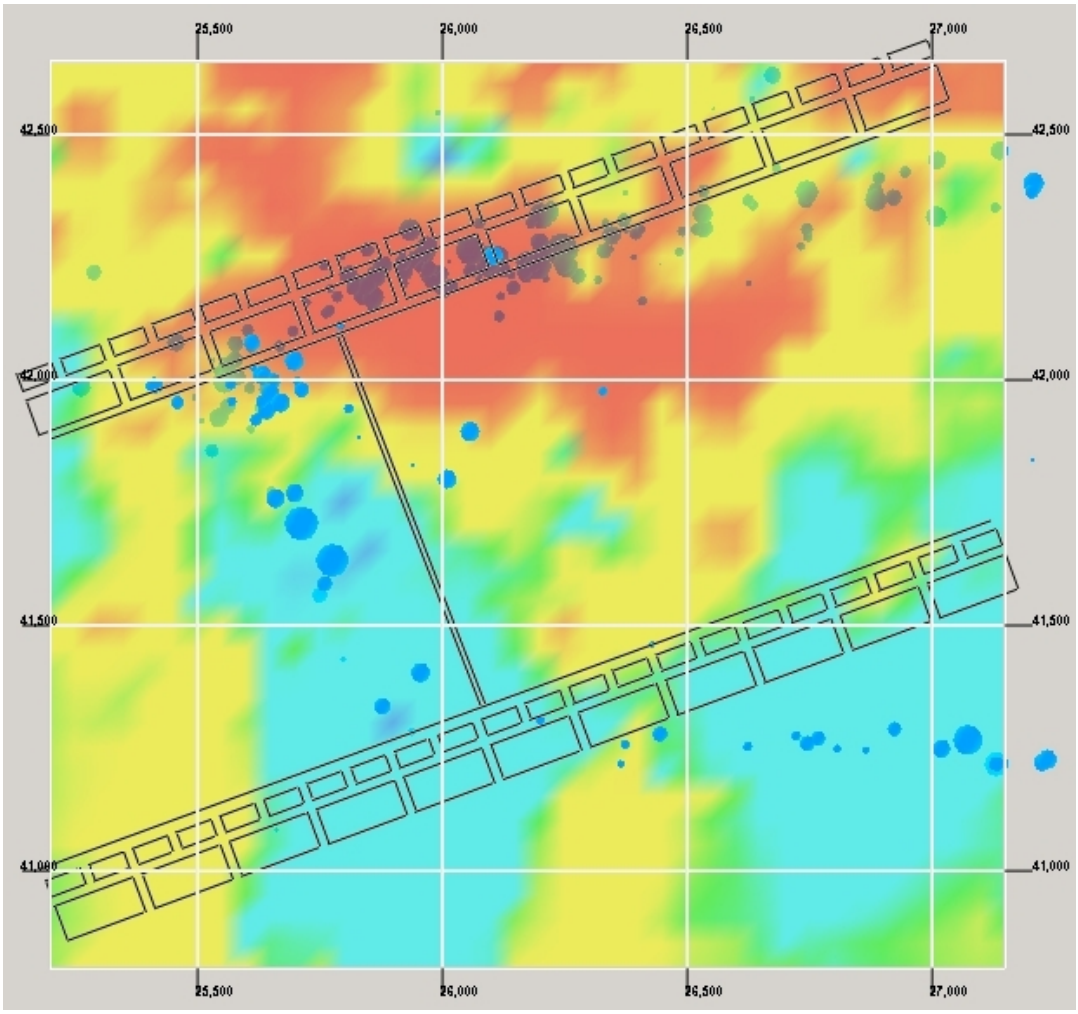

Figure F.14. Velocity Tomogram at Z = 5,550 feet.

Velocity (ft/s)

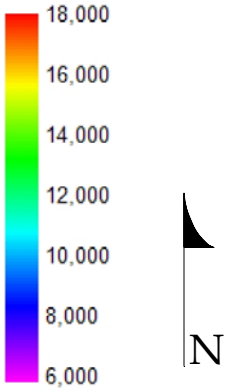

Microseismic Events are represented by blue spheres. The spheres are scaled according to relative magnitude. The layer displayed, at 5,550 feet, is set to 55% transparency so that microseismic events under the seam can be viewed.

08-04-97
Plan View at Z = 5,550 feet (Seam Level)

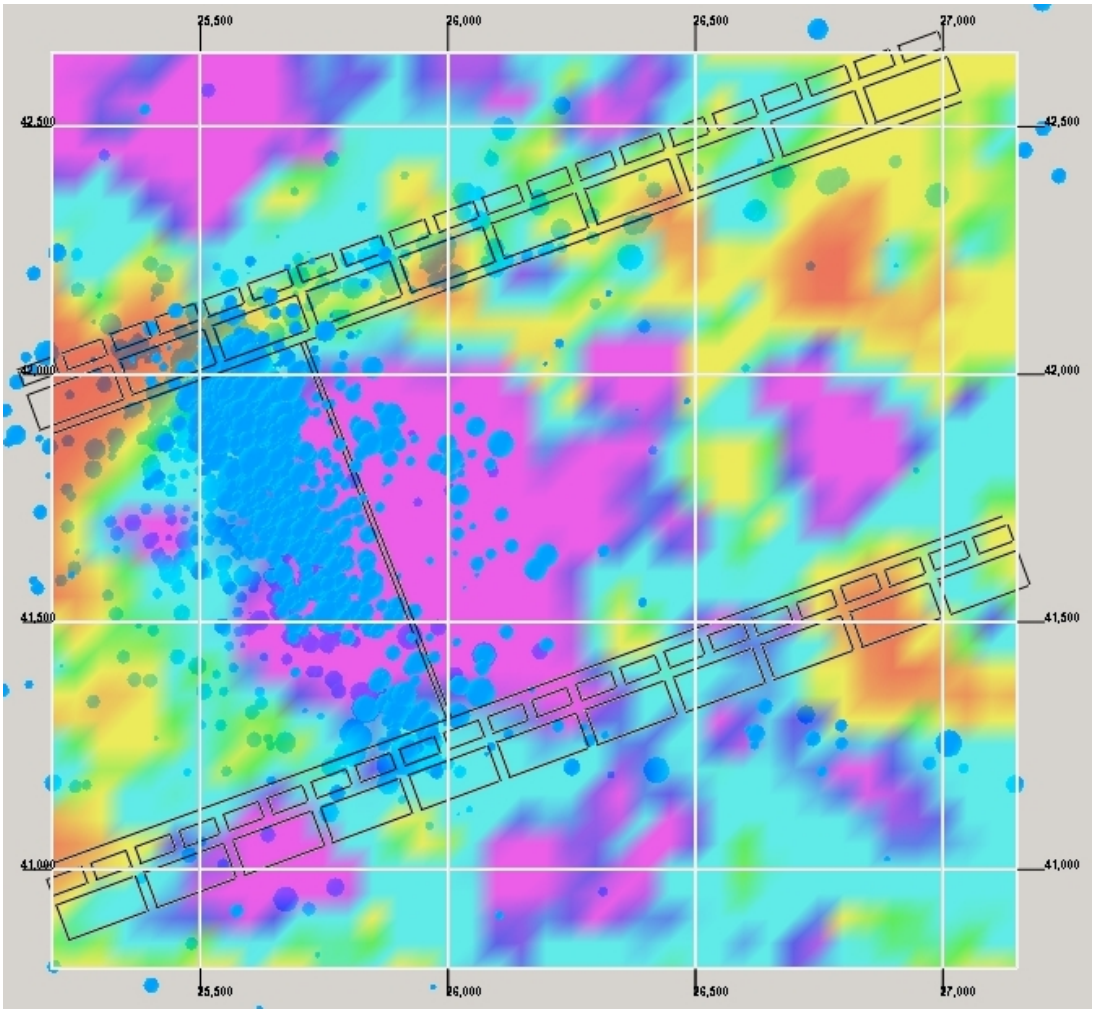

Figure F.15. Velocity Tomogram at Z = 5,550 feet.

Velocity (ft/s)

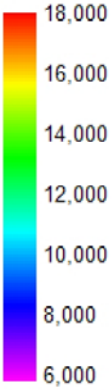

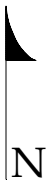

Microseismic Events are represented by blue spheres. The spheres are scaled according to relative magnitude. The layer displayed, at 5,550 feet, is set to 55% transparency so that microseismic events under the seam can be viewed.

08-05-97
Plan View at Z = 5,550 feet (Seam Level)

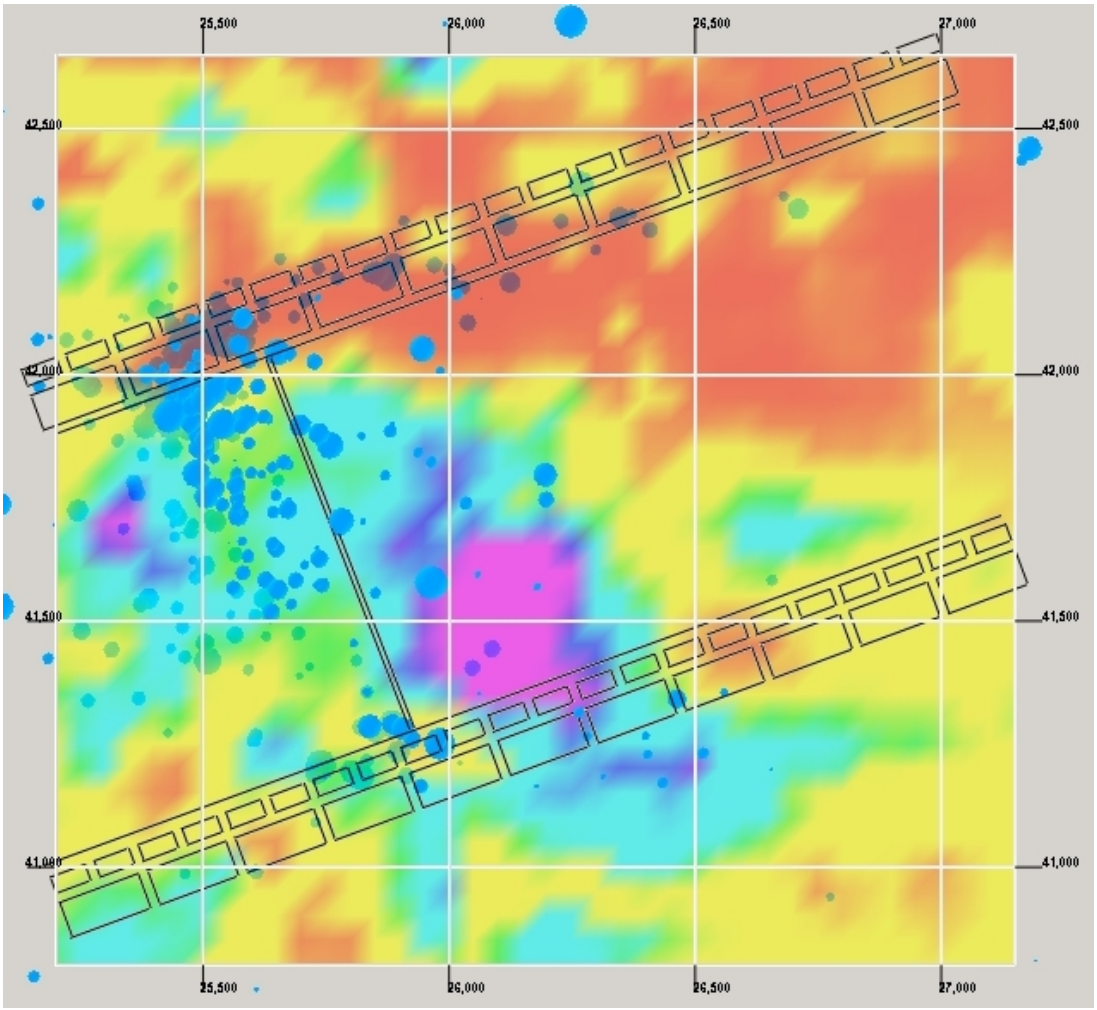

Figure F.16. Velocity Tomogram at Z = 5,550 feet.

Velocity (ft/s)

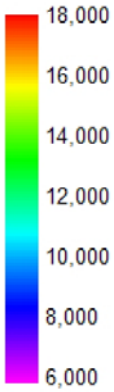

Microseismic Events are represented by blue spheres. The spheres are scaled according to relative magnitude. The layer displayed, at 5,550 feet, is set to 55% transparency so that microseismic events under the seam can be viewed.

08-06-97
Plan View at Z = 5,550 feet (Seam Level)

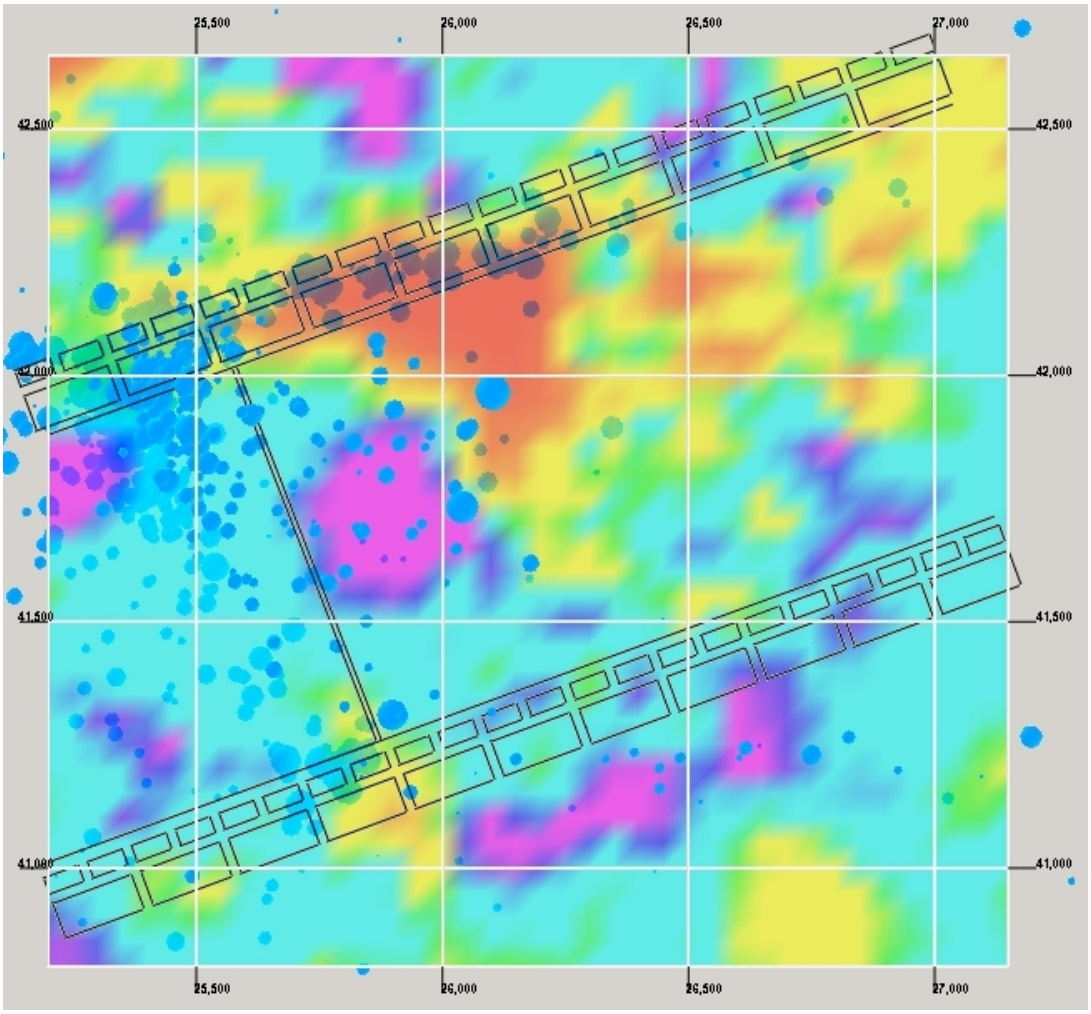

Figure F.17. Velocity Tomogram at Z = 5,550 feet.

Velocity (ft/s)

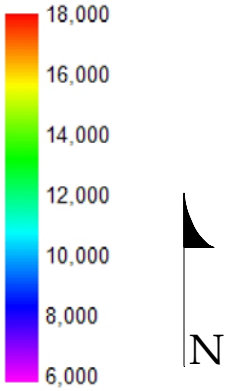

Microseismic Events are represented by blue spheres. The spheres are scaled according to relative magnitude. The layer displayed, at 5,550 feet, is set to 55% transparency so that microseismic events under the seam can be viewed.

08-07-97
Plan View at Z = 5,550 feet (Seam Level)

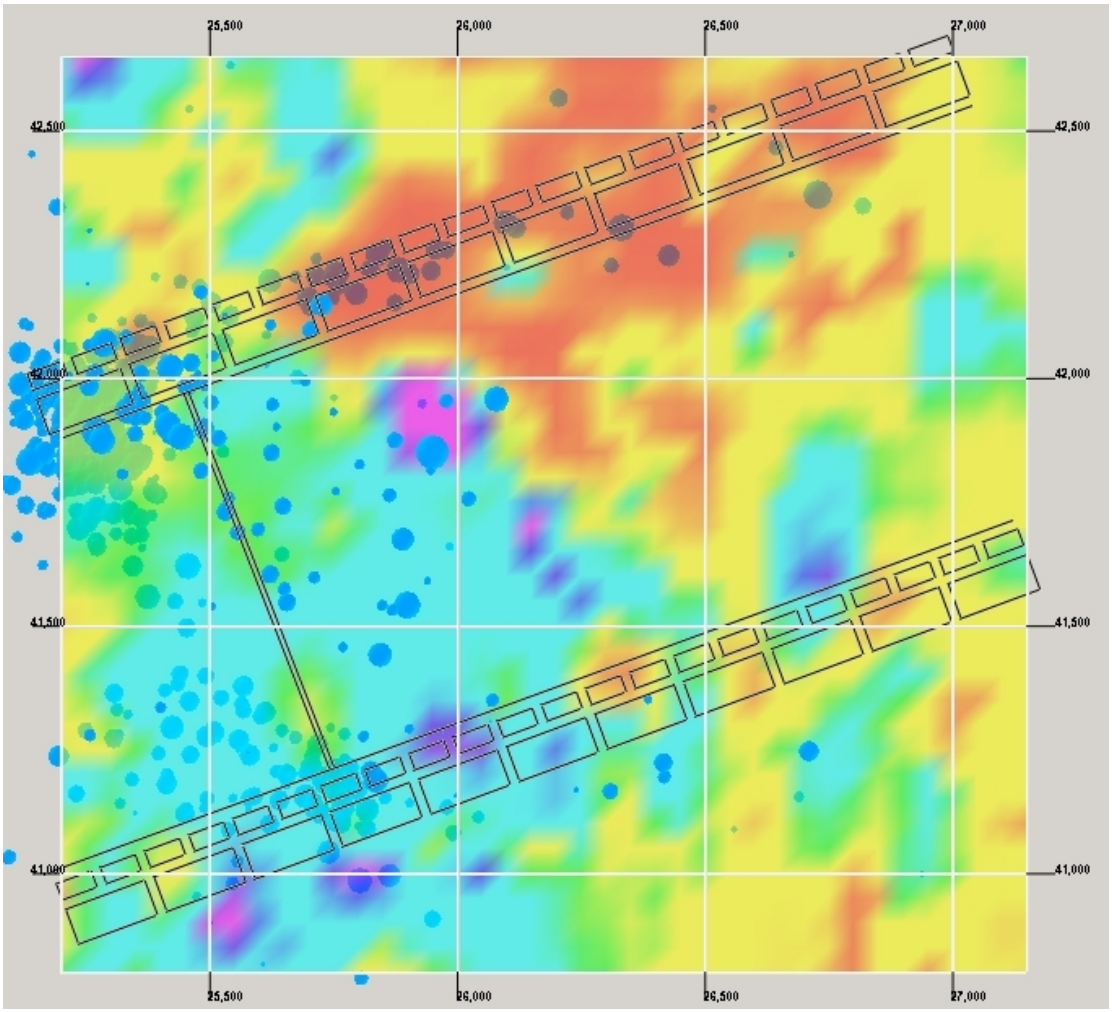

Figure F.18. Velocity Tomogram at Z = 5,550 feet.

Velocity (ft/s)

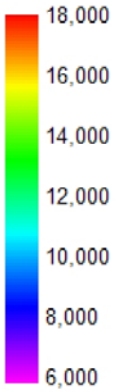

Microseismic Events are represented by blue spheres. The spheres are scaled according to relative magnitude. The layer displayed, at 5,550 feet, is set to 55% transparency so that microseismic events under the seam can be viewed.

APPENDIX G

LAMODEL Stress Plots

SEAM LEVEL
Z = 5, 550 FEET

07-20-97
Plan View at Z = 5,550 feet (Seam Level)

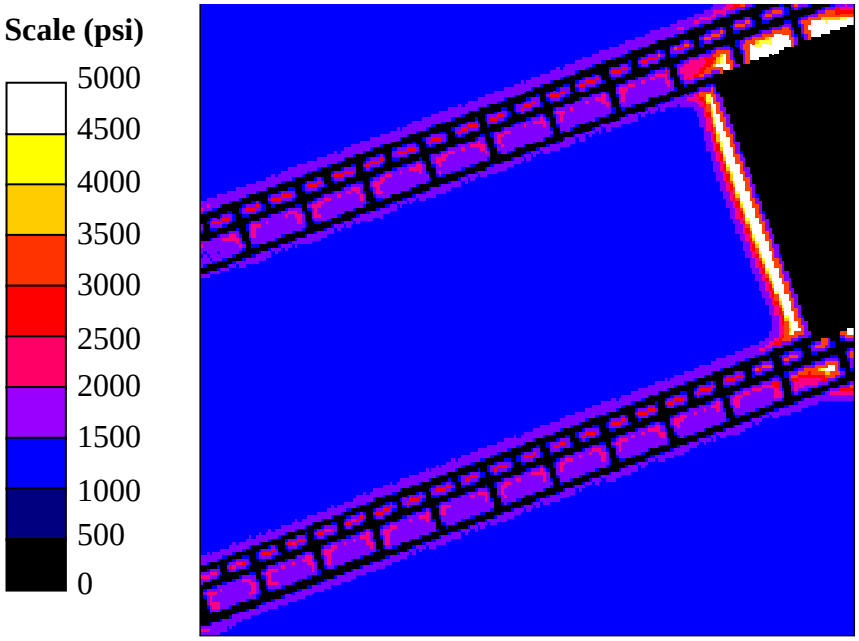

Figure G.1. LAMODEL stress plot at Z = 5,550 feet

07-21-97
Plan View at Z = 5,550 feet (Seam Level)

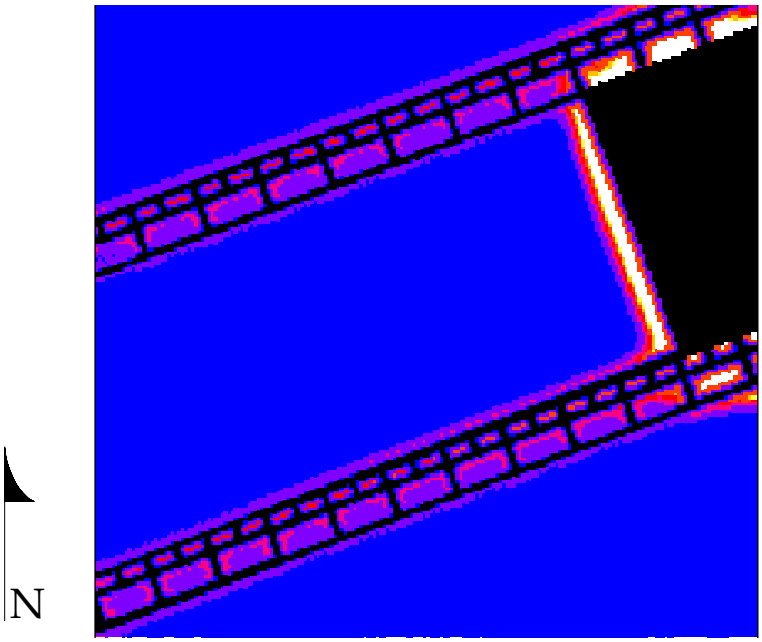

Figure G.2. LAMODEL stress plot at Z = 5,550 feet

07-22-97
Plan View at Z = 5,550 feet (Seam Level)

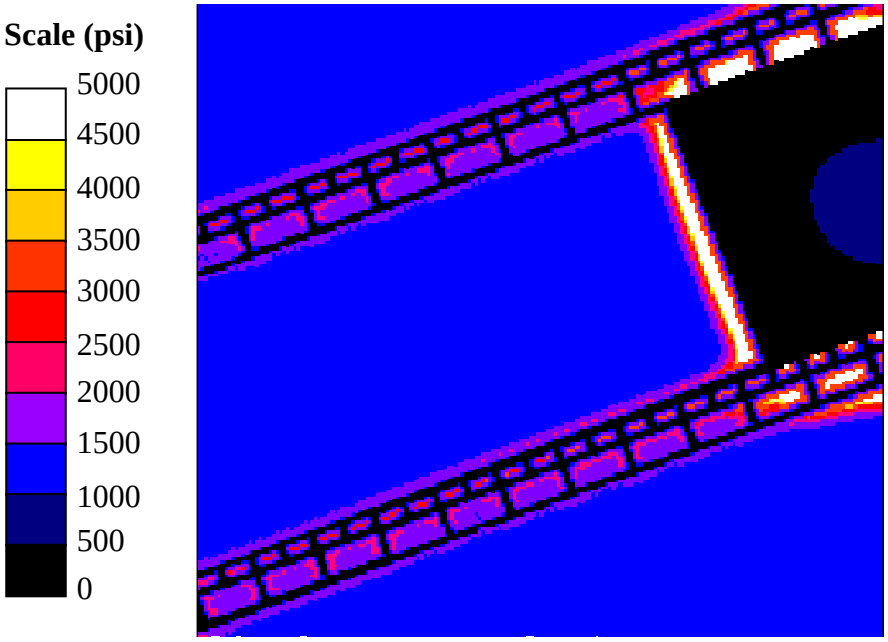

Figure G.3. LAMODEL stress plot at Z = 5,550 feet

07-23-97
Plan View at Z = 5,550 feet (Seam Level)

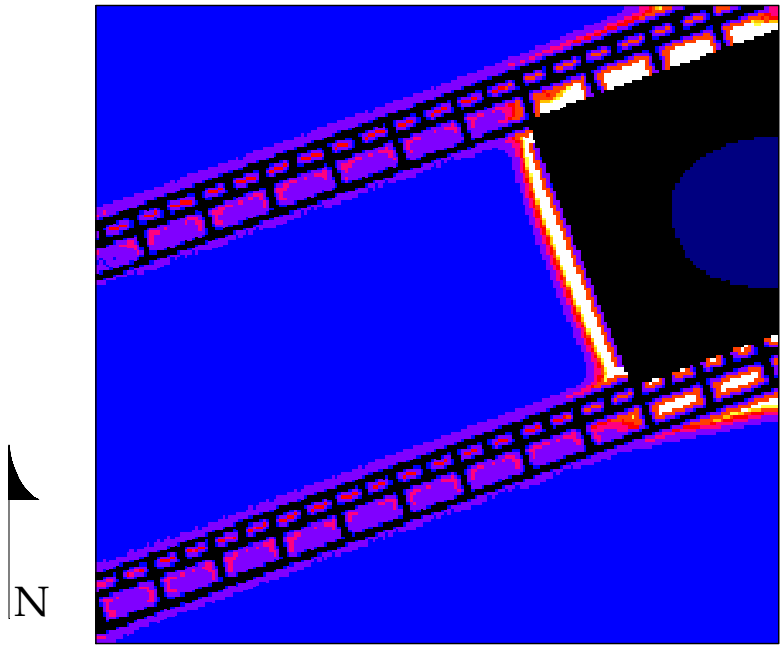

Figure G.4. LAMODEL stress plot at Z = 5,550 feet

07-24-97
Plan View at Z = 5,550 feet (Seam Level)

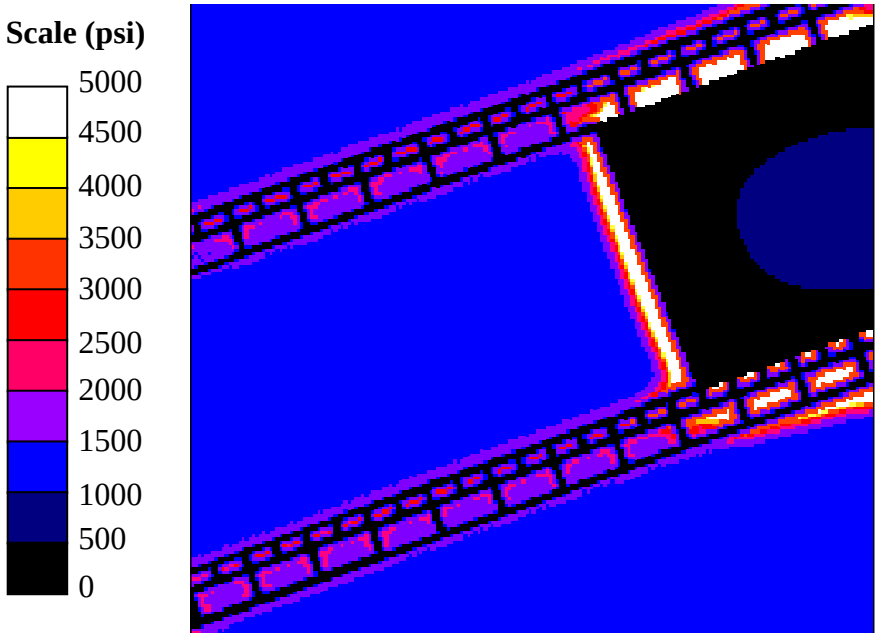

Figure G.5. LAMODEL stress plot at Z = 5,550 feet

07-25-97
Plan View at Z = 5,550 feet (Seam Level)

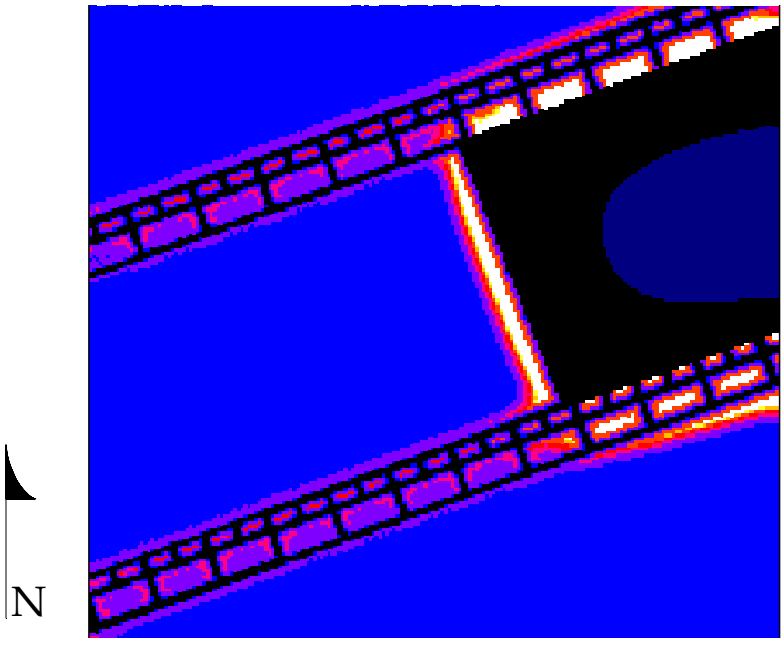

Figure G.6. LAMODEL stress plot at Z = 5,550 feet

07-26-97
Plan View at Z = 5,550 feet (Seam Level)

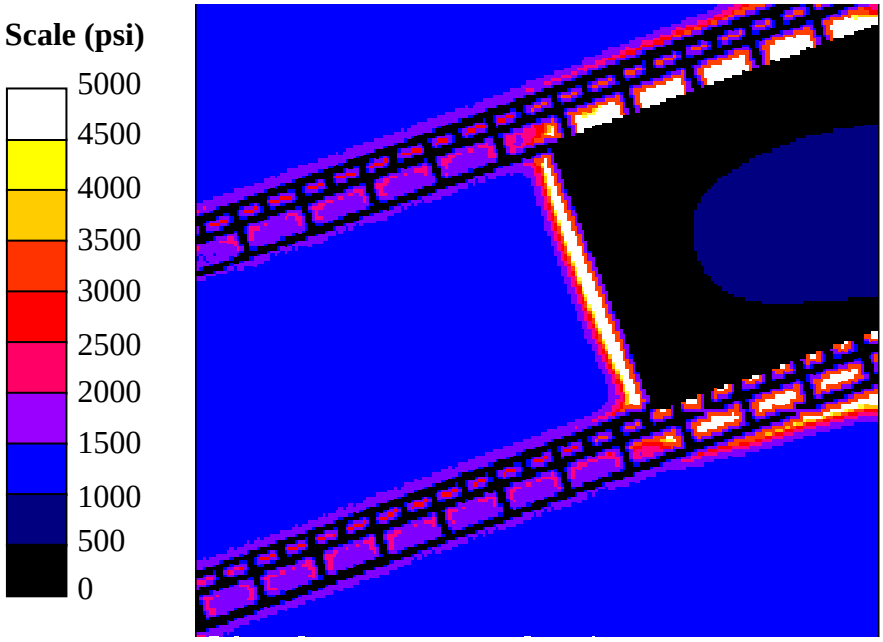

Figure G.7. LAMODEL stress plot at Z = 5,550 feet

07-27-97
Plan View at Z = 5,550 feet (Seam Level)

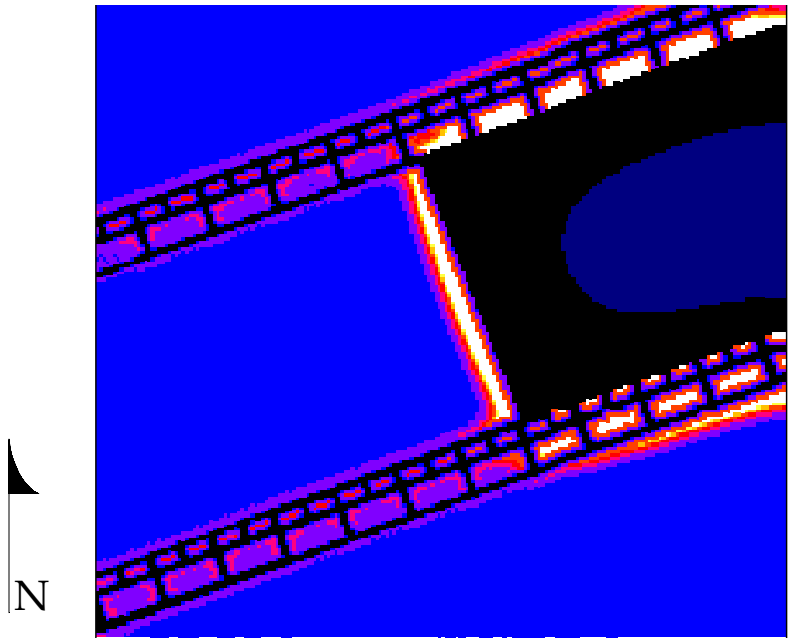

Figure G.8. LAMODEL stress plot at Z = 5,550 feet

07-28-97
Plan View at Z = 5,550 feet (Seam Level)

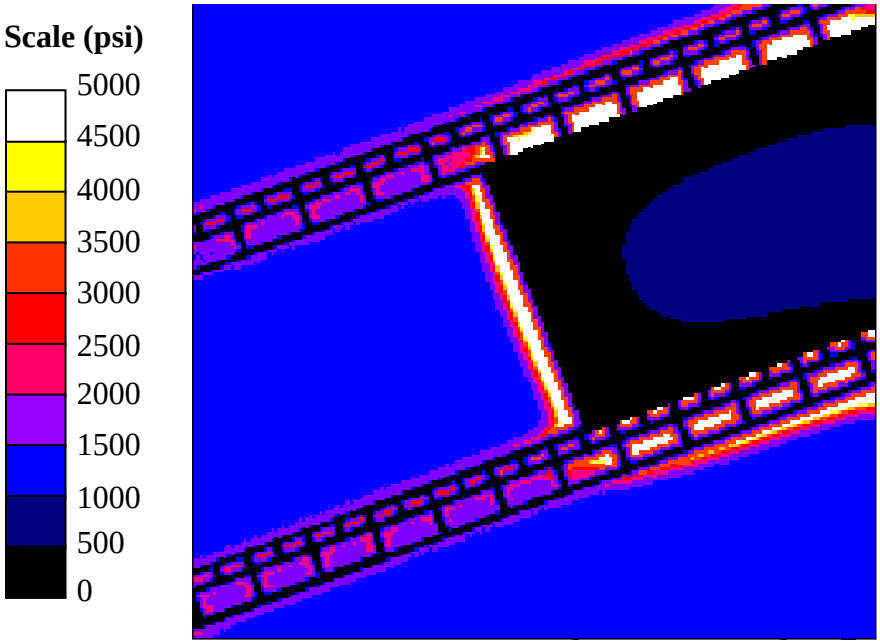

Figure G.9. LAMODEL stress plot at Z = 5,550 feet

07-30-97
Plan View at Z = 5,550 feet (Seam Level)

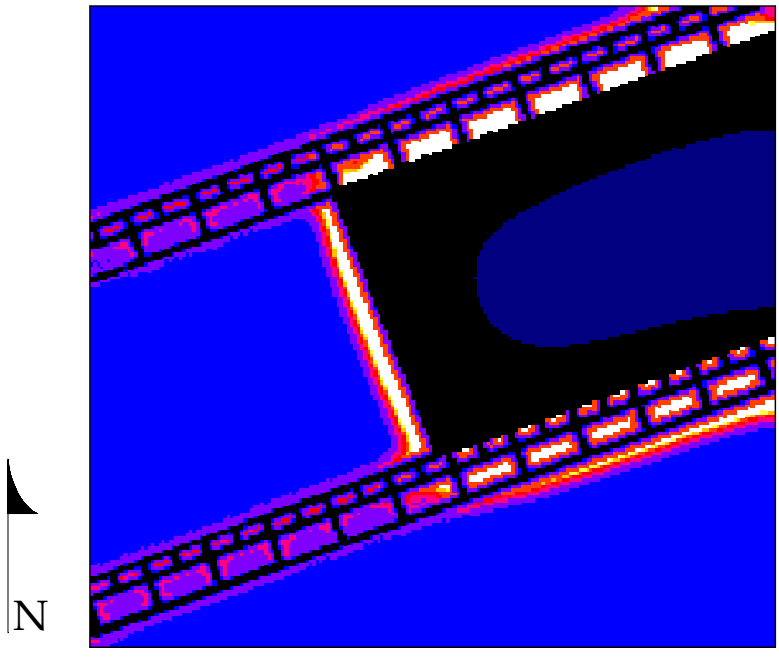

Figure G.10. LAMODEL stress plot at Z = 5,550 feet

07-31-97
Plan View at Z = 5,550 feet (Seam Level)

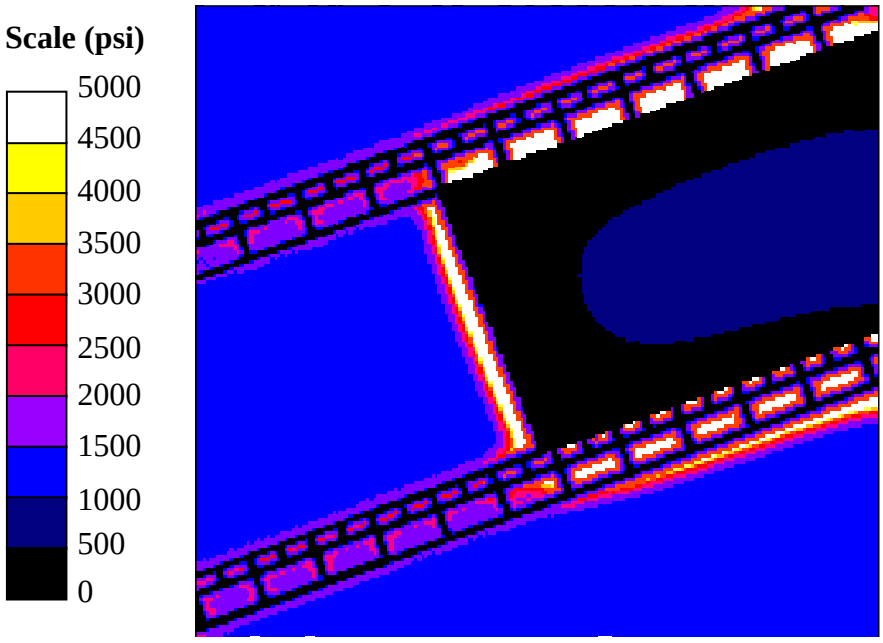

Figure G.11. LAMODEL stress plot at Z = 5,550 feet

08-01-97
Plan View at Z = 5,550 feet (Seam Level)

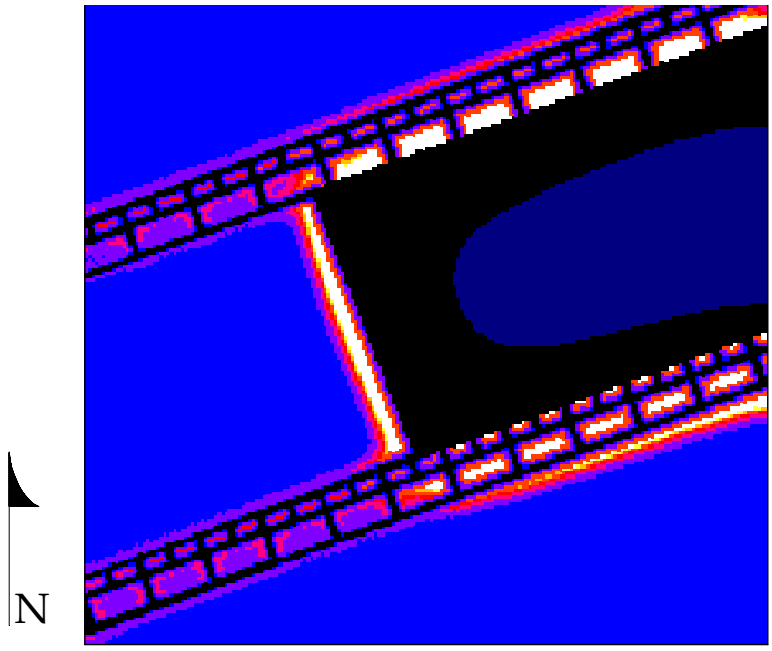

Figure G.12. LAMODEL stress plot at Z = 5,550 feet

08-02-97
Plan View at Z = 5,550 feet (Seam Level)

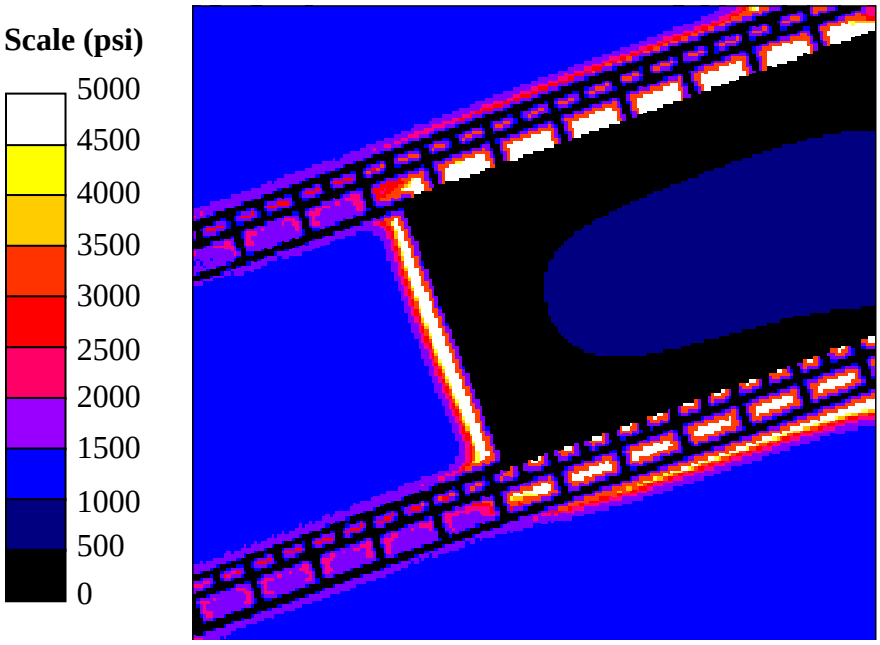

Figure G.13. LAMODEL stress plot at Z = 5,550 feet

08-03-97
Plan View at Z = 5,550 feet (Seam Level)

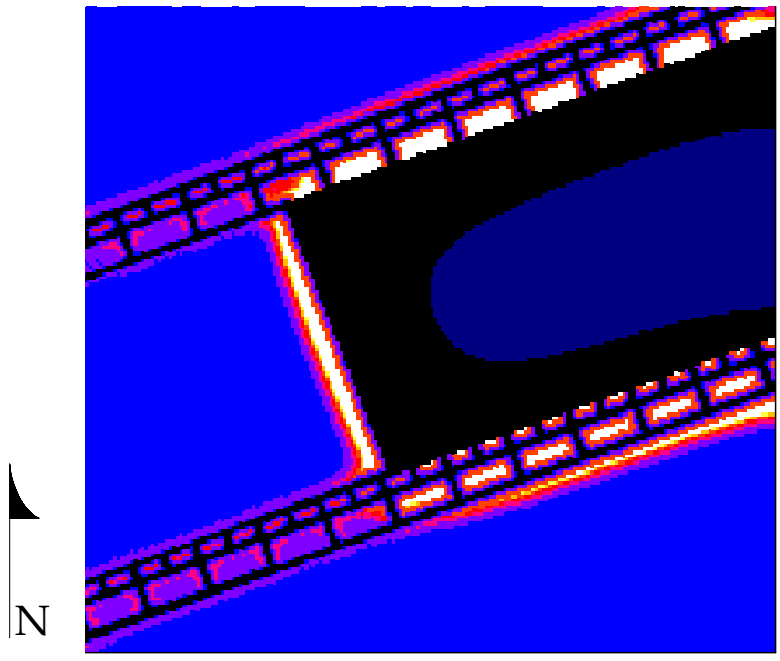

Figure G.14. LAMODEL stress plot at Z = 5,550 feet

08-04-97
Plan View at Z = 5,550 feet (Seam Level)

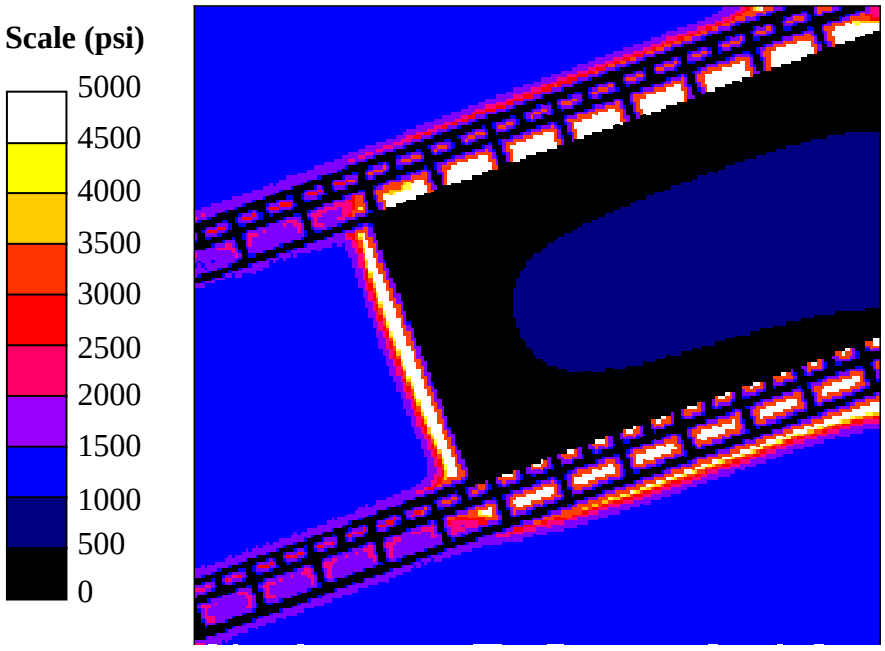

Figure G.15. LAMODEL stress plot at Z = 5,550 feet

08-05-97
Plan View at Z = 5,550 feet (Seam Level)

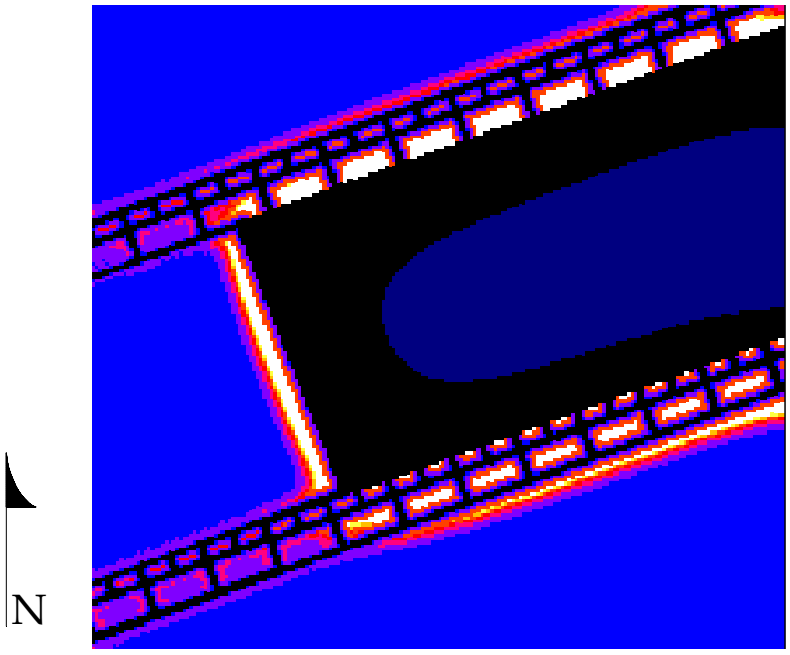

Figure G.16. LAMODEL stress plot at Z = 5,550 feet

08-06-97
Plan View at Z = 5,550 feet (Seam Level)

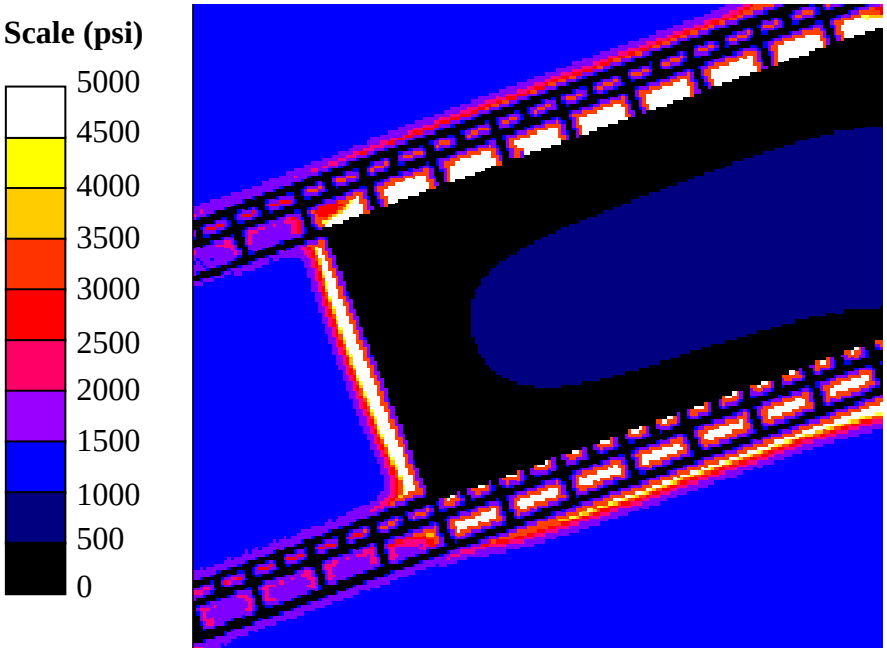

Figure G.17. LAMODEL stress plot at Z = 5,550 feet

08-07-97
Plan View at Z = 5,550 feet (Seam Level)

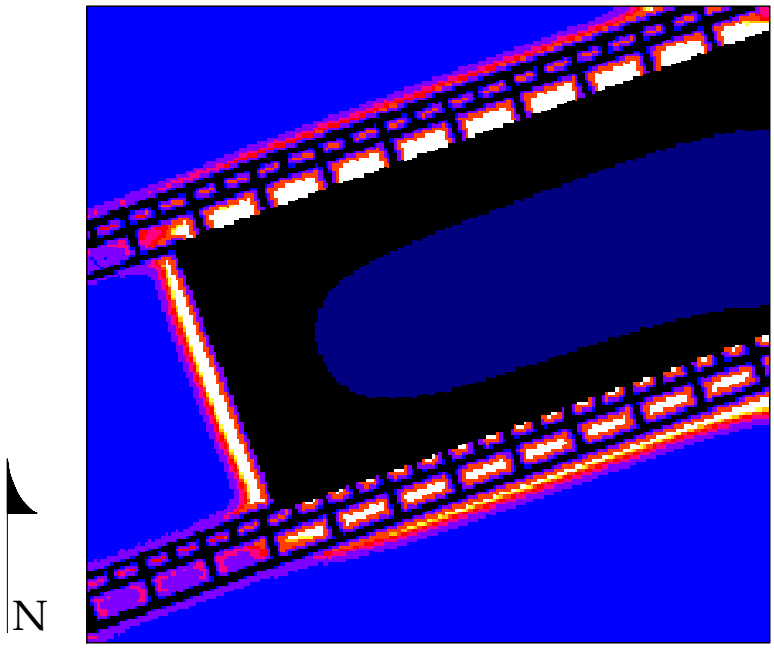

Figure G.18 LAMODEL stress plot at Z = 5,550 feet